Novel Paleoclimate and Paleoenvironmental Applications of Stable and Radiogenic Isotope and Elemental Geochemistry from the Holocene through the Cretaceous

by

Kyle W. Meyer

A dissertation submitted in partial fulfillment
of the requirements for the degree of
Doctor of Philosophy
(Earth and Environmental Sciences)
in The University of Michigan
2018

Doctoral Committee:

Professor Kyger C Lohmann, Co-Chair
Assistant Professor Sierra V. Petersen, Co-Chair
Professor Tomasz K. Baumiller
Professor Joel D. Blum
Professor Donald R. Zak

Kyle W. Meyer

meyerkw@umich.edu

ORCID iD: 0000-0002-1933-2908

DEDICATION

This dissertation is dedicated to Dani McLaughlin, I hope you are at peace in what comes next, my friend. You are missed beyond words.

I also dedicate this to the innumerable volunteers with All Hands and the people of Nepal. No matter how much I tried to give you, you always gave more. I am forever changed and inspired by your resilience, perseverance, and kindness.

.

ACKNOWLEDGMENTS

To begin, I would like to express my appreciation for the tireless efforts of my advisors, Dr. Kyger (Kacey) Lohmann and Dr. Sierra Petersen. Without their guidance and willingness to take a chance on me, I would have never been able to cultivate the tremendous array of experiences offered to me by the University of Michigan Department of Earth and Environmental Sciences.

I am also inestimably grateful and indebted to the ceaseless support of my colleagues, friends, family, and loved ones. This extends to both those I have made whilst enrolled here, and those that have served as constant pillars throughout my life.

The arc of my career trajectory has been unconventional, to say the least, but despite the myriad challenges and complexities there has always been a path to endure. This place has taken a great deal, but it has always given more in the end.

Lastly, I would like to thank you, the reader, for your interest in this work. I wish you the best of luck in finding success on your own path, whatever that may entail. If I may be so bold, I'd like to offer a few words of advice, should you have the time or interest. Please remember to take a step back from things every now and again – perspective is everything, be sure to always keep life in perspective. No matter what difficulties present themselves along the way, there will always be some way forward. Keep walking your path, wherever it may lead you. Know, with confidence, that so long as you continue to do what builds upon your happiness there are no wrong choices.

Most importantly, remember to be kind to yourself.

TABLE OF CONTENTS

CHAPTERS

LIST OF TABLES

TABLE

CHAPTER II

CHAPTER III

CHAPTER IV

LIST OF FIGURES

FIGURE

CHAPTER II

CHAPTER III

CHAPTER IV

LIST OF APPENDICES

APPENDIX

ABSTRACT

Anthropogenic influence on modern climate and the environment is unambiguous and bears profound implications for agriculture, water availability, and natural resource management. These influences are global in extent and require critical examinations of past climatic and environmental perturbations in the geological record to predict the magnitude of anticipated changes (e.g. surface temperature increase) that will impact humanity in the future. This dissertation explores the use of existing and novel geochemical proxies for environmental information ranging from atmospheric circulation patterns of the Pleistocene/Holocene to coastal marine temperatures and volcanism of the Late Cretaceous.

The initial focus of this research has centered on the application of carbonate clumped isotope (Δ_{47}) paleothermometry to marine mollusk fossils in order to reconstruct marine temperatures preceding, during, and after the Cretaceous-Paleogene (K-Pg) extinction. The K-Pg boundary interval serves as an important analogue to modern and future climate projections, with atmospheric CO_2 concentrations estimated at ~400 to 1100 ppm (compared to an annual average of 402.8 ppm in 2016) and a world lacking significant continental ice sheets. The K-Pg boundary is also known for pervasive terrestrial and marine extinctions including the demise of dinosaurian groups. These methods revealed Δ_{47}-derived coastal marine temperatures from the ancient Mississippi Embayment and Atlantic Coast ranging from 7 to 25 °C, which compare closely to modern values in the range of 10 to 29 °C. The similarity between modern and reconstructed paleotemperatures suggests that the surface temperatures required at the subtropics for an unglaciated world may be closer to those observed in the modern than originally believed and implies a shallow equator-to-pole thermal gradient. Cold paleotemperatures along the Atlantic Coast near New Jersey (3 to 14 °C) may provide evidence for the presence of the Gulf Stream current, and subsequent North Atlantic return flow as early as the

Campanian/Maastrichtian. The temperature ranges reconstructed for these sites also compare well to marine temperatures determined using other proxy methods, with the exception of the TEX_{86} organic geochemical temperature proxy, which may be seasonally biased towards summer temperatures.

Coupled with the temperatures reconstructed from Δ_{47} values, we have developed a unique proxy for environmental mercury concentrations, [Hg], in the past using the same mollusk fossils from before, during, and after the K-Pg boundary interval. This work represents the first deep-time application of [Hg] records in biogenic carbonates. We have measured both [Hg] and Δ_{47} values from globally-distributed specimens across a latitudinal range from 70 °N to 67 °S. We found covariation between elevated marine temperatures (~7 to 10 °C excursions) and peak [Hg] between 17 to 42 ng g^{-1} (relative to a background of ~0 to 5 ng g^{-1}) immediately prior to the K-Pg extinction and coinciding with the onset of the main eruptive phase of the Deccan Traps Large Igneous Province (LIP). Evidence of a global signal of volcanogenic emissions (e.g. CO_2 and gaseous elemental Hg) and changing climate prior to the K-Pg boundary suggest causality and serve to clarify the role of the Deccan Traps in terms of extinction patterns. This work also reveals the potential of [Hg] in biominerals at other critical intervals of the geological record in addressing questions relating to LIP volcanism and environmental mercury cycling.

CHAPTER I

Introduction

The earliest applications of measured oxygen isotopic compositions for use as a geochemical proxy for temperature, and what lead to the first quantitative paleoclimate and paleoenvironmental reconstructions, began with the work of Urey (1948), Urey et al. (1951) and Epstein et al. (1951, 1953). These studies redefined low-temperature geochemistry and the application of mass spectrometric analysis in the Earth and environmental sciences. Contemporaneous with the work of Urey, Epstein, and others, advancements in radiogenic isotope compositions and metal isotope systems provided new means of addressing a plethora of geochemical questions (e.g. the age of the Earth; Patterson et al., 1955). The further refinement of gas-source (or gas chromatography) isotope ratio mass spectrometers (IRMS or GC-IRMS; often referred to as "Nier type" magnetic sector instruments) and the advent of multiple filament thermal ionization mass spectrometers (TIMS) permitted the analysis of a broad range of materials to characterize the isotopic compositions of a wide range of elements (Inghram, 1948 and references therein; Inghram and Chupa, 1953). Following these advances in isotopic analysis, came the development of the inductively-coupled plasma mass spectrometer (ICP-MS), which made possible the analysis of nearly the entire periodic table (transition metals, lanthanides, and actinides) and allowed precise determination of minor and trace element concentrations in complicated sample matrices (Wendt and Fassel, 1965; Fassel and Kniseley, 1974; Gray 1974, 1975; Houk et al., 1980; Houk, 1986). The determination of high-precision isotope ratios via ICP-MS only became comparable, and in some cases superior to TIMS analysis, with the implementation of a magnetic sector and an array of Faraday detectors as a multi-collector (MC-)ICP-MS (Bradshaw et al., 1989; Walder and Freedman, 1992; White et al., 2000). Subsequent technological, methodological, and analytical improvements in all of these forms of instrumentation (GC-IRMS, TIMS, MC-ICP-MS) have now permitted investigations into such topics at the forefront of isotope geochemistry including the determination of exceptionally low abundance isotopic compositions, mass-independent fractionations in stable and radiogenic isotope systems, and position- and/or site-specific fractionations within large organic molecules (Eiler et al., 2014, and references therein).

This dissertation employs the use of each of the aforementioned types of mass spectrometry to determine elemental concentrations and isotopic compositions in a variety of natural archive materials to assess past climatic and environmental conditions. In each individual study to follow, we detail new method developments, improved analytical techniques, and novel applications of elemental and isotopic systems to problems that inform concerns relating to climate and the environment, at local and global scales, both present and in the future.

The second chapter of this dissertation, which was published in *Chemical Geology* (Meyer et al., 2017), details measurements of strontium and neodymium isotopic compositions of soluble precipitates and mineral dust from samples of GISP2 ice core retrieved from the Greenland ice sheet drilled at the summit camp from 1988-1993. We successfully determined ε_{Nd} values at unprecedented precision on exceptionally small sample loads (as low as ~150 pg) via the use of prototype 10^{13} Ω resistors. Measured ε_{Nd} values of soluble material (-12.9 ± 2.6 to -7.3 ± 0.9) are interpreted to represent sea salt aerosol based on Sr isotope compositions that resemble seawater values (0.711007 ± 0.000030 to 0.709416 ± 0.000072). The ε_{Nd} of sea salt aerosol likely represents surface water sampling across the North Atlantic, North Pacific, and Arctic Oceans and may reveal past atmospheric circulation patterns at high latitudes through MIS 5. These changes could represent transitions into a climate state with persistent Arctic Oscillation positive anomalies (and thereby pronounced polar vortex conditions at lower latitudes).

In the third chapter, which is in pending an editor's decision with *Cretaceous Research*, we sought to reconstruct coastal marine temperatures at localities across the Gulf and Atlantic Coasts of North America during the Late Cretaceous. The Late Cretaceous experienced elevated atmospheric CO_2 concentrations, and serves as an important analogue for expected future warming from the rise of modern atmospheric CO_2 levels by anthropogenic emissions. We present temperatures from the Late Campanian (~76 – 72 Ma) and Maastrichtian (72 Ma – 66 Ma), as determined by carbonate clumped isotope analysis (Δ_{47}) of fossil marine bivalves and gastropods that range from ~7 – 25 °C across multiple sites from paleolatitudes between 31°N and 36°N. We also compare this temperature range to cooler temperatures (~3 – 14 °C) at sites around 39°N paleolatitude. The temperatures we have determined are very similar to modern temperatures across the same regions, suggesting that the temperature regimes of the mid-latitudes between the modern Earth and a time lacking continental glaciations may be more similar than originally believed. The cooler temperatures recorded at higher latitudes could represent North Atlantic return flow associated with the presence of the Gulf Stream current in the Late Cretaceous. Lastly, we compare the results of the carbonate clumped isotope analyses to published results from other geochemical temperature proxies at sites from comparable latitudes and find agreement with all established proxies with the exception of the organic geochemical proxy TEX_{86} (abbreviated from the tetraether index of 86 carbon atoms). The results of TEX_{86} analyses are dependent on which calibration is used, and the commonly used TEX_{86}^H and TEX_{86}^L calibrations yielded temperatures ranging from ~10 to 12 °C and ~5 °C warmer than the temperatures calculated from our Δ_{47}-

derived results, respectively. All indications suggest that TEX_{86} temperatures overestimate average marine temperatures, likely a product of a seasonal bias towards summer values. We suggest that the TEX_{86}^{L} calibration may be the most appropriate to broadly use for deep time paleoclimate studies and may be useful for determining seasonal variability in these proxy records.

The fourth chapter, in preparation for submission, expands the carbonate clumped isotope results from the previous chapter with temperatures determined for seven additional globally-distributed sample regions spanning modern latitudes from 64 °S to 70 °N. The clumped isotope results are paired with the first-ever deep time records of environmental mercury concentrations, [Hg], from biogenic carbonate in marine mollusk fossil remains, a pioneering new environmental proxy. When compared to current methodologies for analyzing [Hg] in the geological record (e.g. on bulk sediment or rock samples), the ability to simultaneously provide marine temperatures and [Hg] in the same sample material is unprecedented and demonstrates unambiguous links between environmental Hg and climate records. The resulting analyses of Maastrichtian marine mollusk fossil material revealed a detailed global signal of elevated temperatures and [Hg] immediately prior to the Cretaceous–Paleogene (K-Pg) extinction boundary, responsible for the demise of the dinosaurs. At Seymour Island, Antarctica we observe a [Hg] peaks at 17.3 and 16.9 ng g^{-1} corresponding to a 7 to 10 °C increase in temperature and coinciding directly with two phases of volcanic activity from the Deccan Traps Large Igneous Province. In western Alabama, we observed a similar record with peak [Hg] = 42 ng g^{-1} combined with elevated temperatures between ~20 to 25 °C immediately prior to the K-Pg boundary. Our results provide new insights into the nature of extinction patterns observed prior to, during, and after the K-Pg boundary, which appear to be the product of significant climate forcing at the initiation of main phase Deccan eruptions.

This dissertation employs a broad range of geochemical tools to address questions relating to anthropogenic impacts on climate and the environment. Through careful assessment of records of aerosol material in the GISP2 ice core we can infer likely changes to atmospheric circulation patterns as the result of climate forcing from CO_2 emissions (Chapter II). By evaluating ancient coastal marine temperatures across the Gulf and Atlantic Coasts of North America from a time of known comparable and/or elevated CO_2 concentrations relative to the present, we gain crucial insights into how a largely unglaciated world impacts coastal regions in the mid-latitudes (Chapter III). Lastly, through combined estimates of temperatures and environmental [Hg], we can gauge the impact of abrupt, natural climate forcing events (e.g. large igneous province volcanism) and how this may enhance, modify, and/or cause extinction patterns in biota at during major events and perturbations in the geological record (Chapter IV).

References

Bradshaw, N., Hall, E.F.H., Sanderson, N.E., 1989. Communication. Inductively coupled plasma as an ion source for high-resolution mass spectrometry. J. Anal. At. Spectrom. 4, 801–3. doi:10.1039/ja9890400801

Eiler, J.M., Bergquist, B., Bourg, I., Cartigny, P., Farquhar, J., Gagnon, A., Guo, W., Halevy, I., Hofmann, A., Larson, T.E., Levin, N., Schauble, E.A., Stolper, D., 2014. Frontiers of stable isotope geoscience. Chemical Geology 372, 119–143. doi:10.1016/j.chemgeo.2014.02.006

Epstein, S., Buchsbaum, R., Lowenstam, H., Urey, H.C., 1951. Carbonate-Water Isotopic Temperature Scale. Geo. Society Am. Bull. 62, 417. doi:10.1130/0016-7606(1951)62[417:cits]2.0.co;2

Epstein, S., Buchsbaum, R., Lowenstam, H.A., Urey, H.C., 1953. Revised Carbonate-Water Isotopic Temperature Scale. Geo. Society Am. Bull. 64, 1315. doi:10.1130/0016-7606(1953)64[1315:rcits]2.0.co;2

Gray, A.L., 1975. Mass-spectrometric analysis of solutions using an atmospheric pressure ion source. Analyst 100, 289–11. doi:10.1039/an9750000289

Gray, A.L., 1974. It all depends on the source. Proc. Soc. Anal. Chem. 11, 182–2. doi:10.1039/sa9741100182

Houk, R.S., 1986. Mass spectrometry of inductively coupled plasmas. Anal. Chem. 58, 97A–105A. doi:10.1021/ac00292a003

Houk, R.S., Fassel, V.A., Flesch, G.D., Svec, H.J., Gray, A.L., Taylor, C.E., 1980. Inductively coupled argon plasma as an ion source for mass spectrometric determination of trace elements. Anal. Chem. 52, 2283–2289. doi:10.1021/ac50064a012

Inghram, M.G., 1948. Modern Mass Spectroscopy, Advances in Electronics and Electron Physics, Advances in Electronics and Electron Physics. Elsevier. doi:10.1016/s0065-2539(08)61104-x

Inghram, M.G., Chupka, W.A., 1953. Surface Ionization Source Using Multiple Filaments. Rev. Sci. Instrum. 24, 518–520. doi:10.1063/1.1770774

Meyer, K.W., Aciego, S., Koornneef, J.M., 2017. Radiogenic isotopic compositions of low concentration dust and aerosol from the GISP2 ice core. Chemical Geology 472, 31–43. doi:10.1016/j.chemgeo.2017.09.021

Patterson, C., Tilton, G., Inghram, M., 1955. Age of the Earth. Science 121, 69–75. doi:10.2307/1682081?ref=search-gateway:27a22b1e19e120ff8352e40803f58fee

Urey, H.C., 1948. Oxygen Isotopes in Nature and in the Laboratory. Science 108, 489–496. doi:10.2307/1677444?ref=search-gateway:6f9116a9840b9d8a59639ba677bf1e94

Urey, H.C., Lowenstam, H.A., Epstein, S., McKinney, C.R., 1951. Measurement of Paleotemperatures and Temperatures of the Upper Cretaceous of England, Denmark, and the Southeastern United States. Geo. Society Am. Bull. 62, 399. doi:10.1130/0016-7606(1951)62[399:mopato]2.0.co;2

Walder, A.J., Freedman, P.A., 1992. Communication. Isotopic ratio measurement using a double focusing magnetic sector mass analyser with an inductively coupled plasma as an ion source. J. Anal. At. Spectrom. 7, 571–5. doi:10.1039/ja9920700571

Wendt, R.H., Fassel, V.A., 1965. Induction-Coupled Plasma Spectrometric Excitation Source. Anal. Chem. 37, 920–922. doi:10.1021/ac60226a003

White, W.M., Albarède, F., Télouk, P., 2000. High-precision analysis of Pb isotope ratios by multi-collector ICP-MS. Chemical Geology 167, 257–270. doi:10.1016/s0009-2541(99)00182-5

CHAPTER II

Radiogenic Isotopic Compositions of Low Concentration Dust and Aerosol from the GISP2 Ice Core

Citation:
Meyer, K.W., Aciego, S., Koornneef, J.M., 2017. Radiogenic isotopic compositions of low concentration dust and aerosol from the GISP2 ice core. Chemical Geology 472, 31–43. doi:10.1016/j.chemgeo.2017.09.021

Abstract

We have produced a record of radiogenic isotope compositions of particulate and soluble dust fractions from the GISP2 ice core, from basal ice to the surface. For each respective dust fraction we measured Sr and Nd isotope values to constrain the provenance of mineral dust and sea salt aerosol transported to the Greenland Ice Sheet. We have produced high-precision measurements of $\varepsilon_{\mathrm{Nd}}$ values on sub-ng quantities of Nd in ice core samples via TIMS with 10^{13} ohm resistors. The range of measured $\varepsilon_{\mathrm{Nd}}$ values of soluble material (-12.9 ± 2.6 to -7.3 ± 0.9) is interpreted to represent sea salt aerosol based on Sr isotope compositions that resemble seawater values (0.711007 ± 0.000030 to 0.709416 ± 0.000072). Therefore, the $\varepsilon_{\mathrm{Nd}}$ potentially provides important insights to the atmospheric circulation patterns at high latitudes at least through MIS 5. We compare $\varepsilon_{\mathrm{Nd}}$ values of surface seawater from ocean basins and deltas at high latitudes to alternating relatively radiogenic and unradiogenic $\varepsilon_{\mathrm{Nd}}$ at GISP2. We suggest these changes represent transitions between a climate system dominated by enhanced and persistent Arctic Oscillation positive

anomalies (as determined from sea level and ocean bottom pressure measurements), and a state representative of modern atmospheric circulation, which typically exhibits either negative anomalies or none altogether.

1. Introduction

Particulate mineral dust and soluble precipitates deposited on the Greenland Ice Sheet (GrIS) have been used to assess potential source areas of aerosol material in order to understand Northern Hemisphere atmospheric circulation and dynamics through time (Mayewski et al., 1994, 1997; Biscaye et al., 1997; Fischer et al., 2007; Lupker et al., 2010). Radiogenic isotope tracers (Nd, Sr, Hf, U, and Pb) are powerful tools for uniquely fingerprinting different marine and terrestrial dust sources transporting material to the GrIS (Biscaye et al., 1997; Bory et al., 2003; Grousset and Biscaye, 2005; Lupker et al., 2010; Aarons et al., 2013; Aarons et al., 2016a; Aarons et al., 2016b). The radiogenic isotope signatures of soluble precipitates, interpreted to represent marine-derived sea salt aerosol (SSA; Lewis and Schwartz, 2004; Lupker et al., 2010), likely reflect atmospheric “sampling” of surface waters around Greenland and the Arctic Ocean via sea spray, bursting bubbles, and sea ice processes (e.g. frost flower development; Fischer et al., 2007). Aside from a few studies evaluating the radiogenic isotope compositions of dust in Greenland ice cores and surface snow (Biscaye et al., 1997; Bory et al. 2003; Lupker et al., 2010), the signature of the SSA component is largely unconstrained below a core depth of 135 m (e.g. Dye 3; Lupker et al., 2010). Ice core records, such as those retrieved from the Summit Camp in Greenland, bear potential to document changes in SSA compositions with time and may allow us to infer generalized atmospheric circulation patterns for SSA deposition onto the GrIS.

The Greenland Ice Sheet Project 2 (GISP2) retrieved 3053.44 m of ice core from the summit of the GrIS over five drilling seasons from 1988 – 1993, and yielded a continuous 110 ka archive of Northern Hemisphere climate (Grootes et al, 1993; Meese et al., 1997). This ice core has contributed significantly to our understanding of past climate dynamics providing information on temperature variability inferred from oxygen isotope values (δ^{18}O) of the ice (Grootes et al., 1993), mineral dust deposition and flux across the ice sheet (Ram et al., 1995, 2000; Ram and Koenig, 1997; Biscaye et al., 1997), changes in atmospheric CO_2 and CH_4 concentrations (Smith et al., 1997a & 1997b; Brook et al., 1996 & 2000), and volcanic eruptive and biomass burning events (ECM; Taylor et al., 1993 & 1997).

In this study, we present Nd and Sr isotope values of deep ice samples from the GISP2 ice core on bulk soluble and particulate material on sub-ng element concentrations. These measurements provide unprecedented high-precision Nd isotopic results of marine-derived SSA precipitates in the Northern Hemisphere, following similar analytical procedures of Koornneef et al. (2014) and Aarons et al. (2016a, 2016b). We observe statistically significant variability in Nd isotope values, which we suggest represent a proxy for: (1) long-term changes in the phases of Arctic Oscillation/North Atlantic Oscillation (AO/NAO) atmospheric circulation modes, (2) variable sea-ice extent, and/or (3) alternation between local and regional sources of dust deposition (e.g. heterogeneities in surface water or sea ice Nd isotopic compositions).

1.1 Temporal constraints on the ice core record

The GISP2 core from the summit of the GrIS has shown remarkable covariation with the proximal Greenland Ice Core Project (GRIP) core, and both cores have been chronologically constrained to a depth of approximately 2800 m (Grootes et al., 1993). The remaining > 200 m of each core represent sections that are likely disturbed by the dynamic nature of the ice sheet. The oldest age commonly affixed to GISP2 ice is approximately 110 ka (Grootes et al., 1993; Meese et al., 1997) and efforts have been made to extend the timescale of the GISP2 record through dating deep ice (Bender et al., 1994; Ram et al., 1997; Suwa et al., 2006) back to 237 ka or older (Suwa et al., 2006). Recent work using cosmogenic nuclides (^{10}Be and ^{26}Al), organic carbon, and total nitrogen suggests the presence of a stable ice sheet at the summit location for the past 2.6 Ma (Bierman et al., 2014), the first appearance of ice as early as 7.5 Ma (Bierman et al., 2016), whereas Schaefer et al. (2016) argue that prolonged episodes of nearly complete retreat of the GrIS must have occurred over the same interval, underscoring the need for additional geochronologic constraints on the deepest Greenland ice as the amount of time preserved may extend anywhere in the window of 110 ka to 2.6 Ma.

1.2 High latitude atmospheric and Arctic Ocean circulation patterns

Atmospheric and oceanic circulation at high latitudes involves the interplay between the major ocean basins, sea ice extent, influences from the GrIS and Canadian ice caps, and the interactions of the Polar and Ferrel cells in accommodating heat transport from lower latitudes.

The Northern Hemisphere Annular Mode (NAM) describes the dynamics of atmospheric circulation through two phenomena, the Arctic Oscillation and the North Atlantic Oscillation. The Arctic Oscillation (AO) represents a pattern of variability whereby there is bimodal change relating to the strength of the polar jet stream and the relative pressure gradient between the Polar and Ferrel cells (Thompson and Wallace, 1998 & 2000; Wallace, 2000; Ambaum et al. 2001; Wanner et al., 2001). During the positive mode (+) of the AO there exists a high relative pressure gradient (with low sea level and ocean bottom pressure anomalies centered over the Makarov Basin to the Nordic Seas) and a strong, stable polar jet stream acting to confine colder air masses at the pole (Thompson and Wallace, 1998 & 2000; Wallace, 2000; Ambaum et al. 2001; Wanner et al., 2001; Peralta-Ferriz et al., 2014). During the negative mode (-), the pressure gradient weakens permitting destabilization and development of large meander lobes and Rossby waves in the polar jet, which allow the advance of cold air masses to lower latitudes (Figure 1; Ambaum et al., 2001; Wanner et al., 2001). From GRACE satellite observations of ocean bottom pressure (OBP) and reanalysis sea-level pressure (SLP) spanning 2003 to 2012, there is also documented AO variability in the context of “high” AO modes where there is pronounced wintertime AO development (typically corresponding to an AO+ phase) of a strong cyclonic circulation pattern extending from the Canada Basin to the Norwegian Sea, and “low” AO modes (functionally at an AO-neutral phase) with the development of anticyclonic circulation over the Canada Basin (Morison et al., 2012; Peralta-Ferriz et al., 2014).

The second pattern of variability, the North Atlantic Oscillation (NAO), describes the gradient of atmospheric pressure between low pressure over Iceland and high pressure over

Europe (the Icelandic low and Azores high, respectively). This gradient is strong during the positive mode of the NAO (NAO+) and weak during negative phases (NAO-), which are thus anticorrelated with the AO+ mode (Ambaum et al., 2001; Wanner et al., 2001).

It is important to note that both the NAO and the AO exhibit variability on diurnal, monthly, and interannual timescales, and do not represent truly oscillatory or cyclical behavior but rather stochastic processes operating over the aforementioned timescales. However, there are recently documented multi-decadal shifts in the average range of these indices (e.g. an average shift towards a more positive range in AO values from 1989-2010; Morison et al., 2012; Peralta-Ferriz et al., 2014). If shifts in these indices from the modern can be extended through the Pleistocene, then we would anticipate enhanced AO modes of circulation during interglacials, and weaker AO modes during glacial periods with full extent of the Laurentide and Fennoscandian ice sheets. In this study, we use NOAA Hybrid Single Particle Lagrangian Integrated Trajectory Model (HYSPLIT) to perform a first-order assessment of potential air parcel and aerosol transport patterns during each of these modes.

1.3 Aerosol deposition to the Greenland Ice Sheet

Previous studies have evaluated the transport of mineral dust and marine aerosol to the GrIS through non-sea-salt Ca^{2+} ($nssCa^{2+}$) and sea-salt Na^{+} ($ssNa^{+}$) concentrations (Mayewski et al., 1994; Fischer et al., 2007). Records of $ssNa^{+}$ and $nssCa^{2+}$ correlated strongly with one another and were anti-phased with temperature variability, inferred from the GISP2 $\delta^{18}O$ record, with higher concentrations of both ions during the LGM and other stadials by one to two orders of magnitude (Figure 1; Mayewski et al., 1994, 1997; Fischer et al., 2007). The correlation between $nssCa^{2+}$ and $ssNa^{+}$ implies that there are likely similar transport processes for both mineral dust and sea-salt aerosol (Fischer et al., 2007).

Transport to the GrIS is achieved by two mechanisms: dry deposition, as purely advectively transported material, and wet deposition, where aerosols are scavenged by water vapor. The ratio of wet versus dry deposition can be estimated by comparing the total deposition rate determined from $nssCa^{2+}$, $ssNa^{+}$, SO_4^{2-}, and NO_3^{-} concentrations to calculated ice accumulation rates (De Angelis et al., 1997; Mayewski et al., 1997; Cuffey and Clow, 1997; Fischer et al., 1998a, 1998b, 2007). Dry deposition at GISP2 during glacial/stadial intervals is inferred to have increased whereas the accumulation rate decreased by a factor of four, which coincides with an order of magnitude increase in mineral dust and marine aerosol concentrations (Cuffey and Clow, 1997; Fischer et al. 2007). This suggests that dry deposition is the dominant process of dust transport to the ice sheet for the samples measured in this study.

The atmospheric residence time of mineral dust and SSA varies considerably based on factors including wind speed, particle size, seasonal climatic conditions, and storm intensity (Mahowald et al. 1999; Werner et al., 2002). Recent model estimates of arctic SSA residence time indicate significant seasonal variations ranging from less than one day in summer months to more than ten days in winter months (Struthers et al., 2011). In contrast, modeled arctic mineral dust residence times exhibit the opposite seasonality, with higher values (> 15 days) in the spring and summer months and lower values, approximately ten days, in the fall and winter months (Ménégoz et al., 2012). Nilsson and Rannik (2001) measured average bulk aerosol residence times on sea ice floes. Dry deposition of particles was shown to be associated with residence times of approximately five days (Nilsson and Rannik, 2001). But given the short time period of their study, from July to August 1996, dry deposition onto sea ice may ultimately be far more variable annually and intra-annually. However, relatively long atmospheric residence times for both SSA and mineral dust (e.g. > 1 week) allow for the possibility of sourcing from very distal source areas.

1.4 Radiogenic Sr and Nd as provenance tracers

Based on provenance work using radiogenic Sr and Nd isotopes, dust deposition on the GrIS is composed of particulates, dominantly mineral dust, argued to be from a wide variety of terrestrial source regions (e.g. Sahara, Tibetan Plateau), and soluble precipitates believed to be SSA (Biscaye et al., 1997; Bory et al., 2003; Lupker et al., 2010).

Neodymium isotope measurements are evaluated with respect to the Chondritic Uniform Reservoir (CHUR; DePaolo and Wasserburg, 1976). Measured isotope ratios compare the ^{143}Nd/^{144}Nd value to the reference value of (^{143}Nd/^{144}Nd)$_{\text{CHUR}}$ = 0.512638 (Jacobsen and Wasserburg, 1980; Hamilton et al., 1983). These values are then expressed in epsilon notation as follows:

$$\varepsilon_{Nd} = \left(\frac{\left({}^{143}Nd/{}^{144}Nd\right)_{sample}}{\left({}^{143}Nd/{}^{144}Nd\right)_{CHUR}} - 1\right) \times\ 10{,}000 \quad \text{(Eq. 1)}$$

where significant departures of ^{143}Nd/^{144}Nd values from CHUR are typically governed by fractionations associated with crustal rock formation and time through radioactive decay of ^{147}Sm (DePaolo and Wasserburg, 1976; DePaolo, 1981). Strontium isotope measurements are reported as the measured ^{87}Sr/^{86}Sr values and compared to relevant terrestrial compositions of crustal material, and in the context of the range of modern seawater values (0.709060 to 0.709202; Kuznetsov et al., 2012).

Both Sr and Nd isotope compositions evolve with respect to time, where the radioactive decay of ^{87}Rb to ^{87}Sr and ^{147}Sm to ^{143}Nd occur at half-lives of approximately 49 and 106 Byr, respectively (Dickin, 2005). The long half-lives of the radioactive parent isotopes result in only small changes in ^{87}Sr/^{86}Sr and ^{143}Nd/^{144}Nd over long timescales (i.e. Myr). Therefore, the effects of radiogenic Nd and Sr isotopes on source rock isotopic compositions are insignificant over the glacial-interglacial cycles of the GISP2 ice core record (approximately 240 ka). However, Sr and Nd isotope values exhibit a large range of compositions across bedrock lithologies as a consequence of significant differences in Rb/Sr and Sm/Nd ratios. The resulting elemental and isotopic fractionations in Sr and Nd can exhibit distinct radiogenic isotopic compositions for a given region and/or continental landmass (e.g. Precambrian cratons). In turn, sediments derived from these provinces broadly retain these Sr and Nd compositions. In the case of dust, this difference provides a mechanism for determining provenance, and potentially, atmospheric circulation. Weathering of terrestrial material also defines seawater Nd isotopic compositions, which have proven useful for evaluating ocean circulation and riverine sediment fluxes at high latitudes (Figure 2; Lacan and Jeandel, 2004a; 2004b; 2005; Andersson et al., 2008; Porcelli et al., 2009; Lambelet et al., 2016).

Studies have utilized Sr and Nd isotope values as tracers for both particulates and soluble dust fractions, where samples are plotted in a bivariate Sr-Nd isotope space and then can be confined to specific source localities (Figure 3; Biscaye et al., 1997; Bory et al., 2003;

Lupker et al., 2010). We compare our samples to those from modern surface snow at the NorthGRIP site (NGRIP; Bory et al., 2003), samples corresponding to the Last Glacial Maximum (LGM) from GISP2 (Biscaye et al., 1997), and from ~100 m depth of the Dye 3 core (Lupker et al., 2010). The primary source for mineral dust at these sites is hypothesized to be the Mongolian and Chinese deserts (Gobi and Taklimakan) and Ordos plateau (Biscaye et al., 1997; Bory et al., 2003; Fischer et al., 2007; Lupker et al., 2010). In the case of the Dye 3 core, the soluble precipitates were argued to represent SSA sourced from surface waters east of the GrIS (Lupker et al., 2010). In this study, we analyzed core samples from deeper intervals than previously evaluated for the GrIS. Material from terrestrial, open water, and sea ice sources are all believed to potentially contribute to the soluble fraction, however, previous work suggests that the dominant contribution is from SSA (Fischer et al., 2007).

2. Methods

2.1 Ice core processing

Samples of the GISP2 ice core were obtained from the National Ice Core Laboratory (Lakewood, Colorado). We processed two "zero-age" cores (205 m, 206 m) to serve as near-modern analogues. We selected eight samples from 1937–2744 m depth, to which we apply age constraints calculated from an age model fit to the GICC05 depth-age scale from Seierstad et al. (2014) and the NOAA National Climatic Data Center (Figure 12). We processed six samples of deep ice (2802–3037 m) that currently lack firm geochronologic constraints. The core samples were the MCA.02 cut, with a single rounded side from contact with the drill section, and dimensions of ~ 5.5 x 8.5 x 22 cm and mass of ~850-1000 g.

Initial core sample processing and decontamination procedures were adapted from Aciego et al. (2011). The core samples underwent decontamination in a class 100 cleanroom and within class 10 laminar-flow hoods as follows: (1) initial physical removal of frost and debris from the ice using acid-cleaned, perfluoroalkoxy alkane polymer (PFA) chisels embedded with quartz (performed at -20 °C), (2) gradual thermal equilibration (~10 min) of ice samples, followed by rinsing with high-purity distilled ethanol, (3) subsequent physical abrasion and removal of the outer 8-10 mm of the ice surface using additional cleaned PFA chisels, and (4) 2-3 rinses of the ice surface with 18.2 MΩ H_2O and placement in a 2 L PFA capped container.

Following decontamination of the ice, the sample was melted at ambient temperature in the cleanroom (~65 °C). Every hour 10 μL of 5M NH_4NO_3 or 5M NaOH were added to the sample to buffer against the dissolution of carbonates in the particulate dust fraction; in total a maximum volume of 100 μL of the buffering agent was used. The resulting melt water was then filtered (~100 mL aliquots at a time) through a 2-stage acid-cleaned PFA filtration unit pressurized to 5 bar with ultra high purity N_2 gas, and using polytetrafluoroethylene (PTFE) filter membranes to separate particulates at > 30 μm and between 0.2 and 30 μm size fractions, where the latter was used exclusively as the mineral dust fraction for isotopic analysis. The filtered melt water sample was then split into aliquots of ~150 to 180 mL for concentration measurements and ~600 to 800 mL for radiogenic isotope analyses and transferred into pre-cleaned PFA containers. Total procedural blanks for the soluble fraction were processed concurrently with each set of samples; 100-200 mL of 18 MO water and 100 μL of the buffering agent were filtered through the 2-stage acid-cleaned PFA filtration unit with clean PTFE membranes. These blank solutions and sample aliquots for concentration measurements were spiked with enriched ^{150}Nd and ^{84}Sr spike for isotope dilution measurements prior to column chemistry. All samples were subsequently heated at 100°C until dry.

Filtered dust samples were rinsed in distilled ethanol to liberate the trapped particulates from the filter membrane, dried and loaded into 3 mL PFA capped vials with 1 mL of concentrated optima-grade HF and digested for 48 h at 220 °C in a Parr digestion vessel, dried, re-digested in the vessel with 6M HCl for 24 h at 180 °C and dried again.

2.2 Neodymium and strontium column chromatography separations

Chemical separation of Sr and Nd by ion-exchange chromatography was adapted from Aciego et al. (2009). In order to extract Sr and Nd from matrix, three sets of ion-exchange column chromatography were performed for each sample. All column chemistry was conducted using custom-designed columns made from PFA heat-shrink tubing. First, the samples were dissolved in 1 mL of 9M HCl, loaded onto a column packed with 500 μL of Eichrom TruSpec resin (50-100 μm bead size), and then rinsed with 1.5 mL of 9M HCl. These 2.5 ml 9M HCl elutions were collected as they contained the Sr fraction, at a yield of > 90% (Aciego et al., 2009). The Nd was eluted with 1.5 mL 3M HCl followed by 2 mL of 0.25M HCl containing the Nd to be further purified. The Nd fraction was dried and redissolved in 2.5 mL of 3M HCl, loaded onto a column packed with 1000 μL of Eichrom LnSpec resin (100—150 μm bead size), rinsed with 25 ml of 3M HCl and 15 ml of 6M HCl for the selective removal of Yb and Lu, then rinsed with 30 ml of 0.09M citric acid and 1%

H_2O_2 solution, and the retained Nd was collected in 5 ml of 3M HCl-0.1M HF solution and dried. Lastly, the Nd samples were dissolved in 0.5 mL of 0.1M HCl and loaded on a final LnSpec column (2000 μL resin bed; 50—100 μm bead size). The samples were then rinsed with an additional 0.2 mL of 0.1M HCl, 8.5 mL of 0.25M HCl (removal of > 90% La, Ce, and Pr), and then Nd was eluted with 6.5 mL of 0.3M HCl at a yield of > 85% (Aciego et al., 2009).

The Sr fraction collected from the TruSpec column was loaded in 0.3 mL 7.5M HNO_3 on a separate column with 100 μL Eichrom SrSpec resin. The SrSpec column was then rinsed with 3 mL of 7.5M HNO_3 (removal of Ba) and 3 mL of 3M HNO_3 (removal of Rb). Lastly, the final Sr elution was collected with a rinse of 3 mL of 0.05M HNO_3.

2.3 Neodymium and strontium isotopic analysis by TIMS

Particulate dust samples, isotope dilutions, and the soluble fraction Sr splits were analyzed with a Triton *Plus* thermal ionization mass spectrometer (TIMS) at the University of Michigan Glaciochemistry and Isotope Geochemistry Lab (GIGL). All Nd samples measured at GIGL were analyzed in comparison with international reference standard BCR-2, dissolved and passed through column chromatography concurrent with samples, and international instrumental reference material JNdi-1 at $^{143}Nd/^{144}Nd = 0.512613 \pm 0.000007$ ($n = 2, 2\sigma$) and $^{143}Nd/^{144}Nd = 0.512104 \pm 0.000019$ ($n = 9, 2\sigma$), respectively (Table 1). Sr samples were measured in comparison with NIST reference material SRM-987 at $^{87}Sr/^{86}Sr = 0.710263 \pm 0.000008$ (n = 12, 2 S.E.; Table 1).

Due to the exceptionally low concentrations of Nd in the dissolved fraction of each sample and resulting small sample sizes (< 1 ng), these analyses were conducted on a Triton *Plus* TIMS with installed prototype 10^{13} Ω resistors at the Vrije Universiteit Amsterdam. These low noise resistors produce higher precision isotope ratios for small ion beams (<2 x 10^{-13} A) compared to 10^{12} and default 10^{11} *Ω* resistors (Makishima and Nakamura, 2010; Makishima and Nakamura, 2012; Koornneef et al., 2014, 2015; Trinquier and Komander, 2015; Trinquier et al., 2016; von Quadt et al., 2016; Aarons et al., 2016a, 2016b). Faraday gain corrections were performed by normalizing the data to the La Jolla Nd reference material measured once a day using a ^{143}Nd/^{144}Nd value of 0.511841. The dissolved Nd fraction ice core samples were typically run at a ^{144}Nd intensity of 2 x 10^{-13} A (20 mV gain corrected relative to 10^{11} Ω amplifier) for > 200 cycles (8 s integrations). Analytical errors presented in Table 1 are propagated errors including the 2 S.E. errors on the La Jolla reference material. Sample G2-2517-S was large enough to rerun on 10^{11} Ω amplifiers after a 300 cycle measurement on the 10^{13} Ω resistors. The 10^{11} Ω amplifier ^{143}Nd/^{144}Nd data, 0.512231 ± 0.000034 is in excellent agreement with the 10^{13} Ω resistor data (Table 2), confirming the accuracy of the analysis and gain correction procedure. The samples were analyzed in comparison with approximately 20 ng loads of BCR-2 (^{143}Nd/^{144}Nd = 0.512615 ± 0.000034; $n = 3$, 2σ) and AGV-2 (^{143}Nd/^{144}Nd = 0.512779 ± 0.000040; $n = 2$, 2σ) standards run at similar conditions to samples (300 cycles at 2 x 10^{-13} A ^{144}Nd). An in-house standard, CIGO (Centrum Isotopen Geologisch Onderzoek, synthetic Nd_2O_3; Koornneef et al., 2014) run at 100 pg (^{143}Nd/^{144}Nd = 0.511335 ± 0.000050; $n = 13$, 2σ, Table 1) was analyzed to evaluate instrument performance. These results compare to long-term 100 ng loads of CIGO

($^{143}Nd/^{144}Nd$ = 0.511334 ± 0.000010; $n = 28$, 2σ) and 1 ng loads of CIGO on 10^{12} Ω resistors ($^{143}Nd/^{144}Nd$ = 0.511334 ± 0.000010; $n = 17$, 2σ; Koornneef et al., 2013). Standards BCR-2 and AGV-2 were run through the same column chromatographic separations as the ice core samples, whereas CIGO was not. This study is among the first using 10^{13} Ω resistors on natural samples (Aarons et al., 2016a, 2016b), provides consistent and reproducible analyses of natural samples as small as ~150 *p*g, and presents the first Nd isotope results from Greenland ice cores determined with these resistors (Table 1).

3. Results

3.1 Neodymium and strontium isotopic results

The Nd isotopic composition of the dissolved fraction ranged from $^{143}Nd/^{144}Nd$ = 0.511979 ± 0.000132 (ε_{Nd} = -12.9 ± 2.6) to 0.512262 ± 0.000047 (ε_{Nd} = -7.3 ± 0.9), with concentrations ranging from 0.17 to 1.22 ng/kg (Table 1; Figure 1). Dissolved fraction Sr isotopic compositions were between 0.709416 ± 0.000072 and 0.711007 ± 0.000030 with concentrations from 0.4 to 5.3 μg/kg (Table 1). The Nd isotopic composition of the particulate fraction of dust ranged from 0.512059 ± 0.000012 (ε_{Nd} = -11.3 ± 0.2) to 0.512267 ± 0.000048 (ε_{Nd} = -7.2 ± 0.9), and Sr isotope values ranged from 0.714595 ± 0.000024 to 0.721720 ± 0.000091 (Table 1).

In order to interpret the isotopic results, the effect of the blanks first needs to be evaluated. In the case of Sr, total procedural blanks ranged from 0.4 to 1.6 ng, amounting to less than 0.8% of the total sample concentrations for most samples and a maximum of 1.4% for least concentrated samples (205 and 206; Table 4). Total procedural blanks for Nd ranged from 0.4 to 6.5 pg, amounting to less than 2% of the total sample concentration for most samples and 4.5% for the least concentrated sample (2802; Table 4). While these blanks represent higher contributions to the measured samples than traditional high-concentration sample measurements, provided the blank composition is within a natural sample range (0.7 to 0.8 in $^{87}Sr/^{86}Sr$ and -30 to +10 in ε_{Nd}), their impact should be less than the measurement error (100 ppm for Sr and 1 epsilon unit for Nd). The impact of the blank on the isotopic composition can be evaluated by plotting the isotopic compositions of the samples as a function of % blank (Fig. 11). In the figure, there is no correlation ($r^2 = 0.00021$ for Nd) between the ε_{Nd} isotopic composition and blank contribution. However, there is a relatively strong correlation for the $^{87}Sr/^{86}Sr$ composition ($r^2 = 0.75$) where the intercept at 0% blank contribution is 0.70965, closer to the strontium isotopic composition of modern seawater, although does not preclude the possibility of other unradiogenic components to the blank. This observation combined with independent interpretations of the soluble component of Greenland ice cores (Fischer et al., 2007 and references therein; Lupker et al., 2010), allows for the plausible interpretation of this component as SSA. For the sake of providing a test case for the interpretation of these preliminary data, we proceed with this assumption.

The additional slight excursion of the Sr isotope values of the dissolved fraction from the SSA composition can be explained by an interaction with the particulate fraction. The $^{87}Sr/^{86}Sr$ isotopic composition of the soluble fraction is correlated with the particulate fraction in two different sets of ice samples that were processed, with an $r^2 = 0.87$ and 0.60, respectively (Figure 9). No statistically significant correlations were observed between the dissolved and particulate fraction Nd isotope values (which were processed in the same sample set), or between any combination of Sr and Nd compositions of either fraction (Figure 9 and 10). A larger number of samples would, of course, provide better statistics to evaluate these considerations. However, given that these are the first measurements from pre-Holocene ice in Greenland and the technical challenges in collecting this type of data, fifteen samples provides an adequate representation for an initial analysis.

3.2 NOAA HYSPLIT model results

We utilized the NOAA HYSPLIT Model to track air parcel back trajectories for 315 hours prior to final destination and assumed deposition at the Summit Camp of the GrIS (72°34’46.5” N, 38°27’33.07” W; the drilling location for GISP2). We evaluated archival NOAA Climate Prediction Center Arctic Oscillation Index data from 1950 to 2014 and performed HYSPLIT simulations for the most severe AO+ (December, 2010) and AO- (February, 2011) anomalies of the past decade. The full results of these model runs can be found are summarized in Figure 4. We compared ensemble trajectories (multiple back trajectories from the same fixed starting location, at a consistent starting height of 100 m above ground level, AGL) and trajectories from different starting heights (100 m, 250 m, 500 m) and adjusted the initial starting date of the simulation to center on 315 hours of sustained AO+ or AO- conditions (Figure 8). From the model results, we observed two dominant modern transport pathways for air parcels delivered to the Summit Camp in Greenland (Figure 4). Consistent with an AO+ mode, we see the development of a strong, persistent cyclonic circulation over the Arctic Ocean, which appears to deliver airmasses to the GrIS from the west (Figure 4A). Alternatively, for an AO- mode, the resulting circulation patterns appear to more greatly resemble an NAO+ event with a well-developed Icelandic Low and Azores High, where we found exceptionally strong sourcing of air masses from the east of Greenland and tracking through northern Europe (Figure 4B). The HYSPLIT results and previous work regarding oceanic and atmospheric circulation patterns of the high arctic as influenced by the AO (Morison et al. 2012, Peralta-Ferriz et al., 2014) are depicted as a schematic representation of these patterns is presented in Figure 5.

3.3 Nd isotope compositions of High Arctic surface waters

In order to place first-order constraints on the two atmospheric modes observed in the HYSPLIT models that may have influenced the soluble fraction radiogenic isotopic data, we produced a map of surface water ε_{Nd} compositions (Figure 2). The ε_{Nd} values compiled range from -4 to -6 in the Pacific, -8.6 to -24.9 in the North Atlantic, and -9.8 to -11.8 in the Arctic Ocean. We limit surface water ε_{Nd} values used in the map to those collected to a maximum depth of 500 m, where waters to this depth appeared either largely invariant in the sampled profile, or serves to coarsely average the apparent maximum depth threshold for stable surface water masses as suggested in recent GEOTRACES studies of the North Atlantic (Lambelet et al., 2016; van de Flierdt et al., 2016). The surface seawater ε_{Nd} values used (Stordal and Wasserburg, 1986; Lacan and Jeandel, 2004a, 2004b, 2005; Dahlqvist et al., 2007; Andersson et al., 2008; Porcelli et al., 2009; Lambelet et al., 2016) are listed in Table 2.

4. Discussion

4.1 Neodymium and strontium isotope compositions of GISP2 dust samples

Using improved 10^{13} Ω feedback resistors, we have measured Nd isotope values on the dissolved fractions of dust retrieved from 850 to 1000 g ice core samples, or approximately half the sample material utilized in previous studies (Lupker et al., 2010). The corresponding mass of Nd yielded from these core samples was 147 to 1071 pg (Table 2) with an average $\varepsilon_{\mathrm{Nd}}$ analytical uncertainty of ± 1.3 (2 S.E). The analytical uncertainties on the Nd isotope values from this study are identical to previous work that used twice the amount of sample material (Lupker et al., 2010). Furthermore, our smallest sample size (147 pg) resulted in $\varepsilon_{\mathrm{Nd}} = -8.2 \pm 1.1$, highlighting the potential for analysis of different sample matrices with low concentrations of a given analyte using 10^{13} Ω resistors on the current amplifiers for TIMS and MC-ICP-MS. We observed statistically significant variability in Nd isotope compositions between our "zero-age" samples (approximately 205-206 m core depth), serving as modern analogues, and samples from deeper sections of the core both in the chronologically constrained upper 2800 m, and the disturbed bottom 200 m of the ice core (Figure 2). The isotopic variability between samples from both sections of the GISP2 core suggests significant differences in potential sourcing of the soluble fraction of material. Although the disturbed samples may not be useful in an absolutely-resolved time series, they function to provide a basis of comparison for records prior to and after MIS 5.

The measured $^{87}\mathrm{Sr}/^{86}\mathrm{Sr}$ values of the soluble fraction all are slightly more radiogenic than those anticipated for the range of seawater values through the Pleistocene ($^{87}\mathrm{Sr}/^{86}\mathrm{Sr}$ = 0.709060 to 0.709202; Kuznetsov et al., 2012). Moreover, we found that $^{87}\mathrm{Sr}/^{86}\mathrm{Sr}$ values of the soluble fraction correlated with the blank contribution (on the order of 100 ppm, Figure 11) and those measured in the particulate fraction (on the order of 1000 ppm; Figure 11). This correlation suggests that the deviations from predicted seawater $^{87}Sr/^{86}Sr$ values of the soluble fraction of dust are likely attributable to interaction between the soluble and particulate fractions, presumably during initial melting of the ice. The differences in the correlation between our first and second set of core samples ($r^2 = 0.87$ and 0.60, respectively) are possibly due to small differences in processing time of the core samples between sets, the incorporation of basal soluble material in the second set of samples (all samples from the disturbed portion of the core), or small contributions from sources other than sea salt aerosol to the ice sheet. The $^{87}Sr/^{86}Sr$ values of the soluble fraction are suggestive of a prominent marine component for the soluble material, and all exist within the range of values observed previously in the Dye 3 core (Figure 3, Lupker et al., 2010).

The ε_{Nd} and $^{87}Sr/^{86}Sr$ values of the particulate dust fraction all plot within the range of values previously measured in core samples from the GISP2, GRIP, NGRIP, and Dye 3 sites (Figure 3; Biscaye et al., 1997; Svensson et al., 2000; Bory et al., 2003; Lupker et al., 2010). Our data reflect the conclusions of these past studies that the particulate fraction likely represents a mixture of material sourced dominantly from Mongolia and China (e.g. the Gobi Desert, Taklimakan Desert, and the Ordos Plateau) admixed with likely sources from the Sahara.

4.2 Assessing transport mechanisms of dust deposited on the ice sheet

The selection of core samples targeted glacial/stadial time periods with the expectation that there would be higher concentrations of both particulate and soluble fractions of dust in these samples compared to interglacial/interstadial samples, where all samples with the exception of those constrained to ~100 ka were able to capture elevated dust, nssCa^{2+}, and nssNa^{+} concentrations relative to the background of the GISP2 record (Figure 1; Ram et al., 1997; Mayewski et al., 1997; Fischer et al., 2007). For glacial and stadial intervals we also expect decreased accumulation rates at the summit site (Cuffey and Clow, 1997), which would imply that our samples were strongly biased towards dry deposition in terms of transport processes. Further evaluation of core samples from time periods of enhanced accumulation rates would be necessary to evaluate the potential for separating wet and dry deposition in terms of provenance. We presently lack any means of discerning differences between sourcing of sea salt aerosol from either sea ice or open water, although Fischer et al. (2007) argue that the role of sea ice in terms of sea salt aerosol sourcing to the GrIS is likely small both today and during the LGM.

4.3 Neodymium isotope values of arctic surface waters in comparison to GISP2

Given our assumption that the soluble fraction of dust from GISP2 is exclusively sea salt aerosol, we explore the potential sources of seawater Nd that contribute to values measured on the GrIS. Figure 2 depicts every location where seawater Nd has been measured in the arctic (values in boxes with a dashed outline indicate where precise sampling locations are unreported), spanning a range of values from ε_{Nd} = -4.0 in the northern Pacific Ocean to

ε_{Nd} = -24.9 in the northern Atlantic Ocean (Stordal and Wasserburg, 1986; Lacan and Jeandel, 2004a, 2004b, 2005; Dahlqvist et al., 2007; Andersson et al., 2008; Porcelli et al., 2009; Lambelet et al., 2016). We observe that across each of the sampled ocean basins, regionally distinct ranges of ε_{Nd} values become apparent. We have grouped these regions into several different categories: (1) Baffin Bay and the Labrador Sea, (2) the Makarov/Fram Basins and Nordic Seas, (3) the Canada Basin, Bering Strait/Chukchi Sea, and northern Pacific Ocean, and (4) the radiogenic values of the Nansen Fjord/Iceland/Greenland-Scotland Ridge. We have also depicted the ε_{Nd} values of fluvial sediments from major arctic river basins (Andersson et al., 2008; Porcelli et al., 2009; Zimmerman et al; 2009), which may influence (sub)surface seawater ε_{Nd} values (Andersson et al., 2008; Porcelli et al., 2009). We anticipate that atmospheric sampling of arctic surface water masses, without sea ice cover, will result in an aggregated signal of sea salt aerosol that will ultimately be transported to the GrIS. However, given the short residence time of Nd in the ocean (ca. 500 years; Tachikawa et al., 2003), we cannot assume that surface water ε_{Nd} were constant through the Pleistocene as evidenced in work assessing changes in deep water detrital sediment sourcing and evolving weathering inputs through time (Haley et al., 2008a, b; Kurzweil et al., 2010; Chen et al., 2012; Crocket et al., 2012, 2014; Haley and Polyak et al., 2013; Dausmann et al., 2015; Teschner et al., 2016). Seawater Nd isotope records of corals (Wilson et al., 2014) show dynamic oscillations through the Holocene (ε_{Nd} values ranging from approximately -10 to -15), however the contrast of isotopic compositions in the North Atlantic versus the North Pacific may remain intact, which may preserve the relationship with these ocean basins in the modern. If this assumption remains valid, then we can explore the possible role of atmospheric circulation and the Arctic Oscillation as a case study for the Nd isotope data we present.

4.4 Variations in AO as a potential factor in aerosol provenance variability

The results of our HYSPLIT back trajectory modeling are consistent with other studies suggesting the dominant modes of atmospheric circulation in the arctic (Morison et al., 2012; Peralta-Ferriz et al., 2014), and are consistent with our predictions for atmospheric circulation based on modern climatic conditions. Recent work from Peralta-Ferriz et al. (2014) indicates that these two circulation patterns represent the dominant modes of arctic atmospheric circulation, accounting for a combined 70% of variability from GRACE satellite observations in the modern. They describe Mode 1 (50% of observed variability) as a low AO mode (dominated by the long-term prevalence of the AO- phase) and consistent with NAO+ conditions (Figure 5A), and Mode 2 (20% of observed variability) as strongly correlated to high AO conditions (dominantly AO+ phase, Figure 5B; Peralta-Ferriz et al., 2014). These circulation patterns would also have profound effects on Ekman transport and ocean circulation within the arctic, resulting in a situation where in Mode 1 we can anticipate a well-developed Beaufort Gyre (Figure 5C) and in Mode 2 a decreased gyre with enhanced sampling of water from the Bering Strait and northern Pacific (Morison et al., 2012).

4.5 A proposed AO influence on radiogenic isotopes

If the two observed modes of modern atmospheric circulation represent depositional pathways for mineral dust and sea salt aerosol to the GrIS, then we suggest that there may be potential for a proxy for these circulation patterns by evaluating the Nd isotopic composition of the soluble dust fraction within Greenland ice cores. Assuming that these modes are representative of circulation dynamics in the past, we would anticipate the possibility of observing alternations between a dominant Mode 1 and Mode 2 through the Pleistocene.

Otto-Bliesner et al. (2006) produced model estimates that suggest an enhanced AO+ influence relative to modern GRACE observations (Peralta-Ferriz et al., 2014). Enhanced AO+ conditions would be consistent with our observation of higher $\varepsilon_{\mathrm{Nd}}$ values during glacial stadials as a result of either: (1) increased sampling from the Northern Pacific through the expected change in atmospheric circulation, (2) reduced contribution of the primary source of unradiogenic Nd from water in the Northern Atlantic, which would be subducted under a prominent cold halocline (Hebbeln et al., 1994; Bauch et al, 2001; Rasmussen and Thomsen, 2004; Cronin et al., 2012; Jakobsson et al., 2014, 2016), or (3) some combination of these factors (Figure 1, 2). Furthermore, in the only comprehensive study to model polar atmospheric circulation, the presence of the Laurentide Ice Sheet was observed to likely force a mechanical E-W split in the jet stream that predominated in winter, resulting in a northern and southern branch, which scaled linearly with ice sheet height and the strength of the split (Figure 6; Bromwich et al., 2004). The lack of an abrupt change in the split jet stream with ice sheet height suggests that even for recessed or waning conditions of the Laurentide Ice Sheet the split would persist at varying intensity (Bromwich et al., 2004). Therefore, it is possible that during stadials, and the LGM, a split jet stream forced across the Northern Pacific, Arctic Ocean, and Greenland could accommodate distal SSA sampling that is delivered to the GrIS, which could then explain the variability in our measured $\varepsilon_{\mathrm{Nd}}$ values.

We also cannot discount the possibility of reduced sourcing of the relatively unradiogenic North Atlantic surface waters that would likely be forced to subduct beneath arctic water masses.

Ultimately, further evaluation of ε_{Nd} values of the soluble fraction of dust in Greenland ice cores is required to fully explore this suggested proxy. A comprehensive analysis of samples spanning both glacial/interglacial (and stadial/interstadial) intervals would be necessary to test our hypothesized atmospheric circulation patterns during the Pleistocene. Additionally, records of reconstructed arctic surface water ε_{Nd} values would be needed to better assess the possibility of significant compositional changes in seawater ε_{Nd} values. Further sampling of modern seawater ε_{Nd} values is also required to more adequately assess ε_{Nd} of potential source regions to the GrIS. For example, the ε_{Nd} value of proximal surface seawater predicted to be sampled during Mode 2 prevalence draws upon a single sample locality from the Nansen Fjord ($\varepsilon_{Nd} = -5.8$, averaged to 500 m depth). We would predict that the ε_{Nd} value of Nansen Fjord is probably not strongly representative of the rest of old continental crust of East Greenland coast, due to the presence of high radiogenic values $\varepsilon_{Nd} = +8$ of the surficial bedrock in this region (Lacan and Jeandel, 2004b), but would still be representative of local radiogenic SSA sampling associated with material weathered from Iceland. Given the degree of ice sheet and sea ice coverage predicted through the glacial intervals of the Pleistocene and Holocene, it remains unclear as to whether or not SSA with more radiogenic ε_{Nd} values in coastal waterways of Greenland, Iceland and the Greenland-Scotland Ridge would be more or less contributing than distant North Pacific sources.

5. Conclusions

We highlight the potential of analyzing the isotopic composition of minimum amounts of Nd extracted from the soluble fraction of GISP2 ice core samples, and the possibility of adding new constraints on atmospheric circulation patterns and/or changes to the Nd isotopic compositions of SSA source waters in the arctic through the Late Pleistocene. The success of measuring Nd isotopic compositions of sub-ng scale material also allows for myriad other applications where detection limits have been too low or analytical uncertainties have been too high, provided that procedural blanks are low enough to be negligible or could be corrected for when characterized isotopically. Expanding the soluble dust Nd isotope record of Greenland ice cores presented here represents one such case and has exciting potential for insights into past climate of the Northern Hemisphere, and with more ice core Nd isotope data for the Southern Ocean (Lacan et al., 2012; van de Flierdt et al., 2016 and references therein) there may also exist potential to assess Southern Hemisphere circulation patterns as well.

Acknowledgements: Funding for this project was provided by the National Science Foundation Arctic Natural Sciences Program under grant NSF 1107369 to S.M. Aciego. We thank Claudia Bouman and Thermo Fisher Scientific for providing the necessary instrumentation support and prototype amplifiers to conduct the analyses for this study, and Paolo Gabrielli with the Byrd Polar Research Center at the Ohio State University for MC-ICP-MS analyses as comparison to measured concentrations by TIMS.

References

Aarons, S.M., Aciego, S.M., Gleason, J.D., 2013. Variable Hf-Sr-Nd radiogenic isotopic compositions in a Saharan dust storm over the Atlantic: Implications for dust flux to oceans, ice sheets and the terrestrial biosphere. *Chemical Geology* 349-350, 18–26. doi:10.1016/j.chemgeo.2013.04.010

Aarons, S.M., Aciego, S.M., Gabrielli, P., Delmonte, B., Koornneef, J.M., Uglietti, C., Wegner, A., Blakowski, M.A., Bouman, C., 2016a. Ice core record of dust sources in the western United States over the last 300years. *Chemical Geology* 442, 160–173. doi:10.1016/j.chemgeo.2016.09.006

Aarons, S.M., Aciego, S.M., Gabrielli, P., Delmonte, B., Koornneef, J.M., Wegner, A., Blakowski, M.A., 2016b. The impact of glacier retreat from the Ross Sea on local climate: Characterization of mineral dust in the Taylor Dome ice core, East Antarctica. *Earth and Planetary Science Letters* 444, 34–44. doi:10.1016/j.epsl.2016.03.035

Aciego S. M., Bourdon B., Lupker M. and Rickli J. (2009) A new procedure for separating and measuring radiogenic isotopes (U, Th, Pa, Ra, Sr, Nd, Hf) in ice cores. *Chemical Geology* 266, 194–204.

Aciego S. M., Bourdon B., Schwander J., Baur H. and Forieri A. (2011) Toward a radiometric ice clock: uranium ages of the Dome C ice core. *Quaternary Science Reviews* 30, 2389–2397.

Ambaum M., Hoskins B. J. and Stephenson D. B. (2001) Arctic oscillation or North Atlantic oscillation? *Journal of Climate* 14, 3495–3507.

Andersson, P.S., Porcelli, D., Frank, M., Björk, G., Dahlqvist, R., Gustafsson, Ö., 2008. Neodymium isotopes in seawater from the Barents Sea and Fram Strait Arctic–Atlantic gateways. *Geochimica et Cosmochimica Acta* 72, 2854–2867. doi:10.1016/j.gca.2008.04.008

Bauch, D., & Bauch, H. A. (2001). Last glacial benthic foraminiferal δ18O anomalies in the polar North Atlantic: a modern analogue evaluation. *Journal of Geophysical Research* 106, 9135-9143.

Bender M., Sowers T., Dickson M. L. and Orchardo J. (1994) Climate correlations between Greenland and Antarctica during the past 100,000 years. *Nature* 372, 663-666.

Bierman P. R., Corbett L. B., Graly J. A., Neumann T. A. and Lini A. (2014) Preservation of a Preglacial Landscape Under the Center of the Greenland Ice Sheet. *Science*. 344, 6182, 402-405.

Bierman, P.R., Shakun, J.D., Corbett, L.B., Zimmerman, S.R., Rood, D.H., 2016. A persistent and dynamic East Greenland Ice Sheet over the past 7.5 million years. *Nature* 540, 256–260. doi:10.1038/nature20147

Bory A. J. M. (2003) Two distinct seasonal Asian source regions for mineral dust deposited in Greenland (NorthGRIP). *Geophysical Research Letters* 30, 1167.

Biscaye P. E., Grousset F. E., Revel M., Van der Gaast S., Zielinski G. A., Vaars A. and Kukla G. (1997) Asian provenance of glacial dust (stage 2) in the Greenland Ice Sheet Project 2 ice core, Summit, Greenland. *Journal of Geophysical Research* 102, 26765–26–781.

Bromwich D. H., Toracinta E. R., Wei H. L., Oglesby R. J., Fastook J. L. and Hughes T. J. (2004) Polar MM5 simulations of the winter climate of the Laurentide Ice Sheet at the LGM. *J. Climate* 17, 3415–3433.

Brook E. J., Sowers T. and Orchardo J. (1996) Rapid variations in atmospheric methane concentration during the past 110,000 years. *Science* 273, 5278, 1087-1091.

Brook E. J., Harder S., Severinghaus J., Steig E. J. and Sucher C. M. (2000) On the origin and timing of rapid changes in atmospheric methane during the Last Glacial Period. *Global Biogeochem. Cycles* 14, 559–572.

Chen, J., Li, G., Yang, J., Rao, W., Lu, H., Balsam, W., et al. (2007). Nd and Sr isotopic characteristics of Chinese deserts: Implications for the provenances of Asian dust. *Geochimica Et Cosmochimica Acta*, 71 (15), 3904–3914. http://doi.org/10.1016/j.gca.2007.04.033

Chen, T. Y., Frank, M., Haley, B. A., Gutjahr, M., and Spielhagen, R. F. (2012), Variations of North Atlantic inflow to the central Arctic Ocean over the last 14 million years inferred from hafnium and neodymium isotopes, *Earth and Planetary Science Letters* 353, 82-92.

Crocket, K. C., Vance, D., Foster, G. L., Richards, D. A., and Tranter, M. (2012), Continental weathering fluxes during the last glacial/interglacial cycle: insights from the marine sedimentary Pb isotope record at Orphan Knoll, NW Atlantic, *Quaternary Science Reviews* 38, 89-99.

Crocket, K. C., M. Lambelet, T. van de Flierdt, M. Rehkämper, and L. F. Robinson (2014), Measurement of fossil deep-sea coral Nd isotopic compositions and concentrations by TIMS as NdO+, with evaluation of cleaning protocols, *Chemical Geology* 374-375, 128-140.

Cronin, T. M., Dwyer, G. S., Farmer, J., Bauch, H. A., Spielhagen, R. F., Jakobsson, M., et al. (2012). Deep Arctic Ocean warming during the last glacial cycle. *Nature Geoscience*, 5, 631–634. http://doi.org/10.1038/ngeo1557

Cuffey K. M. and Clow G. D. (1997) Temperature, accumulation, and ice sheet elevation in central Greenland through the last deglacial transition. *Journal of Geophysical Research* 102, 26383–26–396.

Dahlqvist R. and Andersson P. S. (2007) Nd isotopes in Bering Strait and Chukchi Sea water. *European Geophysical Union* EGU General Assembly 2015, held 12-17 April, 2015 in Vienna, Austria. id.8776

Dausmann, V., Frank, M., Siebert, C., Christl, M., and Hein, J. R. (2015), The evolution of climatically driven weathering inputs into the western Arctic Ocean since the late Miocene: Radiogenic isotope evidence, *Earth and Planetary Science Letters* 419, 111-124.

De Angelis, M., Steffensen, J.P., Legrand, M., Clausen, H., Hammer, C., 1997. Primary aerosol (sea salt and soil dust) deposited in Greenland ice during the last climatic cycle: Comparison with east Antarctic records. *Journal of Geophysical Research* 102, 26681–26–698.

DePaolo D. J. (1981) Neodymium isotopes in the Colorado Front Range and crust–mantle evolution in the Proterozoic. *Nature Communications* 291, 193–196.

DePaolo D. J. and Wasserburg G. J. (1976) Nd isotopic variations and petrogenetic models. *Geophysical Research Letters* 3, 249–252.

Dickin, A. P. (2005). Radiogenic Isotope Geology, 2nd edition. *Cambridge University Press*.

Fischer, H., Wagenbach, D., Kipfstuhl, J., (1998a). Sulfate and nitrate firn concentrations on the Greenland ice sheet: 1. Large-scale geographical deposition changes. *Journal of Geophysical Research* 103, 21–927–21–934.

Fischer, H., Wagenbach, D., Kipfstuhl, J., (1998b). Sulfate and nitrate firn concentrations on the Greenland ice sheet: 2. Temporal anthropogenic deposition changes. *Journal of Geophysical Research* 103, 21–935–21–942.

Fischer H., Siggaard-Andersen M.-L., Ruth U., Röthlisberger R. and Wolff E. (2007) Glacial/interglacial changes in mineral dust and sea-salt records in polar ice cores: Sources, transport, and deposition. *Reviews of Geophysics* 45, RG1002.

Grootes P. M., Stuiver M. and White J. W. C. (1993) Comparison of oxygen isotope records from the GISP2 and GRIP Greenland ice cores. *Nature* 366, 552-554.

Grousset F. E. and Biscaye P. E. (2005) Tracing dust sources and transport patterns using Sr, Nd and Pb isotopes. *Chemical Geology* 222, 149–167.

Haley, B.A., Frank, M., Spielhagen, R.F., and Eisenhauer, A. (2008a), Influence of brine formation on Arctic Ocean circulation over the past 15 million years, *Nature Geoscience* 1, 68-72.

Haley, B.A., Frank, M., Spielhagen, R.F., and Fietzke, J. (2008b), Radiogenic isotope record of Arctic Ocean circulation and weathering inputs of the past 15 million years, *Paleoceanography* 23, PA1S13.

Haley, B. A. & Polyak, L. (2013). Pre-modern Arctic Ocean circulation from surface sediment neodymium isotopes. *Geophysical Research Letters* 40, 893–897.

Hamilton P. J., O'nions R. K. and Bridgwater D. (1983) Sm-Nd studies of Archaean metasediments and metavolcanics from West Greenland and their implications for the Earth's early history. *Earth and Planetary Science Letters* 62, 263–272.

Hebbeln, D., Dokken, T., Andersen, E. S., & Hald, M. (1994). Moisture supply for northern ice-sheet growth during the Last Glacial Maximum. *Nature*, 370, 357–360. http://doi.org/10.1038/370357a0

Jacobsen, S. B., and G. J. Wasserburg (1980), Sm-Nd isotopic evolution of chondrites, *Earth and Planetary Science Letters* 50, 139-155.

Jakobsson M., Andreassen K., Bjarnadóttir L. R., Dove D., Dowdeswell J. A., England J. H., Funder S., Hogan K., Ingólfsson Ó., Jennings A., Krog Larsen N., Kirchner N., Landvik J. Y., Mayer L., Mikkelsen N., Möller P., Niessen F., Nilsson J., O'Regan M., Polyak L., Nørgaard-Pedersen N. and Stein R. (2014) Arctic Ocean glacial history. *Quaternary Science Reviews* 92, 40–67.

Jakobsson, M., Nilsson, J., Anderson, L., Backman, J., Björk, G., Cronin, T.M., Kirchner, N., Koshurnikov, A., Mayer, L., Noormets, R., Regan, M.O.R., Stranne, C., Ananiev, R., Macho, N.B., Cherniykh, D., Coxall, H., Eriksson, B.O.R., n, T.F.E., Gemery, L., Gustafsson, O.R., Jerram, K., Johansson, C., Khortov, A., Mohammad, R., Semiletov, I., (2016). Evidence for an ice shelf covering the central Arctic Ocean during the penultimate glaciation. *Nature Communications* 7, 1–10. doi:10.1038/ncomms10365

Kanayama, S., Yabuki, S., Zeng, F., & LIU, M. (2005). Size-dependent geochemical characteristics of Asian dust. *Journal of the Meteorological Society of Japan* 83A, 107–120. http://doi.org/10.2151/jmsj.83a.107

Koornneef, J.M., Bouman, C., Schwieters, J.B., Davies, G.R., (2013). Use of 1012 ohm current amplifiers in Sr and Nd isotope analyses by TIMS for application to sub-nanogram samples. *Journal of Atomic Analytical Spectrometry* 28, 749–754. doi:10.1039/c3ja30326h

Koornneef J. M., Bouman C., Schwieters J. B. and Davies G. R. (2014) Measurement of small ion beams by thermal ionisation mass spectrometry using new 1013Ohm resistors. *Analytica Chimica Acta* 819, 49–55.

Koornneef J. M., Nikogosian I., van Bergen M. J., Smeets R., Bouman C. and Davies G. R. (2015) TIMS analysis of Sr and Nd isotopes in melt inclusions from Italian potassium-rich lavas using prototype 1013Ω amplifiers. *Chemical Geology* 397, 14–23.

Kraft, S., Frank, M., Hathorne, E. C., and Weldeab, S. (2013), Assessment of seawater Nd isotope signatures extracted from foraminiferal shells and authigenic phases of Gulf of Guinea sediments, *Geochimica et Cosmochimica Acta* 121, 414-435.

Kurzweil, F., Gutjahr, M., Vance, D., and Keigwin, L. (2010), Authigenic Pb isotopes from the Laurentian Fan: Changes in chemical weathering and patterns of North American freshwater runoff during the last deglaciation, *Earth and Planetary Science Letters* 299, 458-465.

Kuznetsov A. B., Semikhatov M. A. and Gorokhov I. M. (2012) The Sr isotope composition of the world ocean, marginal and inland seas: Implications for the Sr isotope stratigraphy. *Stratigraphy and Geological Correlation* 20, 501–515.

Lacan F. and Jeandel C. (2004a) Denmark Strait water circulation traced by heterogeneity in neodymium isotopic compositions. *Deep Sea Research Part I: Oceanographic Research Papers* 51, 71–82.

Lacan F. and Jeandel C. (2004b) Neodymium isotopic composition and rare earth element concentrations in the deep and intermediate Nordic Seas: Constraints on the Iceland Scotland overflow water signature. *Geochemistry Geophysics Geosystems*. 5, 11.

Lacan F. and Jeandel C. (2005) Acquisition of the neodymium isotopic composition of the North Atlantic Deep Water. *Geochemistry. Geophysics Geosystems.* 6, 1-20.

Lambelet, M., van de Flierdt, T., Crocket, K., Rehkämper, M., Kreissig, K., Coles, B., Rijkenberg, M.J.A., Gerringa, L.J.A., de Baar, H.J.W., Steinfeldt, R., 2016. Neodymium isotopic composition and concentration in the western North Atlantic Ocean: Results from the GEOTRACES GA02 section. *Geochimica et Cosmochimica Acta* 177, 1–29. doi:10.1016/j.gca.2015.12.019

Lewis, E. R. & Schwartz, S. E. (2004) Sea Salt Aerosol Production Fluxes: Estimates and Critical Analysis. Chapter 5: Sea salt aerosol production: mechanisms, methods, measurements, and models-A critical review. *American Geophysical Union*, 299–344. doi:10.1029/152GM05

Lupker M., Aciego S. M., Bourdon B., Schwander J. and Stocker T. F. (2010) Isotopic tracing (Sr, Nd, U and Hf) of continental and marine aerosols in an 18th century section of the Dye-3 ice core (Greenland). *Earth and Planetary Science Letters* 295, 277–286.

Mahowald N., Kohfeld K., Hansson M., Balkanski Y., Harrison S. P., Prentice I. C., Schulz M. and Rodhe H. (1999) Dust sources and deposition during the last glacial maximum and current climate: A comparison of model results with paleodata from ice cores and marine sediments. *Journal of Geophysical Research: Oceans (1978–2012)* 104, 15895–15916.

Makishima A. and Nakamura E. (2010) Precise isotopic determination of Hf and Pb at sub-nano gram levels by MC-ICP-MS employing a newly designed sample cone and a pre-amplifier with a 1012 ohm register. *Journal of Atomic Analytical Spectrometry* 25, 1712–1716.

Makishima, A. and Nakamura, E., 2012. High-resolution MC-ICPMS employing amplifiers with a 1012 ohm resistor for bulk sulfur determination in biological and geological samples. *Journal of Atomic Analytical Spectrometry* 27, 891–895. doi:10.1039/c2ja10337k

Mayewski, P.A., Meeker, L.D., Twickler, M.S., Whitlow, S., Yang, Q., Lyons, W.B., Prentice, M., 1997. Major features and forcing of high-latitude northern hemisphere atmospheric circulation using a 110,000-year-long glaciochemical series. *Journal of Geophysical Research: Oceans (1978–2012)* 102, 26345–26366. doi:10.1029/96JC03365

Mayewski, P.A., Meeker, L.D., Whitlow, S., Twickler, M.S., Morrison, M.C., Bloomfield, P., Bond, G.C., Alley, R.B., GOW, A.J., Meese, D.A., Grootes, P.M., Ram, M., Taylor, K.C., Wumkes, W., 1994. Changes in Atmospheric Circulation and Ocean Ice Cover over the North Atlantic During the Last 41,000 Years. *Science* 263, 1747–1751. doi:10.1126/science.263.5154.1747

Meese D. A., Gow A. J., Alley R. B., Zielinski G. A., Grootes P. M., Ram M., Taylor K. C., Mayewski P. A. and Bolzan J. F. (1997) The Greenland Ice Sheet Project 2 depth-age scale: Methods and results. *Journal of Geophysical Research: Oceans (1978–2012)* 102, 26411–26423.

Ménégoz M., Voldoire A., Teyssèdre H., Salas Y Mélia D., Peuch V. H. and Gouttevin I. (2012) How does the atmospheric variability drive the aerosol residence time in the Arctic region? *Tellus B* 64, 17.

Morison J., Kwok R., Peralta-Ferriz C., Alkire M., Rigor I., Andersen R. and Steele M. (2012) Changing Arctic Ocean freshwater pathways. *Nature Communications* 481, 66–70.

Nilsson E. D. and Rannik Ü. (2001) Turbulent aerosol fluxes over the Arctic Ocean: 1. Dry deposition over sea and pack ice. *Journal of Geophysical Research: Oceans (1978–2012)* 106, 32125–32137.

Otto-Bliesner B. L. (2006) Simulating Arctic Climate Warmth and Icefield Retreat in the Last Interglaciation. *Science* 311, 1751–1753.

Peralta-Ferriz C., Morison J. H., Wallace J. M., Bonin J. A. and Zhang J. (2014) Arctic Ocean Circulation Patterns Revealed by GRACE. *Journal of Climate* 27, 1445–1468.

Porcelli, D., Andersson, P.S., Baskaran, M., Frank, M., Björk, G., Semiletov, I., 2009. The distribution of neodymium isotopes in Arctic Ocean basins. *Geochimica et Cosmochimica Acta* 73, 2645–2659. doi:10.1016/j.gca.2008.11.046

Rasmussen, T. L., & Thomsen, E. (2004). The role of the North Atlantic Drift in the millennial timescale glacial climate fluctuations. *Palaeogeography, Palaeoclimatology, Palaeoecology*, 210, 101–116. http://doi.org/10.1016/j.palaeo.2004.04.005

Ram, M., Illing, M., Weber, P., Koenig, G., Kaplan, M., 1995. Polar ice stratigraphy from laser-light scattering: Scattering from ice. *Geophysical Research Letters* 22, 3525–3527.

Ram M., Donarummo J., Stolz M. R. and Koenig G. (2000) Calibration of laser-light scattering measurements of dust concentration for Wisconsinan GISP2 ice using instrumental neutron activation analysis of aluminum: Results and discussion. *Journal of Geophysical Research: Oceans (1978–2012)* 105, 24731–24738.

Ram M. and Koenig G. (1997) Continuous dust concentration profile of pre-Holocene ice from the Greenland Ice Sheet Project 2 ice core: Dust stadials, interstadials, and the Eemian. *Journal of Geophysical Research* 102, 26641–26–648.

Schaefer, J.M., Finkel, R.C., Balco, G., Alley, R.B., Caffee, M.W., Briner, J.P., Young, N.E., Gow, A.J., Schwartz, R., (2016) Greenland was nearly ice-free for extended periods during the Pleistocene. *Nature* 540, 252–255. doi:10.1038/nature20146

Seierstad, I.K., Abbott, P.M., Bigler, M., Blunier, T., Bourne, A.J., Brook, E., Buchardt, S.L., Buizert, C., Clausen, H.B., Cook, E., Dahl-Jensen, D., Davies, S.M., Guillevic, M., Johnsen, S.J., Pedersen, D.S., Popp, T.J., Rasmussen, S.O., Severinghaus, J.P., Svensson, A., Vinther, B.M., (2014) Consistently dated records from the Greenland GRIP, GISP2 and NGRIP ice cores for the past 104 ka reveal regional millennial-scale delta18O gradients with possible Heinrich event imprint. *Quaternary Science Reviews* 106, 29–46. doi:10.1016/j.quascirev.2014.10.032

Smith, H.J., Wahlen, M., Mastroianni, D., (1997a). The CO2 concentration of air trapped in Greenland Ice Sheet Project 2 ice formed during periods of rapid climate change. *Journal of Geophysical Research* 102, 26–577–26–582.

Smith, H.J., Wahlen, M., Mastroianni, D., Taylor, K.C., (1997b). The CO2 concentration of air trapped in GISP2 ice from the Last Glacial Maximum-Holocene transition. *Geophysical Research Letters* 24, 1–4. doi:10.1029/96GL03700

Stordal M. C. and Wasserburg G. J. (1986) Neodymium isotopic study of Baffin Bay water: sources of REE from very old terranes. *Earth and Planetary Science Letters* 77, 259–272.

Struthers H., Ekman A. M. L., Glantz P., Iversen T., Kirkevåg A., Mårtensson E. M., Seland Ø. and Nilsson E. D. (2011) The effect of sea ice loss on sea salt aerosol concentrations and the radiative balance in the Arctic. *Atmospheric Chemistry and Physics* 11, 3459–3477.

Suwa M., Fischer von J. C., Bender M. L., Landais A. and Brook E. J. (2006) Chronology reconstruction for the disturbed bottom section of the GISP2 and the GRIP ice cores: Implications for Termination II in Greenland. *Journal of Geophysical Research* 111, D02101.

Svensson, A., Biscaye, P.E., Grousset, F.E., (2000) Characterization of late glacial continental dust in the Greenland Ice Core Project ice core. *Journal of Geophysical Research: Oceans (1978–2012)* 105, 4637–4656. doi:10.1029/1999JD901093

Tachikawa, K., 2003. Neodymium budget in the modern ocean and paleo-oceanographic implications. *Journal of Geophysical Research* 108, 3254–13. doi:10.1029/1999JC000285

Taylor K. C., Hammer C. U., Alley R. B., Clausen H. B., Dahl-Jensen D., Gow A. J., Gundestrup N. S., Kipfstuhl J., Moore J. C. and Waddington E. D. (1993) Electrical-Conductivity Measurements From the GISP2 and GRIP Greenland Ice Cores. *Nature* 366, 549–552.

Taylor K. C., Alley R. B., Lamorey G. W. and Mayewski P. (1997) Electrical measurements on the Greenland Ice Sheet Project 2 core. *Journal of Geophysical Research—Oceans* 102, 26511–26517.

Teschner, C., Frank, M., Haley, B.A., Knies, J., 2016. Plio-Pleistocene evolution of water mass exchange and erosional input at the Atlantic-Arctic gateway. *Paleoceanography* 1–18. doi:10.1002/(ISSN)1944-9186

Thompson D. W. J. and Wallace J. M. (1998) The Arctic Oscillation signature in the wintertime geopotential height and temperature fields. *Geophysical Research Letters* 25, 1297–1300.

Thompson D. and Wallace J. M. (2000) Annular modes in the extratropical circulation. Part I: month-to-month variability*. *Journal of Climate* 13, 1000–1016.

Trinquier, A., and Komander, P., 2015. Precise and accurate uranium isotope analysis by modified total evaporation using 1013 ohm current amplifiers. *Journal of Radioanalytical and Nuclear Chemistry* 307, 1927–1932. doi:10.1007/s10967-015-4400-2

Trinquier, A., Touboul, M., Walker, R.J., 2016. High-Precision Tungsten Isotopic Analysis by Multicollection Negative Thermal Ionization Mass Spectrometry Based on

Simultaneous Measurement of W and 18O/ 16O Isotope Ratios for Accurate Fractionation Correction. *Analytical Chemistry* 88, 1542–1546. doi:10.1021/acs.analchem.5b04006

van de Flierdt, T., Griffiths, A.M., Lambelet, M., Little, S.H., Stichel, T., Wilson, D.J., 2016. Neodymium in the oceans: a global database, a regional comparison and implications for palaeoceanographic research. *Philosophical Transactions of the Royal Society A: Mathematical, Physical and Engineering Sciences* 374, 20150293–30. doi:10.1098/rsta.2015.0293

von Quadt, A., Wotzlaw, J.-F., Buret, Y., Large, S.J.E., Peytcheva, I., Trinquier, A., 2016. High-precision zircon U/Pb geochronology by ID-TIMS using new 1013 ohm resistors. *Journal of Atomic Analytical Spectrometry* 31, 658–665. doi:10.1039/C5JA00457H

Wallace J. M. (2000) North Atlantic Oscillation/annular mode: Two paradigms—one phenomenon. *Quarterly Journal of the Royal Meteorological Society* 126, 791–805.

Wanner H., Brönnimann S., Casty C., Gyalistras D., Luterbacher J., Schmutz C., Stephenson D. B. and Xoplaki E. (2001) North Atlantic Oscillation – Concepts And Studies. *Surveys in Geophysics* 22, 321–381.

Werner M., Tegen I. and Harrison S. P. (2002) Seasonal and interannual variability of the mineral dust cycle under present and glacial climate conditions. *Journal of Geophysical Research*. 107, D24.

Wilson, D. J., K. C. Crocket, T. van de Flierdt, L. F. Robinson, and J. F. Adkins (2014), Dynamic intermediate ocean circulation in the North Atlantic during Heinrich Stadial 1: A radiocarbon and neodymium isotope perspective, *Paleoceanography* 29, 1072-1093.

Zimmermann, B., Porcelli, D., Frank, M., Andersson, P.S., Baskaran, M., Lee, D.-C., and Halliday. A.N. (2009), Hafnium isotopes in Arctic Ocean water. *Geochimica et Cosmochimica Acta* 73, 3218-3233.

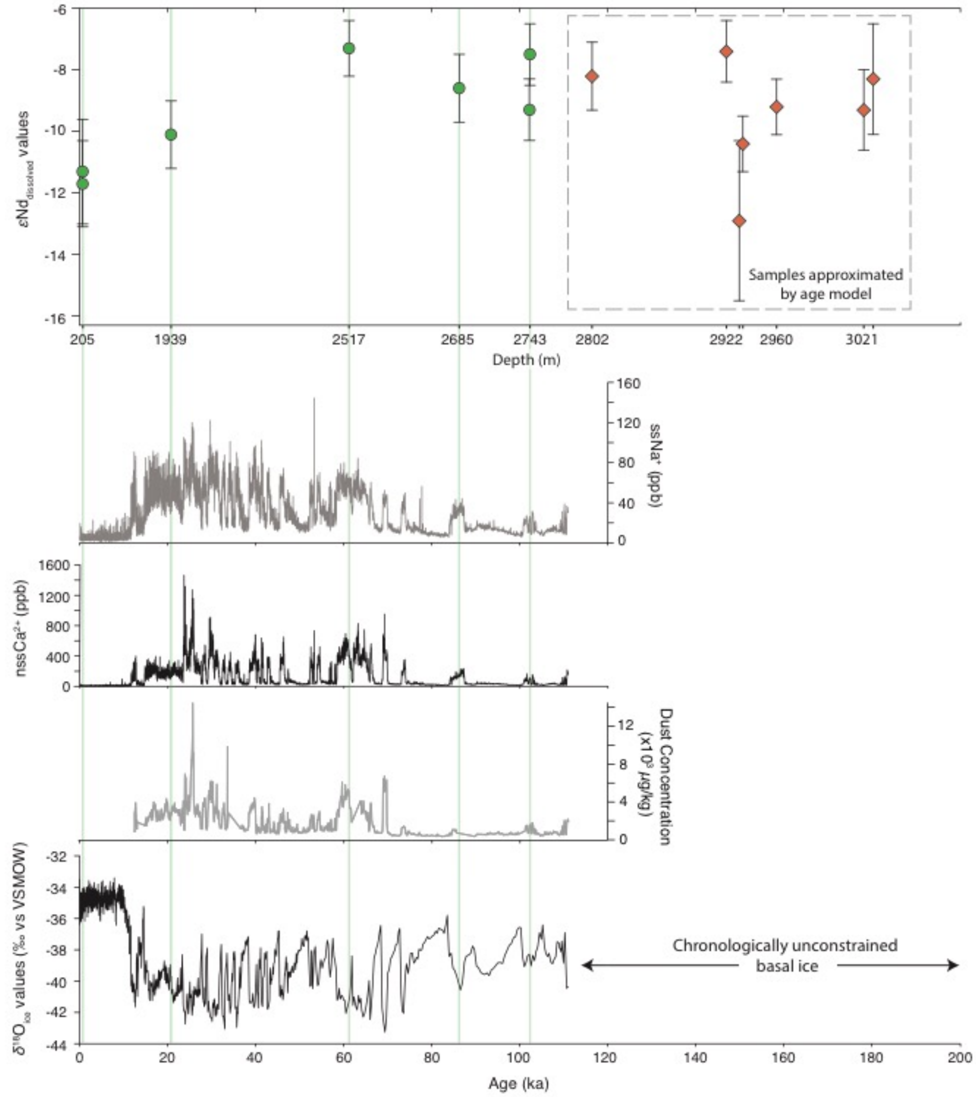

Figure 1. Measured $\varepsilon_{\mathrm{Nd}}$ values of the soluble fraction of dust from the GISP2D ice core (top panel) for chronologically constrained (green circles) and deep ice samples (red diamonds) of the core. The Nd isotope values are placed on an age scale where the unconstrained samples have been approximated by extrapolation of a best-fit depth-age model (see Figure 12). Statistically significant variability is observed in the $\varepsilon_{\mathrm{Nd}}$ compositions of the dust, possibly reflecting changes between stadial and interstadial conditions. Also depicted are sea-salt Na^+ ($ssNa^+$), non-sea-salt Ca^{2+} ($nssCa^{2+}$) concentrations, cumulative dust concentrations, and oxygen isotope information from the core (after Mayewski et al., 1994, 1997; Ram and Koenig, 1997; Grootes et al., 1993).

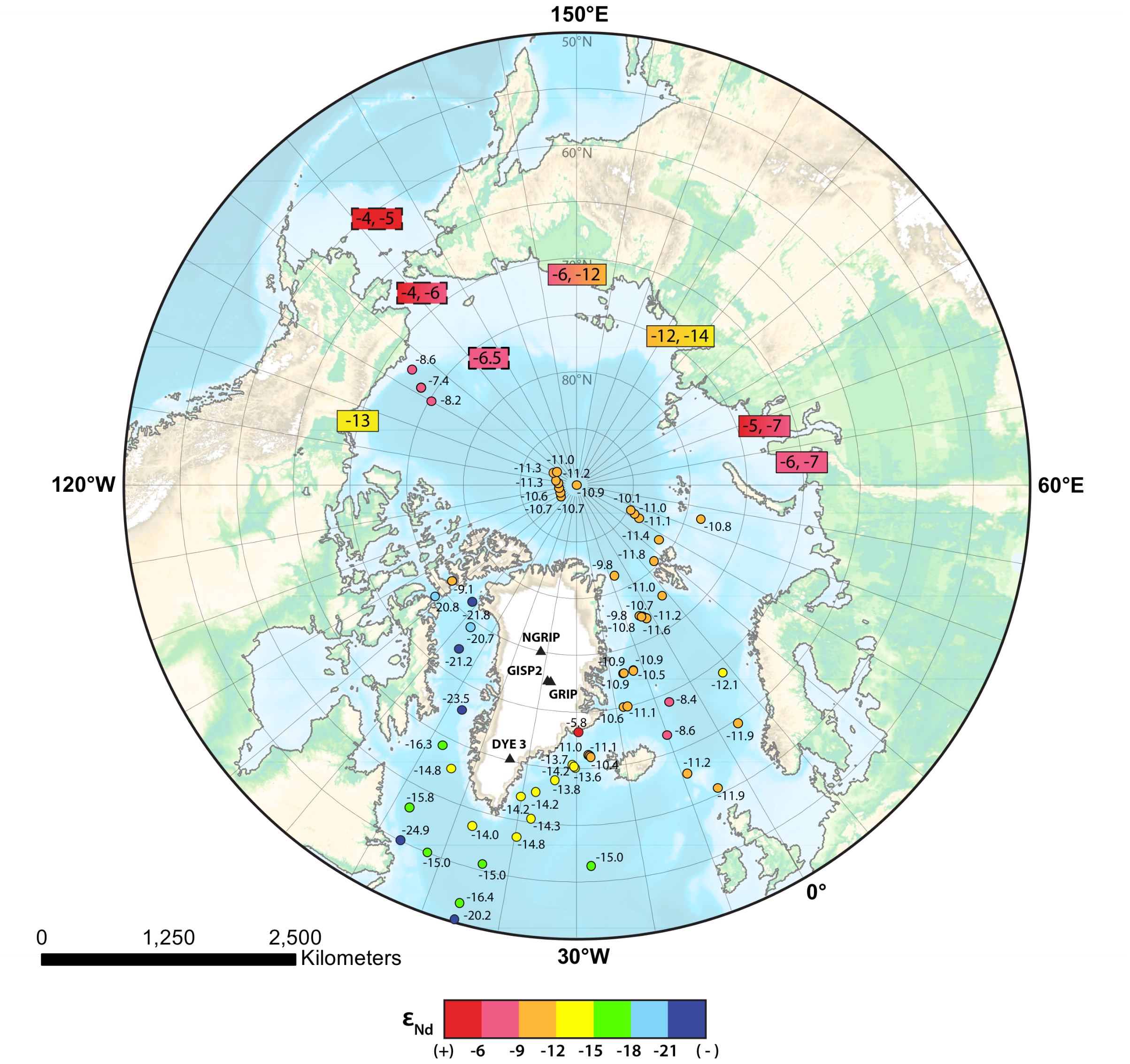

Figure 2. Polar stereographic map of the Arctic depicting Greenland ice core locations (black triangles), surface seawater ε_{Nd} values (circles), and riverine sediments (rectangles) (Stordal and Wasserburg, 1986; Lacan et al., 2004a, 2004b, 2005; Andersson et al., 2008; Porcelli et al., 2009; Zimmerman et al., 2009; Lambelet et al., 2016). Precise locations for surface seawater values of the North Pacific, Bering Strait, and Chukchi Basin (rectangles with dashed outline) are unknown (Dahlqvist et al., 2007).

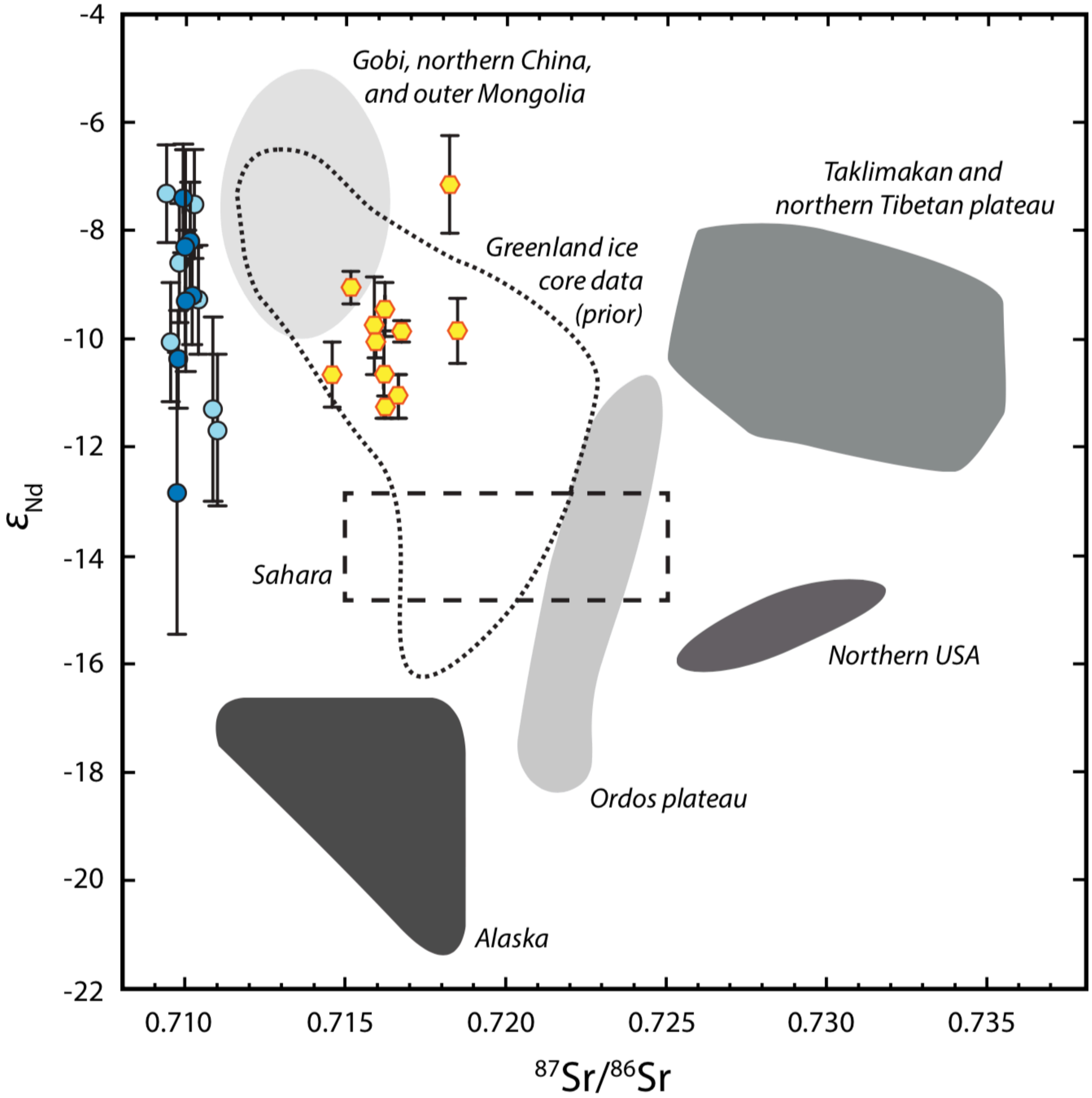

Figure 3. Measured $^{87}Sr/^{86}Sr$ and ε_{Nd} values for the soluble dust (blue circles; constrained ice = light blue, basal ice = dark blue) and particulate mineral dust (yellow hexagons) from the GISP2 ice core. Also depicted are documented ranges of $^{87}Sr/^{86}Sr$ and ε_{Nd} values of previous work from various source regions distributed globally (shaded regions) and on dust from other Greenland ice cores (dashed outline) adapted after Lupker et al. (2010; includes data from Biscaye et al., 1997; Svensson et al., 2000; Bory et al., 2003, 2003; Kanayama et al., 2005; Chen et al., 2007).

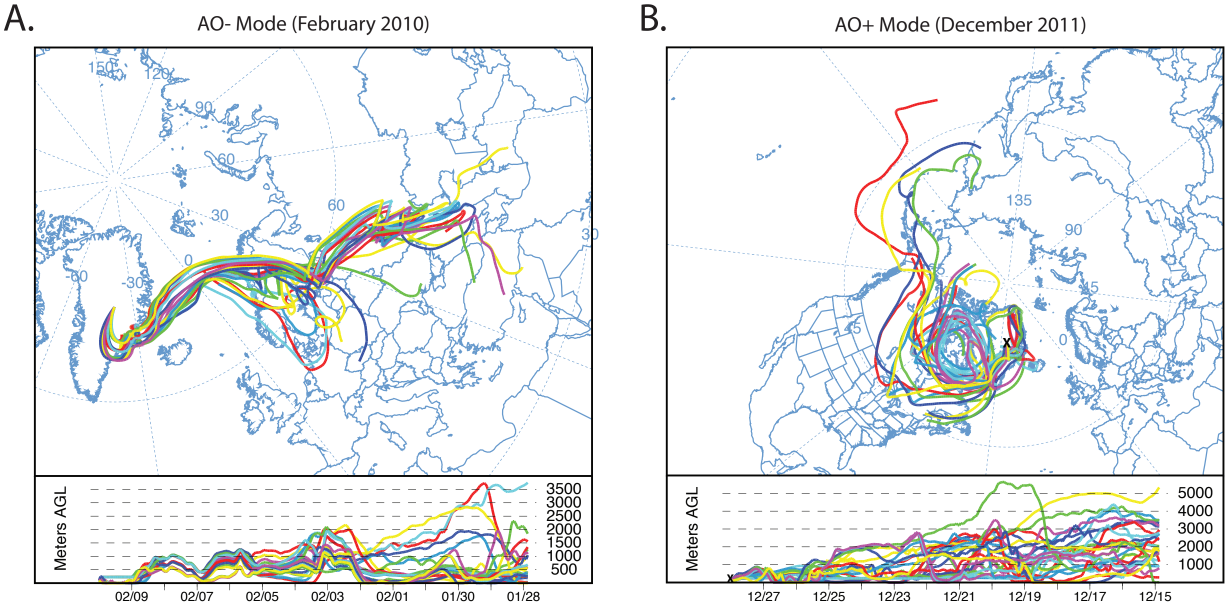

Figure 4. NOAA HYSPLIT ensemble back-trajectories for extreme AO positive (A) and negative (B) anomalies. The model outputs depicted represent some of the idealized circulation conditions for AO+ and AO-, where sourcing of air-masses would be from the west and east of Greenland, respectively. Additional information and model runs can be found in Figure 8.

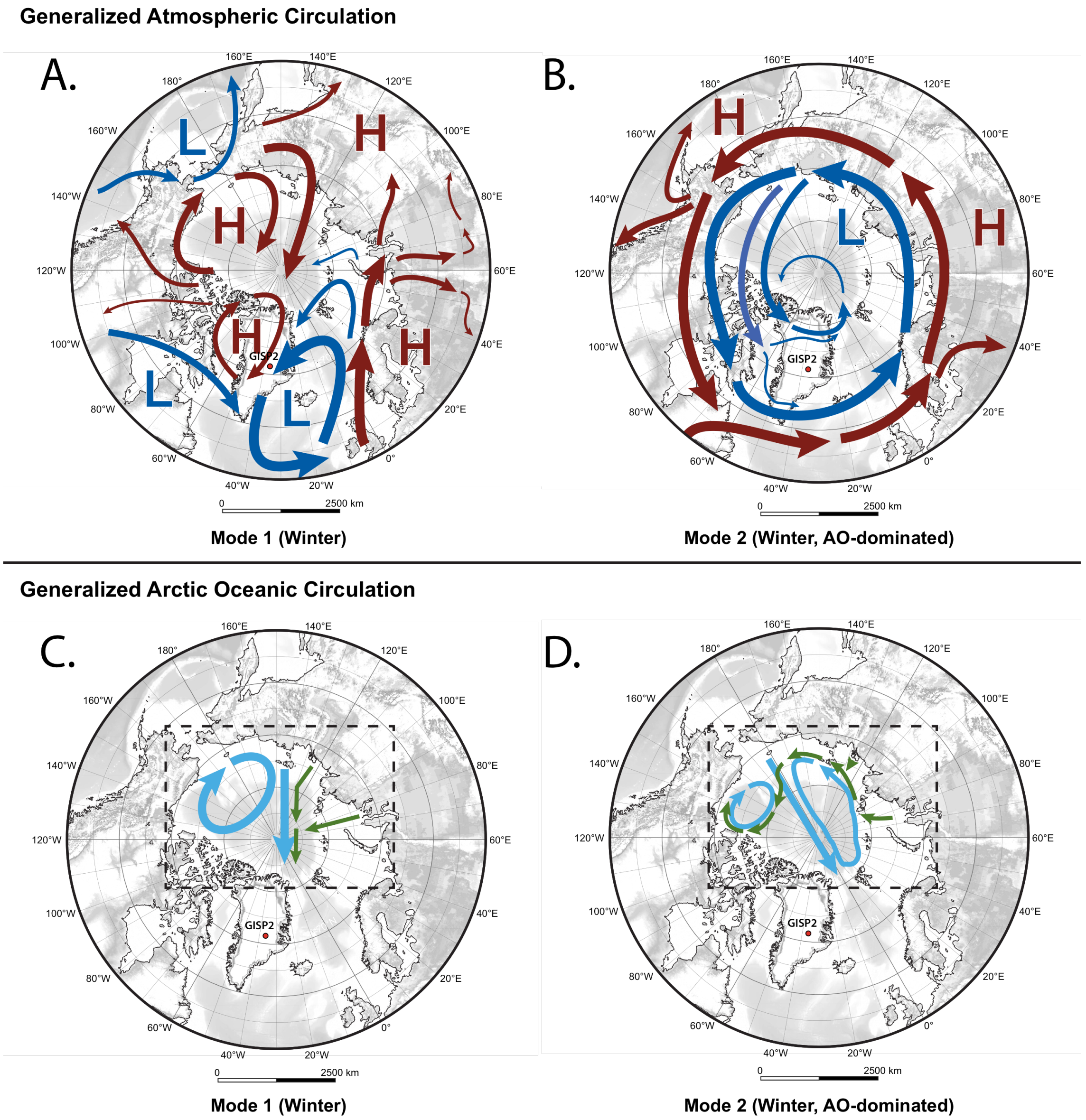

Figure 5. Schematic representation of high arctic atmospheric and oceanic circulation (after Morison et al., 2012 and Peralta-Ferriz et al., 2014). Atmospheric modes in the modern arctic, representing 70% of variability in GRACE satellite observations, show (A) Mode 1 where there is minimal apparent development of the AO and corresponds to a well-developed NAO (AO-), and (B) Mode 2 with high sea level pressure across much of the Arctic (AO+ depicted). Ocean circulation is governed by Ekman transport associated with the atmospheric circulation for both (C) Mode 1 and (D) Mode 2. We suggest that variations in ε_{Nd} of soluble dust in the GISP2 record, may reflect alternating between the dominant of these two modes of circulation.

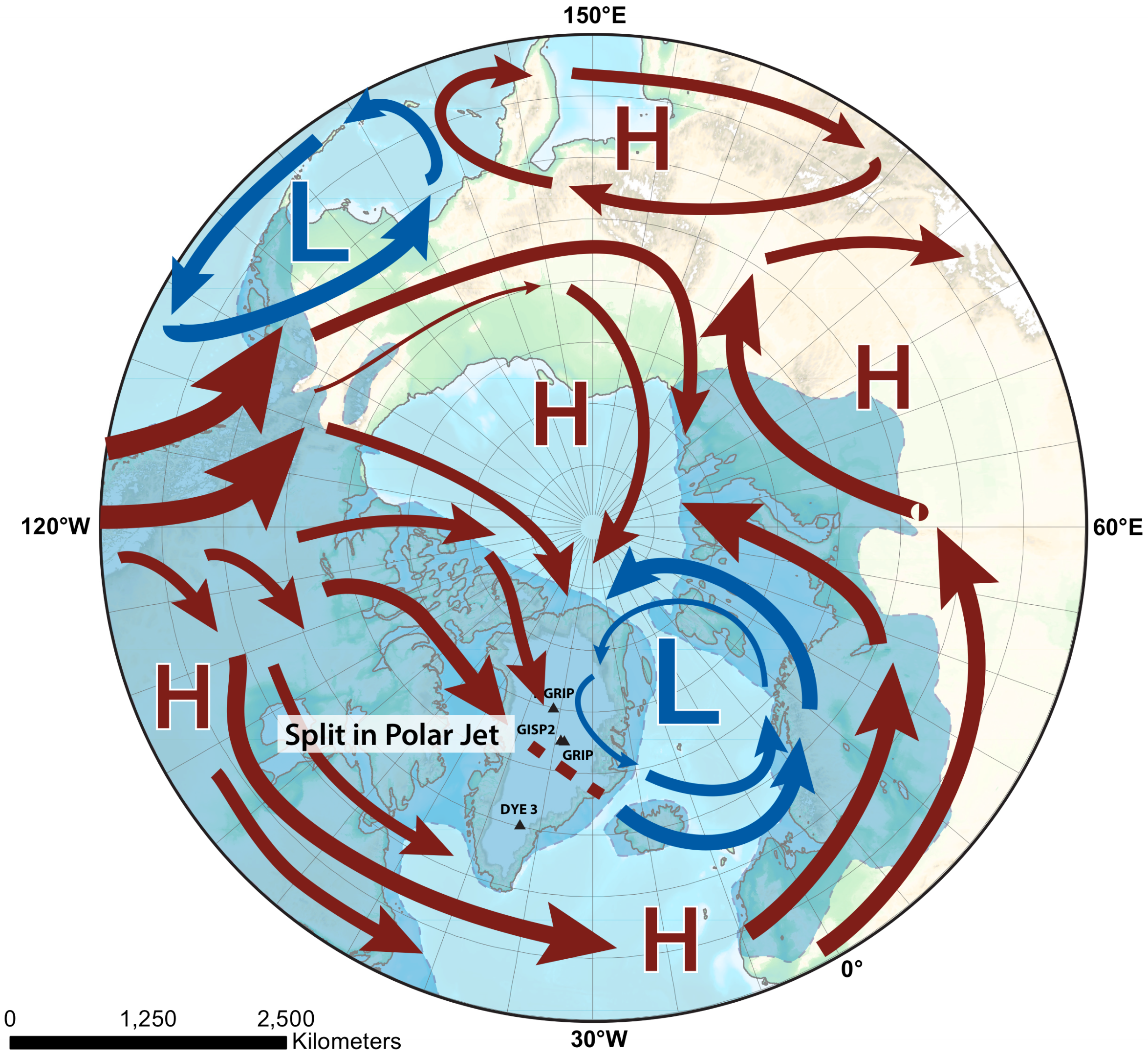

Figure 6. Generalized atmospheric circulation over the Arctic Ocean as approximated from Bromwich et al. (2004). In modeled simulations of circulation patterns, the presence of the Laurentide Ice Sheet over North America mechanically separates the jet stream with greatest effect in winter months, and diverting flow over the Arctic Ocean and Greenland. The split flow path of the polar jet could allow for enhanced SSA deposition from North Pacific and Arctic Ocean sources. The LGM ice sheet extent is depicted as the shaded blue regions, and sea-level is representative of an LGM minimum.

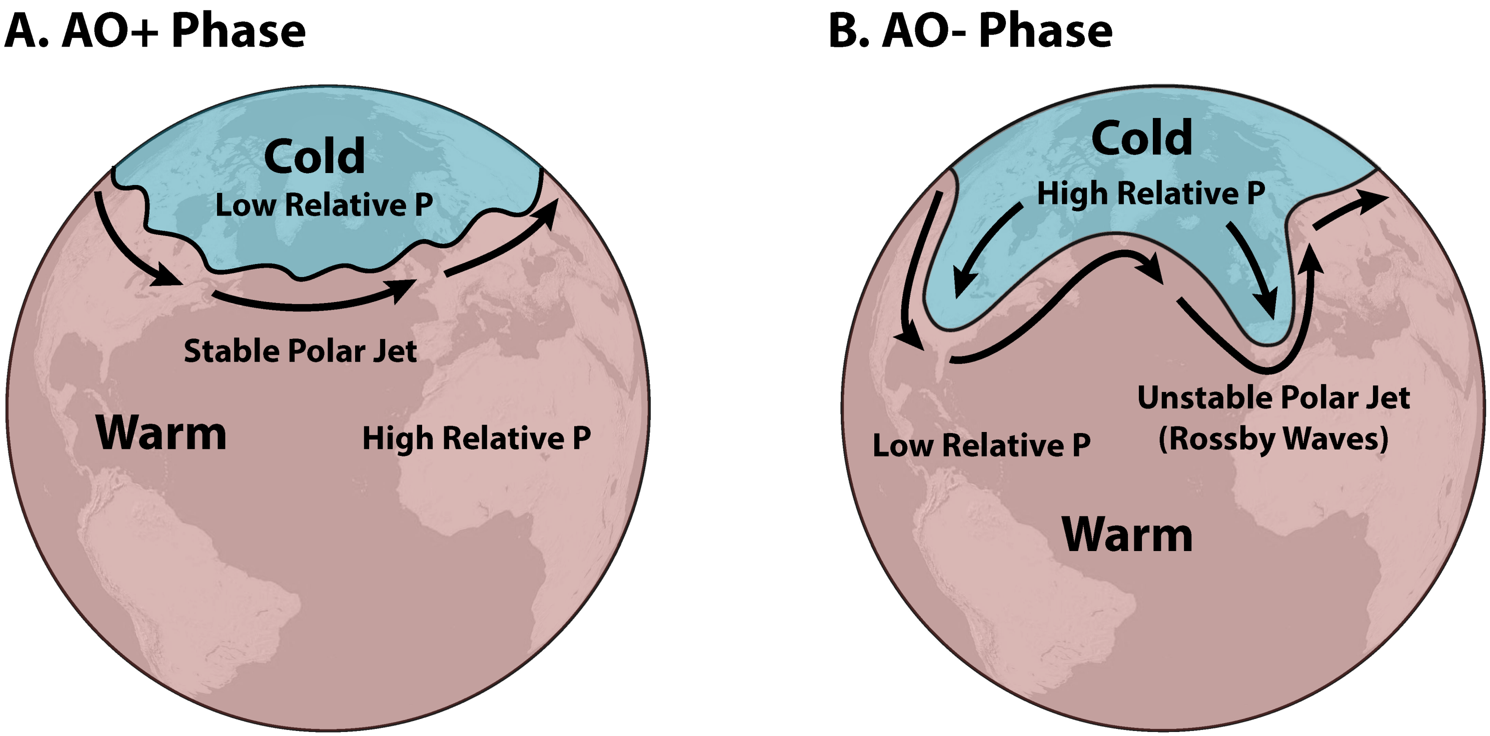

Figure 7. Schematic representation of the Arctic Oscillation positive (A) and negative (B) anomalies. In the positive phase, the polar jet is stable with a large system of cyclonic flow with relatively low pressure over the high arctic relative to the rest of the Northern Hemisphere and restricting cold air over the pole. In contrast, the negative phase experiences higher relative pressure in the arctic and a weaker gradient between the Polar cell and the Ferrel cell, destabilizing the polar jet and resulting in large-scale meanders as Rossby waves and bringing colder air to lower latitudes.

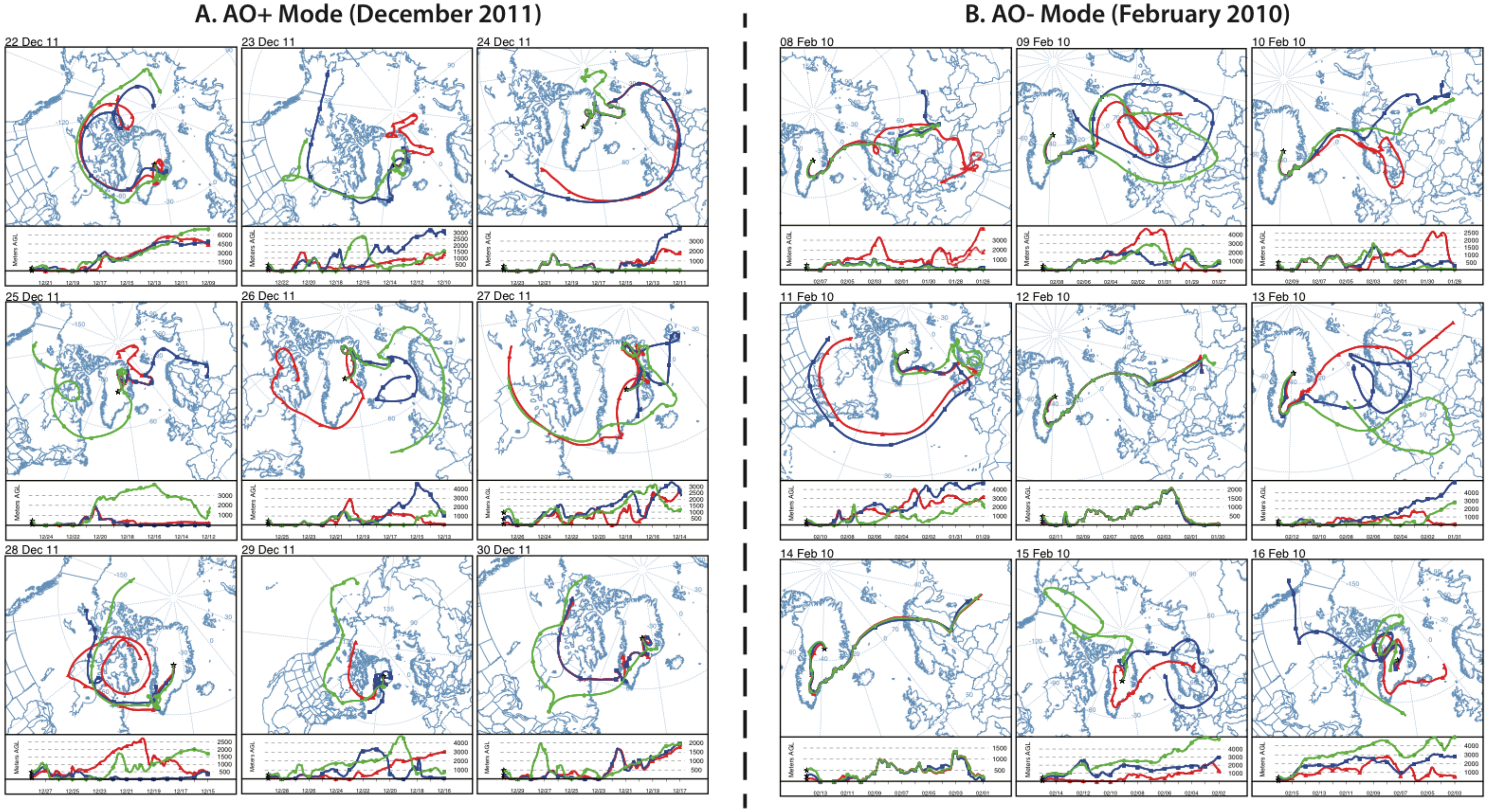

Figure 8. NOAA HYSPLIT back-trajectories for (A) December 2011, extreme AO+ anomaly, and (B) February 2010, extreme AO- anomaly, these time periods were selected to represent the largest magnitude anomalies recorded for the AO index with high-resolution satellite observations of the past 10 years. We observed variable model results using three different starting altitudes of 100 m (red), 250 m (blue), and 500 m (green). We found that during the AO- anomaly, air parcel sourcing was dominantly from east of Greenland, whereas during the AO+ anomaly sourcing was mainly from the west. Complete AO index data for these events is recorded in Table 3 below.

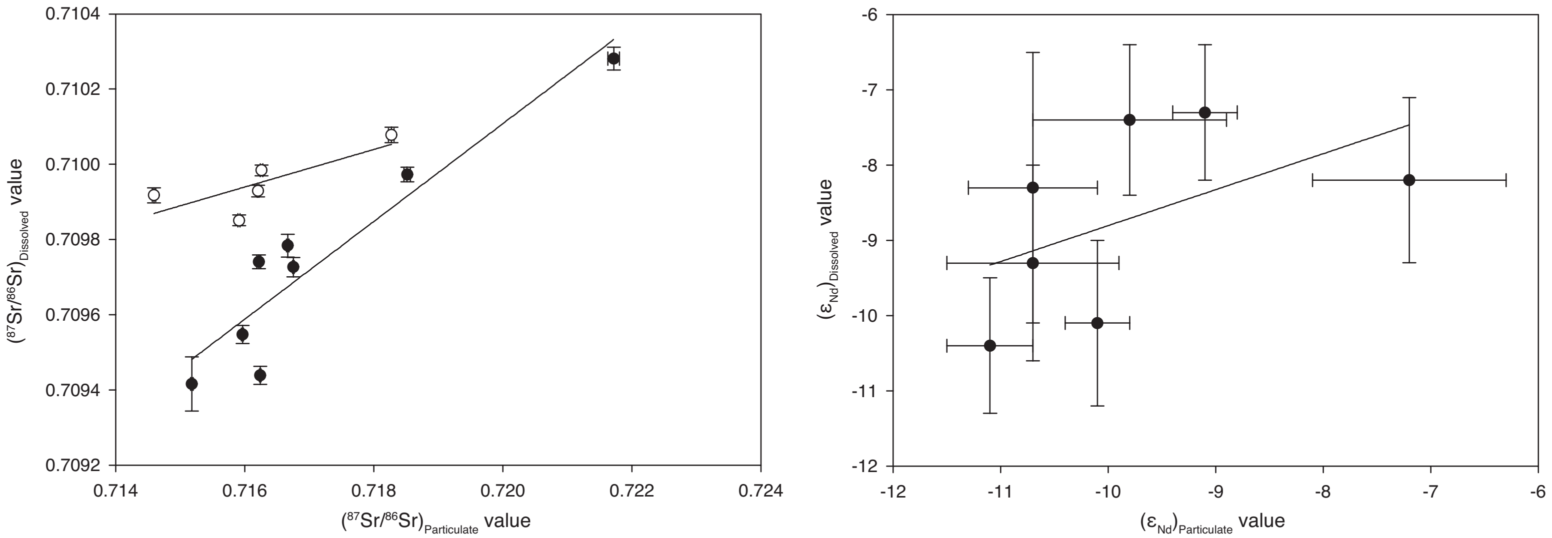

Figure 9. Correlations of measured GISP2D (A) $^{87}Sr/^{86}Sr$ and (B) ε_{Nd} between the particulate and dissolved fractions of dust. The ice core samples were processed in two intervals, the first in March 2013 (filled circles) and January 2014 (open circles). We found that there exists correlation between the $^{87}Sr/^{86}Sr$ values of the dissolved and particulate dust fractions ($r^2 = 0.87$ filled circles, $r^2 = 0.60$ open circles), suggesting that departures from seawater $^{87}Sr/^{86}Sr$ values in the dissolved fraction are likely primarily due to interactions with the particulate fraction during the core melting procedure, where minimizing the filtration of particulate material from solution may limit this effect. In contrast, there is no significant correlation between ε_{Nd} values of the two fractions ($r^2 = 0.26$).

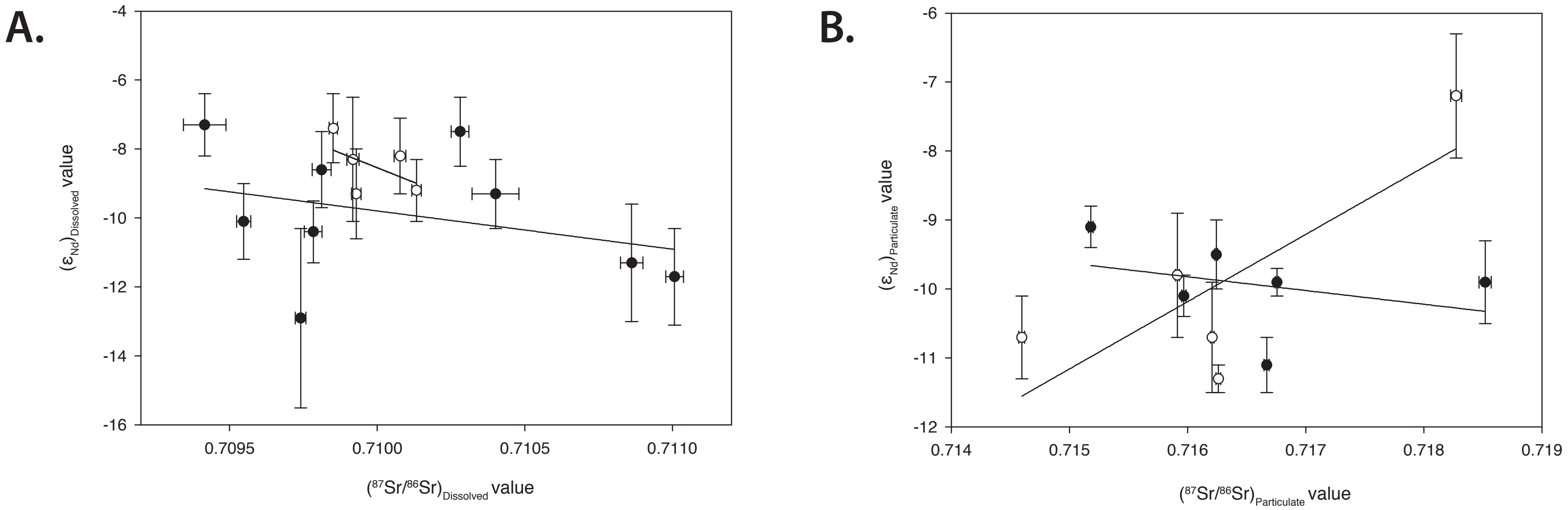

Figure 10. Plots of measured GISP2D $^{87}Sr/^{86}Sr$ and εNd within both (A) dissolved and (B) particulate fractions of dust. The ice core samples were processed in two intervals, the first in March 2013 (filled circles) and January 2014 (open circles). We observed no significant correlation between 87Sr/86Sr and εNd values for the dissolved fraction ($r^2 = 0.26$ filled circles, $r^2 = 0.11$ open circles) and found some correlation in the second sample set for the particulate fraction ($r^2 = 0.11$ filled circles, $r^2 = 0.63$ open circles) the limited number of data and opposing trends between the two sets, however illustrate the coincidental nature of this apparent correlation skewed dominantly by a single point amongst the limited data set.

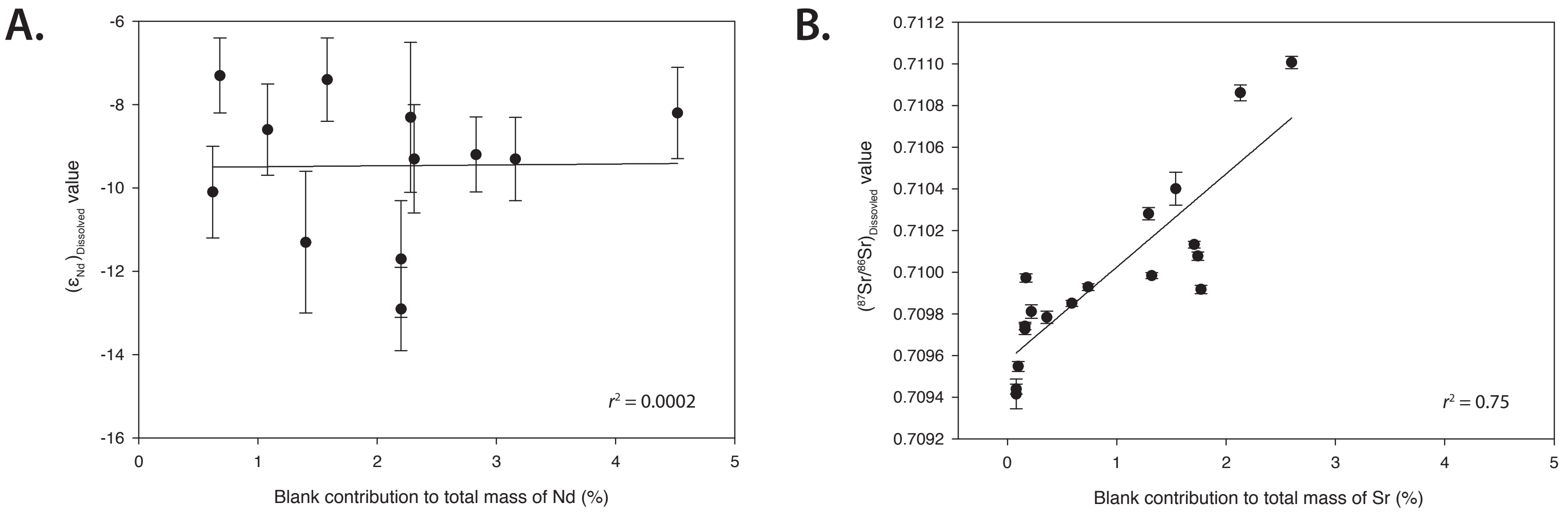

Figure 11. GISP2D Nd (A) and Sr (B) isotopic compositions plotted as a function of their respective blank contributions (expressed as a percentage of the sample mass). We observe no correlation between the Nd isotopic composition and % contribution of the blank. Sr isotopic compositions do correlate with the blank % contribution with an intercept at 0.70965, closer to the isotopic composition of modern seawater, also suggestive of the dissolved dust component of the ice cores being sourced as sea salt aerosol.

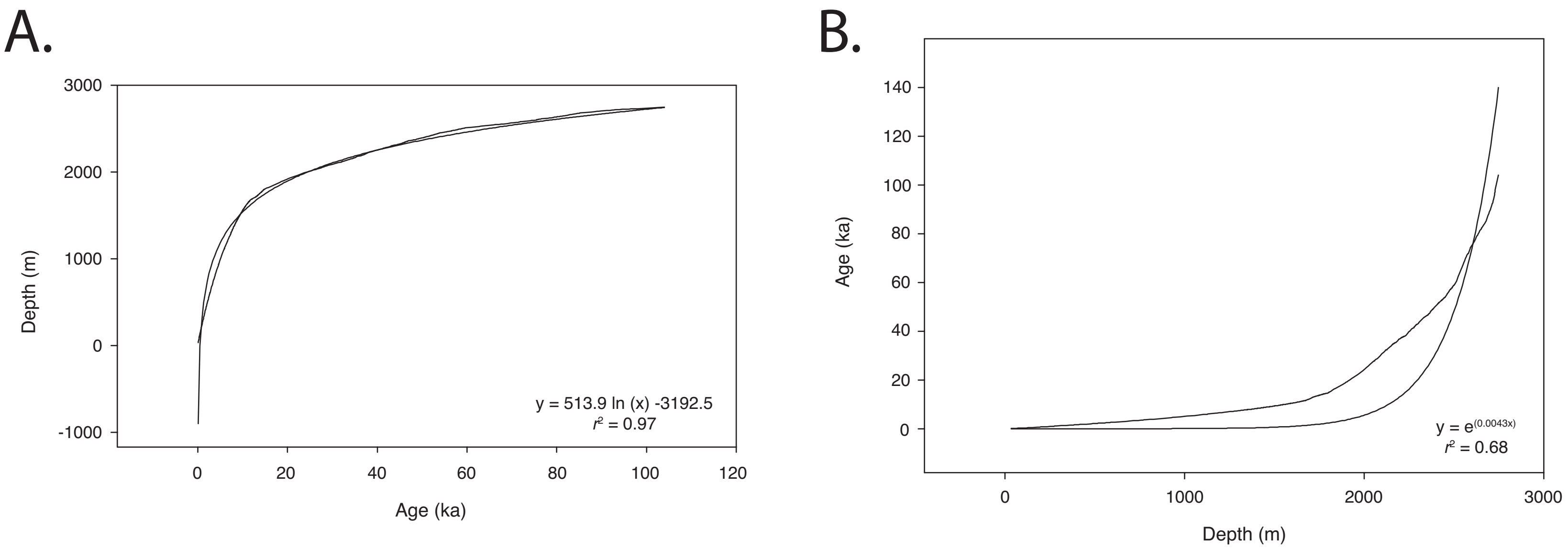

Figure 12. Best-fit model approximations to the GISP2 depth-age scale after Seierstad et al. (2014), which correlated the NGRIP GICC05 age model (Rasmussen et al., 2006, 2008; Svensson et al., 2012; Obrochta et al., 2014) to the chemostratigraphy and tephrochronology of GISP2, improving upon the Meese et al. (1997) model. We attempted to fit modeled (A) logarithmic and (B) exponential functions to the scale, and found that the logarithmic fit yielded the highest correlation ($r^2 = 0.97$). Afterward, we extrapolated the temporally unconstrained core samples as a best estimate for possible ages for the deep and basal ice samples.

Table 1. *GISP2 Neodymium and Strontium Isotope Values*

Sample	Depth	Age (ka)[†]	[Nd] ppt; 10^{-9}g/kg[**]	^{143}Nd/^{144}Nd	2 S.E.	ε_{Nd}	2 S.E.	[Sr] ppb; 10^{-6} g/kg[**]	^{87}Sr/^{86}Sr	2 S.E.
GISP2-D Ice Core Samples *- Soluble*										
G2-205-S	205.22	0.7	0.54	0.512058	0.000089	-11.3	1.7	0.09	0.710862	0.000038
G2-206-S	206.35	0.7	0.35	0.512039	0.000074	-11.7	1.4	0.07	0.711007	0.000030
G2-1937-S	1936.11	20.7	0.37	-	-	-	-	1.11	0.709727	0.000026
G2-1939-S	1938.52	20.8	1.19	0.512122	0.000054	-10.1	1.1	1.82	0.709548	0.000024
G2-2514-S	2514.32	59.2	1.17	-	-	-	-	2.13	0.709439	0.000024
G2-2517-S	2516.22	59.5	1.12	0.512262	0.000047	-7.3	0.9	2.19	0.709416	0.000072
G2-2684-S	2683.32	85.3	0.76	-	-	-	-	1.05	0.709973	0.000020
G2-2685-S	2684.71	85.9	0.69	0.512197	0.000057	-8.6	1.1	0.85	0.709812	0.000032
G2-2743-S	2743.21	99.7	0.23	0.512162	0.000050	-9.3	1.0	0.12	0.710401	0.000079
G2-2744-S	2744.17	99.9	-	0.512252	0.000052	-7.5	1.0	0.14	0.710281	0.000030
G2-2802-S	2801.43	143.3	0.16	0.512220	0.000059	-8.2	1.1	0.10	0.710078	0.000020
G2-2922-S	2921.80	***160.3***	0.48	0.512106	0.000044	-7.4	1.0	0.32	0.709851	0.000014
G2-2932-S	2932.11	***163.4***	0.38	0.511979	0.000132	-12.9	2.6	1.25	0.709741	0.000018
G2-2934-S	2933.15	***163.7***	-	0.512106	0.000044	-10.4	0.9	0.51	0.709784	0.000030
G2-2960-S	2959.32	***172.0***	0.29	0.512159	0.000067	-9.2	0.9	0.12	0.710133	0.000016
G2-3005-S	3004.54	***187.3***	0.40	-	-	-	-	0.16	0.709984	0.000014
G2-3021-S	3020.42	***193.0***	0.33	0.512159	0.000067	-9.3	1.3	0.25	0.709929	0.000016
G2-3027-S	3026.32	***195.1***	0.36	0.512212	0.000093	-8.3	1.8	0.11	0.709918	0.000020
GISP2-D Ice Core Samples *- Particulate*										
G2-1937-I	1936.11	20.7	-	0.512132	0.000011	-9.9	0.2	-	0.716756	0.000014
G2-1939-I	1938.52	20.8	-	0.512118	0.000015	-10.1	0.3	-	0.715967	0.000018
G2-2514-I	2514.32	59.2	-	0.512149	0.000028	-9.5	0.5	-	0.716242	0.000012
G2-2517-I	2516.22	59.5	-	0.512172	0.000016	-9.1	0.3	-	0.715179	0.000020
G2-2684-I	2683.32	85.3	-	0.512129	0.000030	-9.9	0.6	-	0.718519	0.000051
G2-2685-I	2684.71	85.9	-	-	-	-	-	-	-	-
G2-2743-I	2743.21	99.7	-	-	-	-	-	-	-	-
G2-2744-I	2744.17	99.9	-	-	-	-	-	-	0.721720	0.000091
G2-2802-I	2801.43	143.3	-	0.512267	0.000048	-7.2	0.9	-	0.718272	0.000046
G2-2922-I	2921.80	***160.3***	-	0.512137	0.000044	-9.8	0.9	-	0.715913	0.000017
G2-2932-I	2932.11	***163.4***	-	-	-	-	-	-	0.716219	0.000028
G2-2934-I	2933.15	***163.7***	-	0.512068	0.000020	-11.1	0.4	-	0.716668	0.000021
G2-2960-I	2959.32	***172.0***	-	-	-	-	-	-	-	-
G2-3005-I	3004.54	***187.3***	-	0.512059	0.000012	-11.3	0.2	-	0.716260	0.000020
G2-3021-I	3020.42	***193.0***	-	0.512087	0.000040	-10.7	0.8	-	0.716207	0.000015
G2-3027-I	3026.32	***195.1***	-	0.512087	0.000032	-10.7	0.6	-	0.714595	0.000024
Standards[‡]				**^{143}Nd/^{144}Nd**	**1σ**				**^{87}Sr/^{86}Sr**	**1σ**
Jndi-1 (*n* = 9)	-	-	-	0.512104	0.000030	-10.4	0.6	-	-	-
AGV-2[*] (*n* = 2)	-	-	-	0.512779	0.000040	2.8	0.8	-	0.703964	0.000036
BCR-2[*] (*n* = 3)	-	-	-	0.512620	0.000034	-0.4	0.7	-	-	-
BCR-2 (*n* = 2)	-	-	-	0.512613	0.000032	-0.5	0.6	-	0.705020	0.000028
CIGO[*] (*n* = 13)	-	-	-	0.511335	0.000050	-25.4	1.0	-	-	-
SRM-987 (*n* = 12)	-	-	-	-	-	-	-	-	0.710263	0.000008

[†] *Ages are adapted from core section depth intervals the depth-age scale from Meese et al. (1997), bolded ages are extrapolated from an exponential best-fit of the scale.*

[‡] *Standard values represent the average of a given number of replicates (n), full data for each standard can be found in the supplementary material.*

[*] *Samples run on the TIMS at VU Amsterdam*

[**] *Concentrations are expressed as per kg of ice melted, filtered, and processed*

[***] *Concentrations are expressed as per kg of 18.2 MΩ DI water*

Table 2. High-latitude Surface Seawater Data[†]

Site Name	Latitude (°*N*)	Longitude (°*W*)	ε_{Nd}[‡]
Station 1	55.02	52.08	-15.1
Station 2	58.55	47.07	-14.0
Station 3	62.65	53.90	-14.9
Station 4	57.96	57.39	-15.8
Station 5	55.01	56.40	-24.9
Station 6	50.20	45.68	-20.2
Station 7	55.55	43.97	-15.0
Station 8	62.07	40.19	-14.2
Station 9	62.70	37.59	-14.2
Station 12	56.37	27.82	-15.0
Station 14	65.02	30.23	-13.6
Station 15	65.32	30.88	-13.7
Station 16	65.17	30.52	-14.2
Station 20	69.21	6.85	-8.4
Station 21	66.55	10.11	-8.6
Station 22	62.75	9.01	-11.2
Station 23	60.50	5.00	-11.9
Station 25	64.65	-4.18	-11.9
Station 26	69.03	-7.95	-12.1
Station 29	77.67	-7.69	-11.0
Station 30	76.74	2.33	-11.2
Station 32	77.03	3.75	-10.7
Station 42	72.91	12.97	-10.9
Station 45	72.91	15.85	-10.5
SGN33	77.18	29.63	-9.8
SGN32	77.03	4.38	-10.8
SGN30	76.75	3.25	-11.6
SGN46	72.87	2.33	-10.9
SGN42	72.92	16.18	-10.9
SGN50	70.00	12.97	-10.6
SGN48	70.00	18.00	-11.1
SGN54	66.17	17.00	-11.0
SGN55	66.08	27.52	-11.1
SGN56	66.00	27.25	-10.4
Nansen Fjord	68.20	26.98	-5.8
Barents Sea	78.64	-44.68	-10.8
North Svalbard (#2)	80.43	-15.52	-11.8
North Svalbard (#3)	81.28	-26.38	-11.5
Nansen Basin (Stn 10)	83.78	-31.95	-11.0
Nansen Basin (Stn 11)	84.28	-33.66	-11.1
Nansen Basin (Stn 12)	84.73	-35.25	-10.1
Fram Strait	81.34	7.35	-9.8
Canada Basin (Stn 3)	75.21	-149.95	-9.8
Canada Basin (Stn 4)	73.83	-152.01	-9.8
Canada Basin (Stn 5)	72.24	-155.07	-9.4
Amundsen Basin (Stn 20)	88.28	-82.91	-10.7
Amundsen Basin (Stn 21)	88.41	-95.38	-10.7
Amundsen Basin (Stn 22)	88.43	-109.84	-10.6

Amundsen Basin (Stn 24)	88.36	-126.50	-11.2
Amundsen Basin (Stn 26)	87.14	-132.55	-11.3
Amundsen Basin (Stn 28)	87.70	-148.46	-11.3
North Pole	90.00	0.00	-10.9
Makarov Basin	87.92	154.38	-11.0
Davis Strait (Stn 43)	64.17	57.21	-16.3
West Greenland (Stn 45)	67.73	57.03	-23.5
Baffin Bay (Stn 48)	74.35	66.77	-20.7
Baffin Bay (Stn 113)	72.20	65.68	-21.2
Jones Sound (Stn 53)	76.11	82.42	-9.1
Lancaster Sound (Stn 87)	74.11	81.75	-20.8
Smith Sound (Stn 104)	76.20	71.88	-21.8
Station 02.3	64.00	-34.25	-13.8
Station 05.1	60.43	-37.91	-14.3
Station 06.1	58.60	-39.71	-14.8
Station 09.1	51.82	-45.73	-16.4

[†] Seawater ε_{Nd} values are from Stordal and Wasserburg (1986), Lacan et al., (2004a), Lacan et al., (2004b), Lacan et al., (2005), Andersson et al., (2008), Porcelli et al., (2009), and Lambelet et al. (2016).

[‡] Neodymium values are measured against CHUR, where $(^{143}Nd/^{144}Nd)_{CHUR} = 0.512638$.

Table 3. Daily Arctic Oscillation Index (AOI) Data† for February 2010 and December 2011

Year	Month	Day	*AOI* Value
2010	02	08	-4.734
2010	02	09	-4.459
2010	02	10	-4.266
2010	02	11	-4.638
2010	02	12	-4.758
2010	02	13	-4.945
2010	02	14	-5.132
2010	02	15	-4.730
2010	02	16	-4.292
2011	12	22	1.729
2011	12	23	2.329
2011	12	24	2.849
2011	12	25	3.519
2011	12	26	3.342
2011	12	27	3.030
2011	12	28	2.893
2011	12	29	2.615
2011	12	30	2.446

†Data from the NOAA Climate Prediction Center database found at
http://www.cpc.ncep.noaa.gov/products/precip/CWlink/daily_ao_index/ao_index.html

Table 4. *GISP2D Sample Masses*

Sample	Depth	Total Sample Mass (g)	Isotope Split Mass (g)	Nd Sample Mass (pg; 10^{-12} g)	Sr Sample Mass (ng; 10^{-9} g)
***GISP2-D Ice Core Samples** - Soluble*					
G2-205-S	205.22	1026.7	868.6	465.5	75.2
G2-206-S	206.35	939.8	834.3	296.0	61.4
G2-1937-S	1936.11	1020.8	886.4	324.9	985.8
G2-1939-S	1938.52	1031.6	875.5	1040.5	1595.4
G2-2514-S	2514.32	1032.5	890.5	1042.2	1898.1
G2-2517-S	2516.22	1019.1	860.8	962.7	1886.8
G2-2684-S	2683.32	1018.9	875.7	669.7	918.2
G2-2685-S	2684.71	1029.5	874.3	600.4	740.7
G2-2743-S	2743.21	1040.3	878.4	205.5	103.9
G2-2744-S	2744.17	1013.1	865.6	-	124.0
G2-2802-S	2801.43	1078.2	886.2	143.9	91.9
G2-2922-S	2921.80	1010.5	849.7	410.9	272.3
G2-2932-S	2932.11	934.7	787.3	295.4	987.7
G2-2934-S	2933.15	1017.4	868.4	-	441.1
G2-2960-S	2959.32	948.6	780.5	229.7	93.6
G2-3005-S	3004.54	906.6	740.4	297.9	121.1
G2-3021-S	3020.42	1024.5	864.5	281.1	216.9
G2-3027-S	3026.32	971.3	801.7	284.8	90.6
***GISP2-D Ice Core Samples** - Blanks*					
Core Blank-1	-	-	163.5†	6.4	0.006
Core Blank-2	-	-	86.4†	0.4	0.003
Core Blank-3	-	-	328.4†	4.9	0.004

†*Sample masses correspond to aliquots of 18.2 MΩ DI water used for determination by isotope dilution with ^{150}Nd and ^{84}Sr spikes prepared from Oak Ridge National Laboratory enriched ^{150}Nd as Nd_2O_3 and ^{84}Sr as $SrCO_3$*

Table 5. *GISP2D Trace Element and Rare Earth Element ICP-MS Concentrations*

Sample	Depth	[Nd] (ppt; 10^{-9} g/kg)	[U] (ppb; 10^{-9} g/kg)	[La] (ppt; 10^{-9} g/kg)	[Ce] (ppb; 10^{-9} g/kg)	[Pr] (ppb; 10^{-9} g/kg)	[Dy] (ppb; 10^{-9} g/kg)	[Fe] (ppb; 10^{-9} g/kg)	[Ti] (ppb; 10^{-9} g/kg)	[Mn] (ppb; 10^{-9} g/kg)
***GISP2-D Ice Core Samples** - Soluble*										
G2-205-S	205.22	0.71	0.24	0.77	1.45	0.20	0.14	347	31	29
G2-206-S	206.35	-	-	-	-	-	-	-	-	-
G2-1937-S	1936.11	0.50	2.07	0.54	0.95	0.14	0.08	435	528	96
G2-1939-S	1938.52	1.50	2.61	1.65	3.30	0.46	0.30	1716	623	161
G2-2514-S	2514.32	1.73	2.43	1.86	3.80	0.49	0.33	1957	698	173
G2-2517-S	2516.22	2.1	2.96	2.28	4.80	0.61	0.40	1967	691	232
G2-2684-S	2683.32	0.97	1.30	1.16	1.75	0.28	0.14	721	269	166
G2-2685-S	2684.71	0.99	1.34	1.10	2.27	0.29	0.18	410	292	117
G2-2743-S	2743.21	0.66	0.26	0.75	1.53	0.20	0.15	393	45	68
G2-2744-S	2744.17	0.87	0.33	0.88	1.94	0.26	0.18	504	54	64
G2-2802-S	2801.43	-	-	-	-	-	-	-	-	-
G2-2922-S	2921.80	-	-	-	-	-	-	-	-	-
G2-2932-S	2932.11	0.80	1.53	0.82	2.05	0.24	0.16	515	439	129
G2-2934-S	2933.15	0.90	1.29	1.03	2.09	0.26	0.16	597	339	104
G2-2960-S	2959.32	-	-	-	-	-	-	-	-	-
G2-3005-S	3004.54	-	-	-	-	-	-	-	-	-
G2-3021-S	3020.42	-	-	-	-	-	-	-	-	-
G2-3027-S	3026.32	-	-	-	-	-	-	-	-	-
***GISP2-D Ice Core Samples** - Blanks*										
Core Blank-1	-	0.06	0.04	0.02	0.1	0.02	0.01	59	10.6	0.8
Core Blank-2	-	0.07	0.03	0.03	0.08	0.01	0.01	60	7.4	1.0
Core Blank-3	-	0.07	0.02	0.03	0.08	0.01	0.01	43	7.4	0.6

CHAPTER III

Climate of the Late Cretaceous North American Gulf and Atlantic Coasts

In review with Cretaceous Research
Co-authors:
Kyle W. Meyer, Sierra V. Petersen, Kyger C Lohmann, and Ian Z. Winkelstern

Abstract

Understanding the response of temperature to elevated atmospheric CO_2 during past greenhouse intervals such as the Late Cretaceous can constrain hypotheses of expected future warming tied to the rise of modern atmospheric CO_2 levels. Here we present new reconstructions of Gulf and Atlantic Coast coastal marine temperatures through the Late Campanian (~76 – 72 Ma) and Maastrichtian (72 Ma – 66 Ma), as determined by carbonate clumped isotope analysis of marine bivalves and gastropods. We find temperatures in the range of ~7 – 25 °C across multiple sites located between 31°N and 36°N paleolatitude, and cooler temperatures of ~3 – 14 °C at sites around 39°N paleolatitude. Temperatures agree across a variety of taxa, indicating no appreciable organism-specific vital effects. The calculated paleotemperatures are very similar to modern marine temperatures at the same locations, despite the Late Cretaceous generally being considered a warmer interval. Clumped isotope temperatures are cooler than published

temperatures from a nearby site measured using the TEX_{86} paleotemperature proxy, revealing a potential warm bias in TEX_{86} temperature estimates. The best agreement between clumped isotope and TEX_{86} temperatures is achieved when using the TEX_{86}^{L} calibration over TEX_{86}^{H} or BAYSPAR calibrations.

1. Introduction

The Late Cretaceous can be considered an important analogue for modern and future climate due to elevated atmospheric CO_2. Estimates from the Late Campanian (~76 – 72 Ma) through the Maastrichtian (72 Ma – 66 Ma) range from approximately 400-1100 ppm (Berner and Kothavala, 2001; Royer et al., 2012; Wang et al., 2014), compared to the 2016 global mean value of 403 ppm (Dlugokencky and Tans, 2017). Understanding surface temperature responses to elevated pCO_2 during this time interval, carries implications for the amount of warming that might be expected in the coming centuries. Despite comprehensive study of paleontological collections and sedimentological characteristics (Wade, 1926; Sohl, 1960), there have been only a limited number of studies quantifying climate trends in the Gulf and Atlantic coast regions of North America during the Campanian and Maastrichtian (MacLeod et al., 2005; Friedrich et al., 2012; Linnert et al., 2014; Vellekoop et al., 2016). These studies reconstructed marine temperatures and ocean bottom water temperatures by either using: 1) the oxygen isotope ($\delta^{18}O$) paleothermometer applied to planktic (MacLeod et al., 2005) and benthic foraminifera (Friedrich et al., 2012) or the organic geochemical proxy TEX_{86} (Linnert et al., 2014; Vellekoop et al., 2014; Vellekoop et al., 2016). However, limitations exist with these techniques in that temperatures derived from $\delta^{18}O$ values can be compromised by coincident changes in the isotopic composition of seawater ($\delta^{18}O_{sw}$), a value that is progressively more difficult to reliably estimate with increasing geologic age, (Keating-Bitonti et al. 2011; Petersen et al., 2016a). Issues of seasonal biases with respect to the TEX_{86} paleothermometer may favor summer temperatures as opposed to mean annual temperatures, particularly at high latitudes (Ho et al., 2014; Rodrigo-Gámiz et al., 2015). Additionally, a number of different calibrations exist to convert TEX_{86} values to temperature, and there is debate over which calibration is most appropriate to use in deep-time applications, particularly during past greenhouse intervals (Schouten et al., 2013; Taylor et al., 2013; Inglis et al., 2015).

We have analyzed marine macroinvertebrate fossils to provide new reconstructions of Late Cretaceous temperatures from the Gulf and Atlantic Coasts, determined using carbonate clumped isotope paleothermometry and strontium isotope compositions for a chemostratigraphic context of these fossils. The clumped isotope (Δ_{47}) paleothermometer is based on fundamental thermodynamics as opposed to being empirically derived from modern bacteriological communities, which may have differed in the past (as in the case of the TEX_{86} paleothermometer) and does not require independent knowledge of $\delta^{18}O_{sw}$ (Eiler and Schauble, 2004; Eiler, 2011). These new data provide an independent control on temperature in the southeastern U.S. during the Late Cretaceous, particularly in comparison to previously reported warm temperatures produced using the TEX_{86} paleothermometer (Linnert et al., 2014; Vellekoop et al., 2014; 2016).

2. Locality and Sample Selection

2.1 Locality Selection

Fossil shell specimens in this study originated from thirteen localities (Fig. 13): nine along the Mississippi Embayment (Coon Creek, Owl Creek, County Lake, Sumter County, Moscow Landing, Tombigbee River, Marengo County, Safford, Shopton Roadcut), and four along the Atlantic Coast (Poricy Brook, Big Brook, Crosswicks Creek, and Burches Ferry). Authors collected all samples from the Burches Ferry and Moscow Landing/Tombigbee River sites. Additional samples were selected from the invertebrate collections of the University of Michigan Museum of Paleontology and the USGS fossil collection in Lakewood, Colorado (see Sample Locality Information, supplemental material). Sites were selected based on completeness of stratigraphic exposure of Campanian/Maastrictian-aged samples, fossil availability, taxa present, and sample preservation. The Ripley and Prairie Bluff formations, in particular, were targeted based on the excellent preservation of original shell material previously documented from these formations (Ruffin, 1843; Wade, 1926; Siple, 1957; Sohl, 1960; Swift, 1966; Larina et al., 2016).

2.2 Burches Ferry, South Carolina

Approximately 6.5 m of the Peedee Formation was measured at Burches Ferry, South Carolina (Fig. 14), the type locality for the PDB carbonate isotope standard (Ruffin, 1843; Swift, 1963). The outcrop exposure bears three distinct silty to sandy limestone beds containing a fine shell hash. The uppermost of these beds outcrops as discontinuous lenses and is significantly more indurated than the other two marker beds. Shells were collected with respect to the three limestone horizons (Fig. 14). Species collected from this site include *Anomia* sp., *Belemnitella americana*, and *Exogyra costata* (Siple, 1957; Swift, 1966). The locality is interpreted as an open-shelf environment and is restricted to the *E. costata* biozone based on previously identified fauna (Stephenson, 1914; Siple, 1957; Swift, 1966).

2.3 Moscow Landing/Tombigbee River, Alabama

The Moscow Landing location has been described in terms of sedimentology, stratigraphy, and paleontological preservation by several previous studies (Moshkovitz and Habib, 1993; Smit et al, 1996; Smith et al., 1997; Hart et al., 2013; Larina et al., 2016) and includes the Cretaceous Prairie Bluff and Paleocene Clayton formations. The Cretaceous-Paleogene (K-Pg) boundary here is unconformable and does not bear the iridium anomaly at this location. The unconformity at this boundary is variably estimated to be missing less than 200 ka (Moshkovitz and Habib, 1993) or as much as 500 ka (Larina et al., 2016). At Moscow Landing, we measured ~13 m of section through the Cretaceous Prairie Bluff and overlying Paleocene Clayton formations, collecting samples stratigraphically up-section from the first exposure of strata at the water surface of the Tombigbee River, including from a prominent phosphatic lag deposit at 5 m and from large erosional channel features cut into the top of the Prairie Bluff Fm. (Fig. 15). These channels bear reworked large clasts, fossils, and even whole boulders/packages of the Prairie Bluff chalk, with the upper surface of both the channels and adjacent chalk heavily bioturbated by *Thalassinoides,* as described in several other studies (Smit et al., 1996; Hart et al., 2013; Larina et al., 2016). Fossil samples were collected from these channels, but due to their reworked nature, were not considered in stratigraphic time series interpretations.

To collect from the underlying Ripley Formation, the shallow dip of the beds required traversing along strike ~5 km upriver through ~10 m of poor exposure to continue the section (Fig. 15). Because of this geographic separation from the Moscow Landing locality, samples collected from the Ripley Fm. are given the separate locality name ‘Tombigbee River.’ At this location, we measured five additional meters of section below the Ripley Fm. contact.

All samples collected from the Prairie Bluff and Ripley Formations were *E. costata*. In the Paleocene Clayton Fm., samples were limited to the taxa *Ostrea pulaskensis*, following the disappearance of *E. costata* at the K-Pg boundary. *E. costata* are large oyster specimens that can typically range from 2 to 10 cm across, whereas *O. pulaskensis* individuals are significantly smaller ranging a few mm to cm in diameter. The disparity in size between these taxa allowed for isotopic sampling from a small portion of the ventral margin of *E. costata* (typically representing three to five growth bands), but at the expense of nearly an entire shell of *O. pulaskensis* (also found in higher abundance, compared to the more isolated occurrences of *E. costata*).

2.4 Southwest Alabama Composite Section

Two Prairie Bluff samples from Marengo County were incorporated into the Moscow Landing/Tombigbee River stratigraphy using the regional geometry and relative elevation between sites (Monroe and Hunt, 1958). The Marengo County site occurs directly along strike from the Moscow Landing locality (N 70° W), and has near horizontal strata (regional dip ~7.5 to 9.5 m per km; ~0.01°). Therefore, the difference in elevation between sites is equivalent to their relative stratigraphic positions, within error of field measurement. This assumption is supported by the measured stratigraphic separation along section between the top of the Ripley Fm. and the base of the Moscow Landing section (10 m), compared to an elevation difference of approximately 9 m between the two locations.

The elevations of the Marengo County site places the Marengo County samples ~15 m above the lowest Prairie Bluff samples collected at Moscow Landing. Because only ~12 m of Prairie Bluff Fm remain at Moscow Landing, the Marengo County samples are therefore stratigraphically higher than the highest Prairie Bluff samples at Moscow Landing and represent a younger interval that is missing at this site, and convey the variable degrees of impact-related tsunami erosion across the Prairie Bluff Fm. (interpreted as a result of the Chicxulub impactor; Smit et al., 1996). Ammonite biostratigraphy supports this interpretation, showing that the upper Prairie Bluff Fm. at a site (Mooseland) near our Marengo County locality includes a younger ammonite zone and extends closer to the K-Pg boundary than at Moscow Landing (Larina et al., 2016), and would further reinforce the age of these samples as < 500 ka from the actual K-Pg impact event (Moshkovitz and Habib, 1993; Larina et al., 2016).

2.5 Studied taxa

Our 46 mollusk samples include ten different marine macroinvertebrate taxa: eight bivalve (*Agerostrea mesenterica, Anomia tellinoides, An. sp., Cucullaea vulgaris, Exogyra cancellata, E. costata, Ostrea pulaskensis, Crassitellites vadosis*), one gastropod (*Turitella paravertebroides)*, and one belemnite (*Belemnitella americana*) species (individual specimen collection data is detailed in the Sample Locality Information, supplemental material). To date, clumped isotope analysis of a wide variety of modern bivalves and gastropods has not revealed any significant taxa-specific vital effects (Eagle et al., 2013; Henkes et al., 2013; Came et al., 2014); however, it is imperative that extinct species (with unknown physiological processes with respect to isotope discrimination) be evaluated for such effects. By measuring a variety of taxa, we minimize the risk that our results depend on any single extinct species. By analyzing one species (*E. costata*) at multiple sites, direct, site-to-site comparison from a single taxon is possible.

All measured taxa are benthic and sessile, with the exception of *B. americana*, and for the sake of this study we assume that all specimens found *in situ* were not subject to significant postmortem transport (with the notable exception of samples ML-PRB-EXOe and ML-PRB-EXOf retrieved from a phosphatic lag deposit, and sample ML-PRB-EXOi as channel bedload; Fig. 15). As *B. americana* is a free-swimming cephalopod, its isotopic composition could represent a wide range of environments within the water column (50 to 1000 m; based on the depth ranges of modern cephalopods; e.g. nautiloids and most squid taxa; Jereb and Roper, 2005; 2010; Mutterlose et al., 2010; Dunstan et al., 2011; Mettam et al., 2014; Jereb et al., 2016; Chung and Marshall, 2017). Many of the fossil bivalve and gastropod genera measured have extant representatives (e.g. *Anomia, Crassetellites*, *Cucullaea*, *Ostrea, Turritella*), and the two extinct genera (*Exogyra* and *Agerostrea*) have analogous modern taxa within their families (*Gryphidae* and *Ostreidae*, respectively) that display a range from 6 to 140 m (Ebersole, 2009; NOAA NBI, 2017). This is consistent with the paleodepth estimates for the Navesink (~100-150 m; Olsson et al., 2002), Demopolis (65-90 m; Puckett, 1991), and Prairie Bluff formations (~20-40 m; Schulte and Speijer, 2009). Therefore, reconstructed Δ_{47} temperatures represent near-surface (shelf) temperatures, albeit susceptible to seasonal changes in thermocline depth, and recent studies on bivalves at similar depths corroborate that these depth ranges reasonably approximate coastal marine temperatures (e.g. Tao et al., 2013; Johnson et al., 2017).

3. Methods

3.1 *Shell sampling and preservation assessment*

Clumped isotope paleothermometry is susceptible to solid-state reordering under relatively low temperature burial conditions (≥100 °C), resulting in a thermal overprinting of the original carbonate formation temperature (Henkes et al., 2014; Shenton et al., 2015). Recent work has detailed additional influences on $\delta^{18}O$, $\delta^{13}C$, and Δ_{47} compositions from naturally (Ritter et al., 2015) and experimentally (Ritter et al., 2017) altered marine bivalve shell material, concluding that below 100 °C these parameters all remain largely unaltered. In combination with the geochemical results, Ritter et al. (2017) also found that macroscopic features, scanning electron microscopy (SEM) imagery of shell structure, cathodoluminescence, and fluorescence techniques remain unaltered until somewhere between 150 and 175 °C. Therefore, for the sake of paleoclimate reconstructions, it is imperative to screen samples for potential diagenetic alteration as well as solid-state reordering of clumped isotope compositions, and would require samples to have experienced comparatively shallow burial histories and extremely limited tectonic influences to meet preservation criteria.

We subjected all samples to a visual assessment of carbonate fabrics by optical microscopy, eliminating samples with obvious recrystallization (none). For some aragonitic taxa (e.g. *Anomia* sp.), we documented preservation of original nacre, a reasonable initial indicator of well-preserved, primary carbonate. We did not find any clear marine cements/encrustations, and there was no observable dolomitization in any samples. We screened a subset ($n = 7$) samples representing four sample localities (~20% of all samples used in this study; additional screening was limited by available analytical time and/or sample material) for evidence of diagenetic recrystallization beyond visual inspection via SEM imaging. Samples taken for SEM imaging were from bivalve ventral margin sections adjacent to the sampling section for isotopic analyses (or rostrum cross-section for belemnite specimens). Previous paleontological studies have also documented pristine preservation of shell carbonate (e.g. via thin section assessment and isotopic analyses) at several of our sample localities within the Mississippi Embayment (Sohl, 1960;

Jones et al., 1987; Larina et al., 2016). All specimens assessed by SEM imaging exhibited primary shell fabric and distinct growth textures ranging from Preservation Index (PI) values of 2 to 5 (after Cochran et al., 2010; see Fig. 23).

For one bivalve sample (BF-PD-EXOe), we measured oxygen and carbon isotope values of secondary, crystalline calcite from three vugs within the umbo of the shell, and found $\delta^{18}O$ and $\delta^{13}C$ of -2.5 ± 0.3 (1σ, $n = 3$) and -4.5 ± 0.7 (1σ, $n = 3$), respectively, which compared to $\delta^{18}O$ and $\delta^{13}C$ values of -0.2 ± 0.2 (1σ, $n = 3$) and -1.2 ± 0.1 (1σ, $n = 3$) measured from layered shell calcite in the ventral margin of the same sample. The significant difference between the oxygen and carbon isotopic compositions of the crystalline secondary calcite and the well-preserved shell calcite, coupled with the strontium isotope composition of an aliquot of the same powder from the ventral shell material, supports primary preservation in the shell fabric.

More than half the specimens are of the oyster genus *Exogyra* and were sampled near the ventral margin of the shell over a large enough area to represent at least three distinct layers of ordered carbonate in the shell matrix, presumed to be annual growth bands. Carbonate fragments from the ventral margin were ground by hand using a mortar and pestle. Smaller taxa were sampled using a dental drill on the slowest setting (~1000 rpm; *Crasatellites, Cucullaea)* or were crushed in their entirety (*Anomia tellinoides, Agerostrea mesenterica, Ostrea pulaskensis*). For the fast-growing gastropod *T. paravertebroides*, three shell fragments were also sampled for conventional stable isotope analysis at high-resolution with samples approximately every 1-2 mm, with many samples per whorl, to potentially assess seasonal variability (where a single whorl likely represents less than one year of growth; after Jones and Allmon, 1995).

3.2 Clumped Isotope Methodology

Carbonate powders were measured for stable ($\delta^{18}O$, $\delta^{13}C$) and clumped (Δ_{47}) isotopic compositions in the University of Michigan Stable Isotope Laboratory using the same instrumentation and procedure as Defliese et al. (2015), with the Porapak™ trap temperature held between -10 and -15 °C (Petersen et al., 2016b). Raw voltages were converted to isotopic values following Huntington et al. (2009; with $\delta^{18}O$ and $\delta^{13}C$ calculated independently as opposed to being taken from ISODAT). Measured carbonate Δ_{47} values were placed in the absolute reference frame of Dennis et al. (2011) using heated (1000 °C) and H_2O-equilibrated (25 °C) standard gases, and converted to temperature values using the 75°C acid fractionation factor and high-temperature composite calibration of Defliese et al. (2015). $\delta^{18}O_{sw}$ values are calculated from carbonate $\delta^{18}O$ and Δ_{47}-derived temperatures using the relationships of Kim and O'Neil (1997) and Kim et al. (2007) for calcite and aragonite, respectively. All taxa with the exception of *Anomia* and *Turritella* were dominantly calcitic, with the former being partially and the latter fully aragonitic (Lockwood, 2004 and references therein). Measured $\delta^{18}O$, $\delta^{13}C$, Δ_{47}, and calculated paleotemperature and $\delta^{18}O_{sw}$ values for all samples are reported along with gas and carbonate standard data (Table 6 and 7).

Recent work has suggested that improved determination of Δ_{47} values is possible using updated ^{17}O correction parameters and a newly defined value of Vienna Pee Dee Belemnite (VPDB; Daëron et al., 2016; Schauer et al., 2016). At this point, only one published temperature calibration exists using these parameters (Kelson et al., 2017). Due to existing differences between calibrations created in different labs, we have chosen to present our data primarily using older parameters and the temperature calibration developed at University of Michigan (Defliese et al., 2015) until such a time that a universal temperature calibration can be found or temperature-calibration data produced in the same lab as this study can be updated using the new parameters. We present raw data calculated with both old and new parameters to allow for future recalculation (Table 6 and 7). Given that corrections to both measured unknowns and calibration samples within a given lab will likely be similar, we anticipate only small (<1-3 °C) variations between temperatures calculated using the old and new parameters.

3.3 Strontium Isotope Analysis

A subset (*n* = 24) of the shell samples were also analyzed for their strontium isotopic composition. A split from each homogenous carbonate powder was measured for 200 cycles with a reported 2 SE analytical uncertainty for $^{87}Sr/^{86}Sr$ on a Finnegan MAT 262 TIMS in the University of Michigan BEIGL facility. All measured $^{87}Sr/^{86}Sr$ values were corrected within each measurement session relative to the established value of NIST SRM-987 (Thirlwall, 1991; $^{87}Sr/^{86}Sr$ =0.710248 ± 0.000011). The long term mean $^{87}Sr/^{86}Sr$ value for NIST SRM-987 in the BEIGL facility is 0.710238 ± 0.000016 (1σ).

An age for each measured fossil was calculated by comparison to the most recent iteration of the LOWESS global seawater strontium curve for the Late Cretaceous (McArthur et al., 2001; McArthur pers. comm., 2015; Supplementary Material, Table 9). Sample $^{87}Sr/^{86}Sr$ values were matched to the closest $^{87}Sr/^{86}Sr$ value for the Campanian/Maastrichtian portion of the mean LOWESS curve, and the analytical uncertainty of each strontium measurement was propagated through the uncertainty envelope of the LOWESS curve itself to provide the most conservative cumulative uncertainty on any given age (~0.45 to 1.5 Ma per sample; Figs. 16, 17). Finally, due to age overlap and possible ‘reversals’ with respect to Sr isotope compositions commonly found throughout the sampled stratigraphic sections (e.g. Moscow Landing and

Burches Ferry) an average age for each outcrop of a given formation was calculated based on all measured samples from each locality/formation to provide a generalized point of comparison in assessing whether or not samples from different localities represent a roughly coeval period of time. All strontium data and calculated ages can be found in Supplementary Table 9.

4. Results

4.1 Age model construction using $^{87}Sr/^{86}Sr$

Average ^{87}Sr/^{86}Sr ages place the measured Cretaceous formations between 67 and 74 Ma. This is consistent with other studies that have placed the Peedee, Demopolis, Ripley, and Prairie Bluff formations in the *Exogyra costata* zone, which spans the entirety of the Maastrichtian (Stephenson, 1933; Sohl, 1960; Lerman, 1965). In the Late Cretaceous portion of the LOWESS model, ^{87}Sr/^{86}Sr values increase linearly until ~67 Ma, after which values plateau, raising issues of non-uniqueness in age determination at the very end of the Cretaceous (Fig. 17). We find this trend is reflected in our data as well (Figs. 16, 17). Stratigraphically throughout both the Ripley and Prairie Bluff formations, the ^{87}Sr/^{86}Sr data show some apparent reversals amongst generally overlapping data. These reversals may be due to inherent noise in the data or due to sedimentary reworking that has been documented in these sections (Smit et al., 1996; Hart et al., 2013). Additionally, the one sample from the Paleogene Clayton Fm. recorded a ^{87}Sr/^{86}Sr value off the LOWESS curve that cannot be interpreted as an early Paleogene age. Between the uncertainty envelope of the LOWESS curve itself, our measured analytical uncertainty, and the non-uniqueness of global ^{87}Sr/^{86}Sr values near the K-Pg boundary, we choose to interpret trends in temperature based on stratigraphic position rather than calculated ^{87}Sr/^{86}Sr age.

The strontium data broadly supports current interpretations of regional stratigraphy in Alabama. Strontium isotope values place the Ripley Fm. prior to the Prairie Bluff Fm. and the Early Danian Clayton Fm., conforming with the known stratigraphic positions of these units (Figs. 16, 17). The Marengo County Prairie Bluff samples cannot be distinguished from the Moscow Landing samples using ^{87}Sr/^{86}Sr (Figs. 16, 17), but are interpreted to be younger (falling within the missing time interval at Moscow Landing prior to the K-Pg boundary) given the shallow regional dip of the Prairie Bluff Fm.

Based on strontium isotope compositions, the Demopolis Fm. at Sumter County appears to be coeval with the Ripley Fm. at Moscow Landing, although in the regional stratigraphy it clearly underlies the Ripley (Wade, 1926; Monroe and Hunt, 1958; Sohl, 1960). This may be due to spatial variation in age of the formation boundary in central Alabama, where the contact between the Ripley and the Demopolis formations appears time-transgressive and, in places, stratigraphically time-equivalent between the basal Ripley and uppermost Demopolis (Monroe and Hunt, 1958; Sohl, 1960). Given the consistent $\delta^{18}O_{sw}$ compositions calculated for all specimens from along the Mississippi Embayment, the ^{87}Sr/^{86}Sr values not departing from the LOWESS curve, and the correspondence with other published ^{87}Sr/^{86}Sr values of fossil material from other sites in western Alabama (Jones et al., 1987; Becker et al., 2008) we interpret the strontium isotope compositions of these samples to be unaltered. Bryant et al. (1995) suggest that estuarine influence can substantially alter ^{87}Sr/^{86}Sr values, but note that most moderately diverse marine faunal assemblages representing a nearshore environment would be unaffected by freshwater influence. There is no strong evidence for estuarine influence with regards to the deposition of the Navesink, Peedee, Ripley, Demopolis, Prairie Bluff Fms. (Stephenson, 1933;

Sohl, 1960; Swift, 1966; Olsson, 1987) and all bear abundant specimens of *E. costata*, which is interpreted to be explicitly marine compared to *Crassostrea* and *Ostrea* taxa (Lerman, 1965).

Strontium isotope values from Burches Ferry place the Peedee Fm. around 70-72 Ma, overlapping with the lower Prairie Bluff Fm. This is also consistent with biostratigraphic interpretations of both units as within the *E. costata* zone and limited *B. americana* specimens in the upper Ripley and lowermost Prairie Bluff (Stephenson, 1914; Allmon and Knight, 1993). The two Navesink Fm. localities show distinct ages, with the Crosswicks Creek locality distinctly older than Poricy Brook. The latter values are consistent with $^{87}Sr/^{86}Sr$ data from the Navesink Fm. from nearby cores (Sugarman et al., 1995). The single specimen from Crosswicks Creek is *E. cancellata*, a species which occurs in the lower part of the *E. costata* zone and is typically restricted to the underlying Mount Laurel Fm. in the New Jersey region (Sugarman et al., 1995). This specimen may, therefore, have been incorrectly identified as being retrieved from the Navesink by initial collectors, and more likely represents the older Mt. Laurel Formation, as suggested by the $^{87}Sr/^{86}Sr$ data.

4.2 Clumped and stable isotopic results

Figures 17-19 show the clumped isotopic results separated by taxa, locality, and formation. Studied localities record paleotemperatures of ~7 to 25 °C, with the exception of the three New Jersey Navesink sites, which are ~10° farther north (Fig. 12) and yield cooler temperatures (Figs. 18, and 19). Excluding the Navesink Fm. sites, sample mean temperature is 16.1 ± 0.7 °C (*n*=42; 1 SE) for all Gulf and southern Atlantic Coast localities. $\delta^{18}O_{sw}$ values were calculated from Δ_{47}-derived temperatures and the calcite-H_2O (Kim and O'Neil, 1997) and aragonite-H_2O (Kim et al., 2007) fractionation factors, respectively. The mean $\delta^{18}O_{sw}$ value across all sites was -0.9 ± 1.2‰ (*n*=46, 1σ; VSMOW), similar to the average value assumed for an ice-free world (-1‰ VSMOW; Zachos et al., 1994). The Navesink localities show slightly lower average $\delta^{18}O_{sw}$ values (Fig. 21), consistent with modern latitudinal trends in $\delta^{18}O_{sw}$ in terms of magnitude and direction (more negative values at higher latitude; LeGrande and Schmidt, 2006).

The Moscow Landing and Tombigbee River sites, though ~5 km apart, represent a semi-continuous stratigraphy through the Late Campanian, Maastrichtian, and early Paleocene (Danian) (Fig. 18). Within the Prairie Bluff and Ripley formations at these sites, temperatures range from ~7 – 25 °C. Two Marengo County samples, interpreted to be younger than the Moscow Landing Prairie Bluff, record temperatures of 22.2 ± 3.1 °C and 22.9 ± 3.2 °C. After a hiatus of unknown duration, the Danian-aged Clayton Fm. temperatures are ~15 –18 °C. Although reworked, a sample from the channel also recorded temperatures within the uncertainty of other reported Moscow Landing samples at 10.3 ± 3.4 °C.

We observe no systematic offset from the mean in measured temperature of any given taxa, suggesting none of the studied taxa are biased by clumped isotope vital effects (Fig. 8). This is also seen in $\delta^{18}O_{calcite}$, $\delta^{18}O_{sw}$ and $\delta^{13}C$ (Table 6 and 7; Figs. 21 and 22), with one exception. *Ostrea pulaskensis* showed consistently higher $\delta^{13}C$ values than other taxa from the same locality (Fig. 22) which may represent: 1) vital effects in carbon isotopes that do not carry over into the clumped isotope temperature or $\delta^{18}O_{sw}$ values, 2) a substantial difference in the dietary niche of this taxon from the other mollusks sampled, 3) a change in the marine organic carbon pool following the K-Pg extinction event, and/or 4) some other unanticipated effects of the substantial environmental and ecological turnover following the boundary. The consistency in temperature, $\delta^{18}O_{sw}$, and $\delta^{13}C$ (with exception of *O. pulaskensis*) includes taxa with varied physiologies, feeding strategies, and trophic positions, and surprisingly even includes the belemnite *B. americana*, an organism that was potentially mobile through the water column from surface to the mid-shelf marine realm, in contrast to the majority of sampled taxa which are sessile bottom-dwelling bivalves. However, previous isotopic studies have found that belemnites from Seymour Island record isotopic values similar to benthic foraminifera from the Maud Rise at a reconstructed paleodepth of approximately 1500 m or less (Dutton et al., 2007). We also measured conventional $\delta^{18}O$ and $\delta^{13}C$ values for an initial assessment of seasonality from three specimens of *T. paravertebroides* (TRT1 – the same sample as CL-RIP-TURa, TRT2, and TRT3) and report these results in Table 8 and Fig. 24 of the supplement.

Reconstructed temperatures from this study are cooler than recently published temperatures calculated using the TEX_{86} organic proxy from a nearby site in Shuqualak, Mississippi (Fig. 20; Linnert et al., 2014). Figure 20 compares formation-averaged clumped isotope temperatures through time with TEX_{86} temperatures calculated using three different sea surface temperature calibrations. TEX_{86}^{H} data was presented by Linnert et al. (2014) in the main text and TEX_{86}^{L} and BAYSPAR data in the supplement, respectively. All three calibrations produce consistently warmer temperatures than reconstructed using the clumped isotope method. Although the absolute temperature values are different, the broader temporal pattern of temperatures is consistent (Fig. 20).

5. DISCUSSION

5.1 Regional climate similar to modern

Studied localities record paleotemperatures of ~7 – 25 °C across all sites and taxa, with the exception of the three New Jersey Navesink Fm. sites, which are ~10° farther north and yield colder temperatures (~3 – 14 °C; Fig. 12, 17, and 19). The mean temperature and range at the southern sites (excluding the Navesink Fm. localities), is similar to the measured modern seasonal temperature variability observed over the same latitudinal range (~10 – 29 °C, representing the mean of monitoring data from: (1) Charleston, South Carolina and (2) Dauphin Island, (3) 'Coast Guard Sector Mobile', and (4) 'Mobile State Docks', Alabama as nearest geographical analogues to our sampling locations; NOAA NODC, 2017; Fig. 19). In contrast, at a locality in this same latitudinal range in the Eocene, warmer temperatures of 25 – 30 °C were suggested by $\delta^{18}O$, Δ_{47}, TEX_{86}, and MBT/CBT (methylation index of branched tetraether/cyclization ratio of branched tetraether) proxies (Keating-Bitonti et al., 2011).

The temperature range of the Navesink Fm. sites (~3 – 14 °C) also compare reasonably to the modern range of temperatures from sites across at 39-40 °N (~2 – 24 °C, the mean of data from (1) Ship John Shoal, (2) Sandy Hook, (3) Atlantic City, and (4) Cape May, New Jersey; NOAA NODC, 2017; Fig. 19). This suggests that the higher latitudinal position of the Navesink localities likely explains the majority of the temperature difference from the Burches Ferry and Gulf Coast sites (based on decreasing temperature of the latitudinal thermal gradient). Additionally, the paleoenvironment of the Navesink Formation is interpreted to be slightly deeper than the other locations (~100 to 150 m for the Navesink [Olsson et al., 2002], vs. 65 to 90 m for the Demopolis [Puckett, 1991], or 20-40m for the Prairie Bluff formations [Schulte and Speijer, 2009]).

Richaud et al. (2016) compiled modern sea surface, and ocean bottom (shelf = 0 to 200 m, and upper slope = 200 to 600 m) temperatures from the Mid-Atlantic Bight region (Cape Hatteras, North Carolina to Cape Cod, Massachusetts) through the Gulf of Maine, which compares to the data from specimens of the Pee Dee and Navesink Fms. The latitudinal temperature difference (~2 – 7 °C) between the seasonal surface temperature range from present-day North Carolina (~7 – 24 °C) and New Jersey (~5 – 17 °C) of their study closely matches the reconstructed paleotemperatures of this study. Richaud et al. (2016) also found a similar magnitude of temperature difference (~2 to 5 °C) between seasonal sea surface (~7 to 24 °C) and shelf (~5 to 12 °C) temperature ranges in the Mid-Atlantic Bight region, and virtually no temperature variability along the upper slope. Therefore, we interpret the paleotemperature ranges, documented from the fossil bivalves in this study, to capture a seasonal range, but acknowledge that the influences of habitat depth and latitudinal thermal gradient is likely inseparable. An observable seasonal temperature range from fossil bivalve Δ_{47} measurements would also serve to reinforce the paleontological interpretations of depth habitats for these taxa at < 200 m. Some authors suggest that mollusk intraspecific morphological differences (and between other taxa) can be used to determine whether individuals existed in shallow settings or below seasonal thermoclines, which could provide a possible screening process for separating the effects of depth and latitude on paleotemperatures (Holme, 1961; Seed, 1968; Jones, 1980; Arthur et al., 1983; Morley et al., 2010).

The cooler temperatures recorded by the Navesink could also suggest the early existence of the Gulf Stream current along the Atlantic margin of North America. The Gulf Stream is defined in the modern by strong western boundary surface currents that transport heat from lower latitudes, which separate into a distinct 'north wall' interface at Cape Hatteras with strong return flow of cold water from the North Atlantic along the shorelines of present-day New York and New Jersey (Taylor and Stephens, 1998). Variations in the position of the Gulf Stream today occur seasonally and over inter- and intra-annual timescales in conjunction with changes in the North Atlantic Oscillation (Taylor and Stephens, 1998), and accounting for seasonal temperature variations on the New Jersey coast ranging from 20 to 25 °C (NOAA NEFSC, 2017).

Nonetheless, all of these factors for producing cooler temperatures in the Navesink Fm. are likely secondary to the influence of decreasing latitudinal thermal gradient.

This clumped isotope record for the Gulf and Atlantic coasts of the U.S. reveals a mean Late Cretaceous latitudinal thermal gradient (~1.3 °C/° latitude) that appears comparable to modern (~0.8 to 1 °C/° latitude; Greenwood and Wing, 1995), and similar to what has been seen in other published records from the Western Interior Seaway (Petersen et al., 2016b). For the northern mid-latitudes, temperatures from the Maastrichtian differ only slightly from modern temperatures at similar latitudes (Fig. 19). This implies that regional warming expected from projected increases in modern CO_2 concentrations may not be as great for northern mid-latitudes as for other regions, such as the southern high latitudes, which were significantly warmer than modern during the Maastrichtian (Petersen et al., 2016a).

Calculated $\delta^{18}O_{sw}$ values range from similar to modern seawater (~0 ‰, VSMOW) to significantly more negative (average = -1.2 ± 0.7‰, n=46, 1σ, VSMOW; Fig. 21, Supplementary Material). $\delta^{18}O_{sw}$ would be expected to be more negative than today in an ice-free (or at least reduced ice) world, and perhaps most importantly, the variability in these data illustrates the need for independent constraint on $\delta^{18}O_{sw}$ when using carbonate $\delta^{18}O$ as a temperature proxy.

5.2 Seasonality in the Gulf Coast

We measured a partial sub-annual time series of $\delta^{18}O$ and $\delta^{13}C$ values by sampling along the whorls of the columellar axis of three different specimens of the gastropod *Turritella paravertebroides* from the County Lake, Mississippi locality. All three specimens were broken and incomplete, likely recording less than one year of growth each (after Jones and Allmon, 1995), but taken together, the $\delta^{18}O$ recorded in the three shells gives an indication of seasonal temperature ranges at this site (assuming $\delta^{18}O_{sw}$ values were constant over subannual timescales and $\delta^{18}O_{sw}$ = -1.9‰, as determined by clumped isotopic measurement of the one measured specimen). The full seasonal temperature range inferred from the *Turritella* $\delta^{18}O$ values was 6 °C with absolute values (~11 to 17 °C) existing within the average seasonal ranges of sea surface temperatures at modern Gulf and southern Atlantic Coast sites (Fig. 19). The turritellid seasonal temperatures also compare well to temperature estimates from existing published records of Campanian and Maastrichtian bivalves $\delta^{18}O$ analyses at low to mid-latitudes (~7 to 15 °C; Steuber et al., 2005; Dutton et al., 2007).

The modern seasonal average temperature range for Alabama (Dauphin Island = 18.3 °C, Coast Guard Sector Mobile = 17.2 °C, and Mobile State Docks = 19.4 °C), South Carolina (Charleston = 18.9 °C), and New Jersey (Sandy Hook = 20.0 °C, Atlantic City = 21.1 °C, Cape May = 20.6 °C, and Ship John Shoal = 25.0 °C) all exceed the values of the *Turritella* seasonal temperature range (NOAA NODC, 2017; Fig. 19). As a separate point of comparison, TEX_{86}^{L} records, such as the one from nearby Shuqalak Mississippi (Linnert et al., 2014), may demonstrate summertime biases (see section 5.3). If so, then the difference between TEX_{86}^{L} and Δ_{47} temperature records may serve as a minimum or partial estimate of seasonal temperature range. We observe a ~5 °C difference in temperature between TEX_{86}^{L} temperatures and "annual mean" Δ_{47} records, similar to the subannual temperature range seen in Turitella.

5.3 Comparison to TEX_{86}-based and other Gulf Coast and Atlantic temperature proxy records

The TEX_{86} proxy is based on the empirically-derived temperature sensitivity in the ratios of a suite of membrane lipids (GDGTs) produced by single-celled thaumarchaeotal organisms

(Schouten et al., 2002, 2007; Shimada et al., 2002; Wuchter et al., 2004; Kim et al., 2008, 2010). The general trend observed with TEX_{86} documents an increased number of cyclopentyl moieties with increasing temperature, and a higher degree of isomerism in the chrenarcheol compound (Schouten et al., 2013). Out of a large number of temperature calibrations that have been produced through the years (Schouten et al., 2013; Taylor et al., 2013; Inglis et al., 2015), two predominant calibrations utilized for paleoclimate applications are the TEX_{86}^{H} and TEX_{86}^{L} calibrations, which differ in the specific GDGT molecules used. The TEX_{86}^{H} calibration excludes core-top data from modern high-latitude localities and many values associated with the comparatively restricted marine setting of the Red Sea, whereas TEX_{86}^{L} includes these data (Schouten et al., 2013; Taylor et al., 2013; Inglis et al., 2015). In the modern, the two calibrations yield nearly identical results for temperatures >15 °C, and thus, for many paleotemperature applications, particularly in past greenhouse intervals, the TEX_{86}^{H} calibration has been preferred due to its being based upon warmer modern localities, a smaller uncertainty with the calibration error, and a better mechanistic understanding of the sensitivities involved with its calculation (Schouten et al., 2013; Taylor et al., 2013; Hernández-Sánchez et al., 2014). More recently, a spatially varying Bayesian regression model has also been developed for TEX_{86} (BAYSPAR; Tierney and Tingley, 2014; 2015), which can address concerns of region-specific issues that may arise for a given deep-time TEX_{86} temperature record, searching the modern core-top database to select an appropriate modern analogue based on parameters including the raw TEX_{86} value, GDGT [2/3] ratio, and branched versus isoprenoidal tetraether (BIT) for a given locality (Taylor et al., 2013; Inglis et al., 2015).

Clumped isotope temperatures produced in this study are consistently colder than TEX_{86}-based temperatures from similar localities, regardless of the calibration used (Fig. 19). In the

Gulf region, the coldest TEX_{86} temperatures, produced using the TEX_{86}^{L} calibration, are still ~5 °C warmer than the clumped isotope temperatures on average, whereas the TEX_{86}^{H} and BAYSPAR temperatures are ~10-12 °C warmer. TEX_{86}^{H} records from the Brazos River locality in Texas (Vellekoop et al., 2014) and Meirs Farm and Bass River sites in New Jersey (Vellekoop et al., 2016) also indicate significantly higher temperatures (~22 to 30 °C, and 22 to 28 °C, respectively), and show similar offsets (~10 °C) from the closest locality with clumped isotope data. It is possible that due to the benthic habitat of the majority of species used in this study, the clumped isotope temperatures may be recording a slightly cooler, deeper environment than the thaumarchaeota making the GDGT lipids. However, it is unlikely that this difference would be more than a few degrees, due to the shallow interpreted shallow depth habitat of the bivalves within the mixed layer. Additionally, some studies suggest that TEX_{86} temperatures have a summertime bias (Leider et al., 2010; Ho et al., 2014), which could explain the remaining offset between the TEX_{86}^{L} and clumped isotope temperatures. In comparison to the modern range of temperatures at Gulf and Atlantic coasts sites (~10-29°C), we suggest that the TEX_{86}^{L}-calibrated temperatures from Linnert et al. (2014) and clumped isotope temperatures we present may represent summertime and mean annual temperatures respectively, whereas TEX_{86}^{H} temperatures appear unreasonably high.

Although the TEX_{86}^{H} calibration is typically preferred for past greenhouse climates, closer agreement between TEX_{86}^{L} temperatures and independent, non-organic temperature proxies has been noted in a number of other cases. Clumped isotope temperatures had much better agreement with TEX_{86}^{L} temperatures relative to TEX_{86}^{H} temperatures in a study of Eocene bivalves from Seymour Island, Antarctica (Douglas et al., 2014). Temperature estimates from conventional $\delta^{18}O$ and Mg/Ca in a study of Paleogene foraminfera and also found best agreement with TEX_{86}^{L} temperatures (Hollis et al. 2012). In a third study, TEX_{86}, MBT/CBT, Mg/Ca, $\delta^{18}O$, and Δ_{47} data were compared, but an older, TEX_{86} calibration was used (based upon simple linear regression of a subset of modern core-top data), and the authors found generally good agreement between the two proxies (Keating-Bitonti et al., 2011), indicating that the choice of calibration continues to make a large difference to inter-proxy agreement. This repeated agreement between other proxies and TEX_{86}^{L} over TEX_{86}^{H} has led others to argue in favor of the use of TEX_{86}^{L} for many paleoclimate applications (Ho et al., 2014; Taylor et al., 2013; Inglis et al., 2015). These studies cumulatively support our conclusion that the TEX_{86}^{L} calibration may be a better choice than TEX_{86}^{H} for paleoclimate studies in past greenhouse intervals, although there is still a small offset between TEX_{86}^{L} temperatures and our clumped isotope data which may reflect a summertime bias in the TEX_{86} proxy (also independently asserted by other authors; e.g. Ho et al., 2014). It has also been observed by some authors that the ammonia oxidation rate for thaumarcheota (commonly a function of nutrient and O_2 availability) may also drive discrepantly warm TEX_{86} temperatures in modern oceans (Qin et al., 2015; Hurley et al., 2016). Therefore, ocean anoxia, nutrient limitation, and/or archea population compositions of the Late Cretaceous could also influence TEX_{86} values to produce artificially elevated temperatures.

In comparison, reconstructed temperatures from traditional foraminiferal $\delta^{18}O$ values (combined planktic and benthic) and spanning the entire Maastrichtian vary from 5 to 18 °C at Blake Nose (offshore Florida at 35 °N paleolatitude; MacLeod et al., 2005) and approximately 8 to 18 °C through the North Atlantic (Friedrich et al., 2012). These studies may be skewed towards colder temperatures due to the greater proportion of benthic versus planktic foraminifera, and are subject to assumed $\delta^{18}O_{sw}$ values for the Maastrichtian (as discussed in previous sections), but still overlap directly with our observed variability in Δ_{47} temperatures (7 – 25 °C) across the Gulf and Atlantic Coasts.

Other clumped isotope studies on marine mollusk specimens from the Western Interior Seaway have also shown temperature ranges from ~5 to 24 °C across latitudes from 35 to 55 °N (Dennis et al., 2013; Petersen et al., 2016b). Dennis et al. (2013) found substantially warmer temperatures at latitudes comparable to those of the New Jersey Navesink Fm. sites from this study, but this may be a product of potential vital effects in ammonoid taxa (Petersen et al., 2016b), or due to different temperature stratification in the significantly shallower epicontinental Western Interior Seaway. The cooler temperatures we have observed from the Navesink Fm. may also be attributable to some degree of sample aliasing due to the limited number of specimens retrieved from these localities (*n* = 4), where warmer temperatures may exist, but remain simply undocumented.

6. Conclusions

We present new spatial and temporal temperature reconstructions for the Gulf Coast over the Late Cretaceous using the clumped isotope paleothermometer. We find Gulf Coast and Atlantic Coast temperatures similar to modern temperatures in the same regions and, on average, cooler than Eocene temps at a similar locality (Keating-Bitonti et al., 2011). There is also broad agreement between different taxa and across all sites considered, however, the samples from the Navesink Fm. are substantially colder than from the other localities, which are likely due to some combination of: (1) differences in latitude, (2) different depth habitats and/or (3) ocean circulation patterns (perhaps evidence for the presence of the Gulf Stream during the Late Cretaceous). Δ_{47}-derived temperatures were cooler than previous reconstructions made using the

TEX_{86} paleothermometer (Linnert et al., 2014; Vellekoop et al., 2014, 2016). This suggests that the choice of calibration for the TEX_{86} proxy is critical, and that even when using the TEX_{86}^{L} calibration, a summertime seasonal bias in TEX_{86} temperatures may also be influencing reconstructed temperatures. Lastly, the similarity between Late Cretaceous and modern coastal marine temperatures across the Gulf and Atlantic Coasts suggests that atmospheric CO_2 concentrations at roughly 1 to 2.5 times PAL did not cause significantly increased nearshore surface temperatures in the northern mid-latitudes, and may also imply that relatively small perturbations to the climate system may have a profound effect in terms of driving deglaciation.

Acknowledgements. We thank L. Wingate, J. Gleason, S. Scholz, and J. Blum for analytical assistance, D. Miller (UM Museum of Paleontology) and K. McKinney (USGS) for paleontological assistance, and B. Dzombak for assistance in the field. This work was funded by NSF-OCE-PRF #1420902, NSF-EAR #1123733, and the University of Michigan Scott Turner Award. We also thank the editorial contributions and suggestions of two anonymous reviewers and Associate Editor P. Harries.

References

Allmon, W.D., and Knight, J.L., (1993). Paleoecological significance of a turritelline gastropod-dominated assemblage in the Cretaceous of South Carolina. Journal of Paleontology 67, 355–360. doi:10.1017/S0022336000036830

Arthur M. A., Williams D. F. and Jones D. S. (1983) Seasonal temperature-salinity changes and thermocline development in the mid-Atlantic Bight as recorded by the isotopic composition of bivalves. *Geology* **11**, 655.

Berner, R.A., and Kothavala, Z., (2001). Geocarb III: A Revised Model of Atmospheric CO2 over Phanerozoic Time. American Journal of Science 301, 182–204. doi:10.2475/ajs.301.2.182

Came, R.E., Brand, U., and Affek, H.P., (2014). Clumped isotope signatures in modern brachiopod carbonate: *Chemical Geology*, v. 377, p. 20–30, doi: 10.1016/j.chemgeo.2014.04.004.

Chung, W.-S., Marshall, N.J., (2017). Complex Visual Adaptations in Squid for Specific Tasks in Different Environments. Front. Physiol. 8, 239. doi:10.3389/fphys.2017.00105

Daëron, M., Blamart, D., Peral, M., & Affek, H. P. (2016). Absolute isotopic abundance ratios and the accuracy of Δ47 measurements. *Chemical Geology*, *442*(C), 83–96. http://doi.org/10.1016/j.chemgeo.2016.08.014

Defliese, W.F., Hren, M.T., and Lohmann, K.C., (2015). Compositional and temperature effects of phosphoric acid fractionation on Δ47 analysis and implications for discrepant calibrations: *Chemical Geology*, v. 396, no. C, p. 51–60, doi: 10.1016/j.chemgeo.2014.12.018.

Dennis, K.J., Affek, H.P., Passey, B.H., Schrag, D.P., and Eiler, J.M., (2011). Defining an absolute reference frame for “clumped” isotope studies of CO2: *Geochimica et Cosmochimica Acta*, v. 75, no. 22, p. 7117–7131, doi: 10.1016/j.gca.2011.09.025.

Dlugokencky, E. and Tans, P., (2017). ESRL Global Greenhouse Gas Reference Network Trends in Atmospheric Carbon Dioxide, NOAA/ESRL, www.esrl.noaa.gov/gmd/ccgg/trends/ (December 2017).

Douglas, P.M.J., Affek, H.P., Ivany, L.C., Houben, A.J.P., Sijp, W.P., Sluijs, A., Schouten, S., and Pagani, M., (2014). Pronounced zonal heterogeneity in Eocene southern high-latitude sea surface temperatures: *Proceedings of the National Academy of Sciences*, v. 111, no. 18, p. 6582–6587, doi: 10.1073/pnas.1321441111.

Dunstan, A.J., Ward, P.D., Marshall, N.J. (2011). Vertical distribution and migration patterns of Nautilus pompilius. *PLOS ONE*, v. 6, no. 2, e16311

Dutton, A., Huber, B. T., Lohmann, K. C., & Zinsmeister, W. J. (2007). High-resolution stable isotope profiles of a dimitobelid belemnite: Implications for paleodepth habitat and late Maastrichtian climate seasonality. *Palaios*, *22*(6), 642–650. http://doi.org/10.2110/palo.2005.p05-064r

Eagle, R.A., Eiler, J.M., Tripati, A.K., Ries, J.B., Freitas, P.S., Hiebenthal, C., Wanamaker, A.D., Jr., Taviani, M., Elliot, M., Marenssi, S., Nakamura, K., Ramirez, P., and Roy, K., (2013). The influence of temperature and seawater carbonate saturation state on ^{13}C –^{18}O bond ordering in bivalve mollusks: *Biogeosciences*, v. 10, no. 7, p. 4591–4606, doi: 10.5194/bg-10-4591-2013.

Ebersole, S.M., (2009). Biostratigraphy, Paleogeography, and Paleoenvironments of the Upper Cretaceous (Campanian) Northern Mississippi Embayment: *[Ph.D. Dissertation], The University of Alabama*, p. 1–189.

Eiler, J.M., and Schauble, E., (2004). 18O13C16O in Earth's atmosphere: *Geochimica et Cosmochimica Acta*, v. 68, no. 23, p. 4767–4777, doi: 10.1016/j.gca.2004.05.035.

Eiler, J.M., (2011). Paleoclimate reconstruction using carbonate clumped isotope thermometry: *Quaternary Science Reviews*, v. 30, no. 25-26, p. 3575–3588, doi: 10.1016/j.quascirev.2011.09.001.

Friedrich, O., Norris, R. D., & Erbacher, J. (2012). Evolution of middle to Late Cretaceous oceans--A 55 m.y. record of Earth's temperature and carbon cycle. *Geology*, *40*(2), 107–110. http://doi.org/10.1130/G32701.1

Greenwood, D. R., & Wing, S. L. (1995). Eocene continental climates and latitudinal temperature gradients. *Geology*, *23*(11), 1044. http://doi.org/10.1130/0091-7613(1995)023<1044:eccalt>2.3.co;2

Hart, M.B., Harries, P.J., and Cárdenas, A.L., (2013). The Cretaceous/Paleogene Boundary Events in the Gulf Coast: Comparisons between Alabama and Texas: *The Gulf Coast Association of Geological Societies*, p. 1–21.

Henkes, G.A., Passey, B.H., Wanamaker, A.D., Jr, Grossman, E.L., Ambrose, W.G., Jr, and Carroll, M.L., (2013). Carbonate clumped isotope compositions of modern marine mollusk and brachiopod shells: *Geochimica et Cosmochimica Acta*, v. 106, no. C, p. 307–325, doi: 10.1016/j.gca.2012.12.020.

Henkes, G.A., Passey, B.H., Grossman, E.L., Shenton, B.J., Perez-Huerta, A., Yancey, T.E., (2014). Temperature limits for preservation of primary calcite clumped isotope paleotemperatures. Geochimica et Cosmochimica Acta 139, 362–382. doi:10.1016/j.gca.2014.04.040

Hernández-Sánchez, M. T., Woodward, E. M. S., Taylor, K. W. R., Henderson, G. M., & Pancost, R. D. (2014). Variations in GDGT distributions through the water column in the South East Atlantic Ocean. *Geochimica Et Cosmochimica Acta*, *132*, 337–348. http://doi.org/10.1016/j.gca.2014.02.009

Ho, S.L., Mollenhauer, G., Fietz, S., Martínez-Garcia, A., Lamy, F., Rueda, G., Schipper, K., Méheust, M., Rosell-Melé, A., Stein, R., and Tiedemann, R., (2014). Appraisal of TEX86 and thermometries in subpolar and polar regions: *Geochimica et Cosmochimica Acta*, v. 131, no. C, p. 213–226, doi: 10.1016/j.gca.2014.01.001.

Holme N. A. (1961) Shell form in Venerupis rhomboides. *J. Mar. Biol. Ass.* **41**, 705–722.

Hollis, C. J., Taylor, K. W. R., Handley, L., Pancost, R. D., Huber, M., Creech, J. B., et al. (2012). Early Paleogene temperature history of the Southwest Pacific Ocean Reconciling proxies and models. *Earth and Planetary Science Letters*, *349-350*(C), 53–66. http://doi.org/10.1016/j.epsl.2012.06.024

Huntington, K.W., Eiler, J.M., Affek, H.P., Guo, W., Bonifacie, M., Yeung, L.Y., Thiagarajan, N., Passey, B., Tripati, A., Daëron, M., and Came, R., (2009). Methods and limitations of "clumped" CO_2 isotope (Δ_{47}) analysis by gas-source isotope ratio mass spectrometry: *Journal of Mass Spectrometry*, v. 44, no. 9, p. 1318–1329, doi: 10.1002/jms.1614.

Hurley, S.J., Elling, F.J., Könneke, M., Buchwald, C., Wankel, S.D., Santoro, A.E., Lipp, J.S., Hinrichs, K.-U., Pearson, A., (2016). Influence of ammonia oxidation rate on thaumarchaeal lipid composition and the TEX 86temperature proxy. Proceedings of the National Academy of Sciences 113, 7762–7767. doi:10.1073/pnas.1518534113

Inglis, G. N., Farnsworth, A., Lunt, D., Foster, G. L., Hollis, C. J., Pagani, M., et al. (2015). Descent toward the Icehouse: Eocene sea surface cooling inferred from GDGT distributions. *Paleoceanography*. http://doi.org/10.1002/(ISSN)1944-9186

Jereb, P., and Roper, C.F.E., (2010). Cephalopods of the World: An Annotated and Illustrated Catalogue of Cephalopod Species Known to Date Volume 2. Myopsid and Oegopsid Squids. Food & Agriculture Org.

Jereb, P., and Roper, C.F.E., (2005). Cephalopods of the World: An Annotated and Illustrated Catalogue of Cephalopod Species Known to Date Volume 1. Chambered nautiluses and sepioids (Nautilidae, Sepiidae, Sepiolidae, Sepiadariidae, Idiosepiidae, and Spirulidae). Food & Agriculture Org.

Jereb, P., Roper, C.F.E., and Finn, J.K., (2016). Cephalopods of the world. An Annotated and Illustrated Catalogue of Cephalopod Species Known to Date Volume 3. Octopods and Vampire Squids. Food & Agriculture Org.

Johnson, A.L.A., Valentine, A., Leng, M.J., Sloane, H.J., Schöne, B.R., Balson, P.S., (2017). Isotopic temperatures from the Early and Mid-Pliocene of the US Middle Atlantic Coastal Plain, and their implications for the cause of regional marine climate change. PALAIOS 32, 250–269. doi:10.2110/palo.2016.080

Jones D. L., Silberling N. J. and Hillhouse J. (1977) Wrangellia—A displaced terrane in northwestern North America. *Canadian Journal of Earth Sciences* **14**, 2565–2577.

Jones D. S. (1980) Annual cycle of shell growth increment formation in two continental shelf bivalves and its paleoecologic significance. *Paleobiology* **6**, 331–340.

Jones, D.S., Mueller, P.A., Bryan, J.R., Dobson, J.P., Channell, J.E.T., Zachos, J.C., Arthur, M.A., (1987). Biotic, geochemical, and paleomagnetic changes across the Cretaceous/Tertiary boundary at Braggs, Alabama. Geology 15, 311. doi:10.1130/0091-7613(1987)15<311:bgapca>2.0.co;2

Jones, D.S., and Allmon, W.D., (1995). Records of upwelling, seasonality and growth in stable-isotope profiles of Pliocene mollusk shells from Florida. Lethaia 28, 61–74. doi:10.1111/j.1502-3931.1995.tb01593.x

Keating-Bitonti, C.R., Ivany, L.C., Affek, H.P., Douglas, P., and Samson, S.D., (2011). Warm, not super-hot, temperatures in the early Eocene subtropics: *Geology*, v. 39, no. 8, p. 771–774, doi: 10.1130/G32054.1.

Kelson, J. R., Huntington, K. W., Schauer, A. J., Saenger, C., & Lechler, A. R. (2017). Toward a universal carbonate clumped isotope calibration: Diverse synthesis and preparatory methods suggest a single temperature relationship. *Geochimica Et Cosmochimica Acta*, *197*, 104–131. http://doi.org/10.1016/j.gca.2016.10.010

Kim, J.-H., Schouten, S., Hopmans, E. C., Donner, B., & Sinninghe Damsté, J. S. (2008). Global sediment core-top calibration of the TEX86 paleothermometer in the ocean. *Geochimica Et Cosmochimica Acta*, *72*(4), 1154–1173. http://doi.org/10.1016/j.gca.2007.12.010

Kim, J.-H., van der Meer, J., Schouten, S., Helmke, P., Willmott, V., Sangiorgi, F., Koç, N., Hopmans, E.C., and Damsté, J.S.S., (2010). New indices and calibrations derived from the distribution of crenarchaeal isoprenoid tetraether lipids: Implications for past sea surface temperature reconstructions: *Geochimica et Cosmochimica Acta*, v. 74, no. 16, p. 4639–4654, doi: 10.1016/j.gca.2010.05.027.

Kim, S.T., and O'Neil, J.R., (1997). Equilibrium and nonequilibrium oxygen isotope effects in synthetic carbonates: *Geochimica et Cosmochimica Acta*, v. 61, no. 16, p. 3461–3475.

Kim, S.-T., O'Neil, J. R., Hillaire-Marcel, C., & Mucci, A. (2007). Oxygen isotope fractionation between synthetic aragonite and water: Influence of temperature and Mg2+ concentration. *Geochimica Et Cosmochimica Acta*, *71*(19), 4704–4715. http://doi.org/10.1016/j.gca.2007.04.019

Larina, E., Garb, M., Landman, N., Dastas, N., Thibault, N., Edwards, L., Phillips, G., Rovelli, R., Myers, C., and Naujokaityte, J., (2016). Upper Maastrichtian ammonite biostratigraphy of the Gulf Coastal Plain (Mississippi Embayment, southern USA): *Cretaceous Research*, v. 60, no. c, p. 128–151, doi: 10.1016/j.cretres.2015.11.010.

LeGrande, A.N., Schmidt, G.A., 2006. Global gridded data set of the oxygen isotopic composition in seawater. Geophysical Research Letters 33, 15833–5. doi:10.1029/2006GL026011

Leider, A., Hinrichs, K.-U., Mollenhauer, G., and Versteegh, G.J.M., (2010). Core-top calibration of the lipid-based U37K′ and TEX86 temperature proxies on the southern Italian shelf (SW Adriatic Sea, Gulf of Taranto): *Earth and Planetary Science Letters*, v. 300, no. 1-2, p. 112–124, doi: 10.1016/j.epsl.2010.09.042.

Lerman, A., (1965). Evolution of Exogyra in the Late Cretaceous of the Southeastern United States: *Journal of Paleontology* 39, 414–435. doi:10.2307/1301715?ref=search-gateway:b4fe84722b190b697b1897c406a59b72

Linnert, C., Robinson, S.A., Lees, J.A., and Bown, P.R., (2014). Evidence for global cooling in the Late Cretaceous: *Nature Communications*, v. 5, no. 4194, doi: 10.1038/ncomms5194.

Lockwood, R., (2003). Abundance not linked to survival across the end-Cretaceous mass extinction: Patterns in North American bivalves: *Proceedings of the National Academy of Sciences*, v. 100, no. 5, p. 2478–2482, doi: 10.1073/pnas.0535132100.

MacLeod, K. G., Huber, B. T., & Isaza-Londoño, C. (2005). North Atlantic warming during global cooling at the end of the Cretaceous. *Geology*, *33*(6), 437–4. http://doi.org/10.1130/G21466.1

McArthur, J.M., Howarth, R.J., and Bailey, T.R. (2001). Strontium isotope stratigraphy: LOWESS version 3: Best fit to the marine Sr-isotope curve for 0-509 Ma and accompanying look-up table for deriving numerical age: *Journal of Geology*, v. 109, no. 2, p. 155–170.

Mettam, C., Johnson, A.L.A., Nunn, E.V., Schöne, B.R., (2014). Stable isotope (δ18O and δ13C) sclerochronology of Callovian (Middle Jurassic) bivalves (Gryphaea (Bilobissa) dilobotes) and belemnites (Cylindroteuthis puzosiana) from the Peterborough Member of the Oxford Clay Formation

(Cambridgeshire, England): Evidence of palaeoclimate, water depth and belemnite behaviour. Palaeogeography, Palaeoclimatology, Palaeoecology 399, 187–201. doi:10.1016/j.palaeo.2014.01.010

Monroe, W.H. and Hunt, J.L. (1958). Geology of the Epes Quadrangle, Alabama: *United States Geological Survey*, Geologic map of the Epes Quadrangle, Alabama.

Morley S. A., Clark M. S. and Peck L. S. (2010) Depth gradients in shell morphology correlate with thermal limits for activity and ice disturbance in Antarctic limpets. *Journal of Experimental Marine Biology and Ecology* **390**, 1–5.

Moshkovitz, S., and Habib, D., (1993). Calcareous nannofossil and dinoflagellate stratigraphy of the Cretaceous-Tertiary boundary, Alabama and Georgia: *Micropaleontology*, v. 39, no. 2, p. 167, doi: 10.2307/1485838.

Mutterlose, J., Malkoč, M., Schouten, S., Sinninghe Damsté, J.S., Forster, A., (2010). TEX86 and stable δ18O paleothermometry of early Cretaceous sediments: Implications for belemnite ecology and paleotemperature proxy application. Earth and Planetary Science Letters 298, 286–298. doi:10.1016/j.epsl.2010.07.043

NOAA NBI, (2017). National Benthic Inventory, https://nbi.noaa.gov/ (April 2017).

NOAA NEFSC, (2017). Ecology of the Northeast US Continental Shelf: Oceanography, https://www.nefsc.noaa.gov/ecosys/ecosystem-ecology/oceanography.html (October 2017).

NOAA NODC, (2017). National Oceanographic Data Center Coastal Water Temperature Guide, https://www.nodc.noaa.gov/dsdt/cwtg/index.html (April 2017).

Olsson, R.K., (1987). Cretaceous stratigraphy of the Atlantic Coastal Plain, Atlantic Highlands of New Jersey, Centennial Field Guide Volume 5: Northeastern Section of the Geological Society of America. Geological Society of America. doi:10.1130/0-8137-5405-4.87

Olsson, R. K., Miller, K. G., Browning, J. V., Wright, J. D., & Cramer, B. S. (2002). Sequence stratigraphy and sea-level change across the Cretaceous-Tertiary boundary on the New Jersey passive margin. *Geological Society of America Special Paper*, *356*, 97–108.

Petersen, S. V., Dutton, A., and Lohmann, K. C., (2016a). End-Cretaceous extinction in Antarctica linked to both Deccan volcanism and meteorite impact via climate change: *Nature Communications*, 7:12079, doi: 10.1038/ncomms12079.

Petersen, S.V., Tabor, C.R., Lohmann, K.C., Poulsen, C.J., Meyer, K.W., Carpenter, S.J., Erickson, J.M., Matsunaga, K.K.S., Smith, S.Y., Sheldon, N.D., (2016b). Temperature and salinity of the Late Cretaceous Western Interior Seaway: *Geology* G38311.1–4. doi:10.1130/G38311.1

Petersen, S.V., Winkelstern, I.Z., Lohmann, K.C., and Meyer, K.W., (2016c). The effects of Porapak™ trap temperature on $\delta^{18}O$, $\delta^{13}C$, and Δ_{47} values in preparing samples for clumped isotope analysis: *Rapid Communications in Mass Spectrometry*, v. 30, no. 1, p. 199–208, doi: 10.1002/rcm.7438.

Puckett, T. M. (1991). Absolute paleobathymetry of Upper Cretaceous chalks based on ostracodes-Evidence from the Demopolis Chalk (Campanian and Maastrichtian) of the northern Gulf Coastal Plain. *Geology*, *19*(5), 449–452. http://doi.org/10.1130/0091-7613(1991)019<0449:APOUCC>2.3.CO;2

Qin, W., Carlson, L.T., Armbrust, E.V., Devol, A.H., Moffett, J.W., Stahl, D.A., Ingalls, A.E., (2015). Confounding effects of oxygen and temperature on the TEX 86signature of marine Thaumarchaeota. Proceedings of the National Academy of Sciences 112, 10979–10984. doi:10.1073/pnas.1501568112

Richaud B., Kwon Y.-O., Joyce T. M., Fratantoni P. S. and Lentz S. J. (2016) Surface and bottom temperature and salinity climatology along the continental shelf off the Canadian and U.S. East Coasts. *Continental Shelf Research* **124**, 165–181.

Ritter, A.-C., Kluge, T., Berndt, J., Richter, D.K., John, C.M., Bodin, S., Immenhauser, A., (2015). Application of redox sensitive proxies and carbonate clumped isotopes to Mesozoic and Palaeozoic radiaxial fibrous calcite cements. Chemical Geology 417, 306–321. doi:10.1016/j.chemgeo.2015.10.008

Ritter, A.-C., Mavromatis, V., Dietzel, M., Kwiecien, O., Wiethoff, F., Griesshaber, E., Casella, L.A., Schmahl, W.W., Koelen, J., Neuser, R.D., Leis, A., Buhl, D., Niedermayr, A., Breitenbach, S.F.M., Bernasconi, S.M., Immenhauser, A., (2017). Exploring the impact of diagenesis on (isotope) geochemical and microstructural alteration features in biogenic aragonite. Sedimentology 64, 1354–1380. doi:10.1111/sed.12356

Rodrigo-Gámiz, M., Rampen, S.W., de Haas, H., Baas, M., Schouten, S., and Sinninghe Damste, J.S., (2015). Constraints on the applicability of the organic temperature proxies U^{K'}₃₇, TEX₈₆ and LDI in the subpolar region around Iceland: *Biogeosciences*, v. 12, no. 22, p. 6573–6590, doi: 10.5194/bg-12-6573-2015.

Royer, D.L., Pagani, M., and Beerling, D.J., (2012). Geobiological constraints on Earth system sensitivity to CO2 during the Cretaceous and Cenozoic: *Geobiology*, no. 10, p. 298–310, doi: 10.1111/j.1472-4669.2012.00320.x.

Ruffin, E., (1843). Report on the Commencement and Progress of the Agricultural Survey of South Carolina, p. 1–194.

Sarmiento, J.L., Gruber, N., (2006). Ocean Biogeochemical Dynamics. Princeton University Press, Princeton, New Jersey, p. 19–68.

Schauer, A. J., Kelson, J., Saenger, C., & Huntington, K. W. (2016). Choice of 17O correction affects clumped isotope (Δ 47) values of CO 2measured with mass spectrometry. *Rapid Communications In Mass Spectrometry*, *30*(24), 2607–2616. http://doi.org/10.1002/rcm.7743

Schouten, S., Hopmans, E. C., & Schefuß, E. (2002). Distributional variations in marine crenarchaeotal membrane lipids: a new tool for reconstructing ancient sea water temperatures? *Earth and Planetary Science Letters*, *204*(1-2), 265–274. http://doi.org/10.1016/S0012-821X(02)00979-2

Schouten, S., Huguet, C., Hopmans, E. C., Kienhuis, M. V. M., & Sinninghe Damsté, J. S. (2007). Analytical Methodology for TEX 86Paleothermometry by High-Performance Liquid Chromatography/Atmospheric Pressure Chemical Ionization-Mass Spectrometry. *Analytical Chemistry*, *79*(7), 2940–2944. http://doi.org/10.1021/ac062339v

Schouten, S., Hopmans, E.C., and Damsté, J.S.S., (2013). The organic geochemistry of glycerol dialkyl glycerol tetraether lipids: A review: *Organic Geochemistry*, v. 54, no. C, p. 19–61, doi: 10.1016/j.orggeochem.2012.09.006.

Schulte, P., & Speijer, R. P. (2009). Late Maastrichtian-Early Paleocene sea level and climate changes in the Antioch Church Core (Alabama, Gulf of Mexico margin, USA): a multi-proxy approach. *Geologica Acta*, *7*(1-2), 11–34. http://doi.org/10.1344/105.000000279

Seed R. (1968) Factors Influencing Shell Shape in the Mussel Mytilus Edulis. *J. Mar. Biol. Ass.* **48**, 561.

Shenton, B.J., Grossman, E.L., Passey, B.H., Henkes, G.A., Becker, T.P., Laya, J.C., Perez-Huerta, A., Becker, S.P., Lawson, M., (2015). Clumped isotope thermometry in deeply buried sedimentary carbonates: The effects of bond reordering and recrystallization. Geo. Society Am. Bull. B31169.1–16. doi:10.1130/B31169.1

Shimada, H., Nemoto, N., Shida, Y., Oshima, T., & Yamagishi, A. (2002). Complete Polar Lipid Composition of Thermoplasma acidophilum HO-62 Determined by High-Performance Liquid Chromatography with Evaporative Light-Scattering Detection. *Journal of Bacteriology*, *184*(2), 556–563. http://doi.org/10.1128/JB.184.2.556-563.2002

Siple, G.E., (1957). Guidebook for the South Carolina Coastal Plain Field Trip of the Carolina Geological Society: *Carolina Geological Society,* Nov. 16-17, 1957.

Smit, J., Roep, T.B., Alvarez, W., Montanari, A., Claeys, P., Grajales-Nishimura, J.M., and Bermudez, J., (1996). Coarse-grained, clastic sandstone complex at the K/T boundary around the Gulf of Mexico: Deposition by tsunami waves induced by the Chicxulub impact?: *Geological Society of America Special Papers*, v. 307, p. 151–182, doi: 10.1130/0-8137-2307-8.151.

Smith, C.C., (1997). The Cretaceous-Tertiary Boundary at Moscow Landing, West-Central Alabama: *Gulf Coast Association of Geological Societies Transactions*, v. 47, p. 533–540.

Sohl, N.F., (1960). Archeogastropoda, Mesogastropoda, and stratigraphy of the Ripley, Owl Creek, and Prairie Bluff Formations: *USGS Professional Paper 331-A*.

Stephenson, L. W. (1914). Cretaceous deposits of the eastern Gulf region and species of Exogyra from the eastern Gulf region and the Carolinas: *USGS Professional Paper 81*.

Stephenson, L.W., (1933). The zone of Exogyra cancellata traced twenty-five hundred miles: *AAPG Bulletin* 17. doi:10.1306/3d932bc8-16b1-11d7-8645000102c1865d

Steuber, T., Rauch, M., Masse, J.-P., Graaf, J., & Malkoč, M. (2005). Low-latitude seasonality of Cretaceous temperatures in warm and cold episodes: *Nature Communications*, *437*(7063), 1341–1344. http://doi.org/10.1038/nature04096

Sugarman, P. J., Miller, K. G., & Bukry, D. (1995). Uppermost Campanian–Maestrichtian strontium isotopic, biostratigraphic, and sequence stratigraphic framework of the New Jersey Coastal Plain. *Geological Society of America Bulletin,* v.107, no. 1, p. 19-37.

Swift, D.J.P., (1966). The Black Creek - Peedee Contact in South Carolina: *Geologic Notes of the Division of Geology State Development Board Columbia*, S.C, v. 10, p. 1–23.

Tao, K., Robbins, J.A., Grossman, E.L., O'Dea, A., (2013). Quantifying upwelling and freshening in nearshore tropical American environments using stable isotopes in modern gastropods. BMS 89, 815–835. doi:10.5343/bms.2012.1065

Taylor, K. W. R., Huber, M., Hollis, C. J., Hernandez-Sanchez, M. T., & Pancost, R. D. (2013). Re-evaluating modern and Palaeogene GDGT distributions: Implications for SST reconstructions. *Global and Planetary Change*, *108*(C), 158–174. http://doi.org/10.1016/j.gloplacha.2013.06.011

Taylor, A.H., and Stephens, J.A., (1998). The North Atlantic Oscillation and the latitude of the Gulf Stream. Tellus A 50, 134–142. doi:10.1034/j.1600-0870.1998.00010.x

Thirlwall, M. F. (1991). Long-term reproducibility of multicollector Sr and Nd isotope ratio analysis: *Chemical Geology (Isotope Geoscience Section)*, v. 94, p. 85-104

Tierney, J. E., & Tingley, M. P. (2014). A Bayesian, spatially-varying calibration model for the TEX86 proxy. *Geochimica Et Cosmochimica Acta*, *127*(C), 83–106. http://doi.org/10.1016/j.gca.2013.11.026

Tierney, J. E., & Tingley, M. P. (2015). A TEX86 surface sediment database and extended Bayesian calibration. *Scientific Data*, *2*, 150029–10. http://doi.org/10.1038/sdata.2015.29

Vellekoop, J., Sluijs, A., Smit, J., Schouten, S., Weijers, J. W. H., Sinninghe Damste, J. S., & Brinkhuis, H. (2014). Rapid short-term cooling following the Chicxulub impact at the Cretaceous-Paleogene boundary. *Proceedings of the National Academy of Sciences*, *111*(21), 7537–7541. http://doi.org/10.1073/pnas.1319253111

Vellekoop, J., Esmeray-Senlet, S., & Miller, K. G. (2016). Supplemental Information for: Evidence for Cretaceous-Paleogene boundary bolide "impact winter" conditions from New Jersey, USA. *Geology*, *44*(8), 619–622. http://doi.org/10.1130/g37961.1

Wade, B., (1926). The Fauna of the Ripley Formation on Coon Creek, Tennessee: *USGS Professional Paper 137* , p. 272.

Wang, Y., Huang, C., Sun, B., Quan, C., Wu, J., and Lin, Z. (2014). Paleo-CO 2 variation trends and the Cretaceous greenhouse climate: *Earth-Science Reviews*, doi: 10.1016/j.earscirev.2013.11.001.

Wuchter, C., Schouten, S., Coolen, M. J. L., & Sinninghe Damsté, J. S. (2004). Temperature-dependent variation in the distribution of tetraether membrane lipids of marine Crenarchaeota: Implications for TEX 86paleothermometry. *Paleoceanography*, *19*(4), n/a–n/a. http://doi.org/10.1029/2004PA001041

Zachos, J.C., Stott, L.D., Lohmann, K.C., (1994). Evolution of Early Cenozoic marine temperatures. Paleoceanography 9, 353–387. doi:10.1029/93PA03266

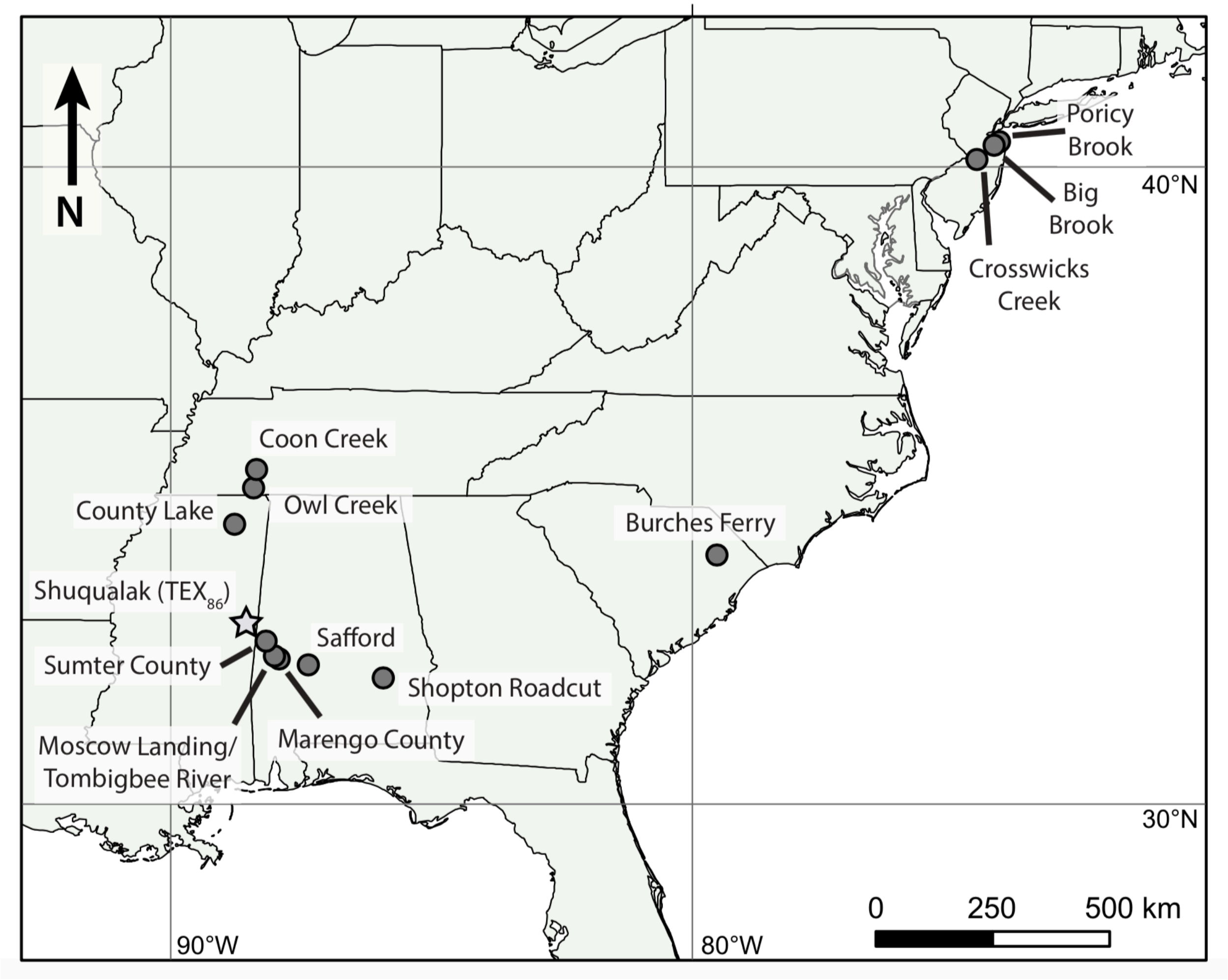

Figure 13. Map of sample localities used in this study. The location of the published TEX_{86} record shown in Figure 20 is depicted with a star (Shuqualak, Mississippi).

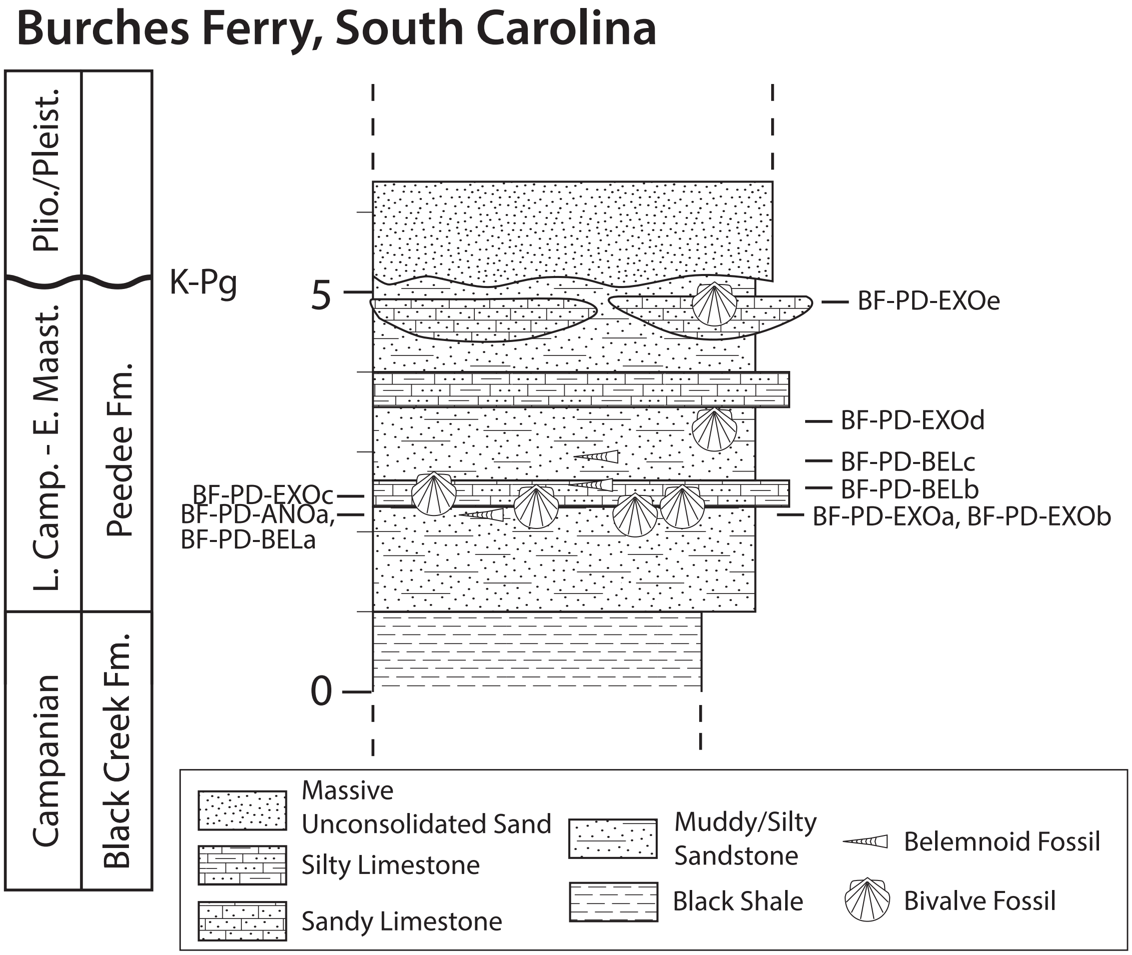

Figure 14. Stratigraphic Section of the Burches Ferry site. Sample names are listed at the stratigraphic position at which they were collected. The K-Pg boundary at this locality is unconformable with an undetermined, yet significant, amount of time missing (Siple, 1957; Swift, 1966).

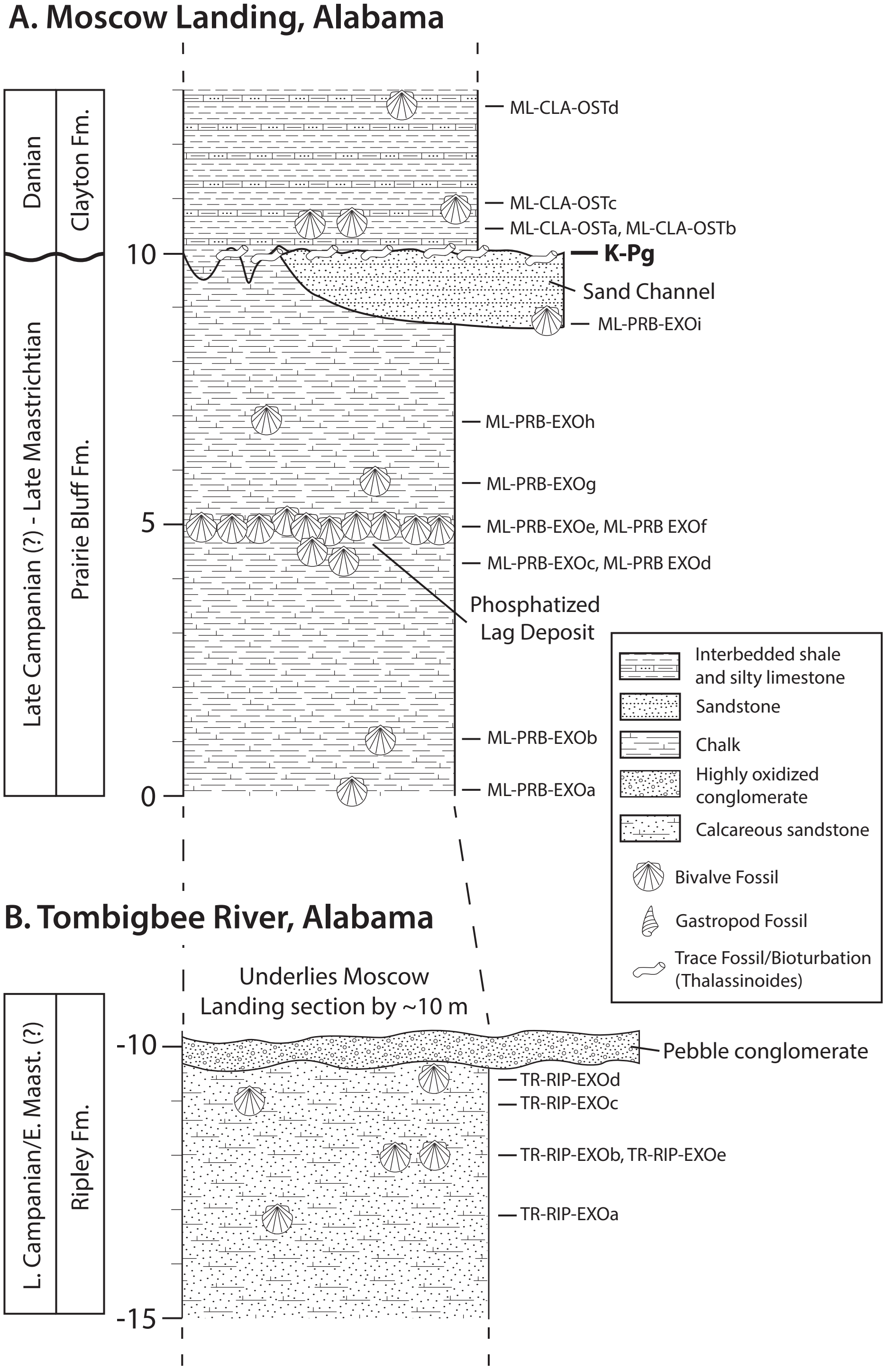

Figure 15. Stratigraphic Section of the Moscow Landing/Tombigbee River site. Sample names are listed at the stratigraphic position at which they were collected. The Tombigbee River site is located ~5 km east of the Moscow Landing site, and the stratigraphic columns are separated by ~10 m of poor exposure. The K-Pg at this locality is unconformable with possibly 100 to 500 ka of time missing (Moshkovitz and Habib, 1993; Larina et al., 2016).

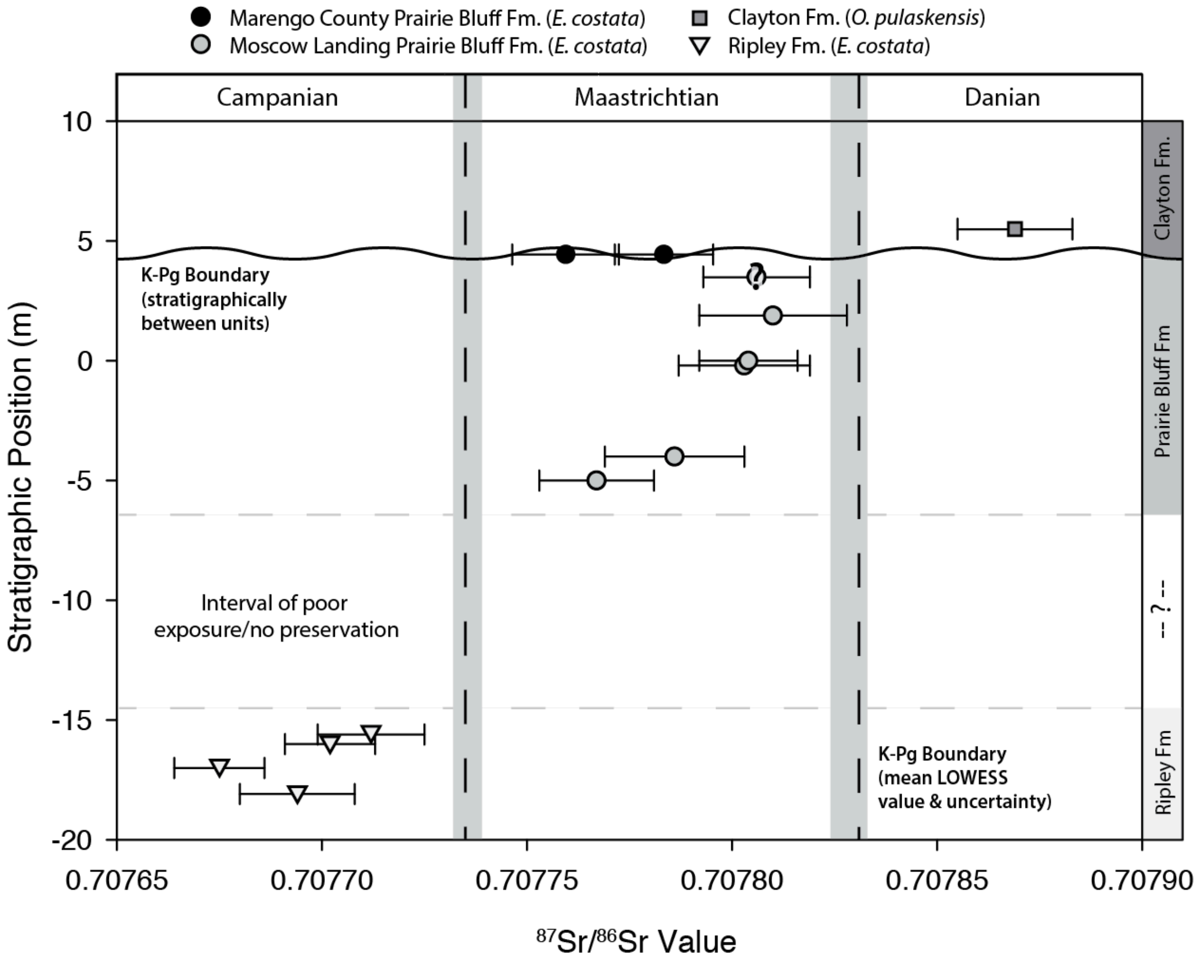

Figure 16. Strontium isotope values of samples from Moscow Landing/Tombigbee River/Marengo County composite section. Measured ^{87}Sr/^{86}Sr values of shells from the Moscow Landing/Tombigbee River/Marengo County localities vs. stratigraphic position, with 2 S.E. uncertainty. The physical location of the unconformable contact between the Prairie Bluff and Clayton formations (horizontal oscillatory line) is offset from the mean ^{87}Sr/^{86}Sr value and associated uncertainties for the K-Pg boundary reported in the LOWESS model (McArthur, 2001; McArthur, pers. comm. 2015), which is likely due to missing time at the unconformable boundary. The K-Pg (Maastrichtian-Danian) and Campanian-Maastrichtian boundaries are represented by vertical dashed lines, with mean value and maximum uncertainties from the LOWESS model (grey). The sample point demarcated with a '?' was retrieved from the base of a reworked channel deposit and does not represent a true stratigraphic position. The samples are clearly separated by formation based on measured ^{87}Sr/^{86}Sr values, but are inseparable within each of these formations.

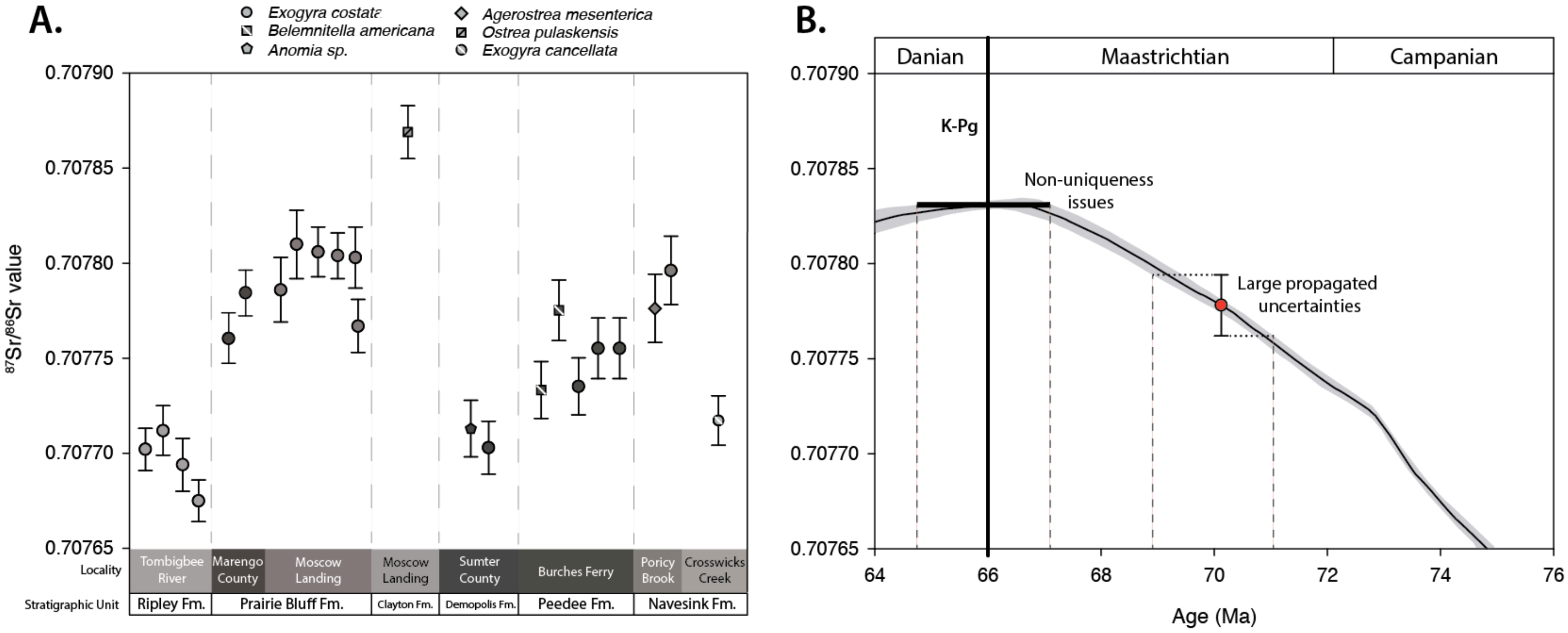

Figure 17. Strontium isotope values by sample locality. All measured $^{87}Sr/^{86}Sr$ values plotted with respect to sample location and formation (A), with symbols denoting taxa, arranged by relative geographic orientation of the sample locality from southwest (left) to northeast (right). $^{87}Sr/^{86}Sr$ values can then be converted to a mean age using the strontium seawater LOWESS model curve (B) (McArthur, 2001; McArthur, pers. comm. 2015). Analytical uncertainties result in large propagated age uncertainties (based on where the analytical error bars intersect the uncertainty envelope of the LOWESS curve) with respect to an assigned mean age. As well, the 'flattening' of the LOWESS curve at the K-Pg boundary further complicates age uncertainties due to non-uniqueness issues, compounded by the uncertainties on the LOWESS curve itself, stressing the utility of $^{87}Sr/^{86}Sr$ chemostratigraphy as a coarse geochronologic tool for determining relative age relations between formations (e.g. Late Maastrichtian samples compared to Early Maastrichtian samples) as opposed to high-resolution age model construction within a formation.

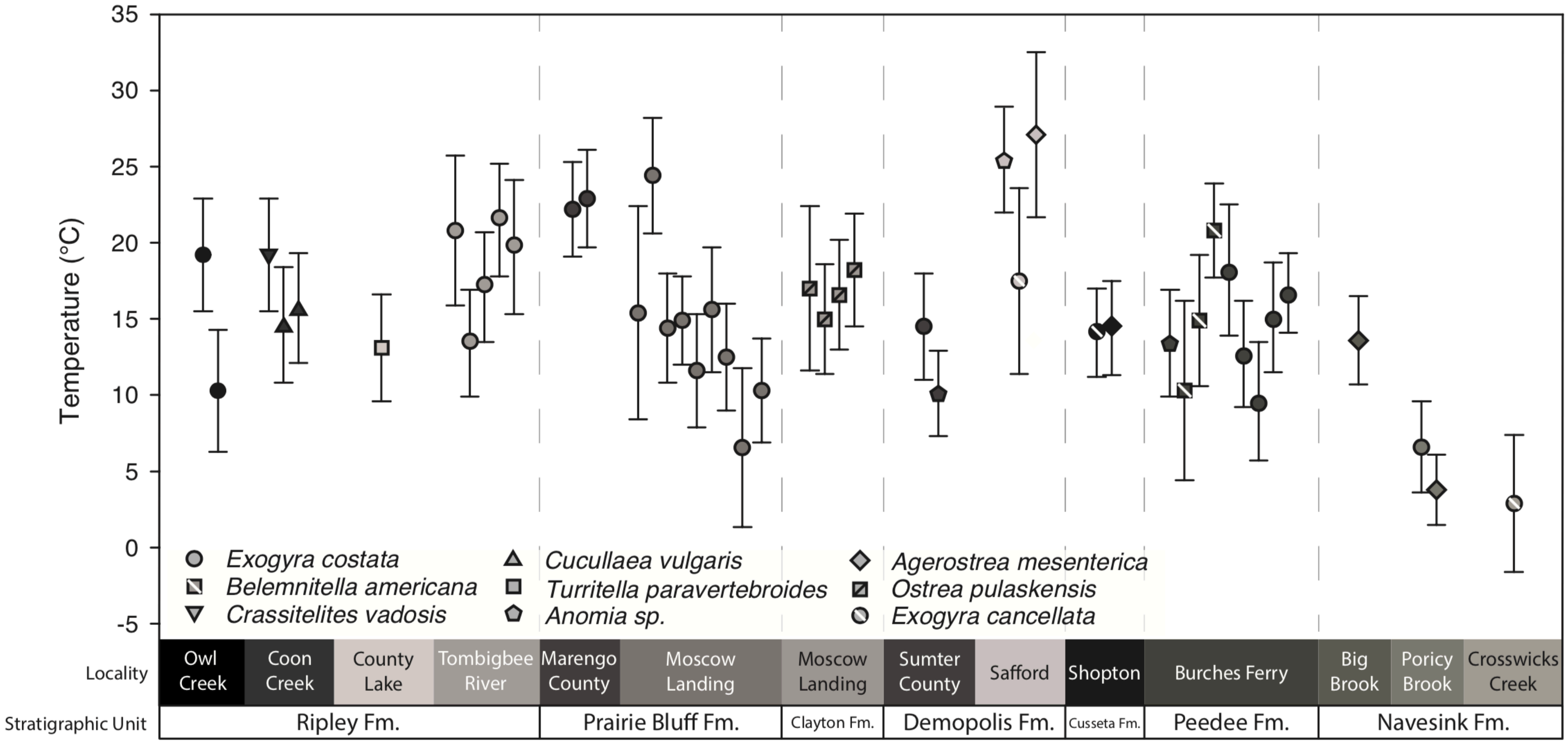

Figure 18. Clumped Isotope Temperature for all localities, separated by taxa. Each point represents 3-6 replicates of a single shell sample. Error bars represent 1 SE. Samples are grouped by their associated stratigraphic formation and locality and taxa are designated by symbol and are arranged by relative geographic orientation of the sample locality from southwest (left) to northeast (right).

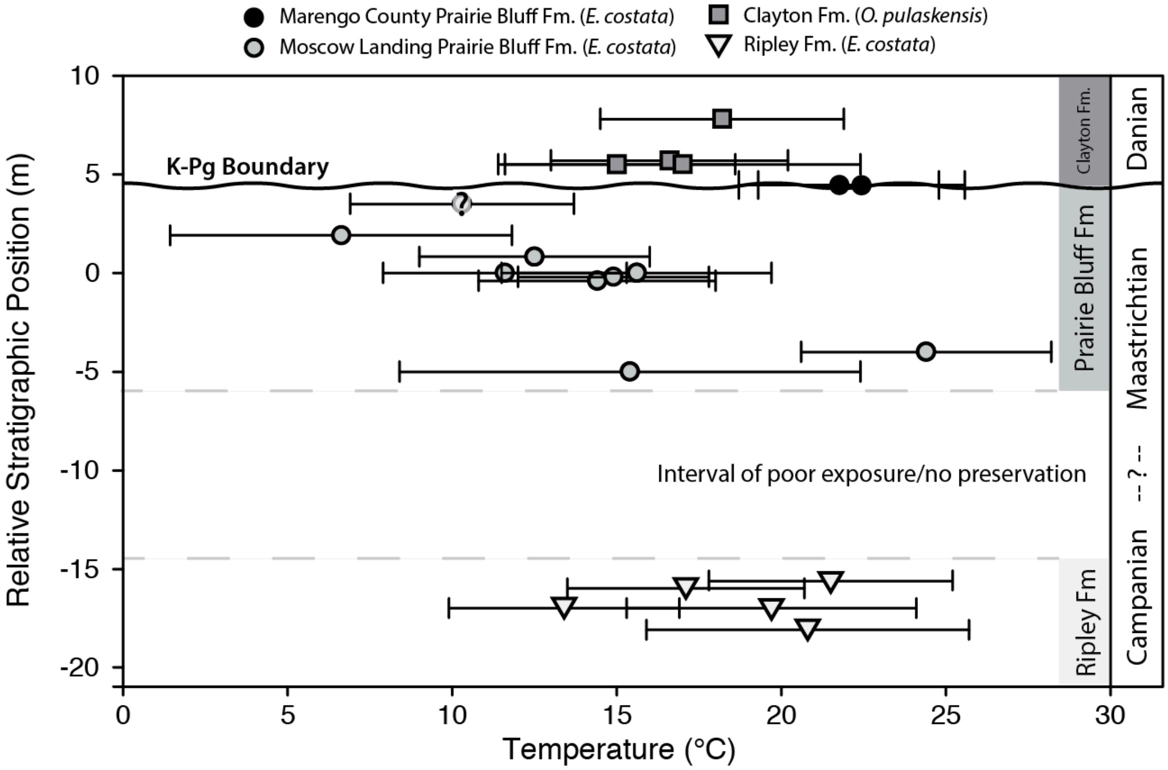

Figure 19. Clumped Isotope Temperatures vs. Stratigraphic Position for the Moscow Landing/Tombigbee River/Marengo County composite section All Cretaceous samples are *E. costata*, and all post-Cretaceous samples are *O. pulakensis*. At this site, the K-Pg boundary is unconformable with as much as 500 ka missing (Larina et al., 2016). Triangles correspond to samples of the Ripley Fm., circles represent the Prairie Bluff Fm., and squares belong to the Clayton Fm. Samples retrieved from the University of Michigan Museum of Paleontology from the Marengo County site of the Prairie Bluff Fm. are depicted by black circles, and are stratigraphically higher than the Moscow Landing samples (refer to Section 4.1 of text). The sample point demarcated with a '?' was retrieved from the base of a reworked channel deposit and is uncertain in terms of a true stratigraphic position.

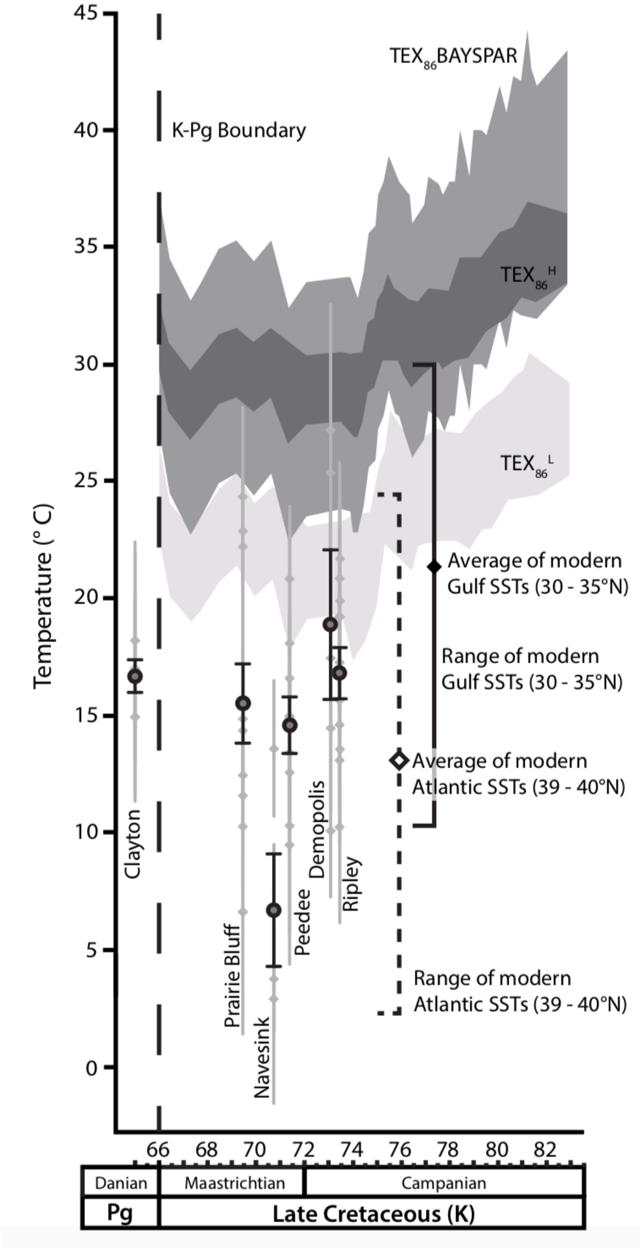

Figure 20. Regional Temperature Record over the Campanian and Maastrichtian compared to published TEX_{86} records. Formation-average clumped isotope temperature (dark circles, 1σ uncertainty) and individual sample temperatures (light grey diamonds, 1 SE error bars) vs. Formation-average age from $^{87}Sr/^{86}Sr$ (±0.45 to ±1.50 Ma uncertainty for any single measured strontium value; section 3.3). The Clayton Fm. is depicted at 65 Ma due to large uncertainty of the LOWESS curve near the K-Pg boundary and the single anomalous Sr/Sr measurement. The paleolatitudes for all sites span ~33 – 36.5 °N with the exception of the Navesink Fm. (~37 – 38 °N), comparative temperature ranges for modern monitoring sites are depicted as well (see text, section 5.1). TEX_{86} paleotemperatures from the Shuqualak locality are shown for three different calibrations (TEX_{86}^{H}, TEX_{86}^{L}, and BAYSPAR) (Linnert et al., 2014). BAYSPAR results are shown with a median uncertainty values of 5 °C reported in Tierney and Tingley (2015), acknowledging that uncertainty propagations from the regression model spatially vary from 1.2 to 10 °C.

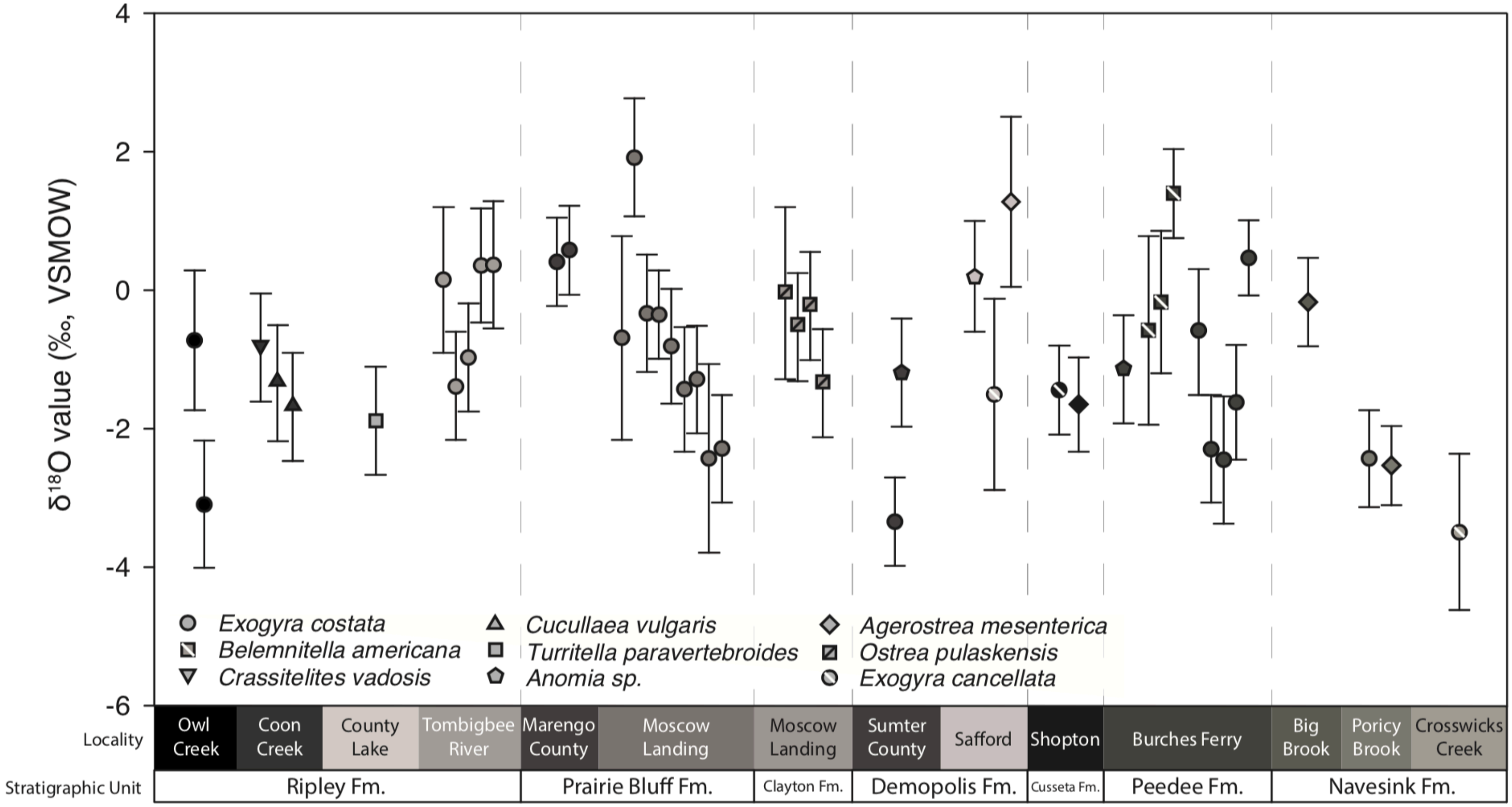

Figure 21. **$\delta^{18}O_{sw}$ Values of Specimens by Formation**

Calculated $\delta^{18}O_{sw}$ values for all measured taxa, by locality. We find that the range in seawater oxygen isotope compositions is comparable across all sites, with the Navesink sites showing slightly lower $\delta^{18}O_{sw}$ values, comparatively. The mean $\delta^{18}O_{sw}$ value is -1.0 ± 1.2‰ (n=46, 1σ; VSMOW), comparable to the global average value of $\delta^{18}O_{sw}$ = -1‰ often assumed for a “greenhouse” (ice-free) Earth. Within a given site $\delta^{18}O_{sw}$ varies by up to ~5.5‰, which challenges typical assumptions of spatially and temporally uniform $\delta^{18}O_{sw}$.

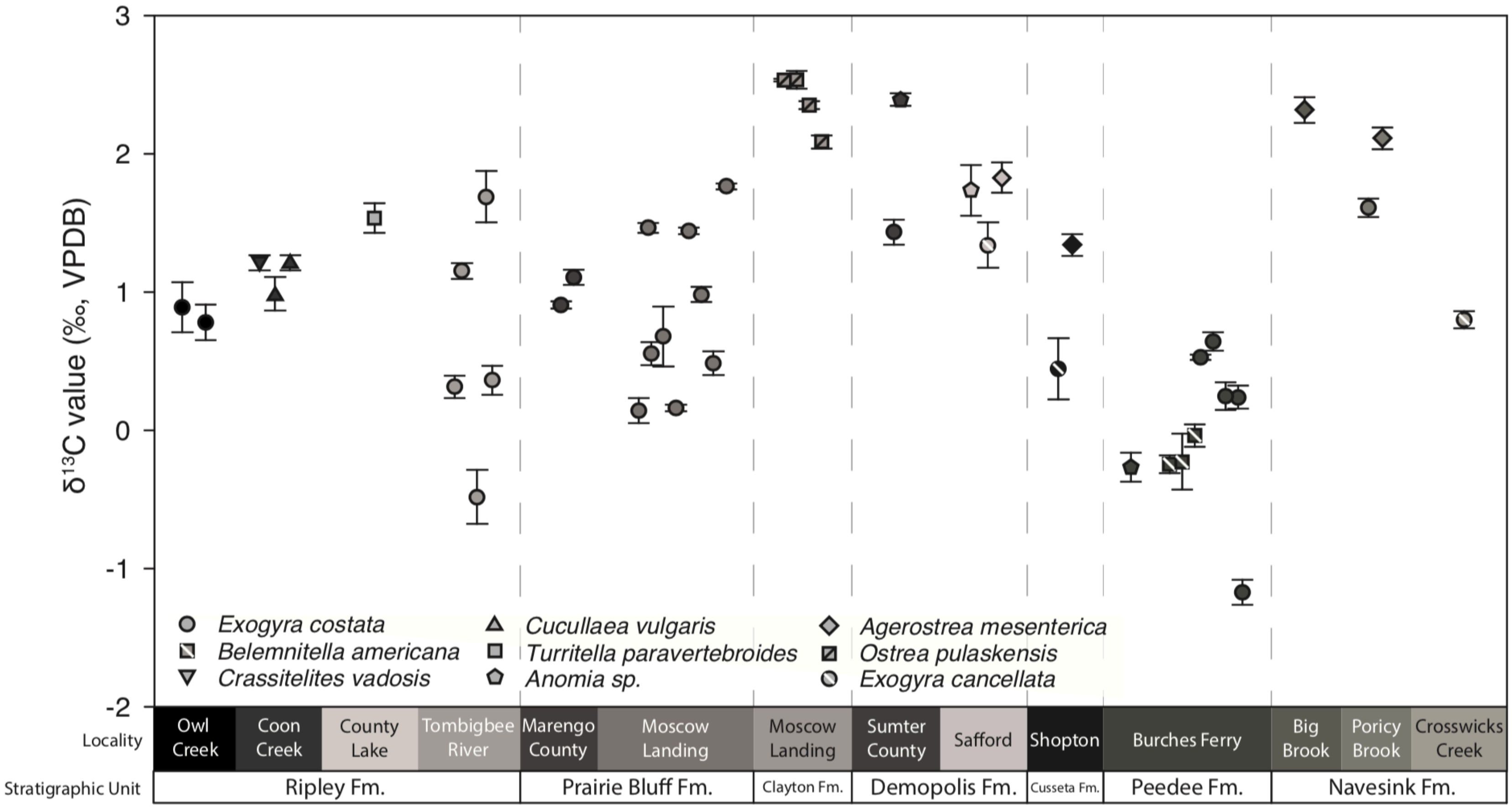

Figure 22. δ^{13}C Values of Specimens by Formation
Measured δ^{13}C values for all taxa, by locality. Samples of the Peedee formation (Burches Ferry) records lower δ^{13}C values than other formations. A clear shift occurs between the Maastrichtian Prairie Bluff (Moscow Landing and Marengo County) and Danian Clayton formations (Moscow Landing), although this shift also corresponds to a change in measured taxa from *Exogyra costata* to *Ostrea pulaskensis*, making the cause of the shift unclear.

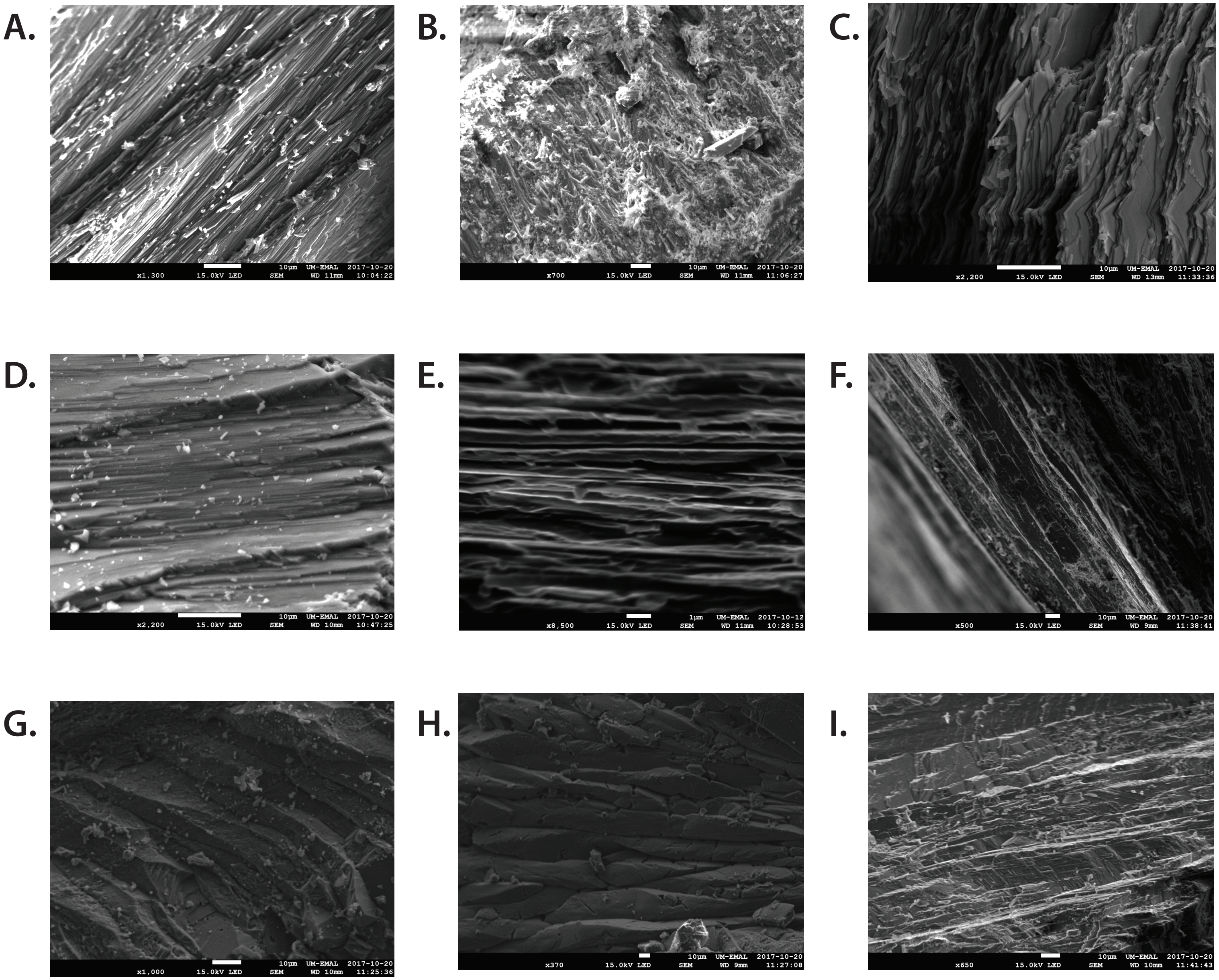

Figure 23. SEM Images of Shell Material. A modern sample of *Crassostrea virginica* collected in 2017 is depicted as a point of comparison to fossil mollusks in terms of preservation index (PI) as defined by Cochran et al. (2010), and where pristine layering (A) versus disordered structural calcite (B) exhibits the variability observed in the shell fabric for even a present-day, unaltered specimen. A representative subset of seven shell were imaged all showing PI ≥ 2 across all the specimens, these samples included: SC-DEM-ANOa (Sumter County, Alabama; C), MC-PRB-EXOa (Marengo County, Alabama; D), MC-PRB-EXOb (Marengo County, Alabama; E), BF-PD-EXOc (Burches Ferry, South Carolina; F), ML-PRB-EXOb (Moscow Landing, Alabama; G), BF-PD-BELc (Burches Ferry, South Carolina; H), and ML-PRB-EXOd (Moscow Landing, Alabama; I).

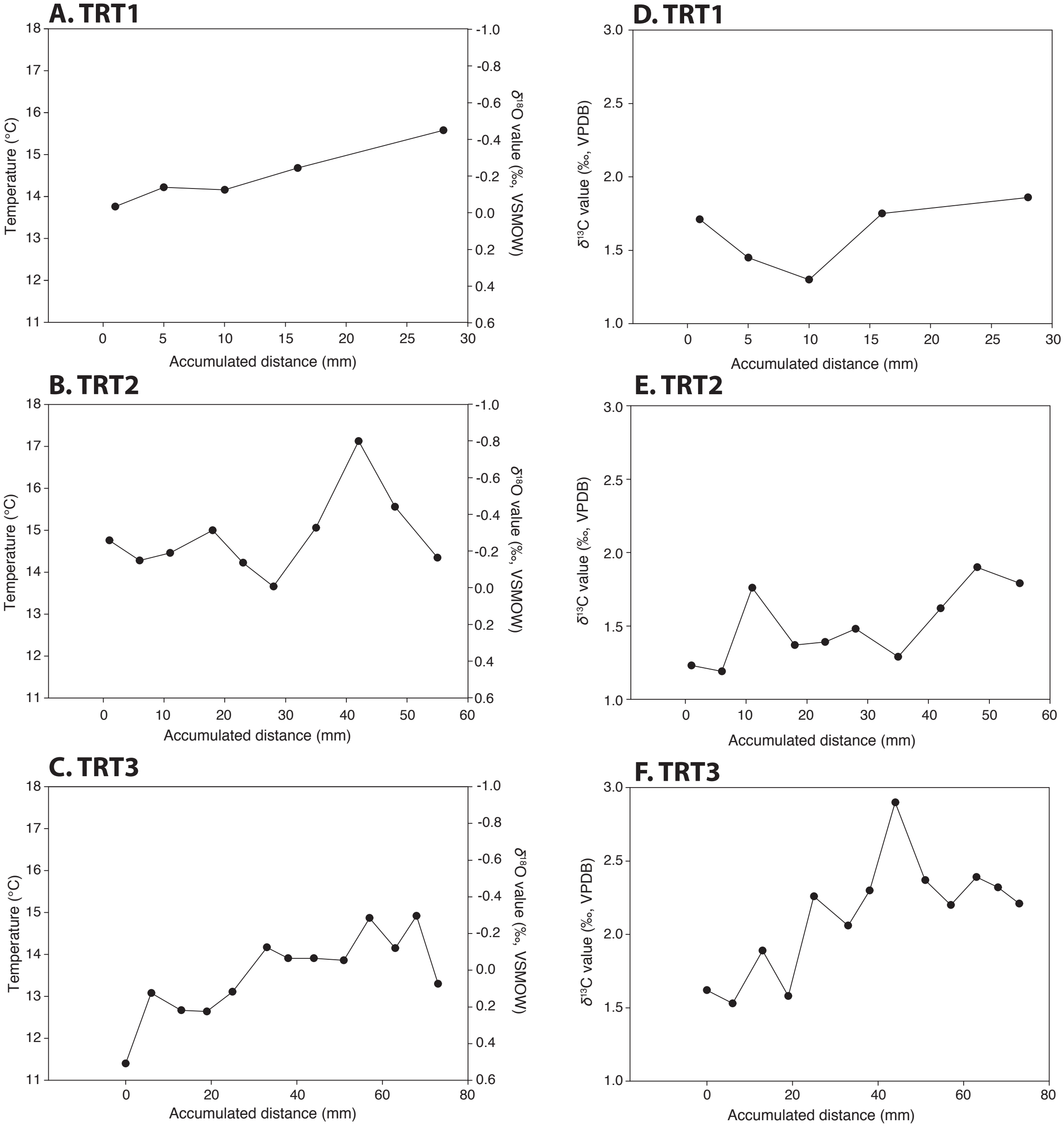

Figure 24. *T. paravertebroides* seasonality data

Plots of temperatures (A, B, C) calculated from measured δ^{18}O and a single Δ_{47}-derived $\delta^{18}O_{sw}$ value (-1.79‰ from TRT1), and δ^{13}C (D, E, F) for three specimens of the gastropod *T. paravertebroides*. Each specimen was sampled along the growth axis of a broken shell fragment containing 1-3 whorls, exhibiting incomplete records of seasonality. Temperatures were calculated using the mollusk-only calibration of Grossman and Ku (1986).

Table 6. Raw clumped isotope data

Raw data tables containing gas standard, carbonate standard, and sample data from five measurement sessions in (A) January 2015 (B) June 2015 (C) September 2015 (D) December 2015 and (E) February 2016. Bad replicates are indicated in red and excluded from further analysis. Data is presented in both old 'Santrock' parameters and new 'Brand' parameters (Daeron et al., 2016; Schauer et al., 2016). All temperature calculations, interpretations, and analysis in the main text are done on the 'Santrock' data.

Table 7. Sample average clumped isotope data

Sample average $\delta^{13}C$, $\delta^{18}O$, Δ_{47}, Temperature, and $\delta^{18}O_w$ values, taken as the mean of typically 3 to 5 replicates (column: N_good). Replicates that did not meet thresholds for contamination (e.g. had elevated Δ_{48} values (Huntington et al., 2009)) or had a procedural or analytical failure are indicated and have been excluded from the calculation of the sample means. Errors on the mean were taken as 1σ for $\delta^{13}C$ and $\delta^{18}O$ and 1 SE for Δ_{47}, Temperature, and $\delta^{18}O_w$ of multiple replicates (internal error). External error for Δ_{47} is taken as the larger of the internal 1 SE or the long-term reproducibility of Carrara standard (1 sd = 0.019‰) divided by the square-root of *n* replicates. For two to five replicates, this gives a 1 SE of 0.013‰, 0.011‰, 0.009‰, and 0.008‰. The external error on temperature is calculated as half of T(mean Δ_{47}-extSE) - T(mean Δ_{47}+extSE), where T(*x*) is the Δ_{47}-Temperature calibration function (Defliese et al., 2015) and 'extSE' is the external error replacing the calculated internal SE. The external error on $\delta^{18}O_w$ is assigned to be 0.92‰, 0.78‰, 0.64‰, and 0.57‰ for n= 2-5 replicates, respectively, based on typical 1 SE values on $\delta^{18}O_w$ for a sample with a Δ_{47}-error of 0.013‰, 0.011‰, 0.009‰, and 0.008‰. External error is used in all main text and supplemental figures. All data in this table is calculated using the 'Santrock' parameters.

Table 8. *Turritella paravertebroides* seasonality data

Raw data table corresponding to Figure 24, indicating the measured $\delta^{13}C$ and $\delta^{18}O$ values for each sample (TRT1, TRT2, TRT3). Also included are the calculated values of $\delta^{18}O_{sw}$ a single Δ_{47}-derived $\delta^{18}O_{sw}$ value (-1.79‰ from TRT1, denoted for clumped isotope analysis as CL-RIP-TURa), temperature values from the calibration by Defliese et al. (2015) and the mollusk-specific calibration from Grossman and Ku (1986). Consecutive samples were taken beginning with the largest whorl present, moving towards the narrower (younger) end. Accumulated distance was measured from the first sample location, along the growth axis.

Table 9. Strontium Isotope Data

Data table reporting all measured $^{87}Sr/^{86}Sr$ values, and calculated mean, minimum, and maximum ages from the LOWESS model after McArthur et al. (2001) and McArthur (2015, personal communication). Measured $^{87}Sr/^{86}Sr$ values were corrected for analytical drift between measurement sessions based on the reported value for NIST SRM-987 (NBS 987) after Thirlwall (1991; $^{87}Sr/^{86}Sr$ =0.710248 ± 0.000011) and are reported with 2 SE analytical error. Final adjusted $^{87}Sr/^{86}Sr$ values were matched to $^{87}Sr/^{86}Sr$ values from the LOWESS model to determine the corresponding age. In the case of no exact match (i.e. $^{87}Sr/^{86}Sr$ value for sample is bracketed by two adjacent 0.05 Ma tie points), the corresponding ages to the bracketing $^{87}Sr/^{86}Sr$ values were averaged to determine the mean value for a sample. The same procedure was carried out for the upper and lower limits of the measured $^{87}Sr/^{86}Sr$ value (mean + 2 SE, mean – 2 SE), matching to the lower and upper limit LOWESS curves to determine a maximum and minimum age from the combined analytical uncertainty and the maximum/minimum age from the LOWESS model. Formation averages were taken as the mean of mean age for all samples within a given formation.

Table 10. Specimen stratigraphic positions

Measured relative stratigraphic positions for all collected specimens from the field by the authors in this study. In all cases samples are reported relative to a designated sampling datum. For the Prairie Bluff Fm. this datum constituted a well-recognized phosphatic lag deposit. The datum for the Ripley Fm. was a distinct and unconformably deposited pebble conglomerate horizon at the top of the section. Lastly, for the Peedee Fm., we used the basal contact between the Peedee Fm. and the shales of the uppermost Black Creek Fm. as described by Swift (1966).

Table 11. Latitude/Longitude of sample locations

Locality Identifier*	**Modern Latitude** (°N)	**Modern Longitude** (°W)	**Mean LOWESS Sr Age**	**Paleolatitude**[†] (°N)
CC-RIP	35.33448	-88.43049	73.4	36.61 ± 2.8
MC-PRB	32.38778	-87.92324	69.5	33.81 ± 2.6
ML-CLA	32.42992	-88.03679	65[‡]	33.23 ± 2.4
ML-PRB	32.42992	-88.03679	69.5	33.88 ± 2.6
OC-RIP	35.11934	-88.4147	73.4	36.40 ± 2.7
SA-DEM	32.28715	-87.36739	73.2	33.45 ± 2.7
SC-DEM	32.67189	-88.17945	73.2	34.04 ± 2.7
SR-CUS	32.07988	-85.93557	-	-
TR-RIP	32.45545	-87.99628	73.4	33.77 ± 2.7
BF-PD	34.06439	-79.52852	71.4	33.04 ± 2.6
BB-NAV	40.31978	-74.21916	70.7	37.48 ± 2.6
CC-NAV	40.10732	-74.5503	70.7	37.37 ± 2.6
PB-NAV	40.36915	-74.11958	70.7	37.50 ± 2.6

*Locality identifier matches the first 5-6 characters of corresponding sample names and is listed with location details below.

[†] Paleolatitude determined after Torsvik et al. (2012) via www.paleolatitude.org, and from the mean formation age based on the measured $^{87}Sr/^{86}Sr$ values and the LOWESS curve after McArthur (2001).

[‡] Uncertainties in the LOWESS curve for this sample are too large to confine to a single reliable age estimate, therefore we base this age of biostratigraphy that confines the age of this unit to no younger than 65 Ma (Moshkovitz and Habib, 1993; Larina et al., 2016).

Appendix A.
Chapter III Sample Locality Information

Selma Group (Demopolis, Ripley, Prairie Bluff formations) and equivalents (Cusseta Sand) – Gulf Coast

Locality Identifier: ML-CLA ("Moscow Landing (Clayton)") **Formation:** Clayton
Locality Identifier: ML-PRB ("Moscow Landing (Prairie Bluff)") **Formation:** Prairie Bluff
Samples collected here:
Clayton Formation

- ML-CLA-OSTa: *Ostrea pulaskensis* (Harris)
- ML-CLA-OSTb: *Ostrea pulaskensis* (Harris)
- ML-CLA-OSTc: *Ostrea pulaskensis* (Harris)
- ML-CLA-OSTd: *Ostrea pulaskensis* (Harris)

Prairie Bluff Formation

- ML-PRB-EXOa: *Exogyra costata* (Say)
- ML-PRB-EXOb: *Exogyra costata* (Say)
- ML-PRB-EXOc: *Exogyra costata* (Say)
- ML-PRB-EXOd: *Exogyra costata* (Say)
- ML-PRB-EXOe: *Exogyra costata* (Say)
- ML-PRB-EXOf: *Exogyra costata* (Say)
- ML-PRB-EXOg: *Exogyra costata* (Say)
- ML-PRB-EXOh: *Exogyra costata* (Say)
- ML-PRB-EXOi: *Exogyra costata* (Say)

Location: Exposure of the Clayton and Prairie Bluff Formations at Moscow Landing, Alabama.
Collection site description: Clayton samples were collected from three prominent limestone beds (Pine Barren Member) immediately overlying the Prairie Bluff Formation. Prairie Bluff samples were collected across the entire exposure, from the bottom of the section to the base of the large sand channels near the unconformable boundary at the top of the unit. Refer to stratigraphic column found in Figure 15.
Collected by: K.W. Meyer, May 14th, 2015
Sample obtained from: collected by authors

Locality Identifier: TR-RIP ("Tombigbee River") **Formation:** Ripley
Samples collected here:

- TR-RIP-EXOa: *Exogyra costata* (Say)
- TR-RIP-EXOb: *Exogyra costata* (Say)
- TR-RIP-EXOc: *Exogyra costata* (Say)
- TR-RIP-EXOd: *Exogyra costata* (Say)

Location: Exposure of the Ripley Formation near Moscow Landing, Alabama, for ~1.5 km along the northern shoreline directly east of where Alabama State Highway 8 crosses the Tombigbee River.

Collection site description: Samples were collected from 4 m of exposure of the Ripley formation below a prominent ~10 cm thick conglomerate layer as an unconformable upper contact on the unit. Refer to stratigraphic column found in Figure 15.
Collected by: K.W. Meyer, May 14th, 2015
Sample obtained from: collected by authors

Locality Identifier: MC-PRB ("Marengo County") **Formation:** Prairie Bluff
Samples collected here:

- MC-PRB-EXOa: *Exogyra costata* (Say)
- MC-PRB-EXOb: *Exogyra costata* (Say)

Location: Roadcuts, both sides of Alabama Highway 28, 1.6 miles west of Jefferson, Marengo Co., Alabama (coordinates approximated from sample description, site reexamined by authors on May 14th, 2015 as small roadcut – no new samples were collected)
Collection site description: GSA 80th Annual Meeting (Alabama Geological Society), p. 66-67
Collected by: D.B. Macurda Jr., Nov. 1967
Sample obtained from: University of Michigan Museum of Paleontology

Locality Identifier: CC-RIP ("Coon Creek") **Formation:** Ripley
Samples collected here:

- CC-RIP-CRAa: *Crassatellites vadosus* (Morton)
- CC-RIP-CUCa: *Cucullaea vulgaris* (Morton) *(measured in 2 places on the same shell)*

Location: Coon Creek, McNairy County, Tennessee, Dave Week's Farm
Collection site description: Coordinates approximated from sample description, and existing museum at former owner's property, and described by Wade (1926).
Collected by: I.G. Reimann, 1955
Sample obtained from: University of Michigan Museum of Paleontology

Locality Identifier: CL-RIP ("County Lake") **Formation:** Ripley
Samples collected here:

- CL-RIP-TURa (or TRT1 for seasonality data): *Turritella paravertebroides* (Morton)
- TRT2: *Turritella paravertebroides* (Morton)
- TRT3: *Turritella paravertebroides* (Morton)

Location: HWY 30, Tallahatchie River, Union Co. Lk., Mississippi
Collection site description: No additional details provided
Collected by: Unknown – March 10, 1985
Sample obtained from: University of Michigan Museum of Paleontology

Locality Identifier: OC-RIP ("Owl Creek") **Formation:** Ripley
Samples collected here:

- OC-RIP-EXOa: *Exogyra costata* (Say)
- OC-RIP-EXOb: *Exogyra costata* (Say)

Location: Owl Creek, McNairy County, Tennessee
Collection site description:
Collected by: A.R. Cahn, 1938
Sample obtained from: University of Michigan Museum of Paleontology

Locality Identifier: SA-DEM ("Safford") **Formation:** Demopolis

Samples collected here:

- SA-DEM-ANOa: *Anomia sp.* (?)
- SA-DEM-EXOa: *Exogyra cancellata* (Stephenson)
- SA-DEM-MESa: *Agerostrea mesenterica* (Morton)

Location: Demopolis fm., near Safford, Alabama
Collection site description: No additional details provided
Collected by: Fred Peterson
Sample obtained from: USGS Denver Collection
Other identifiers: Selma **(**G21a-4)

Locality Identifier: SC-DEM ("Sumter County") **Formation:** Demopolis

Samples collected here:

- SC-DEM-ANOa: *Anomia tellinoides* (Morton)
- SC-DEM-EXOa: *Exogyra costata* (Say)

Location: "5½ sec. 27, T.20N, R.2W., Sumter County, Alabama"
Collection site description: GSA 80th Annual Meeting (Alabama Geological Society), p. 63
Collected by: D.B. Macurda, Jr., Nov. 1967
Sample obtained from: University of Michigan Museum of Paleontology

Locality Identifier: SR-CUS ("Shopton Roadcut") **Formation:** Cusseta Sand

Samples collected here:

- SR-CUS-EXOa: *Exogyra cancellata* (Stephenson)
- SR-CUS-MESa: *Agerostrea mesenterica* (Morton)

Location: Shopton, Alabama
Collection site description: "E side of Alabama State Highway 37, 2.3 mi S of US 82 at Shopton roadcut, east side of road"
(coordinates approximated from sample description)
Cusseta Sand, near the top, *Exogyra Ponderosa* zone (equivalent to Demopolis Fm.)
Collected by: G.R. Scott, May 6th, 1961
Sample obtained from: University of Michigan Museum of Paleontology
Other identifiers: Cusseta (G21a-4)

Peedee Formation – Southern Atlantic Coast

Locality Identifier: BF-PD ("Burches Ferry") **Formation:** Peedee

Samples collected here:

- BF-PD-ANOa: *Anomia sp.* (?)
- BF-PD-BELa: *Belemnitella americana* (d'Orbigny)
- BF-PD-BELb: *Belemnitella americana* (d'Orbigny)
- BF-PD-BELc: *Belemnitella americana* (d'Orbigny)
- BF-PD-EXOa: *Exogyra costata* (Say)
- BF-PD-EXOb: *Exogyra costata* (Say)
- BF-PD-EXOc: *Exogyra costata* (Say)

- BF-PD-EXOd: *Exogyra costata* (Say)
- BF-PD-EXOe: *Exogyra costata* (Say)

Location: Type section of the Pee Dee Belemnite carbon isotope standard reference material (PDB) at Burches Ferry, South Carolina (Ruffin, 1843; Siple, 1957; Swift, 1966).

Collection site description: Samples were collected from ~6.5 m of exposure of the Peedee formation from three distinct calcareous mudstone horizons bearing a mixed shell hash. Upper contact of the unit is unconformable. Refer to stratigraphic column Fig. 14

Collected by: K.W. Meyer, May 7th, 2015

Sample obtained from: collected by authors

Navesink Formation – Northern Atlantic Coast

Locality Identifier: BB-NAV ("Big Brook") **Formation:** Navesink

Samples collected here:

- BB-NAV-MESa: *Agerostrea mesenterica* (Morton)

Location: Big Brook, Monmouth Co., New Jersey

Collection site description: "200' – 1800' E of boundary road of Earle Ammo Depot on Big Brook, 6500' N of Montrose"

Collected by: G.R. Scott, August 8th, 1958

Sample obtained from: USGS Denver Collection

Other identifiers: D7868

Locality Identifier: CC-NAV ("Crosswicks Creek") **Formation:** Navesink

Samples collected here:

- CC-NAV-EXOa: *Exogyra cancellata* (Stephenson)

Location: Crosswicks Creek, Monmouth and Ocean Co., New Jersey

Collection site description: "Branch of Crosswicks Creek 2170 yds south of northern edge of quad and 2 miles + 1000 yds west of eastern edge of quad (150 ft east of road)"

Collected by: G.R. Scott, August 7th, 1958

Sample obtained from: USGS Denver Collection

Other identifiers: D7864

Locality Identifier: PB-NAV ("Poricy Brook") **Formation:** Navesink

Samples collected here:

- PB-NAV-EXOa: *Exogyra costata* (Say)
- PB-NAV-MESa: *Agerostrea mesenterica* (Morton)

Location: Poricy Brook, Monmouth Co., New Jersey

Collection site description: "200' E of Middleton Rd. on Poricy Brook, near Fairview"

Collected by: G.R. Scott, August 9th, 1958

Sample obtained from: USGS Denver Collection

Other identifiers: D7871

CHAPTER IV

End Cretaceous Mercury Concentrations Reveal Climate Influence of the Deccan Traps Large Igneous Province

In preparation for submission

Co-authors:
Kyle W. Meyer, Sierra V. Petersen, Kyger C Lohmann, Joel D. Blum, Spencer J. Washburn, Marcus W. Johnson, James D. Gleason, Aaron Y. Kurz, and Ian Z. Winkelstern

Abstract

We present the first deep-time records of environmental mercury concentrations, [Hg], from biogenic carbonate in marine mollusk fossils. Unlike current methodologies for producing [Hg] data from the geological record (in bulk sediment or rock samples), we simultaneously provide coastal marine temperature data from carbonate clumped isotope (Δ_{47}) measurements with [Hg] analyses from the same samples, demonstrating unambiguous linkages with past climate variability. An assessment of Maastrichtian marine mollusk fossils revealed a global signal of elevated temperatures and [Hg] prior to the Cretaceous–Paleogene (K-Pg) boundary impact event, known for the extinction of the dinosaurs. On Seymour Island, Antarctica we observe a [Hg] background ranging from ~0 to 5 ng g^{-1}, with peaks at 17.3 and 16.9 ng g^{-1} aligning with a temperature increase from ~3 to 7 °C to ~10 to 12 °C, and coinciding with two phases of volcanic activity from the Deccan Traps Large Igneous Province. In western Alabama, we observe a similar record with peak [Hg] = 42 ng g^{-1} occurring with a temperature increase from ~5 to 10 °C to ~20 to 25 °C immediately prior to the K-Pg boundary. The coincidence of elevated [Hg] and increased temperature during the Deccan Traps eruption interval provides the first direct link between

observed climate change and distal LIP volcanism and establishes a new basis for interpreting the intensely debated extinction patterns observed prior to, during, and after the K-Pg boundary.

1. Introduction

Large igneous provinces (LIPs) have recently garnered renewed attention at critical extinction intervals and climate perturbations of the geological record through the application of mercury concentrations and isotopic compositions (Font et al., 2016; Sial et al., 2016; Grasby et al., 2016; Thibodeau et al., 2016; Charbonnier et al., 2017; Percival et al., 2017; Jones et al., 2017). LIP volcanism involves sustained large-scale (>10^5 km^3 to >10^6 km^3) typically mafic or ultramafic volcanism over relatively short (< 5 million years; Ma) spans of geologic time (Ernst and Youbi, 2017, and references therein). For the past 2.5 billion years (Ga), LIPs have occurred at a frequency of one major event every ~20 to 30 Ma and are often closely associated with continental breakup and rifting (Ernst and Youbi, 2017). At nearly every major mass extinction event in the geological record there has been a corresponding LIP eruptive episode observed, which has led to numerous suggestions that LIPs have been either the dominant or contributing mechanism driving these extinctions. This is hypothesized to be achieved via indirect influence on climate and environmental conditions through the emission of volatiles, principally volcanogenic CO_2 (Percival et al., 2015; Ernst and Youbi, 2017, and references therein). With significant volcanic emissions, anticipated climate and environmental responses include: global warming through CO_2-forcing, terrestrial biomass burning (either an indirect product from enhanced aridity, directly by volcanic ash distribution, and/or both), anoxia, and ocean acidification (Ernst and Youbi, 2017).

The Deccan Traps Large Igneous Province (LIP) extruded >10^6 km^3 of flood basalt lava during semi-continuous eruptions over a ~1 Ma interval roughly centered around the end-

Cretaceous (K-Pg) mass extinction and Chicxulub meteorite impact event (Renne et al., 2015; Schoene et al., 2015). The role of the Deccan Traps in the extinction of the dinosaurs and many other organisms compared to the role of the meteorite impact has been the subject of longstanding debate (McLean, 1985; Schulte et al., 2010; Archibald et al., 2010; Courtillot and Fluteau, 2010; Keller et al., 2010). One hurdle in this debate is the ability to distinguish the relative timing of these geographically distant and temporally overlapping events compared to the timing of extinction. Recent advancements in dating have improved the absolute dates on Deccan Traps lava flows, which suggest roughly 30–50% of the lava was emplaced in the 250 thousand years (ka) prior to the K-Pg boundary (Renne et al., 2010; Schoene et al., 2010), coincident with a sudden increase in global temperatures observed in many records (MacLeod et al., 2005; Friedrich et al., 2012; Bowman et al., 2013; Tobin et al., 2014; Linnert et al, 2014; Petersen et al., 2016; Thibault and Husson, 2016). The material erupted prior to the boundary comprises eruptive units belonging to the Kalsubai and Lonavala Subgroups, and those following the boundary are described collectively as the Wai Subgroup (Cox and Hawkesworth, 1985; Beane et al., 1986). The presence of 'red boles' (interpreted as ancient soil horizons, or paleosols, intercalated between flood basalt flows) indicates hiatuses in eruptive activity, and the higher frequency of red boles in the Wai has been used as evidence of larger, less frequent eruptive events following the K-Pg boundary (Renne et al., 2015). Therefore, it could be assumed that eruptions of the Kalsubai and Lonavala subgroups would provide more continuous input of CO_2 (and other volatiles including Hg^0) to the atmosphere, whereas the eruptions associated with the Wai subgroup would only introduce CO_2 intermittently. Recent work suggests that as much as 10,000 to 35,000 Pg of carbon was released from the Deccan Traps, and that this injection of CO_2 could account for high-magnitude warming events (~3 to 15 °C) over 350 ka following the initiation of the Deccan Traps main eruptive phase, particularly when compared to two other LIPs with similar ranges of atmospheric CO_2 loading such as the North Atlantic Igneous Province during the Paleocene-Eocene Thermal Maximum (55.6 Ma) and the Siberian Traps at the Permo-Triassic Boundary (251 Ma; (Chenet et al., 2009; Saunders et al., 2015; Ernst and Youbi, 2017; Gutjahr et al., 2017; Tobin et al., 2017 and references therein). During the Paleocene-Eocene Thermal Maximum (56 Ma), the North Atlantic Igneous Province has been estimated to produce at least 10,000 to 12,000 Pg C, resulting in a globally-averaged warming anomaly of 4-5 °C manifested over a much shorter timespan (~20-150 kyr; Gutjahr et al., 2017). Therefore, with clear potential as a major climate and environmental stressor to biota existing during the Late Cretaceous, the Deccan Traps serve as an important analogue for understanding present and future carbon emissions scenarios, and in understanding the role of LIPs with regard to mass extinctions.

Observed indicators of volcanism from the literature, particularly with respect to the K-Pg extinction, have lacked an unambiguous direct connection to climate variability and have not been measured within the same sample material (Font et al., 2016; Sial et al., 2016). We address this through the use of biogenic carbonate ($CaCO_3$) from marine mollusk fossil remains as a new geochemical archive material for Hg in deep time paleoclimate reconstructions. We have paired total Hg concentrations, [Hg], coastal marine temperature estimates derived from measured carbonate clumped isotope (Δ_{47}) values, in the same sample material from given fossil specimens.

1.1 Volcanic Hg production and existing [Hg] records at the K-Pg Boundary

Volcanogenic emissions of gaseous elemental mercury (Hg^0) represents the largest natural source of Hg to the atmosphere (Pyle and Mather, 2003; Zambardi et al., 2009), where Hg^0 has an atmospheric residence time of ~0.5 to 1.5 years (Butler et al., 2007) allowing global distribution before undergoing photochemical oxidation to Hg(II) and subsequent dissolution in rainfall or surficial attachment to aerosols and/or other airborne particles. Upon entering the marine realm, Hg(II) becomes highly reactive/sorptive to particulates and organic matter, and/or will form various complexes with available ligands (commonly $-Cl_2$; Butler et al., 2007; Lindberg et al., 2007; Percival et al., 2015). Roughly 70% of subaqueous Hg(II) will be photochemically reduced back to Hg^0 and re-released to the atmosphere and continue a cycle of wet/dry deposition and evasion back to the atmosphere, but the remaining proportion will be adsorbed to particulates and/or organic matter and sequestered into marine sediments (Butler et al., 2007; Lindberg et al., 2007). The estimated average residence time of mercury in the oceans is ~350 years (in some cases estimated to range from as short as a few decades up to 1000 years; Matsunaga, 1981; Gill and Fitzgerald, 1988; Gworek et al., 2016).

Sial et al. (2013) produced the first records of [Hg] across the K-Pg boundary from outcrop and core samples of marine mudstones, marls, and bulk limestone at several sites in Brazil and Denmark that revealed a complicated multi-episodic record of elevated [Hg] relative to distinct background concentrations at each site. This work was expanded upon by Sial et al. (2016) and Font et al. (2016), showing an even wider number of sites bearing episodically increased [Hg] prior to and following the K-Pg boundary, interpreted to represent eruptive activity of the Deccan Traps. To account for potentially enhanced rates of Hg sequestration in sediments with higher proportions of organic matter, a new practice was then employed to effectively normalize [Hg] with respect to percentage of total organic carbon (wt % TOC; Percival et al., 2015; Sial et al., 2016; Font et al., 2016). However, this approach may dilute a legitimate signal of [Hg] values, due to the fact that different organic carbon species may have higher affinities to adsorbing mercury (Ravichandran, 2004). Normalizing with respect to % TOC, without a means of characterizing the type of organic carbon present in a sediment sample could misrepresent the magnitude of environmental [Hg] values, but the preservation of organic matter in the geological record may not allow for detailed assessment of specific organic carbon compounds. The issue regarding % TOC highlights another shortfall of bulk rock/sediment [Hg] records, in addition to the potential averaging or 'smoothing' of original [Hg] signals due to sediment bioturbation. Neither of these issues would be as great a concern for analyses of biogenic carbonate.

1.2 Natural cycling of Hg in marine environments and connections to the biosphere

Upon entry into a marine setting, Hg(II) can be methylated by bacteria in the water column, producing the most bioaccumlative form of mercury through methylation into monomethylmercury, $CH_3Hg(Cl,OH)$ or simply methylmercury (MeHg). MeHg occurs in most natural settings at concentrations one to two orders of magnitude less than Hg(II), and may co-occur with dimethylmercury (DMM). DMM is volatile and dissociates in surface and mixed layer marine environments) and, along with MeHg, may demethylate reversibly to Hg(II) (Lindberg et al., 2007; Le Faucheur et al., 2014). In the scope of this study, all measured Hg concentrations will be a measure of total Hg (which could, in concept, include trace amounts of MeHg and DMM, however, fossil preservation of these compounds is unlikely), and will simply be reported henceforth as [Hg].

Hg uptake in phytoplankton is achieved by passive diffusion of $HgCl_2^0$ and CH_3HgCl^0 complexes through algal membranes, or active transport of Hg(II) and MeHg directly. All of these Hg species are ultimately broken-down to Hg(II), which occurs as the dominant speciation of mercury in phytoplankton (La Faucheur et al., 2014). As the primary biomass of marine foodwebs, consumption of phytoplankton serves as the starting point for bioaccumulation of Hg through trophic position (Morel et al., 1998; Ullrich et al., 2001; Blum et al., 2013). One of the earliest consumers of phytoplankton are benthic (and often sessile) marine mollusks (principally bivalves; Pan and Wang, 2011), which can also directly uptake Hg sequestered in sediments (as adsorbed to particulates and organic matter).

1.3 Biogenic carbonate and other biominerals as geochemical proxies of environmental Hg

The use of [Hg] in mollusk carbonate shells (calcite and aragonite; $CaCO_3$) as an indicator of environmental [Hg] has only been demonstrated in two modern studies of environmental water quality (Brown et al., 2005; Ahmad et al., 2013), but with limited application and no attempt at further developing quantitative historical records. We have produced the first deep time paleoclimate record of [Hg] in mollusk biogenic carbonate, demonstrating the potential for this archive across a broad range of timescales from the modern through the entire Phanerozoic. Other studies of [Hg] in biogenic carbonate utilize modern/recent sample material and include: (1) a single study of [Hg] in fish otoliths (Geffen et al., 1998), and (2) an extensive literature of [Hg] in avian eggshells (e.g. Peakall and Lincer, 1972, Faber and Hickey, 1973, Wolfe et al., 1998, and Peterson et al., 2017). The only historical study of [Hg] in biogenic carbonate is a 700-year record of eggshells from the South China Sea that show increasing [Hg] initiated ca. 1800 AD, correlated to the onset of anthropogenic industrial emissions (Xu et al., 2011). Several studies have evaluated other biominerals, (almost exclusively hydroxylapatite, $Ca_{10}(PO_4)_6(OH)_2$) in avian and cod bones (Rothschild et al., 2005; Murray et al., 2015) and in the teeth of cetaceans, walrus, and moose (Frodello et al., 2000; Outridge et al., 2002; Outridge et al., 2009; Vucetich et al., 2009), illustrating the potential for other well-preserved fossil materials to address questions pertaining to environmental mercury in the geological record.

2. Methods

2.1 Selected taxa and sample localities

The samples analyzed for [Hg] in this study include the same specimens sampled for clumped isotope compositions by Petersen et al. (2016) from Seymour Island, Antarctica, and detailed previously in Chapter III above (across the Gulf and Atlantic Coasts of the southeast U.S.; Meyer et al., *in review*). In addition to the aforementioned samples and localities, we also analyzed fossils for [Hg], Δ_{47}, $\delta^{18}O$, $\delta^{13}C$, and $^{87}Sr/^{86}Sr$ values from Late Cretaceous deposits at localities in Argentina, India, Egypt, Libya, Sweden, and the U.S. states of Alaska, California, and Washington (Fig. 25; Table 12; see Appendix B for additional sample locality information and descriptions). The Argentina, Egypt, Libya, and India sample regions range from middle to latest Maastrichtian and were selected as possible records of direct comparison to Seymour Island and Moscow Landing, Alabama (Meyer et al., *in review*). The samples from Washington and Sweden are known to be of earliest Maastrichtian age from biostratigraphic constraints and were intended to serve as controls with respect to measured [Hg], existing entirely outside of the eruptive windows of the Deccan Traps, and thus expected to bear [Hg] values near background. The latitudinal range of sample localities spans from 70 °N (Ocean Point, Alaska; 83–85 °N paleolatitude; Salazar-Jaramillo et al., 2015) to 64 °S (Seymour Island, Antarctica; 67 °S paleolatitude; van Hinsbergen et al., 2015). Additional samples used in this study included twenty-eight specimens from eight distinct regions, detailed as follows: six *Glycymerita aleuta* (Mt. Katmai region, Alaska), three *Glycymeris* sp. and two *Gryphaea* sp. (Merced County, California), one *Cyrtodaria* sp. (Ocean Point, Colville River, North Slope, Alaska), two *Arca vancouverensis* (San Juan Islands, Washington), four *Exogyra overwegyi* (Kharga Oasis, Egypt), two *Agerostrea ungulata* (Fezzan Region, Libya and Cauvery Basin, India), three *Pycnodonte vesicularis* (Neuquén basin, Argentina), two *Belemnitella* sp. (Scania, Sweden) and three unidentified bivalves (one from Scania, Sweden and two specimens from the Mt. Katmai and North Slope regions of Alaska, respectively). Specimens were either collected in the field by the authors and/or collaborators, or were loaned courtesy of the University of Michigan Museum of Paleontology (Ann Arbor, Michigan) and the University of California Museum of Paleontology (Berkeley, California). We also have collected four modern bivalve specimens from Sabin Point Park along the estuary of the Providence River in Providence, Rhode Island, which included: *Crepidula fornicata* (MOD-PRO-FORa), *Crassostrea virginica* (MOD-PRO-VIRa), *Geukensia demissa* (MOD=PRO-DEMa), and an unidentified bivalve (MOD-PRO-BIVa).

2.2 Shell sampling and preservation assessment

All samples were subject to a visual assessment by optical microscopy of carbonate fabrics, eliminating samples with obvious recrystallization, and/or sampling away from recrystallized vugs or portions of any given shell specimen. We applied the same preservational criteria outlined in Chapter III. Roughly half the specimens are of the oyster genus *Exogyra*, and were sampled near the ventral margin of the shell over a large enough area to represent at least 3 distinct layers of ordered carbonate in the shell matrix, presumed to be annual growth bands. Carbonate fragments from the ventral margin were ground by hand using a mortar and pestle. Some smaller individual samples were crushed and used in their entirety (e.g. *Anomia*, *Cyrtodaria*).

2.3 Mercury concentration preparation and determination

With no established standard for the determination of [Hg] in carbonate samples, we selected a variety of carbonate reference materials to use for both in-house standards and to propose as community-accepted standards. We compared NIST SRM-88b (dolomitic limestone quarried near Skokie, Illinois, U.S.), NBS-20 (Solnhofen limestone, Germany; exhausted in terms of commercial availability), USGS COQ-1 (carbonatite from the Oka complex, Lake of Two Mountains, Canada), IAEA-B-7 (limestone collected near Maiella, Abruzzo, Italy), Carrara marble (Italy), and in-house standard LV-3 (limestone from Lake Valley Formation, New Mexico) to two reference materials of known [Hg] values, NRC MESS-3 (Beaufort Sea marine sediment; 91 ± 9 ng/g, certified value) and USGS SGR-1 (Green River Shale; 0.3 µg/g, certified value). As additional points of comparison we also measured [Hg] in the following reference materials: ATHO (Icelandic rhyolite obsidian), USGS AGV-2 (andesite from Guano Valley, Oregon), USGS BCR-2 (basalt from the Bridal Veil Flow Quarry near the Columbia River, Oregon), and USGS BHVO-2 (surface pahoehoe lava from the Halemaumau crater, Hawaii). Initial comparisons of a sample unknown (MC-PRB-EXOb, please refer to Chapter III for details), reference materials, and proposed carbonate concentration standards were digested in a range of acid normalities from 4N to concentrated solutions of both HNO_3 and Lefort aqua regia (also referred to as 'inverse aqua regia,' 3:1 HNO_3:HCl; Townsend and Adams, 1869) to ensure that Hg dissolution was consistent, and to test for any loss by volatilization through the acid reaction. Splits of SRM-88b, NBS-20, and MC-PRB-EXOb were measured in aliquots ranging from 10 to 300 mg, and were digested in 3 ml of 4N HNO_3 in capped 7 ml acid-cleaned polytetrafluoroethylene (PTFE) or perfluoroalkoxy alkane polymer (PFA) vials to assess any potential matrix effects (e.g. the influence of impure sample matrix to enhance or suppress analytical detection) in these materials. To minimize sample material consumption, carbonate sample unknowns were routinely dissolved in 3 ml 4N HNO_3 in 7 ml PTFE/PFA vials with sample loads between 50 and 150 mg, and all non-carbonate material was routinely digested in 2 ml of Lefort aqua regia with identical sample loads. We tested the scalability of larger sample loads in acid digestions for future isotopic analyses with up to 500 mg of NBS-20 and 1000 mg of MESS-3 in 16 ml of Lefort aqua regia in 180 ml PTFE/PFA vials, later diluted by 50% with 16 ml 18.2 MΩ deionized water prior to analysis. Digestions were conducted at 80 °C for between 12 and 48 hours, after which an aliquot of the acid digestate (50 to 200 μl) was diluted with 5 ml of a 1% BrCl and 40 μl $(NH_3OH)Cl$ solution, before being loaded onto a Nippon Instruments Inc. RA-3000FG+ cold vapor atomic fluorescence spectroscopy (CV-AFS) analyzer for [Hg] determination at the University of Michigan Biogeochemistry and Environmental Geochemistry Laboratory.

2.4 Clumped isotope methodology

We have utilized the carbonate clumped isotope paleothermometer from measured Δ_{47} values to determine the temperature of formation in which the fossil mollusk taxa from this study have precipitated their shells (see Petersen et al., 2016 and Chapter III of this dissertation constituting Meyer et al., *in review*). These formation temperatures are interpreted to represent coastal marine temperatures, where from the same sample aliquot we can obtain both [Hg] and temperatures directly reflecting the environment that these organisms resided in.

Aliquots of 3 to 5 mg per replicate of sampled biogenic carbonate powder were measured for $\delta^{18}O$, $\delta^{13}C$, and Δ_{47} isotopic compositions in the University of Michigan Stable Isotope Laboratory using the same instrumentation and procedure as Defliese et al. (2015) Petersen et al., (2016a), and Meyer et al., (*in review*), with a Porapak^{TM} trap temperature held between -10 and -15 °C. Isotopic values were determined from measured voltage intensities by the approach of

Huntington et al. (2009). Measured carbonate Δ_{47} values were placed in the absolute reference frame of Dennis et al. (2011) using heated (1000 °C) and H_2O-equilibrated (25 °C) standard gases, and converted to temperature values using the acid fractionation factor and high-temperature composite calibration of Defliese et al. (2015). $\delta^{18}O_{sw}$ values are calculated from carbonate $\delta^{18}O$ and Δ_{47}-derived temperatures using the fractionation factors determined by Kim and O'Neil (1997) and Kim et al. (2007) for calcite and aragonite as described by the following equations:

$$\mathbf{1000 \ln \alpha_{calcite-H_2O} = 18.03(10^3 T^{-1}) - 32.42} \qquad (1)$$

$$\mathbf{1000 \ln \alpha_{aragonite-H_2O} = 17.88(10^3 T^{-1}) - 31.14} \qquad (2)$$

where *T* is temperature on the Kelvin scale (K). All taxa were dominantly calcite with the exception of *Anomia, Turritella, and Cyrtodaria* which were aragonitic. Measured $\delta^{18}O$, $\delta^{13}C$, Δ_{47}, and calculated paleotemperature and $\delta^{18}O_{sw}$ values for all samples are reported along with gas and carbonate standard data in Table 13.

In the same approach as Chapter III (Meyer et al., *in review*), and due to existing differences between calibrations created in different labs, we have chosen to present our data using parameters after Santrock et al. (1985) until such a time that a universal temperature calibration can be found or temperature-calibration data produced in the same lab as this study can be updated using the new parameters. We present raw data calculated with both old and new parameters in Table 13 for future recalculation. Given that corrections to both measured unknowns and calibration samples within a given lab will likely be similar, we anticipate only small (<1-3 °C) variations between temperatures calculated using the old and new parameters. Analytical uncertainties on single samples are reported in terms of 1 S.E. (determined on a minimum of 3 replicates per sample), and locality or region average temperatures are determined for multiple specimens, and reported with 1σ uncertainties.

Clumped isotope paleothermometry is susceptible to solid-state reordering under relatively low temperature burial conditions (≥100 °C), resulting in a thermal overprinting of the original carbonate formation temperature. For the sake of paleoclimate reconstructions, it is imperative to screen samples for potential diagenetic alteration as well as solid-state reordering of clumped isotope compositions, and requires samples to have experienced comparatively shallow burial histories and extremely limited tectonic influences. For more detailed discussion regarding these considerations, please refer to Chapter III (Meyer et al., *in review*).

2.5 Strontium isotope analysis

Carbonate samples were also analyzed for strontium isotopic compositions following methods detailed in Chapter III. Briefly, a split from each homogenous carbonate powder was digested in 7.5 M HNO_3 and Sr was separated using column chromatography with Eichrom Sr resin (after Meyer et al., 2017). The Sr elutions collected from column separations were loaded onto rhenium filaments and measured for 200 cycles on either a Finnegan MAT 262 or Thermo Scientific Triton Plus^{TM} TIMS at the University of Michigan BEIGL and GIGL facilities. Measurement sessions where $^{87}Sr/^{86}Sr$ values of the standard NIST SRM-987 deviated from a published, accepted value (Thirlwall, 1991; $^{87}Sr/^{86}Sr = 0.710248 \pm 0.000011$), would then be re-normalized (after McArthur et al., 2001; Table 14). The long-term mean $^{87}Sr/^{86}Sr$ value for NIST SRM-987 in the BEIGL facility is 0.710238 ± 0.000016 (1σ).

An age for each measured fossil was calculated by comparison to the most recent iteration of the LOWESS global seawater strontium curve for the Late Cretaceous (McArthur et al., 2001; McArthur pers. comm., 2015; Table 14). McArthur et al. (2001) developed the LOWESS regression from compilations of published $^{87}Sr/^{86}Sr$ data throughout the Phanerozoic, then addressed potential interlaboratory biases by shifting these data by the same degree as any deviations from accepted values of standards SRM-987 and/or EN-1 (0.710248 and 0.709175, respectively). Sample $^{87}Sr/^{86}Sr$ values were matched to the closest $^{87}Sr/^{86}Sr$ value for the Campanian/Maastrichtian portion of the mean LOWESS curve, and the analytical uncertainty of each strontium measurement was propagated through the uncertainty envelope of the LOWESS curve itself to provide the most conservative cumulative uncertainty on any given age (~0.45 to 1.5 Ma per sample).

3. Results

3.1 Mercury concentrations of reference materials and biogenic carbonate

All sample and standard [Hg] data is summarized in Table 15. Analytical and process blanks had an average [Hg] = 0.0079 ± 0.021 ng g^{-1} (1σ, $n = 93$). All samples had measureable levels of mercury in excess of the blanks. Standards of established [Hg] (MESS-3 and SGR-1) produced values in agreement with certified values. Non-carbonate reference materials (ATHO, AGV-2, BHVO-2, and BCR-2) yielded [Hg] values of 1.81 to 3.00 ng g^{-1}. Carbonate reference materials (IAEA-B-7, LV-3, Carrara, NIST SRM-88b, NBS 20, and COQ-1) produced [Hg] values from 1.32 to 69.6 ng g^{-1}. [Hg] in modern bivalve specimens from Providence, Rhode Island were between 0.247 and 4.29 ng g^{-1}.

Fossil marine mollusk biogenic carbonates [Hg] values varied substantially by region, with the lowest range of concentrations (0.201 to 0.466 ng g^{-1}) in samples from Sweden (Scania, Balsvik Quarry) to the highest range in concentrations (0.06 to 42.0 ng g^{-1}) in western Alabama (Mississippi Embayment), these sample regions also recorded the lowest and highest measured

[Hg] values.. Analytical uncertainties varied substantially across replicated samples, but never exceed ± 10% (1σ) of any given measured [Hg] value.

3.2 Clumped isotope results

Raw voltage intensities, measured $\delta^{18}O$ and $\delta^{13}C$ values, and calculated $\delta^{18}O_{sw}$, Δ_{47}, and temperature values for the Alabama, South Carolina, and Antarctica localities are reported in Petersen et al. (2016) and Chapter III (summarized as mean temperature values of the total number of analyzed replicates). All remaining localities are presented with measured and calculated $\delta^{18}O$, $\delta^{13}C$, $\delta^{18}O_{sw}$, Δ_{47}, and temperature values in Table 13. Nineteen fossil mollusk specimens were analyzed to calculate Δ_{47}-derived temperatures, nine of which yield temperatures that would suggest thermal alteration by solid-state reordering (approximately ≥ 30 °C for latitudes above 30 °N/30 °S, corroborated by anomalous strontium isotope compositions; see section 3.3), including all specimens from southwestern Alaska (Mt. Katmai region) and from Washington (San Juan Islands). For the remaining 10 unaltered samples, temperatures representing an average for a given region were: Merced County, California = 18.4 ± 5.3 °C (1σ, $n = 4$), Ocean Point, Alaska = 8.7 ± 1.8 °C (1 S.E., $n = 1$), Scania, Sweden = 15.7 ± 6.0 °C (1σ, $n = 3$), and Fezzan, Libya = 32.0 ± 0.0 °C (1σ, $n = 2$). In combination with strontium isotope results (Section 3.3), we present time-series for both clumped isotope temperatures (adapted from Petersen et al., 2016 and Meyer et al., *in review*) and [Hg] values for the Seymour Island (Antarctica), Moscow Landing (Alabama), North Slope (Alaska), and Merced County (California) sample regions (Figs. 27 and 29).

3.3 Strontium isotope results

Measured $^{87}Sr/^{86}Sr$ values and calculated LOWESS model ages (where applicable; after McArthur et al., 2001) for all sites can be found in Table 14. Uncertainties with respect to LOWESS model ages can range from 0.5 to 1.5 Ma, if not larger when propagated with analytical uncertainties. In some instances, measured $^{87}Sr/^{86}Sr$ values exhibit a clear influence drawing values to more non-radiogenic compositions (e.g. samples of the Mt. Katmai region) yielding anomalously low ages, non-unique ages, or a value that completely falls beneath the LOWESS model curve entirely (IL-KAG-BIVa, $^{87}Sr/^{86}Sr = 0.706650 \pm 0.000012$). Lower $^{87}Sr/^{86}Sr$ values than expected for the age of a given formation could either be the product of diagenetic alteration, or contributions of weathering of non-radiogenic source material in an estuarine environment. Mean $^{87}Sr/^{86}Sr$ values by sample region are as follows: Mt. Katmai = 0.707252 ± 0.000289 (1σ, $n = 8$), North Slope = 0.707622 ± 0.000238 (1σ, $n = 2$), Merced County = 0.707714 ± 0.000102 (1σ, $n = 4$), San Juan Islands = 0.707015 ± 0.000076 (1σ, $n = 2$), Scania = 0.707764 ± 0.000044 (1σ, $n = 2$), Fezzan = 0.707757 ± 0.000008 (1σ, $n = 2$), and Kharga Oasis = 0.707789 ± 0.000035 (1σ, $n = 2$).

4. Discussion

4.1 Conceptual model for the incorporation of volcanic Hg into marine mollusk (bivalve) fossils

Volcanism provides the largest natural input of Hg^0 to the atmosphere, which can be distributed globally based on short atmospheric residence and interhemispheric mixing times. After undergoing photochemical oxidation to Hg(II) and incorporation into marine environments, Hg(II) is sequestered in sediment and is taken up by phytoplankton. Bivalves filter feed principally on phytoplankton (most abundantly on diatoms), other marine microorganisms, and loose organic matter (Galtsoff, 1964). For example, the modern oyster, *Crassostrea virginica*, can filter water at a rate of 1 to 34 L hr^{-1}, and in turbid water can process and mechanically precipitate several grams of clays and other suspended sediment per day from turbid water (Galtsoff et al, 1964). Some bivalve taxa also actively disturb and uptake sediment through movement and burrowing (Luoma and Bryan, 1984). Each of these pathways (phytoplankton, organic matter, and sediment) permits the uptake of Hg(II) into bivalve tissue where it can bioaccumulate to higher concentrations (in comparison to MeHg which typically accumulates at rates 10%, 15%, and 95% higher in phytoplankton, zooplankton, and fish, respectively; Morel et al., 1998). Pan and Wang (2011) demonstrated that various bivalve taxa accumulate elevated [Hg] in viscera (dominantly as Hg(II) and ranging between roughly 50 and 90% of total Hg concentrations). Brown et al. (2005) documented elevated [Hg] in the shells of recent and historical bivalves exposed to a Hg-contaminated fluvial system near Saltville, Virginia. Based on this demonstration of Hg accumulation in shell carbonate, we propose a conceptual model for how enhanced environmental Hg loading from large igneous province eruptions, such as the Deccan Traps, may be recorded by marine bivalves (Fig. 26). This model follows a pathway of: (1) emission to the atmosphere, (2) photochemical oxidation to Hg(II) and deposition into shallow marine systems at a global scale, (3) brief residence times in surface waters before uptake by phytoplankton and sorption to sediment and organic matter, (4) filter feeding and environmental bioaccumulation of Hg(II) into bivalve viscera, (5) chemical precipitation of Hg(II), principally as $HgCO_3$, in the shells of bivalves, (6) death, burial, and fossilization of bivalve biogenic carbonate preserving an original signal of volcanically-elevated [Hg] in the fossil.

4.2 Sample preservation regarding [Hg], Δ_{47}, and $^{87}Sr/^{86}Sr$ compositions

The material we used in this study displays exceptional preservation for both carbonate clumped isotopes (Petersen et al., 2016) as well as for the determination of [Hg]. The mercury preserved in these specimens appears to be of primary origin, and is likely the product of direct, but disordered substitution as inorganic Hg(II). Ahmad et al. (2013) support this interpretation through the observation of defects in shell organic matrix seen in scanning and transmission electron microscopy of modern bivalves from Hg contaminated sites in Portugal, but the mechanism for how Hg is incorporated into mollusk shells is unknown (either by direct incorporation in the shell carbonate or entrapment in the shell organic matrix).

In this study, we have relied on Δ_{47} and ^{87}Sr/^{86}Sr values for determining coastal marine temperatures and approximate age relationships, respectively. We also used both of these isotopic compositions as our primary means of evaluating the potential for diagenetic alteration of carbonate in analyzed specimens, which could also be indicators for diagenetic influence on [Hg] values. Measured ^{87}Sr/^{86}Sr values for these samples were compared to values predicted with the LOWESS model (McArthur et al., 2001; McArthur, pers. comm., 2015). Samples with ^{87}Sr/^{86}Sr values outside the range given by the LOWESS curve for the Late Campanian through the Late Maastrichtian were thought to be either influenced by enhanced terrigenous inputs (e.g. in estuarine environments), or by diagenetic alteration (as described by Bryant et al., 1995). Eight samples exhibited anomalous ^{87}Sr/^{86}Sr values, which implied some process of alteration. In all of these cases, where Δ_{47} was also measured, the Δ_{47} values supported an interpretation of thermal alteration, as defined by elevated Δ_{47}-derived temperatures of a sample region (temperatures ≥ 35 °C globally, or temperatures ≥ 20 °C collected from latitudes ≥ 50 °N; please refer to Table 13; Chapter III). In the seven instances where both Δ_{47} and ^{87}Sr/^{86}Sr values suggested possible alteration, samples were classified as ‘altered’ and excluded from interpretations of [Hg]; this comprised all specimens from the Mt. Katmai and San Juan Islands regions. These regions represent parts of the accreted Wrangellia and Peninsular Terranes of western North America (Jones et al., 1977; Greene et al., 2005) and have been subjected to intensely deformational tectonic histories (Flores et al., 2007; Wartes et al., 2012; Peecook and Sidor, 2015; Flaig and van der Kolk, 2015), compared to all other sample regions considered in this study with comparatively passive tectonic settings and relatively shallow burial histories (Ball, 1900; Goudarzi, 1970; Christensen, 1998; Tantawy et al., 2001; Ali Kalefa El-ghali, 2005; Nagendra et al., 2011; Zakharov et al., 2011; Petersen et al., 2016; de Winter et al., 2017). It is possible that a sample may be altered in terms of clumped isotope composition (by solid-state bond reordering), but not in terms of $^{87}Sr/^{86}Sr$ and/or [Hg] values. In many respects, the most sensitive of indicators of thermal overprinting or diagenetic alteration in a biogenic carbonate is the Δ_{47} composition of a given sample followed by potential low-temperature overprinting of $^{87}Sr/^{86}Sr$ (e.g. Bryant et al., 1995), whereas influences of diagenesis on [Hg] are presently unknown.

In making a first attempt at evaluating the role of diagenetic influences on [Hg] in biogenic carbonates, we determined [Hg] in Carrara marble. Carrara marble, a common geologic reference material has been extensively used as a traditional $\delta^{18}O$ and $\delta^{13}C$ isotope standard, and has been studied in a variety of capacities ranging from assessments of archeological trade routes of the Roman Empire (Herz and Waelkens, 1988) to numerous fundamental petrophysical properties (Costagliola et al., 1999; Leiss and Molli, 2003). The boiling point of metallic Hg is 357 °C (Lide, 2004), and is readily capable of volatilizing at surface temperatures (e.g. evaporation from soils; Schlüter, 2000). Alternatively, Hg(II)-bearing phases such as mercury sulfides (HgS) and mercury oxides (HgO) have been demonstrated to have peak thermal decomposition temperatures (at surface pressures) of between 360 to 470 °C and 470 to 500 °C, respectively (Leckey and Nulf, 1994; Baláž and Godočikoyá, 2001). In the case of Carrara marble, peak metamorphic temperatures of 430 to 450 °C have been observed (Leiss and Molli, 2003) as well as records of pervasive fluid alteration at approximately 400 °C (Costagliola et al., 1999). Given the constraints on the metamorphic history of Carrara marble, we would not expect any metallic Hg^0 to be present in these samples, and only small quantities of Hg(II) mineral phases. We determined [Hg] in Carrara marble to be 1.4 ng g^{-1}, significantly elevated above average analytical values of 0.0079 ± 0.021 ng g^{-1}. The presence of Hg in Carrara marble implies a number of possibilities: (1) diagenetic influence on a $HgCO_3$ phase is nominal and/or the thermal decomposition of $HgCO_3$ occurs at temperatures comparable to (or higher than) those of HgO, (2) a bulk rock sample containing Hg may thermally decompose Hg phases at higher temperatures than isolated purified mineral phases of $HgCO_3$, HgS, and/or HgO, (3) at increased pressures the temperature for peak thermal decomposition of Hg-bearing phases is depressed and permits greater retention, and/or (4) the transport of Hg into a carbonate from some exogenous fluid source. Nonetheless, the retention of Hg in Carrara marble is encouraging for evaluating Hg in carbonates of various origins throughout the geological record given the possibility for Hg retention at elevated metamorphic temperatures/conditions. For the samples of biogenic carbonate measured for [Hg] in this study, there is only minor concern of [Hg] values being altered (based on Δ_{47} and $^{87}Sr/^{86}Sr$ compositions with the former limiting burial temperatures to ≤ 100 °C), but we acknowledge the need for Hg-specific screening methods for diagenetic alteration.

4.3 Reference material mercury concentrations

In addition to Carrara marble, we also analyzed [Hg] in non-carbonate reference materials in order to provide additional method development with respect to conducting sample digestions under varying acid strengths, temperatures for dissolution, and duration of acid reaction. We used the analysis of these reference materials as a proof of concept approach to understanding Hg in high-temperature diagenesis and volcanism, which can inform the limits of preservation of Hg in carbonate fossils and the introduction of Hg to the environment volcanically.

NBS-20 (69.6 ± 7.1 ng g^{-1}) and COQ-1 (37.4 ng g^{-1}) yielded the highest measured [Hg]. NBS-20 has been exhausted and is no longer commercially available, but COQ-1 can still be obtained from the USGS. COQ-1, a 120 Ma calcite-rich carbonatite from the Oka complex in Canada (Chen et al., 2013), bears surprisingly high [Hg] compared to other lava samples, where we would anticipate Hg^0 and Hg(II)-bearing mineral phase thermal decomposition to occur readily at high magmatic temperatures. The only modern active carbonatite eruptions occur at Oldoinyo Lengai (Tanzania), where alkaline natrocarbonatite (Na- and K-rich) is produced at eruptive temperatures ranging from ~490 to 545 °C. These eruptions are several hundred degrees cooler than all comparative modern silicate lavas and have lower average viscosities than modern basalts (Krafft and Keller, 1989; Chen et al., 2013). The [Hg] of COQ-1 compares to the [Hg] of reference materials that are also flow units of eruptive lavas including: BCR-2 (1.8 ng g^{-1}), BHVO-2 (3.0 ng g^{-1}), AGV-2 (2.8 ng g^{-1}), and ATHO (2.0 ng g^{-1}). BHVO-2 is a modern Hawaiian basalt, BCR-2 (basalt) and AGV-2 (andesite) are Cenozoic volcanics from Oregon, and ATHO is a Cenozoic rhyolite obsidian from Iceland. With an order of magnitude lower [Hg] values than COQ-1, these lavas may exhibit a greater effectiveness at thermally decomposing Hg(0) and Hg(II) phases (and/or exhibit higher volatile loss before these phases can crystallize). Fundamental compositional differences and/or post-depositional alteration could explain the discrepancies in these materials, or the crystallization of a higher proportion of Hg-retentive mineral phases in the lower temperature carbonatite melt prior to eruption (possibly due to less volatile loss of Hg). We anticipate that Hg-retentive mineral phases will be uncommon in volcanic settings due to the high degree of Hg^0 volatilization and likely thermal decomposition of Hg(II)-bearing mineral phases from the generation of melt. The presence of significant [Hg] in all measured reference materials, carbonate and non-carbonate, shows promise in the determination of [Hg] throughout the geological record across a broad range of preserved materials.

4.4 Records of [Hg] in Late Cretaceous biogenic carbonate

From the Antarctic (Seymour Island) and Alabama (Moscow Landing) sample regions, we see a distinct linkage between [Hg] and latest Maastrichtian temperatures (Fig. 27). Temperature varies at both sites by as much as 15 °C over the entire record, and appears to reflect similar temporal trends through the Maastrichtian (despite significant missing time in the Alabama record) with an abrupt warming (between 6 to 12 °C) immediately prior to the K-Pg boundary. At Seymour Island, the abrupt warming interval is contemporaneous with the onset of main phase Deccan volcanism (based on comparison of magnetostratigraphy-based age model from Seymour Island and U-Pb and Ar/Ar dates of Deccan Traps lava flows), and is hypothesized to be the result of climate forcing driven by the emission of CO_2 (Petersen et al., 2016). In the same samples that show elevated temperatures, we also find elevated [Hg]. In the Antarctic section, we observe peak [Hg] at 15 to 17 ng g^{-1} coinciding with the peak warming, resolvable from a background of 0.1 to 5 ng g^{-1}. In the Alabama section, we see similar coupling prior to the K-Pg boundary with a higher and more discrete peak in [Hg] at 43.7 ng g^{-1} relative to a similar background of 0.1 to 5 ng g^{-1} (Fig. 27), but acknowledge that the boundary is unconformable at this location (see Chapter III). The section in Alabama lacks the same degree of age control that exists for the Antarctic section (Petersen et al., 2016), but is chronologically constrained by a combination of sample stratigraphic position, biostratigraphy, and measured strontium isotope chemostratigraphy (Chapter III; Meyer et al., *in review*). The correspondence of the temperature and [Hg] records between the two sites supports the tentative age model construction, which assumes that the Alabama record is nearly complete up to the K-Pg boundary. The Antarctic section also shows a second, earlier interval of elevated [Hg] around 67.5 Ma, prior to the onset of main phase Deccan volcanism, that is not captured in the Alabama record and likely due to the poor exposure and lack of fossil preservation in this portion of the Alabama section. We tentatively correlate this earlier [Hg] peak to a known smaller phase of eruptive activity of the Deccan Traps described by Chenet et al. (2007) as transitional flow units up to 100 m thick, with an initiation occurring near the magnetostratigraphic C30r/C30n reversal, and continuing through the early portion of C30n. Therefore, these samples demonstrate the first directly quantifiable linkage between observed past climate change and a record of past volcanic activity at the K-Pg from the same sample material.

Additionally, we present [Hg] data corresponding to a small number of Late Cretaceous specimens from globally-distributed sample regions (Fig. 28) in Alaska (Mt. Katmai and North Slope), California (Merced County), Washington (San Juan Islands), South Carolina (Pee Dee River), Argentina (Neuquén Basin), Egypt (Kharga Oasis), Libya (Fezzan), India (Cauvery Basin), and Sweden (Scania). Samples from these sites span a large range of time from the Late Campanian to the K-Pg Boundary at the end of the Maastrichtian. For many of these sample regions specimens were collected from a number of localities within the region, and some samples were collected over 100 years ago (e.g. Egypt region with samples from Djebel Ter and Kharga Oasis; please refer to Appendix B detailing all specimen details including localities). Therefore, a precise stratigraphic position is unknown for many of the specimens, but in instances where there was some known detail of stratigraphic position and/or successful application of independent age constraints (e.g. strontium isotope chemostratigraphy), a more direct comparison could be made between these sample regions and the Moscow Landing and Seymour Island [Hg] records (Fig. 28, 29). The Neuquén Basin, Kharga Oasis, Fezzan, and Cauvery Basin regions are all mid- to Late Maastrichtian as determined by biostratigraphy (Ball, 1900; Goudarzi, 1970; Tantawy et al., 2001; Ali Kalefa El-ghali, 2005; Nagendra et al., 2011; Zakharov et al., 2011; de Winter et al., 2017), but only the Neuquén and Kharga regions show significant [Hg] variability (0.7 to 6.4 ng g^{-1} and 1.9 to 10.1 ng g^{-1}, respectively; Fig. 28).

The Neuquén Basin samples are known to be collected from near the K-Pg boundary (de Winter et al., 2017), but the boundary at this site is unconformable, with biostratigraphic records implying that ~450 ka is missing from the latest Maastrichtian at this region (Keller et al., 2007). Woelders et al. (2017) acknowledge the lack of any absolute dating methods for this region, but suggest that a single peak in TEX_{86}-derived temperatures (an increase of ~2 to 3.5 °C) from the Neuquén Basin record correlates with a $\delta^{18}O$ record of marine temperatures at Walvis Ridge (ODP Site 1262), implying that < 20 ka is missing at the Neuquén Basin unconformity. However, in lieu of any further justification of this correlation, we assume that the Keller et al. (2007) interpretation of ages at Neuquén Basin is most accurate, and from Δ_{47}-derived temperature values, we observe no statistically significant variability (mean value = 18.3 ± 3.1 °C, 1σ, $n = 4$; Table 13) from samples spanning 8 m prior to the K-Pg boundary. The TEX_{86}-derived temperatures may conform with the Late Maastrichtian Δ_{47}-derived temperature variability we observe at the Moscow Landing and Seymour Island sample regions, but it is currently impossible to correlate these records any further without independent means of age determination. The paucity of samples from Neuquén Basin used in this study may have simply missed similar variability in the Woelders et al.

(2017) record due to sample aliasing, which may be resolved by additional sampling, but for the scope of interpretation we categorize it as temporally unresolvable.

The Kharga Oasis samples were recovered from an established biostratigraphic horizon (*Exogyra overwegi* zone; Tantawy et al., 2001) of the Maastrichtian. Measured $^{87}Sr/^{86}Sr$ values of the two Kharga Oasis specimens (KO-DAK-EXOa = 0.707814 ± 0.000019 and KO-DAK-EXOb = 0.707760 ± 0.000013) would place these samples in alignment with the eruptive window of the Deccan also seen in the Alabama and Antarctic records (Fig. 27-29), but stratigraphic position relative to the K-Pg boundary is still unknown.

The Mt. Katmai and San Juan Islands regions also exhibit substantial variability in [Hg] values (2.1 to 14.2 ng g^{-1} and 4.2 to 15.6 ng g^{-1}, respectively; Fig. 28). However, based on measured Δ_{47} and $^{87}Sr/^{86}Sr$ values, sample from these regions are interpreted to be diagenetically altered (see Section 4.1). It is possible that [Hg] in biogenic carbonates may not be as sensitive as Δ_{47} and $^{87}Sr/^{86}Sr$ values to diagenetic alteration (as suggested by Carrara marble in Section 4.2), but this is presently unknown. The Pee Dee River and Scania regions were both known to be from deposits significantly older than the Deccan eruptive phases (Late Campanian to Early Maastrichtian; Christensen, 1998; Chapter III, Meyer et al., *in review*), and as such were anticipated to have little environmental Hg present at these times. This was confirmed by [Hg] values measured to be effectively zero (Fig. 28).

Lastly, large [Hg] variability was observed for the Merced County (3.6 to 15.4 ng g^{-1}) and North Slope (8.8 to 30.7 ng g^{-1}) localities, which are both described as Late Maastrichtian (Flores et al., 2007; Flaig and van der Kolk, 2015; Peecook and Sidor, 2015) and compare in magnitude to the Moscow Landing and Seymour Island records (Fig. 28, 29).

Each assessed sample region in this study may ultimately require a region or locality-specific determination of background [Hg] values, in order to account for potential localized, high-concentration sources of Hg to a given depositional environment (e.g. modern anthropogenically-contaminated sites or naturally-occurring cinnabar deposits). Nonetheless, we observe comparable background [Hg] values across all sites that may lend to the suggestion of an average global background bivalve [Hg] value. Based on the [Hg] data from all our measured sample regions, we propose this possible global [Hg] background at a threshold of ≤ 5 ng g^{-1}, defined from the median of [Hg] values from all sample regions (median = 3.88 ng g^{-1} + 1 S.E. = 1.02 ng g^{-1}; Fig. 28).

We also compared the [Hg] data of fossil biogenic carbonate to values from modern biogenic carbonate of four bivalve specimens collected by the authors at Sabin Point Park (Providence, Rhode Island; Fig. 28). Sabin Point Park resides in an estuary subject to substantial anthropogenic influence (e.g. waterfront industrial plants and active shipping lanes) through combustion of diesel and gasoline (where these fuel sources have been documented with [Hg] between 180 to 600 ng L^{-1}; Won et al., 2007). The range in [Hg] values for the shell carbonate in these modern specimens was 0.2 to 4.3 ng g^{-1}, and conforms to the hypothetical [Hg] background we have proposed. Therefore, we infer that a significant environmental disturbance would be necessary to account for the magnitude of elevated [Hg] at the scale we have observed for specimens coinciding with the Deccan eruptive phases. With evidence of four roughly contemporaneous and geographically disparate regions that bear an elevated [Hg] signal (Seymour Island, Moscow Landing, Merced County, and North Slope; Fig. 28, 29), we conclude that this pattern represents a global signal of volcanically-sourced [Hg] that can be linked directly to Δ_{47} temperatures and implies that the Deccan Traps LIP was responsible for significant climatic forcing prior to the K-Pg boundary.

A final consideration involves comparisons of measured [Hg] to temperatures (Fig. 29A) and measured $^{87}Sr/^{86}Sr$ values (Fig. 29B). The sample regions from the Deccan eruptive window do not indicate any clear temperature dependence with respect to [Hg]. This does not refute the possibility of a temperature dependence with respect to the partitioning of environmental Hg into shell carbonate and is a question that can best be addressed by a modern study of analogous extant taxa. However, no statistically significant correlations exist between measured [Hg] and temperatures in samples preceding the Deccan Traps eruptive window. At all four sample regions, the peak [Hg] values occur nearest the K-Pg boundary, and are largely indistinguishable from one another in terms of $^{87}Sr/^{86}Sr$ ratio (Fig. 29). Given the 'coarseness' of strontium isotope chemostratigraphy as a geochronologic tool it would be impossible to place the records from these sample regions in a more precisely-resolved chronology to interpret the timing of volcanic Hg emissions from the Deccan Traps. However, the observation of increased [Hg] with $^{87}Sr/^{86}Sr$ ratios that would confine sample ages to within the Deccan Traps eruptive window reinforces the possibility for evaluating secular trends in [Hg] of biogenic carbonate at timescales ≥ 1 to 10 Ma in the geological record.

5. Conclusions

We have measured [Hg] in a series of established geologic reference materials and fossil marine mollusks, with particular focus on biogenic carbonate. The assessment of reference materials has revealed that USGS COQ-1, a calcium-rich carbonatite, exhibits the best potential as a standard for [Hg] in carbonates based on its availability and elevated [Hg] at 37.4 ng g^{-1}. Measured [Hg] values well above CV-AFS detection limits of 0.0079 ± 0.021 ng g^{-1} (1σ, $n = 93$) in all reference materials suggests potential for reconstructing [Hg] records throughout the Earth history in a wide range of geological archives. A comparison of [Hg] values across a wide range of volcanic materials and in Carrara marble suggests that original Hg may be preserved in carbonates despite high temperature conditions that would result in thermal decomposition and/or volatilization of Hg phases and may imply a relatively low susceptibility to diagenetic influence.

We have reconstructed detailed Late Maastrichtian records linking elevated Δ_{47}-derived temperatures and [Hg] at Seymour Island (Antarctica) and Moscow Landing and surrounding areas along the Mississippi Embayment in Alabama. At Seymour Island, we observe a resolvable [Hg] background ranging from ~0.7 to 5 ng g^{-1}, with peaks at 17.3 and 16.9 ng g^{-1} corresponding to elevated temperatures ranging from ~10 to 15 °C and coinciding directly with two phases of Deccan Traps Large Igneous Province volcanic eruptive activity. In the Moscow Landing region, we observe a record truncated by an unconformity and poor exposure, but still bearing peak [Hg] = 42 ng g^{-1} co-occurring with elevated temperatures between ~20 to 25 °C immediately prior to the K-Pg boundary. At both of these locations, these temperatures represent a temperature excursion of approximately 7 to 10 °C associated with the elevated [Hg] profiles, and provide a direct link between eruptions of the Deccan Traps and climate forcing as a consequence of volcanic CO_2 emissions demonstrated from analyses of the same biogenic carbonate samples.

In addition to these detailed records, we have determined [Hg] in specimens for ten other Late Cretaceous sample regions. For five of these regions, with known contemporaneous records, (Antarctica, Alabama, California, Alaska, and Egypt) we found evidence that further corroborates a global signal of elevated [Hg] associated with the Deccan Traps. Four modern bivalve specimens from Providence, Rhode Island have similar [Hg] to Cretaceous samples outside the eruptive window, suggesting a possible global background for [Hg] in marine mollusks (<0.7 to 5 ng g^{-1})

for sites that do not bear major anthropogenic contamination (e.g. Oak Ridge National Laboratory, Tennessee).

Ultimately, the application of [Hg] in fossilized biogenic carbonate provides a unique means to constrain the timing of large volcanic eruptive episodes in the geological record distal to the source of the eruption. Through this application, biogenic carbonate [Hg] records may also inform the mechanisms behind mass extinctions and climatic perturbations throughout Earth history, and possibly address questions of paleoecological Hg-cycling in marine environments. Biogenic carbonate provides the potential for directly comparable records of temperature (through measured Δ_{47} values) and environmental [Hg] that cannot be achieved with existing methodologies for reconstructing past Hg (e.g. bulk sediment or rock records).

Acknowledgements. We thank L. Wingate for analytical assistance, D. Miller (UM Museum of Paleontology), K. McKinney (USGS) and E. Clites (University of California Museum of Paleontology) for paleontological assistance and for access to sample collections. We thank R. Gabelman and B. Dzombak for their invaluable contributions in the field. This work was funded by NSF-OCE-PRF #1420902, NSF-EAR #1123733, and the University of Michigan Scott Turner Award.

References

Ahmad, I., Singh, M.K., Pereira, M.L., Pacheco, M., Santos, M.A., Duarte, A.C., Pereira, E., Grácio, J., (2013) Morphological, compositional and ultrastructural changes in the Scrobicularia plana shell in response to environmental mercury – An indelible fingerprint of metal exposure? Chemosphere 90, 2697–2704. doi:10.1016/j.chemosphere.2012.11.049

Ali Kalefa El-ghali, M., (2005) Depositional environments and sequence stratigraphy of paralic glacial, paraglacial and postglacial Upper Ordovician siliciclastic deposits in the Murzuq Basin, SW Libya. Sedimentary Geology 177, 145–173. doi:10.1016/j.sedgeo.2005.02.006

Archibald, J. D., Clemens, W. A., Padian, K. & Rowe, T. (2010) Cretaceous extinctions: multiple causes. *Science*. doi:10.1029/2008JB005644

Baláž, P., Godočiková, (2001) Thermal Reduction of Mechanically Activated Cinnabar (HgS) and Stibnite (Sb2S3). Journal of Thermal Analysis and Calorimetry **65**, 51–57.

Ball, J., (1900) Kharga Oasis: Its Topography and Geology. Cairo National Printing Department.

Beane, J. E., Turner, C. A., Hooper, P. R., Subbarao, K. V. & Walsh, J. N. (1986) Stratigraphy, composition and form of the Deccan Basalts, Western Ghats, India. *Bulletin of Volcanology* **48,** 61–83.

Blakey, R. (2017). Global Paleogeography: Mollewide Plate Tectonics Maps, http://jan.ucc.nau.edu/rcb7/mollglobe.html (October 2017).

Blum J. D., Popp B. N., Drazen J. C., Anela Choy C. and Johnson M. W. (2013) Methylmercury production below the mixed layer in the North Pacific Ocean. *Nature Geosci* **6**, 879–884.

Bowman, V. C., Francis, J. E. & Riding, J. B. (2013) Late Cretaceous winter sea ice in Antarctica? *Geology* **41,** 1227–1230.

Brosgé, W.P., Whittington, C.L., Morris, R.H., (1966). Geology of the Umiat-Maybe Creek Region, Alaska, USGS Professional Paper 303-H.

Brown, M. E., Kowalewski, M., Neves, R. J., Cherry, D. S. & Schreiber, M. E. (2005) Freshwater Mussel Shells as Environmental Chronicles: Geochemical and Taphonomic Signatures of Mercury-Related Extirpations in the North Fork Holston River, Virginia. *Environ. Sci. Technol.* **39,** 1455–1462.

Butler, T., Likens, G., Cohen, M. & Vermeylen, F. (2007) Final Report Mercury in the Environment and Patterns of Mercury Deposition from the NADP/MDN Mercury Deposition Network. *National Oceanic and Atmospheric Administration Air Resources Laboratory*.

Bryant, J.D., Jones, D.S., Mueller, P.A., (1995) Influence of freshwater flux on 87Sr/86Sr chronostratigraphy in marginal marine environments and dating of vertebrate and invertebrate faunas. Journal of Paleontology 69, 1–6. doi:10.1017/S002233600002686X

Charbonnier, G., Föllmi, K.B., (2016) Mercury enrichments in lower Aptian sediments support the link between Ontong Java large igneous province activity and oceanic anoxic episode 1a. Geology 45, 63–66. doi:10.1130/G38207.1

Chen, W., Kamenetsky, V.S., Simonetti, A., (2013) Evidence for the alkaline nature of parental carbonatite melts at Oka complex in Canada. Nat Comms 4, 1. doi:10.1038/ncomms3687

Chenet, A., Quidelleur, X., Fluteau, F., Courtillot, V., Bajpai, S., (2007) 40K–40Ar dating of the Main Deccan large igneous province: Further evidence of KTB age and short duration. Earth and Planetary Science Letters 263, 1–15. doi:10.1016/j.epsl.2007.07.011

Chenet, A.-L., Courtillot, V., Fluteau, F., Gérard, M., Quidelleur, X., Khadri, S.F.R., Subbarao, K.V., Thordarson, T., (2009) Determination of rapid Deccan eruptions across the Cretaceous-Tertiary boundary using paleomagnetic secular variation: 2. Constraints from analysis of eight new sections and synthesis for a 3500-m-thick composite section. Journal of Geophysical Research 114, 183–38. doi:10.1029/2008JB005644

Christensen, W.K., (1998) Belemnitella from the lowermost Maastrichtian of Scania, southern Sweden. Bulletin of the Geological Society of Denmark 45, 1–12.

Costagliola, P., Benvenuti, M., Maineri, C., Lattanzi, P., Ruggieri, G., (1999) Fluid circulation in the Apuane Alps core complex: evidence from extension veins in the Carrara marble. Mineralogical Magazine 63, 111–111. doi:10.1180/002646199548231

Courtillot, V. & Fluteau, F. (2010) Cretaceous extinctions: the volcanic hypothesis. *Science* **328,** 973–974.

Cox, K. G. & Hawkesworth, C. J. (1985) Geochemical stratigraphy of the Deccan Traps at Mahabaleshwar, Western Ghats, India, with implications for open system magmatic processes. *Journal of Petrology* **26,** 355–377.

Defliese, W. F., Hren, M. T. & Lohmann, K. C. (2015) Compositional and temperature effects of phosphoric acid fractionation on Δ47 analysis and implications for discrepant calibrations. *Chemical Geology* **396,** 51–60.

Dennis, K. J., Affek, H. P., Passey, B. H., Schrag, D. P. & Eiler, J. M. (2011) Defining an absolute reference frame for 'clumped' isotope studies of CO2. *Geochimica et Cosmochimica Acta* **75,** 7117–7131.

Dennis K. J., Cochran J. K., Landman N. H. and Schrag D. P. (2013) The climate of the Late Cretaceous New insights from the application of the carbonate clumped isotope thermometer to Western Interior Seaway macrofossil. *Earth and Planetary Science Letters* **362**, 51–65.

Detterman, R.L., Bickel, R.S., Gryc, G., 1963. Geology of the Chandler River Region, Alaska, USGS Professional Paper 303-E.

de Winter, N.J., Vellekoop, J., Vorsselmans, R., Golreihan, A., Soete, J., Petersen, S.V., Meyer, K.W., Casadio, S., Speijer, R.P., Claeys, P., (2017) An assessment of latest Cretaceous <i>Pycnodonte vesicularis</i> (Lamarck, 1806) shells as records for palaeoseasonality: A multi-proxy investigation. Clim. Past Discuss. 1–36. doi:10.5194/cp-2017-120

Dickin, A.P., (2005) Radiogenic Isotope Geology 2nd (second) edition published by Cambridge University Press [Paperback] 2005. Cambridge University Press.

Eiler, J. M. & Schauble, E. (2004) 18O13C16O in Earth's atmosphere. *Geochimica et Cosmochimica Acta* **68,** 4767–4777.

Eiler, J. M. (2011) Paleoclimate reconstruction using carbonate clumped isotope thermometry. *Quaternary Science Reviews* **30,** 3575–3588.

Eiler, J. M. *et al.* (2014) Frontiers of stable isotope geoscience. *Chemical Geology* **372,** 119–143.

Ernst, R.E., Youbi, N., (2017) How Large Igneous Provinces affect global climate, sometimes cause mass extinctions, and represent natural markers in the geological record. Palaeogeography, Palaeoclimatology, Palaeoecology **478**, 30–52. doi:10.1016/j.palaeo.2017.03.014

Faber, R. A. & Hickey, J. J. (1973) Eggshell thinning, chlorinated hydrocarbons, and mercury in inland aquatic bird eggs, 1969 and 1970. *Pesticides Monitoring Journal* **7,** 27–36.

Flaig, P. P. & van der Kolk, D. A. (2015) Depositional Environments of the Prince Creek Formation along the East Side of the Toolik River, Sagavanirktok Quadrangle, North Slope, Alaska.

Font, E., Adatte, T., Sial, A.N., Drude de Lacerda, L., Keller, G., Punekar, J., (2016) Mercury anomaly, Deccan volcanism, and the end-Cretaceous mass extinction. Geology 44, 171–174. doi:10.1130/G37451.1

Friedrich, O., Norris, R.D., Erbacher, J., (2012) Evolution of middle to Late Cretaceous oceans--A 55 m.y. record of Earth's temperature and carbon cycle. Geology 40, 107–110. doi:10.1130/G32701.1

Frodello, J. P., Roméo, M. & Viale, D. (2000) Distribution of mercury in the organs and tissues of five toothed-whale species of the Mediterranean. *Environmental Pollution* **108,** 447–452.

Galtsoff P. S. (1964) *The American Oyster, Crassostrea Virginica Gmelin*, Fishery Bulletin, v. **64**. United States Government Printing Office, Washington, D. C.

García-Alix, A., Minwer-Barakat, R., Martín Suárez, E., Freudenthal, M. & Delgado Huertas, A. (2012) Cinnabar mineralization in fossil small mammal remains as a consequence of diagenetic processes. *Lethaia* **46,** 1–6.

Geffen, A. J., Pearce, N. J. G. & Perkins, W. T. (1998) Metal concentrations in fish otoliths in relation to body composition after laboratory exposure to mercury and lead. *Marine Ecology Progress Series* **165,** 235–245.

Gill G. A. and Fitzgerald W. F. (1988) Vertical mercury distributions in the oceans. *Geochimica et Cosmochimica Acta* **52**, 1719–1728.

Goudarzi, G.H., (1970) Geology and mineral resources of Libya a reconnaissance. USGS Professional Paper 660.

Grasby, S. E., Shen, W., Yin, R., Gleason, J. D., Blum, J. D., Lepak, R. F., et al. (2016). Isotopic signatures of mercury contamination in latest Permian oceans. *Geology*, G38487.1–4. http://doi.org/10.1130/G38487.1

Gutjahr, M., Ridgwell, A., Sexton, P.F., Anagnostou, E., Pearson, P.N., Pälike, H., Norris, R.D., Thomas, E., Foster, G.L., (2017) Very large release of mostly volcanic carbon during the Palaeocene–Eocene Thermal Maximum. Nature Publishing Group **548**, 573–577. doi:10.1038/nature23646

Gworek B., Bemowska-Kałabun O., Kijeńska M. and Wrzosek-Jakubowska J. (2016) Mercury in Marine and Oceanic Waters—a Review. *Water Air Soil Pollut*, 1–19.

Herz, N., Waelkens, M., (1988) Classical Marble: Geochemistry, Technology, Trade. Springer Science & Business Media, Series E: Applied Sciences, **153**.

Huntington, K.W., Eiler, J.M., Affek, H.P., Guo, W., Bonifacie, M., Yeung, L.Y., Thiagarajan, N., Passey, B., Tripati, A., Daëron, M., Came, R., (2009) Methods and limitations of "clumped" CO 2isotope (Δ 47) analysis by gas-source isotope ratio mass spectrometry. J. Mass Spectrom. 44, 1318–1329. doi:10.1002/jms.1614

Jones D. L. and Gryc G. (1960) *Upper Cretaceous Pelecypods of the Genus Inoceramus from Northern Alaska*, USGS Professional Paper 334-E

Jones, D. S., Martini, A. M., Fike, D. A. & Kaiho, K. (2017) A volcanic trigger for the Late Ordovician mass extinction? Mercury data from south China and Laurentia. *Geology* **45,** 631–634.

Keller, G., Adatte, T., Tantawy, A.A., Berner, Z., Stinnesbeck, W., Stueben, D., Leanza, H.A., (2007) High stress late Maastrichtian – early Danian palaeoenvironment in the Neuquén Basin, Argentina. Cretaceous Research 28, 939–960. doi:10.1016/j.cretres.2007.01.006

Keller, G., Adatte, T., Pardo, A., Bajpai, S. & Khosla, A. (2010) Cretaceous Extinctions: Evidence Overlooked [with Response]. *Science* **328,** 974–975.

Kelson, J. R., Huntington, K. W., Schauer, A. J., Saenger, C. & Lechler, A. R. (2017) Toward a universal carbonate clumped isotope calibration: Diverse synthesis and preparatory methods suggest a single temperature relationship. *Geochimica et Cosmochimica Acta* **197,** 104–131.

Krafft, M., Keller, J., (1989) Temperature Measurements in Carbonatite Lava Lakes and Flows from Oldoinyo Lengai, Tanzania. Science 245, 168–170. doi:10.1126/science.245.4914.168

Leckey, J.H., Nulf, L.E., (1994) Thermal decomposition of mercuric sulfide, Oak Ridge National Laboratory Technical Report Y/DZ-1124. doi:10.2172/41313

Leiss, B., and Molli, G., (2003) "High-temperature" texture in naturally deformed Carrara marble from the Alpi Apuane, Italy. Journal of Structural Geology 25, 649–658. doi:10.1016/s0191-8141(02)00148-7

Lide, D.R., (2004) CRC Handbook of Chemistry and Physics, 85th Edition. CRC Press.

Linnert, C., Robinson, S.A., Lees, J.A., Bown, P.R., Perez-Rodriguez, I., Petrizzo, M.R., Falzoni, F., Littler, K., Arz, J.A., Russell, E.E., 2014. Evidence for global cooling in the Late Cretaceous. Nat Comms 5, 699. doi:10.1038/ncomms5194

Lindberg, S., Bullock, R. & Ebinghaus, R. (2007) A synthesis of progress and uncertainties in attributing the sources of mercury in deposition. *AMBIO: A Journal of the Human Environment* **36,** 19–33.

Luoma S. N. and Bryan G. W. (1982) A statistical study of environmental factors controlling concentrations of heavy metals in the burrowing bivalve Scrobicularia plana and the polychaete Nereis diversicolor. *Estuarine, Coastal and Shelf Science* **15**, 95–108.

MacLeod, K.G., Huber, B.T., Isaza-Londoño, C., (2005) North Atlantic warming during global cooling at the end of the Cretaceous. Geology 33, 437–4. doi:10.1130/G21466.1

Matsunaga K. (1981) Oceanic Residence Time of Mercury. *Bulletin of the Faculty of Fisheries Hokkaido University* **32**, 199–202.

McLean, D.M., (1985) Deccan traps mantle degassing in the terminal Cretaceous marine extinctions. Cretaceous Research 6, 235–259. doi:10.1016/0195-6671(85)90048-5

Morel, F.M.M., Kraepiel, A.M.L., Amyot, M., (1998) The Chemical Cycle and Bioaccumulation of Mercury. Annual Review of Ecology and Systematics 29, 543–566. doi:10.1146/annurev.ecolsys.29.1.543

Murray, M. S., McRoy, C. P. & Duffy, L. K. (2015) Biogeochemical analysis of ancient Pacific Cod bone suggests Hg bioaccumulation was linked to paleo sea level rise and climate change. *Frontiers in Environmental Science* **3,** 1114.

Outridge, P. M., Hobson, K. A., McNeely, R. & Dyke, A. (2002) A Comparison of Modern and Preindustrial Levels of Mercury in the Teeth of Beluga in the Mackenzie Delta, Northwest Territories, and Walrus at Igloolik, Nunavut, Canada. *ARCTIC* **55,** 123–132.

Outridge, P. M., Hobson, K. A. & Savelle, J. (2009) Long-term changes of mercury levels in ringed seal (Phoca hispida) from Amundsen Gulf, and beluga (Delphinapterus leucas) from the Beaufort Sea, western Canadian Arctic. *Science of the Total Environment, The* **407,** 6044–6051.

Pan K. and Wang W.-X. (2011) Mercury accumulation in marine bivalves: Influences of biodynamics and feeding niche. *Environmental Pollution* **159**, 2500–2506.

Pasch, A.D., May, K.C., (1997) First occurrence of a Hadrosaur (Dinosauria) from the Matanuska Formation (Turonian) in the Talkeetna Mountains of south-central Alaska. Alaska Division of Geological & Geophysical Surveys. doi:10.14509/2335

Peakall, D. B. & Lincer, J. L. (1972) Methyl mercury: Its effect on eggshell thickness. *Bulletin of Environmental Contamination and Toxicology* **8,** 89–90.

Peecook, B.R., Sidor, C.A., (2015) The First Dinosaur from Washington State and a Review of Pacific Coast Dinosaurs from North America. PLoS ONE 10, e0127792–15. doi:10.1371/journal.pone.0127792

Percival, L.M.E., Witt, M.L.I., Mather, T.A., Hermoso, M., Jenkyns, H.C., Hesselbo, S.P., Al-Suwaidi, A.H., Storm, M.S., Xu, W., Ruhl, M., (2015) Globally enhanced mercury deposition during the end-Pliensbachian extinction and Toarcian OAE: A link to the Karoo–Ferrar Large Igneous Province. Earth and Planetary Science Letters 428, 267–280. doi:10.1016/j.epsl.2015.06.064

Percival, L., Ruhl, M. & Hesselbo, S. P. (2017) Mercury evidence for pulsed volcanism during the end-Triassic mass extinction. *Proceedings of the National Academy of Science.* doi:10.1073/pnas.1705378114

Petersen, S. V., Dutton, A. & Lohmann, K. C. (2016) End-Cretaceous extinction in Antarctica linked to both Deccan volcanism and meteorite impact via climate change. *Nat Comms* **7,** 12079.

Peterson, S.H., Ackerman, J.T., Eagles-Smith, C.A., Hartman, C.A., Herzog, M.P., (2017) A critical evaluation of the utility of eggshells for estimating mercury concentrations in avian eggs. Environ Toxicol Chem 36, 2417–2427. doi:10.1002/etc.3777

Pyle, D. M. & Mather, T. A. (2003) The importance of volcanic emissions for the global atmospheric mercury cycle. *Atmospheric Environment* **37,** 5115–5124.

Ravichandran, M., (2004) Interactions between mercury and dissolved organic matter—a review. Chemosphere 55, 319–331. doi:10.1016/j.chemosphere.2003.11.011

Renne P. R., Sprain C. J., Richards M. A., Self S., Vanderkluysen L. and Pande K. (2015) State shift in Deccan volcanism at the Cretaceous-Paleogene boundary, possibly induced by impact. *Science* **350**, 76–78.

Roberts, A.C., Groat, L.A., Raudsepp, M., Ercit, T.S., Erd, R.C., Moffatt, E.A., Stirling, J.A.R., (2001) Clearcreekite, A New Polymorph of $Hg^{1+}{}_3(CO_3)(OH)2H_2O$, from the Clear Creek Claim, San Benito County, California. The Canadian Mineralogist 39, 779–784. doi:10.2113/gscanmin.39.3.779

Roberts, A. C., Ercit, T. S. & Groat, L. A. (1995) Peterbaylissite, $Hg^{1+}{}_3(CO_3)(OH)2H_2O$, a new mineral species from the Clear Creek Claim, San Benito County, California. *The Canadian Mineralogist* **33**, 47-53.

Rothschild, R. F. N. & Duffy, L. K. (2005) Mercury concentrations in muscle, brain and bone of Western Alaskan waterfowl. *Science of The Total Environment* **349,** 277–283.

Salazar-Jaramillo, S., Fowell, S.J., McCarthy, P.J., Benowitz, J.A., Śliwiński, M.G., Tomsich, C.S., (2016) Terrestrial isotopic evidence for a Middle-Maastrichtian warming event from the lower Cantwell Formation, Alaska. Palaeogeography, Palaeoclimatology, Palaeoecology 441, 360–376. doi:10.1016/j.palaeo.2015.09.044

Santrock J., Studley S. A. and Hayes J. M. (1985) Isotopic analyses based on the mass spectra of carbon dioxide. *Anal. Chem.* **57**, 1444–1448.

Saunders, A.D., (2015) Two LIPs and two Earth-system crises: the impact of the North Atlantic Igneous Province and the Siberian Traps on the Earth-surface carbon cycle. Geol. Mag. 153, 201–222. doi:10.1017/S0016756815000175

Scheirer A. H. and Magoon L. B. (2007) Age, distribution, and stratigraphic relationship of rock units in the San Joaquin Basin Province, California. Petroleum Systems and Geologic Assessment of Oil and Gas in the San Joaquin Basin Province, California.

Schoene B., Samperton K. M., Eddy M. P., Keller G., Adatte T., Bowring S. A., Khadri S. F. R. and Gertsch B. (2015) U-Pb geochronology of the Deccan Traps and relation to the end-Cretaceous mass extinction. *Science* **347**, 182–184.

Schulte P., Alegret L., Arenillas I., Arz J. A., Barton P. J., Bown P. R., Bralower T. J., Christeson G. L., Claeys P., Cockell C. S., Collins G. S., Deutsch A., Goldin T. J., Goto K., Grajales-Nishimura J. M., Grieve R. A. F., Gulick S. P. S., Johnson K. R., Kiessling W., Koeberl C., Kring D. A., MacLeod K. G., Matsui T., Melosh J., Montanari A., Morgan J. V., Neal C. R., Nichols D. J., Norris R. D., Pierazzo E., Ravizza G., Rebolledo-Vieyra M., Reimold W. U., Robin E., Salge T., Speijer R. P., Sweet A. R., Urrutia-Fucugauchi J., Vajda V., Whalen M. T. and Willumsen P. S. (2010) The Chicxulub Asteroid Impact and Mass Extinction at the Cretaceous-Paleogene Boundary. *Science* **327**, 1214–1218.

Schlüter, K., (2000) Review: evaporation of mercury from soils. An integration and synthesis of current knowledge. Environmental Geology 39, 249–271. doi:10.1007/s002540050005

Sial, A.N., Lacerda, L.D., Ferreira, V.P., Frei, R., Marquillas, R.A., Barbosa, J.A., Gaucher, C., Windmöller, C.C., Pereira, N.S., (2013) Mercury as a proxy for volcanic activity during extreme environmental turnover: The Cretaceous–Paleogene transition. Palaeogeography, Palaeoclimatology, Palaeoecology 387, 153–164. doi:10.1016/j.palaeo.2013.07.019

Sial A. N., Chen J., Lacerda L. D., Frei R., Tewari V. C., Pandit M. K., Gaucher C., Ferreira V. P., Cirilli S., Peralta S., Korte C., Barbosa J. A. and Pereira N. S. (2016) Mercury enrichment and Hg isotopes in Cretaceous-Paleogene boundary successions: Links to volcanism and palaeoenvironmental impacts. *Cretaceous Research* **66**, 60–81.

Smith, C. N., Kesler, S. E., Blum, J. D. & Rytuba, J. J. (2008) Isotope geochemistry of mercury in source rocks, mineral deposits and spring deposits of the California Coast Ranges, USA. *Earth and Planetary Science Letters* **269,** 399–407.

Tantawy, A.A., Keller, G., Adatte, T., Stinnesbeck, W., Kassab, A., Schulte, P., (2001) Maastrichtian to Paleocene depositional environment of the Dakhla Formation, Western Desert, Egypt: sedimentology, mineralogy, and integrated micro- and macrofossil biostratigraphies. Cretaceous Research 22, 795–827. doi:10.1006/cres.2001.0291

Tobin, T.S., Wilson, G.P., Eiler, J.M., Hartman, J.H., (2014) Environmental change across a terrestrial Cretaceous-Paleogene boundary section in eastern Montana, USA, constrained by carbonate clumped isotope paleothermometry. Geology 42, 351–354. doi:10.1130/G35262.1

Tobin, T. S., Bitz, C. M. & Archer, D. (2017) Modeling climatic effects of carbon dioxide emissions from Deccan Traps volcanic eruptions around the Cretaceous–Paleogene boundary. *Palaeogeography, Palaeoclimatology, Palaeoecology* **478,** 139–148.

Townsend, W.A., Adams, (1869) The Chemical News and Journal of Physical Science: A Journal of Practical Chemistry Vol. IV. The New York Printing Company.

Thibault, N., Husson, D., (2016) Climatic fluctuations and sea-surface water circulation patterns at the end of the Cretaceous era: Calcareous nannofossil evidence. Palaeogeography, Palaeoclimatology, Palaeoecology 441, 152–164. doi:10.1016/j.palaeo.2015.07.049

Thibodeau, A. M. & Bergquist, B. A. (2016) Do mercury isotopes record the signature of massive volcanism in marine sedimentary records? *Geology* **45,** 95–96.

Ullrich, S.M., Tanton, T.W., Abdrashitova, S.A., (2001) Mercury in the Aquatic Environment: A Review of Factors Affecting Methylation. Critical Reviews in Environmental Science and Technology 31, 241–293. doi:10.1080/20016491089226 van Hinsbergen, D.J.J., de Groot, L.V., van Schaik, S.J., Spakman, W., Bijl, P.K., Sluijs, A., Langereis, C.G., Brinkhuis, H., (2015) A Paleolatitude Calculator for Paleoclimate Studies. PLoS ONE 10, e0126946–21. doi:10.1371/journal.pone.0126946

Vucetich, J. A., Outridge, P. M., Peterson, R. O., Eide, R. & Isrenn, R. (2009) Mercury, lead and lead isotope ratios in the teeth of moose (Alces alces) from Isle Royale, U.S. Upper Midwest, from 1952 to 2002. *J. Environ. Monit.* **11,** 1352–8.

Wang Z., Chen J., Feng X., Hintelmann H., Yuan S., Cai H., Huang Q., Wang S. and Wang F. (2015) Mass-dependent and mass-independent fractionation of mercury isotopes in precipitation from Guiyang, SW China. *Comptes Rendus Geoscience* **347**, 358–367.

Wartes, M.A., Decker, P.L., Stanley, R.G., Herriott, T.M., Helmold, K.P., Gillis, R.J. (2012) Preliminary stratigraphy and facies analysis of the Upper Cretaceous Kaguyak Formation, including a brief summary of newly discovered oil stain, upper Alaska Peninsula. Overview of 2012 field studies: Upper Alaska Peninsula and west side of lower Cook Inlet, Alaska 25–32. doi:10.14509/24849

Woelders, L., Vellekoop, J., Kroon, D., Smit, J., Casadío, S., Prámparo, M.B., Dinarès-Turell, J., Peterse, F., Sluijs, A., Lenaerts, J.T.M., Speijer, R.P. (2017) Latest Cretaceous climatic and environmental change in the South Atlantic region. Paleoceanography 32, 466–483. doi:10.1002/2016PA003007

Wolfe, M. F., Schwarzbach, S. & Sulaiman, R. A. (1998) Effects of mercury on wildlife: A comprehensive review. *Environ Toxicol Chem* **17,** 146–160.

Won, J.H., Park, J.Y., Lee, T.G., (2007). Mercury emissions from automobiles using gasoline, diesel, and LPG. Atmospheric Environment 41, 7547–7552. doi:10.1016/j.atmosenv.2007.05.043

Xu, L.-Q., Liu, X.-D., Sun, L.-G., Chen, Q.-Q., Yan, H., Liu, Y., Luo, Y.-H., Huang, J. (2011) A 700-year record of mercury in avian eggshells of Guangjin Island, South China Sea. Environmental Pollution 159, 889–896. doi:10.1016/j.envpol.2010.12.021

Zambardi, T., Sonke, J. E., Toutain, J. P., Sortino, F. & Shinohara, H. (2009) Mercury emissions and stable isotopic compositions at Vulcano Island (Italy). *Earth and Planetary Science Letters* **277,** 236–243.

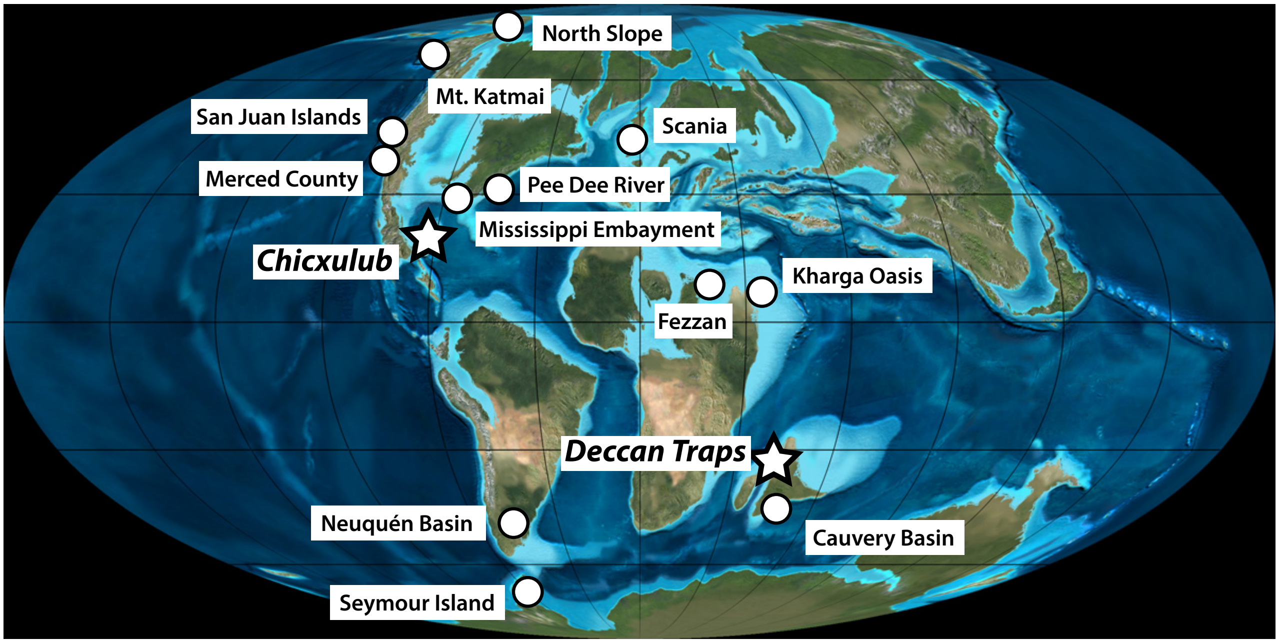

Figure 25. Paleogeographic reconstruction of the Late Cretaceous adapted from Blakey (2017), labeled with specimen sample regions. Individual regions often constitute several localities where sampling occurred either historically or by the authors. Additional specimen details can be found in Appendix B. Locations of the Deccan Traps Large Igneous Province and the Chicxulub impact event are demarcated with star-shaped symbols.

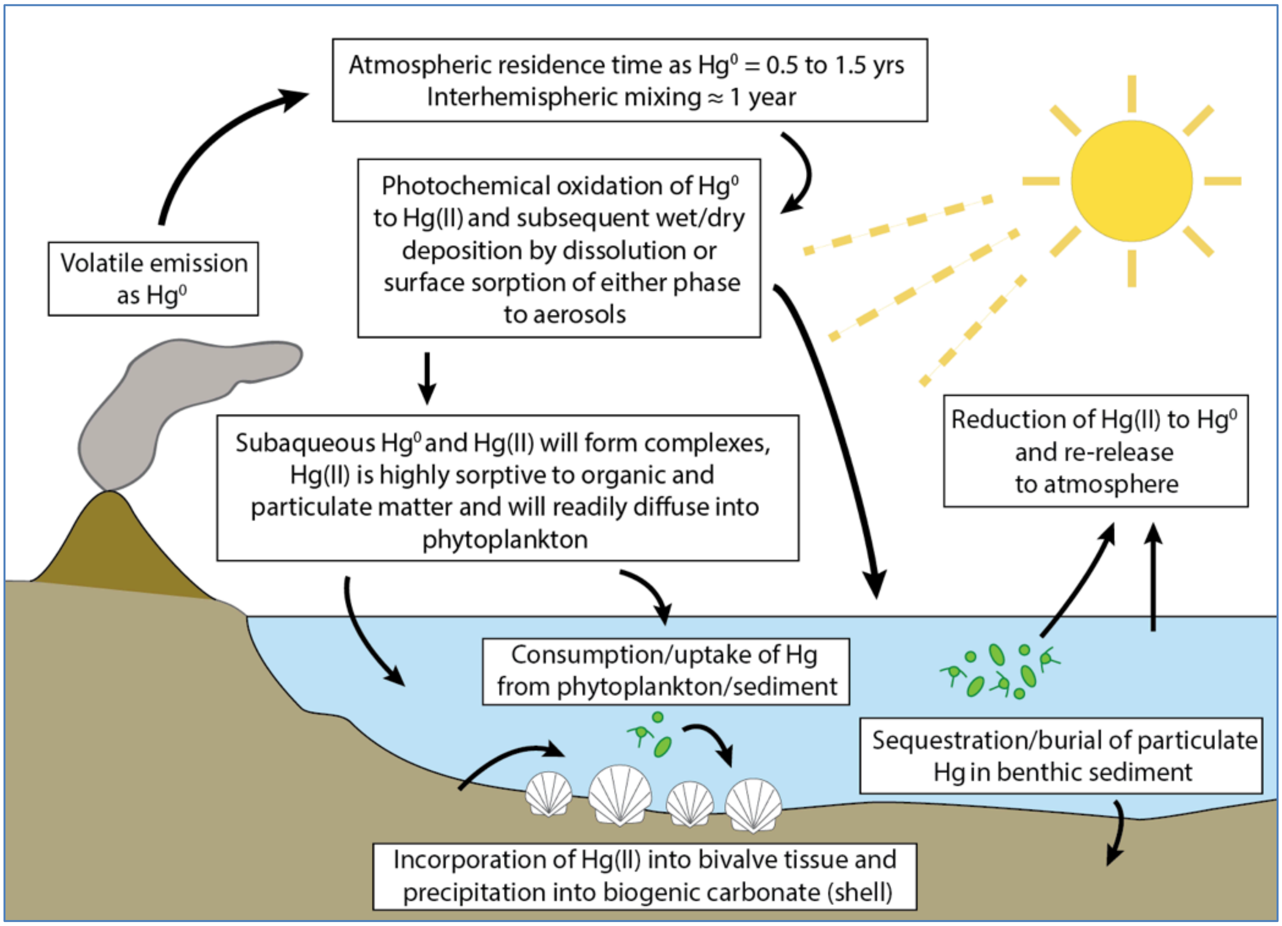

Figure 26. Conceptual model of volcanogenic Hg emission and subsequent incorporation into marine biota. Gaseous elemental mercury (Hg^0) is released in addition to other volatiles (e.g. CO_2), where in the atmosphere it is photochemically oxidized to Hg(II) and either adsorbed to particulate and/or organic matter, reduced and re-released back to the atmosphere, or incorporated into phytoplankton through various uptake pathways. Benthic, sessile filter-feeding marine mollusks can then bioaccumulate Hg(II) from either the consumption of algae or from the sediment directly. Refer to sections 2.X and 2.X in the text for in-depth explanation.

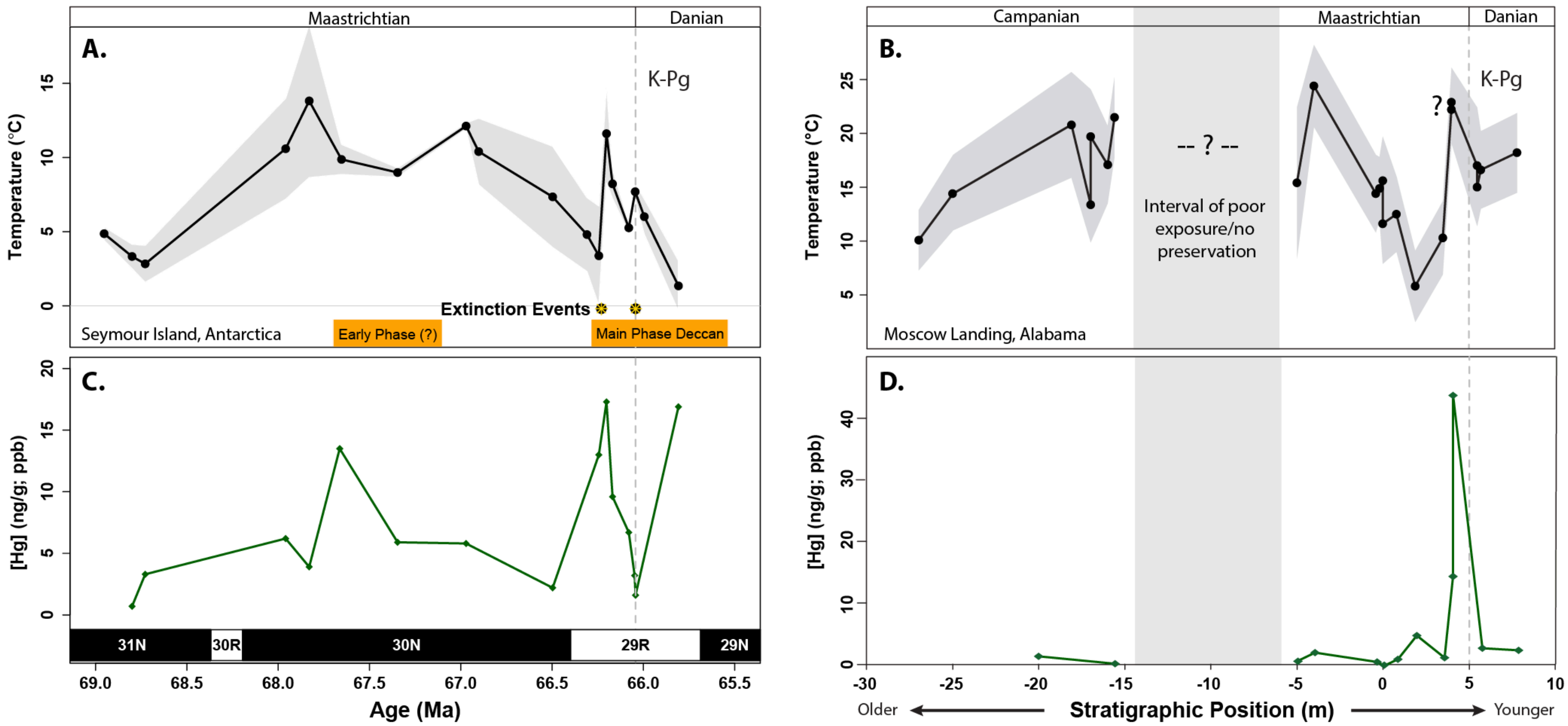

Figure 27. Δ_{47}-derived coastal marine temperatures (A, B) and [Hg] records (C, D) for Seymour Island, Antarctica (adapted from Petersen et al., 2016) and Moscow Landing, Alabama (adapted from Chapter III, Meyer et al., *in review*). The Moscow Landing records lack the same degree of age constraints that are present at Seymour Island through combined biostratigraphy, magnetostratigraphy, strontium isotope chemostratigraphy, and the presence of the iridium layer to demarcate the K-Pg Boundary. The K-Pg boundary at Moscow Landing is an unconformable contact between the Maastrichtian Prairie Bluff Chalk and the Danian Clayton Formation, and the Maastrichtian-aged section as a whole is most likely only a portion of what is preserved at Seymour Island. Nonetheless, at both sites we observe a close coupling between elevated [Hg] and temperatures immediately prior to the boundary.

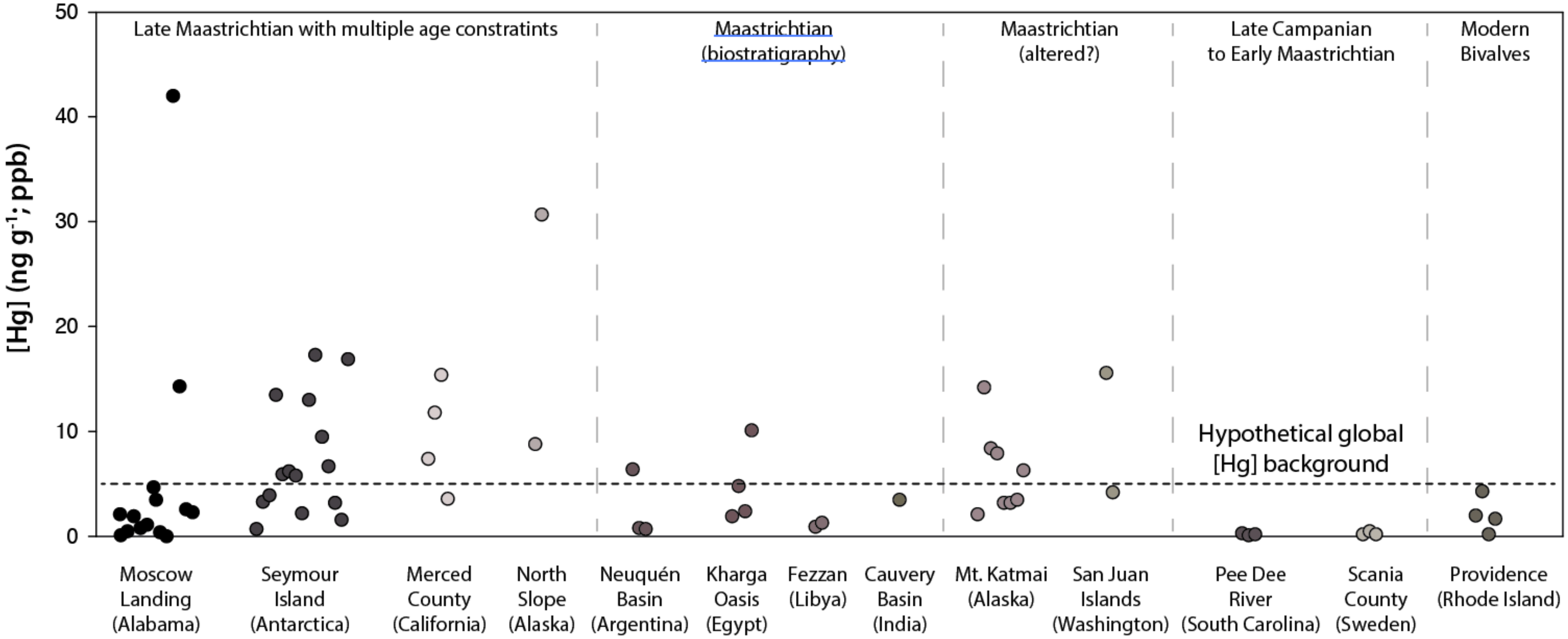

Figure 28. Measured [Hg] values by sample region divided temporally and by age constraints. Samples from Moscow Landing, Seymour Island, Merced County, and North Slope regions all are Late Maastrichtian in age and are constrained by some combination of biostratigraphy, magnetostratigraphy, strontium isotope stratigraphy, and/or the presence of the iridium layer (Flores et al., 2007; Flaig and van der Kolk, 2015; Peecook and Sidor, 2015; Petersen et al., 2016; Meyer et al., *in review*). Specimens from Neuquén Basin, Kharga Oasis, Fezzan, and Cauvery Basin are acknowledged to be from the Middle to Late Maastrichtian (Ball, 1900; Goudarzi, 1970; Tantawy et al., 2001; Ali Kalefa El-ghali, 2005; Nagendra et al., 2011; Zakharov et al., 2011; de Winter et al., 2017), but only have biostratigraphic age constraints. Mt. Katmai and San Juan Islands sample regions are acknowledged to be Late Maastrichtian and Early Maastrichtian (Wartes et al., 2013; Peecook and Sidor, 2015), respectively, but based on Δ_{47} and $^{87}Sr/^{86}Sr$ values appear to be at least partially thermally reset and potentially diagenetically altered. Pee Dee River and Scania sample regions are known to span the Late Campanian to Early Maastrichtian (Christensen, 1998; Meyer et al., *in review*), well outside the eruptive window of the Deccan Traps, and therefore expectedly exhibit negligible [Hg]. For comparison, four modern bivalve taxa collected from Sabin Point Park, Rhode Island are also depicted. A first attempt is made at defining a global [Hg] background (horizontal dashed line, [Hg] = 5 ng g^{-1}) defined from the median of [Hg] values from all sample regions, past and modern (median = 3.88 ng g^{-1} + 1 S.E. = 1.02 ng g^{-1}).

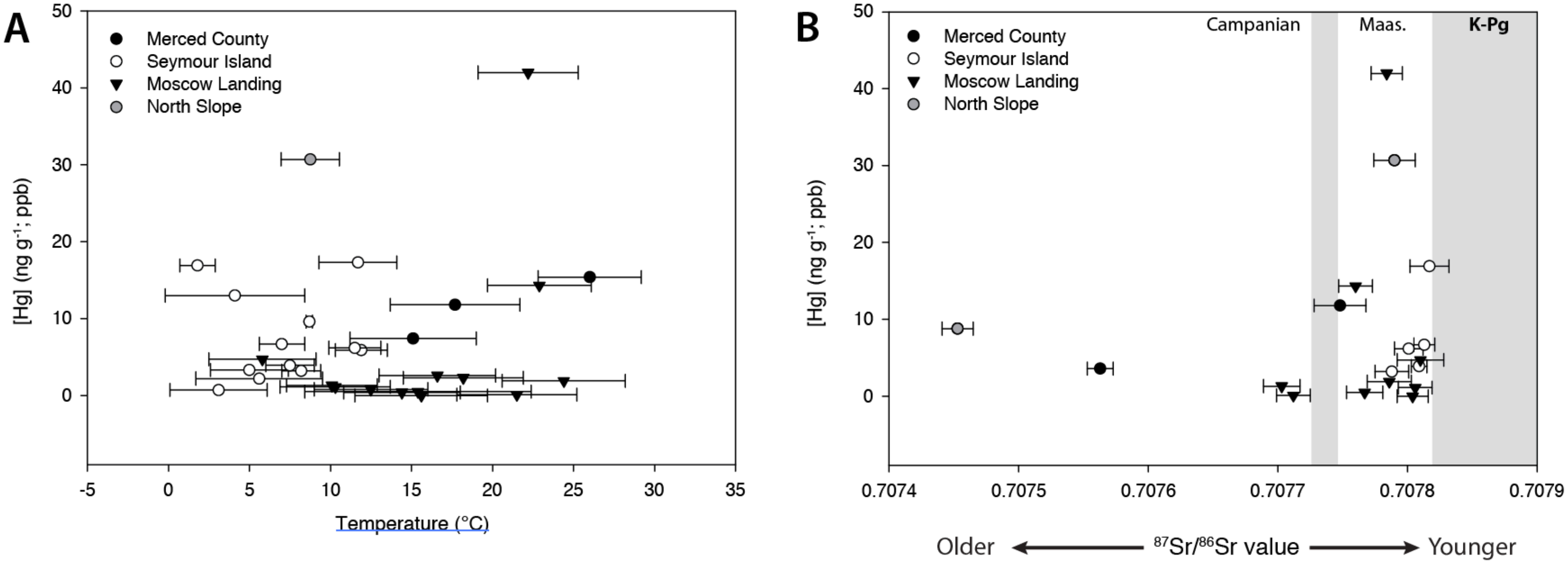

Figure 29. Plots of calculated Δ_{47}-derived coastal marine temperatures (A) and measured $^{87}Sr/^{86}Sr$ values (B) against [Hg] in the same specimens from the Merced County (California), Seymour Island (Antarctica), Moscow Landing (Alabama), and North Slope (Alaska) sample regions. There are no observed trends between [Hg] and either temperatures or $^{87}Sr/^{86}Sr$ values. On the basis of $^{87}Sr/^{86}Sr$ values exclusively, samples follow a relative age relationship subject to large analytical uncertainties on each measurement and the long residence time of strontium in seawater (~2.5 Ma; Dickin, 2005). These factors result in non-uniquenesses between samples of the Late Maastrichtian, and particularly indistinguishable near the K-Pg boundary. Although there is a paucity of data from the Merced County and North Slope regions, across all four regions the highest [Hg] values occur near the K-Pg boundary. Where independent age constraints and known stratigraphic position are available (Moscow Landing and Seymour Island regions), measured [Hg] values peak immediately prior to the K-Pg boundary. These data are suggestive of a global signal of elevated [Hg] from records of biogenic carbonate.

Table 12. Latitude/Longitude of sample locations

Locality Identifier	**Modern Latitude** (°N)	**Modern Longitude** (°W)	**Paleolatitude**[†]
AF-KAG	58.92691	-153.9989	~62 °N[‡]
IL-KAG	59.01667	-153.96533	~62 °N[‡]
MK-KAG	58.88942	-154.05224	~62 °N[‡]
EL-SCH	69.40365	-151.90194	~83–85 °N[*]
OP-PRI	70.08333	-151.41667	~83–85 °N[*]
WI-NAN	48.71139	-123.00917	~30 °N[**]
SI-NAN	48.75023	-122.91	~30 °N[**]
MC-MOR	36.95583	-120.8775	~21 ± 5 °N[***]
SC-BAL	56.16611	14.35806	46 °N
DT-DAK	25.535	30.55444	8 °N
KO-DAK	25.48639	30.55278	8 °N
LI-FEZ	26.54778	12.73694	10.5 °N
IN-KAL	11.23778	79.29056	~35 °S
BJ-VES	-38.10292	-68.38903	~43 °S[****]

[†] Paleolatitude determined after Torsvik et al. (2012) via www.paleolatitude.org

[‡] Paleolatitude estimated in Pasch and May (1997).

[*] Paleolatitdue estimated by Salazar-Jaramillo et al. (2015).

[**] Paleolatitude estimated by Peecook and Sidor (2015).

[***] Paleolatitude estimated by Kodama and Ward (2001).

[****] Paleolatitude estimated by de Winter et al. (2017).

Table 13. Measured oxygen, carbon, and clumped isotopic results

*A) Raw Data – Brand Parameters**

Analysis Date	Name	BRd13C	BRse13	BRd18O	BRse18	BRD47	BRse47	BRD48	BRD49	D47rfac
7/7/17	AF-KAG-GLYa	0.808	1.1	33.293	2.6	-0.335	9.9	-2.369	3.963	0.675
7/7/17	EL-SCH-BIVa	1.985	0.9	37.496	2.3	-0.185	10.8	0.679	-5.695	0.684
7/7/17	IL-KAG-BIVa	2.359	0.9	36.944	2.5	-0.199	13.2	0.66	-7.228	0.675
7/4/17	LI-FEZ-UNGa	1.779	0.8	35.878	1.9	-0.229	12.2	-1.956	-2.018	0.688
7/9/17	LI-FEZ-UNGa	1.526	1.2	35.151	2.7	-0.275	9.7	-1.548	-2.116	0.668
7/14/17	LI-FEZ-UNGa	1.66	1	35.466	2	-0.246	9.9	-0.999	-1.478	0.672
7/7/17	LI-FEZ-UNGb	1.475	1	35.732	2.8	-0.254	11.3	-1.389	-2.662	0.675
7/14/17	LI-FEZ-UNGb	1.402	0.9	35.565	2.1	-0.24	11.1	-0.361	-2.036	0.682
7/23/17	LI-FEZ-UNGb	1.681	0.8	35.704	2	-0.24	11.6	-1.76	-1.686	0.671
7/7/17	MC-GAR-GRYa	2.884	0.9	37.173	1.9	-0.121	9.7	-0.58	-5.894	0.733
7/24/17	MC-GAR-GRYa	3.3	1	37.516	1.6	-0.094	12.9	3.753	-9.98	0.722
7/25/17	MC-GAR-GRYa	3.254	1.4	37.411	1.9	-0.128	10	5.689	-15.778	0.693
7/13/17	MC-GAR-GRYb	1.471	1.2	36.35	3.2	-0.167	10.9	-2.39	-1.692	0.731
7/24/17	MC-GAR-GRYb	1.874	0.8	36.546	1.5	-0.141	9.7	1.355	-4.566	0.74
7/25/17	MC-GAR-GRYb	1.902	1	36.747	2	-0.175	8.6	0.662	-3.772	0.701
7/2/17	MC-MOR-GLYa	0.809	0.9	32.337	2.2	-0.378	9.1	-2.472	4.271	0.657
7/9/17	MC-MOR-GLYa	0.71	0.8	32.123	2.5	-0.421	10	-2.94	5.017	0.622

7/2/17	MC-MOR-GLYb	-5.421	0.9	38.319	1.7	-0.333	10.9	-0.45	-1.607	0.706
7/8/17	MC-MOR-GLYb	-5.806	0.7	38.255	2.3	-0.164	10.5	-5.656	0.054	0.885
7/9/17	MC-MOR-GLYb	-6.077	0.9	38.155	1.9	-0.322	12.1	0.013	-1.428	0.737
7/13/17	MC-MOR-GLYb	-6.246	0.9	38.293	2.1	-0.288	9.7	-0.107	-0.205	0.764
7/23/17	MC-MOR-GLYb	-6.052	1	38.57	2.2	-0.347	12	0.876	0.111	0.693
7/13/17	MC-MOR-GLYd	-1.104	0.9	38.445	2	-0.235	10.7	-0.427	-3.155	0.675
7/24/17	MC-MOR-GLYd	-0.48	0.8	38.989	1.7	-0.181	9.4	2.204	-7.217	0.697
7/25/17	MC-MOR-GLYd	-0.801	0.8	38.814	2	-0.188	10.1	1.16	-6.365	0.704
7/4/17	MC-PRB-EXOa	0.813	0.8	37.53	2.5	-0.205	10.2	-1.129	-5.299	0.693
7/8/17	MK-KAG-BIVa	-11.502	0.9	34.252	3	-0.434	9.5	-9.182	12.544	0.866
7/11/17	MK-KAG-BIVa	-11.516	0.8	34.432	1.8	-0.641	12	-2.167	15.771	0.655
7/2/17	MK-KAG-GLYa	-13.668	0.8	27.72	2.5	-0.892	12.7	-4.595	28.807	0.634
7/2/17	MK-KAG-GLYd	1.489	0.8	33.014	2	-0.354	8.4	-3.546	4.307	0.646
7/2/17	OP-PRI-CYRa	0.33	1	36.688	3	-0.201	10	-1.661	-1.751	0.732
7/8/17	OP-PRI-CYRa	0.426	0.8	36.571	2.5	-0.02	10.5	-7.284	-1.156	0.912
7/11/17	OP-PRI-CYRa	0.044	0.9	36.57	2.2	-0.17	9.4	-0.897	-3.496	0.76
7/13/17	OP-PRI-CYRa	0.452	0.9	37.065	2.2	-0.177	9.7	1.742	-5.397	0.729
7/14/17	OP-PRI-CYRa	0.28	0.8	36.702	1.6	-0.17	11.1	-1.105	-2.128	0.751
7/24/17	OP-PRI-CYRa	0.264	1	36.681	1.7	-0.172	9.3	-0.33	-3.26	0.749
7/6/17	SC-BAL-BELa	1.006	1.1	40.256	2.4	-0.113	10.7	0.872	-12.086	0.709
7/13/17	SC-BAL-BELa	0.73	0.9	39.845	2.2	-0.135	11.2	2.537	-8.508	0.688
7/23/17	SC-BAL-BELa	0.622	1	39.704	2.2	-0.111	11.9	1.567	-9.195	0.718

7/8/17	SC-BAL-BELb	1.496	0.9	39.161	5.8	0.273	12.2	-19.971	5.53	1.108
7/11/17	SC-BAL-BELb	1.097	0.8	39.628	2.1	-0.115	13.1	1.3	-10.514	0.704
7/14/17	SC-BAL-BELb	1.196	1	39.458	2.7	-0.079	11.3	-2.325	-6.537	0.742
7/23/17	SC-BAL-BELb	1.098	1	39.643	2.4	-0.102	10.9	0.664	-8.076	0.716

7/4/17	SC-BAL-BIVa	2.102	0.7	38.516	1.6	-0.113	11.8	-0.867	-8.322	0.726
7/9/17	SC-BAL-BIVa	2.211	1	38.917	2.7	-0.086	11	-0.273	-9.256	0.739
7/14/17	SC-BAL-BIVa	2.466	0.8	39.048	2.1	-0.038	11.5	-2.487	-6.49	0.76
7/23/17	SC-BAL-BIVa	2.287	20.8	38.803	136.8	-0.488	418.3	1.593	-8.172	0.325

7/4/17	SI-NAN-VANa	2.824	0.9	36.777	2	-0.222	11.1	-1.365	-5.849	0.645
7/9/17	SI-NAN-VANa	2.732	0.8	36.567	2.2	-0.255	9.9	-0.634	-5.605	0.62

7/4/17	Wi-NAN-VANa	-1.889	0.8	34.73	1.8	-0.394	11.8	-2.277	3.408	0.648

Carbonate Standards

7/1/18	Carrara1	1.91	1.2	36.833	3.1	-0.511	9.9	-1.967	-4.022	0.4
7/1/18	Carrara2	1.974	1.1	36.928	3.3	-0.504	10.4	-1.995	-3.023	0.402
7/5/18	Carrara3	0.813	0.8	37.53	2.5	-0.205	10.2	-1.129	-5.299	0.693
7/8/18	Carrara4	1.842	0.7	36.821	2	-0.496	8.2	-0.732	-5.278	0.397
7/13/18	Carrara5	2.06	0.9	37.249	2.1	-0.462	10	-0.258	-5.355	0.397
7/17/18	Carrara6	1.961	0.9	36.913	2.1	-0.481	9.7	0.048	-4.494	0.39
7/21/18	Carrara7	1.999	1	37.008	2.5	-0.469	9	0.591	-2.7	0.398
7/24/18	Carrara8	1.977	0.7	36.889	1.6	-0.487	10.7	-0.889	-4.529	0.386

7/1/18	Ooids1	4.651	1.2	39.103	2.6	-0.1	11.5	1.402	-15.898	0.675
7/3/18	Ooids2	4.787	0.7	39.555	2.4	-0.084	11.1	-0.73	-14.59	0.659
7/6/18	Ooids3	4.183	1	38.166	2.4	-0.045	9.4	-0.128	-13.698	0.749

7/11/18	Ooids4	4.95	0.8	39.685	2.1	-0.026	12.1	1.453	-13.324	0.689
7/15/18	Ooids5	4.828	1	39.466	2.1	-0.045	10.1	0.704	-12.897	0.679
7/19/18	Ooids6	4.765	0.9	39.676	2.1	-0.037	10.3	2.428	-14.984	0.683
7/23/18	Ooids7	4.79	0.7	39.451	2.3	-0.054	11.9	9.355	-11.232	0.67

Gas Standards

7/2/17	2xEV 25C	-41.282	1.1	71.542	2.8	-0.108	10.4	10.828	-28.935
7/5/17	2xEV 25C	-41.12	1	71.891	3.1	-0.135	10.1	12.508	-27.745
7/8/17	2xEV 25C	-41.309	0.7	71.022	2.2	-0.122	11.5	12.897	-30.399
7/12/17	2xEV 25C	-41.238	0.8	71.337	1.9	-0.086	11.2	14.109	-27.92
7/18/17	2xEV 25C	-41.355	1	71.247	1.8	-0.122	11.9	14.736	-30.243
7/23/17	2xEV 25C	-41.306	0.9	71.568	2	-0.144	11.1	15.105	-27.211
7/26/17	2XEV 25C	-41.438	0.9	70.602	1.7	-0.134	11.1	15.191	-26.987
6/30/17	2xEV HG	-41.203	0.8	57.905	2.3	-1.341	10.1	5.519	2.098
7/7/17	2xEV HG	-41.202	0.8	57.284	2.7	-1.394	8.4	6.88	0.604
7/13/17	2xEV HG	-41.147	0.9	61.454	2.2	-1.273	10.5	10.137	-9.531
7/20/17	2xEV HG	-41.579	1.6	50.175	2.5	-1.575	11.1	**9.337**	8.825
6/30/17	2xEV25C	-41.436	0.7	71.548	1.9	-0.131	7.3	10.688	-27.731
7/1/17	AAS25C	-41.488	0.9	18.059	2.7	-1.502	10.4	-8.822	87.441
6/30/17	Carrara HG	1.912	1.3	29.957	2.5	-1.022	11.9	-3.116	10.408
7/5/17	Carrara HG	1.787	1.1	36.507	2.2	-0.757	11.4	-2.456	-2.862
7/16/17	Carrara HG	1.938	1	30.963	2.1	-0.975	9.9	-2.283	7.229
7/22/17	Carrara HG	1.867	1	34.988	2.2	-0.862	11	-1.543	-0.99
7/25/17	Carrara HG	1.919	1	35.811	2.7	-0.862	9.9	-1.975	0.059
7/10/17	Carrara HG	1.89	0.9	28.821	1.9	-0.969	9	-5.404	12.246
7/1/17	EVAP 25C	-41.243	0.9	47.253	2.5	-0.748	9.6	1.868	23.693
7/3/17	EVAP 25C	-41.198	1	46.99	2.6	-0.745	10.8	3.138	18.648
7/9/17	EVAP 25C	-41.353	0.8	47.047	1.5	-0.773	11	3.699	19.39
7/14/17	EVAP 25C	-41.249	0.7	47.188	2.2	-0.755	9.3	3.92	20.084
7/16/17	EVAP 25C	-41.365	1.3	46.323	2.5	-0.748	11	**6.633**	-3.571
7/24/17	EVAP 25C	-41.117	0.8	47.656	1.5	-0.79	11.3	4.696	18.423
7/6/17	Evap HG	-41.282	0.7	43.674	2.7	-1.715	10.1	1.504	27.751

7/11/17	EVAP HG	-41.023	1.1	41.046	2.2	-1.83	11.1	0.607	34.916
7/4/17	MATH HG	-3.681	1.1	31.216	2.7	-1.103	9.8	-4.791	15.549
7/1/17	MDIW 25C	-41.155	0.8	30.124	2	-1.163	11.6	-3.966	59.788
7/4/17	MDIW 25C	-40.919	0.9	31.312	3	-1.149	11.3	-3.698	55.229
7/7/17	MDIW 25C	4.618	0.7	31.99	1.7	0.037	10.6	-2.986	1.53
7/11/17	MDIW 25C	-41.018	0.9	30.776	2.7	-1.222	11.7	-4.051	59.096
7/15/17	MDIW 25C	-41.176	0.7	32.135	2.4	-1.211	11.3	-3.538	55.351
7/19/17	MDIW 25C	-41.398	0.8	31.65	1.6	-1.236	11.2	-2.238	53.9
7/20/17	MDIW 25C	-41.246	0.8	32.195	2.4	-1.246	10	-3.475	55.239
7/22/17	MDIW 25C	-41.132	0.9	32.336	2.7	-1.22	12.9	-2.583	54.77
7/1/17	MDIW HG	-41.009	1.2	29.141	2.9	-2.114	12.2	-4.96	63.228
7/24/17	MDIW HG2	-41.19	0.8	29.999	1.4	-2.223	11.6	0.113	56.849
6/30/17	MDIW25C	-41.221	0.9	30.553	2.2	-1.151	12	-3.127	58.568
7/9/17	Ooids HG	4.873	1.3	35.2	2.4	-0.797	10.6	-2.811	-1.765
7/17/17	Ooids HG	4.537	0.9	25.36	2.1	-0.154	11.7	-3.285	12.022
7/18/17	Ooids HG	4.499	1	27.784	2	-0.958	11.9	-5.059	8.291
7/21/17	Ooids HG	4.497	0.9	34.784	1.8	-0.727	10.6	**3.595**	-3.742
7/24/17	Ooids HG	4.41	0.8	24.498	1.9	-1.044	9	-6.551	16.952
7/26/17	Ooids HG	4.571	0.9	31.78	1.8	-0.701	12.9	-2.455	-0.543
7/14/17	Ooids HG	4.97	0.8	35.604	2.1	-0.724	10.1	-0.066	-7.832
6/30/17	OoidsHG	4.678	1.4	36.23	2.7	-0.799	13	-0.571	-5.945

**Red text denotes samples that were discarded due ^{87}Sr/^{86}Sr and Δ_{47} values that indicate alteration , orange text corresponds to samples interpreted to have been thermal reset, and purple text indicates a replicate that was discarded due to analytical issues.*

B) Raw Data – Santrock Parameters

Analysis Date	Name	d13C	se13	d18O	se18	d45	d46	d47	d48	d49	D47	se47	D48	D49	D47rfac
7/7/17	AF-KAG-GLYa	0.8	1.1	33.293	2.6	4.161	-1.619	2.359	-5.596	5.211	-0.332	9.9	-2.369	3.97	0.699
7/7/17	EL-SCH-BIVa	1.982	0.9	37.496	2.3	5.406	2.44	7.804	5.57	4.836	-0.184	10.8	0.679	-5.692	0.706

7/7/17	IL-KAG-BIVa	2.355	0.9	36.944	2.5	5.738	1.908	7.607	4.483	2.593	-0.197	13.2	0.66	-7.224	0.698
7/4/17	LI-FEZ-UNGa	1.773	0.8	35.878	2	5.158	0.878	5.96	-0.203	5.201	-0.226	12.2	-1.956	-2.013	0.712
7/9/17	LI-FEZ-UNGa	1.52	1.2	35.151	2.7	4.897	0.176	4.95	-1.197	3.44	-0.273	9.7	-1.548	-2.11	0.69
7/14/17	LI-FEZ-UNGa	1.654	1	35.466	2	5.033	0.481	5.42	-0.039	4.827	-0.244	9.9	-0.999	-1.473	0.695
7/7/17	LI-FEZ-UNGb	1.47	1	35.732	2.8	4.868	0.736	5.495	0.082	3.965	-0.252	11.3	-1.389	-2.657	0.698
7/14/17	LI-FEZ-UNGb	1.397	0.9	35.565	2.1	4.795	0.575	5.274	0.789	4.198	-0.238	11.1	-0.361	-2.031	0.705
7/23/17	LI-FEZ-UNGb	1.676	0.9	35.704	2	5.061	0.71	5.682	-0.343	5.1	-0.238	11.6	-1.76	-1.681	0.693
7/7/17	MC-GAR-GRYa	2.879	0.9	37.173	1.9	6.238	2.131	8.422	3.684	4.911	-0.119	9.7	-0.58	-5.889	0.757
7/24/17	MC-GAR-GRYa	3.296	1	37.517	1.6	6.64	2.463	9.195	8.704	1.858	-0.092	12.9	3.753	-9.976	0.746
7/25/17	MC-GAR-GRYa	3.249	1.4	37.411	1.9	6.593	2.361	9.011	10.444	-4.256	-0.126	10	5.689	-15.773	0.716
7/13/17	MC-GAR-GRYb	1.467	1.2	36.35	3.2	4.886	1.333	6.19	0.271	6.137	-0.165	10.9	-2.39	-1.688	0.756
7/24/17	MC-GAR-GRYb	1.87	0.8	36.546	1.5	5.27	1.523	6.801	4.407	4.024	-0.139	9.7	1.355	-4.562	0.765
7/25/17	MC-GAR-GRYb	1.898	1	36.747	2	5.303	1.718	6.994	4.102	5.243	-0.173	8.6	0.662	-3.768	0.724
7/2/17	MC-MOR-GLYa	0.8	0.9	32.337	2.2	4.13	-2.542	1.373	-7.536	3.66	-0.374	9.1	-2.472	4.28	0.682
7/9/17	MC-MOR-GLYa	0.701	0.8	32.123	2.5	4.031	-2.749	1.023	-8.413	3.89	-0.417	10	-2.94	5.026	0.646
7/2/17	MC-MOR-GLYb	-5.414	0.9	38.319	1.7	-1.511	3.219	1.266	5.995	3.099	-0.336	10.9	-0.45	-1.614	0.724
7/8/17	MC-MOR-GLYb	-5.799	0.7	38.255	2.3	-1.874	3.157	0.999	0.632	4.256	-0.168	10.5	-5.656	0.047	0.906
7/9/17	MC-MOR-GLYb	-6.07	0.9	38.155	1.9	-2.132	3.06	0.479	6.142	2.301	-0.325	12.1	0.013	-1.435	0.757
7/13/17	MC-MOR-GLYb	-6.238	0.9	38.293	2.1	-2.286	3.192	0.484	6.288	3.625	-0.292	9.7	-0.107	-0.212	0.783
7/23/17	MC-MOR-GLYb	-6.044	1	38.57	2.2	-2.095	3.46	0.885	7.815	4.674	-0.351	12	0.876	0.103	0.711
7/13/17	MC-MOR-GLYd	-1.103	0.9	38.445	2	2.541	3.35	5.687	6.281	6.136	-0.236	10.7	-0.427	-3.156	0.696
7/24/17	MC-MOR-GLYd	-0.478	0.8	38.989	1.7	3.145	3.876	6.885	9.988	3.711	-0.182	9.4	2.204	-7.219	0.718

7/25/17	MC-MOR-GLYd	-0.799	0.7	38.814	2	2.838	3.706	6.393	8.595	3.912	-0.189	10.1	1.16	-6.367	0.724
7/4/17	MC-PRB-EXOa	0.811	0.8	37.53	2.5	4.308	2.471	6.678	3.813	4.127	-0.205	10.2	-1.129	-5.297	0.715
7/8/17	MK-KAG-BIVa	-11.493	0.9	34.251	3	-7.35	-0.72	-8.716	-10.608	3.192	-0.438	9.5	-9.182	12.536	0.887
7/11/17	MK-KAG-BIVa	-11.508	0.8	34.431	1.8	-7.357	-0.546	-8.759	-3.256	6.724	-0.645	12	-2.167	15.763	0.672
7/2/17	MK-KAG-GLYa	-13.667	0.8	27.72	2.5	-9.601	-7.028	-17.624	-18.538	4.264	-0.893	12.7	-4.595	28.805	0.654
7/2/17	MK-KAG-GLYd	1.48	0.8	33.014	2	4.79	-1.887	2.723	-7.302	5.696	-0.35	8.4	-3.546	4.316	0.67
7/2/17	OP-PRI-CYRa	0.328	1	36.688	3	3.827	1.657	5.382	1.65	5.587	-0.2	10	-1.661	-1.749	0.755
7/8/17	OP-PRI-CYRa	0.423	0.9	36.571	2.5	3.913	1.544	5.542	-4.215	6.056	-0.019	10.5	-7.284	-1.154	0.939
7/11/17	OP-PRI-CYRa	0.042	0.9	36.57	2.2	3.555	1.542	5.019	2.187	3.315	-0.169	9.4	-0.897	-3.494	0.784
7/13/17	OP-PRI-CYRa	0.45	0.9	37.065	2.2	3.954	2.021	5.897	5.795	2.766	-0.176	9.7	1.742	-5.395	0.753
7/14/17	OP-PRI-CYRa	0.278	0.8	36.702	1.6	3.78	1.67	5.378	2.235	5.184	-0.169	11.1	-1.105	-2.126	0.774
7/24/17	OP-PRI-CYRa	0.262	1	36.681	1.7	3.765	1.65	5.34	2.972	3.988	-0.171	9.3	-0.33	-3.258	0.772
7/6/17	SC-BAL-BELa	1.008	1.1	40.256	2.4	4.581	5.102	9.651	11.111	2.715	-0.114	10.7	0.872	-12.088	0.729
7/13/17	SC-BAL-BELa	0.732	0.9	39.845	2.2	4.308	4.705	8.956	11.993	5.276	-0.136	11.2	2.537	-8.51	0.709
7/23/17	SC-BAL-BELa	0.623	1	39.704	2.2	4.201	4.569	8.735	10.74	4.197	-0.111	11.9	1.567	-9.196	0.739
7/8/17	SC-BAL-BELb	1.496	0.9	39.161	5.8	5.003	4.046	9.436	-12.024	18.945	0.273	12.3	-19.971	5.53	1.138
7/11/17	SC-BAL-BELb	1.098	0.8	39.628	2	4.645	4.497	9.119	10.325	3.19	-0.115	13.1	1.3	-10.515	0.726
7/14/17	SC-BAL-BELb	1.196	1	39.458	2.7	4.732	4.333	9.083	6.339	6.993	-0.079	11.3	-2.325	-6.537	0.765
7/23/17	SC-BAL-BELb	1.099	1	39.643	2.4	4.646	4.511	9.146	9.712	5.691	-0.103	10.9	0.664	-8.078	0.736
7/4/17	SC-BAL-BIVa	2.1	0.6	38.517	1.6	5.55	3.426	9	5.99	4.271	-0.112	11.8	-0.867	-8.32	0.749
7/9/17	SC-BAL-BIVa	2.21	1	38.917	2.7	5.666	3.812	9.529	7.364	4.208	-0.085	11	-0.273	-9.255	0.763

7/14/17	SC-BAL-BIVa	2.464	0.8	39.048	2.1	5.909	3.939	9.955	5.387	7.522	-0.037	11.5	-2.487	-6.488	0.784
7/23/17	SC-BAL-BIVa	2.285	21	38.803	136.8	5.733	3.703	9.088	9.038	5.143	-0.488	418.2	1.593	-8.17	0.337
7/4/17	SI-NAN-VANa	2.819	0.9	36.778	2	6.168	1.749	7.871	2.13	4.129	-0.219	11.1	-1.365	-5.844	0.668
7/9/17	SI-NAN-VANa	2.726	0.8	36.567	2.2	6.075	1.546	7.54	2.457	3.876	-0.253	9.9	-0.634	-5.6	0.641
7/4/17	Wi-NAN-VANa	-1.892	0.8	34.73	1.8	1.68	-0.238	1.105	-2.752	4.735	-0.393	11.8	-2.277	3.41	0.669

Carbonate Standards

7/1/18	Carrara1	1.906	1.2	36.834	3.1	5.313	1.801	6.747	1.631	5.166	-0.51	9.9	-1.967	-4.019	0.419
7/1/18	Carrara2	1.97	1.1	36.928	3.3	5.377	1.892	6.911	1.785	6.422	-0.502	10.4	-1.995	-3.019	0.423
7/5/18	Carrara3	0.811	0.8	37.53	2.5	4.308	2.471	6.678	3.813	4.127	-0.205	10.2	-1.129	-5.297	0.715
7/8/18	Carrara4	1.838	0.7	36.821	2	5.249	1.788	6.684	2.845	3.805	-0.494	8.2	-0.732	-5.275	0.414
7/13/18	Carrara5	2.057	0.9	37.249	2.1	5.468	2.202	7.354	4.151	4.777	-0.46	10	-0.258	-5.351	0.415
7/17/18	Carrara6	1.957	0.9	36.913	2.1	5.364	1.877	6.906	3.806	4.896	-0.479	9.7	0.048	-4.49	0.407
7/21/18	Carrara7	1.995	1	37.008	2.5	5.403	1.969	7.048	4.535	6.928	-0.467	9	0.591	-2.697	0.416
7/24/18	Carrara8	1.973	0.7	36.889	1.6	5.378	1.854	6.892	2.82	4.83	-0.485	10.7	-0.889	-4.525	0.402
7/1/18	Ooids1	4.647	1.2	39.103	2.6	7.96	3.997	12.074	9.423	0.262	-0.098	11.5	1.402	-15.894	0.702
7/3/18	Ooids2	4.783	0.7	39.555	2.4	8.103	4.434	12.671	8.151	2.6	-0.082	11.1	-0.73	-14.587	0.681
7/6/18	Ooids3	4.178	1	38.167	2.3	7.49	3.092	10.746	6.066	0.226	-0.043	9.4	-0.128	-13.694	0.774
7/11/18	Ooids4	4.947	0.8	39.685	2.1	8.26	4.559	13.017	10.605	4.301	-0.025	12.1	1.453	-13.321	0.711
7/15/18	Ooids5	4.824	1	39.466	2.1	8.138	4.348	12.661	9.424	4.191	-0.044	10.1	0.704	-12.893	0.701
7/19/18	Ooids6	4.761	0.9	39.676	2.1	8.086	4.551	12.817	11.572	2.41	-0.035	10.3	2.428	-14.981	0.706
7/23/18	Ooids7	4.786	0.7	39.452	2.3	8.102	4.334	12.602	18.122	5.819	-0.052	11.9	9.355	-11.229	0.692
7/1/18	Carrara1	1.906	1.2	36.834	3.1	5.313	1.801	6.747	1.631	5.166	-0.51	9.9	-1.967	-4.019	0.419

Gas Standards

				6/30/17										
6/30/17	2xEV25C	-41.436	0.7	71.548	1.9	-34.18	35.216	-2.04	83.126	2.702	-0.131	7.3	10.688	-27.731
7/2/17	2xEV 25C	-41.282	1.1	71.542	2.8	-34.036	35.211	-1.867	83.266	1.612	-0.108	10.4	10.828	-28.935
7/5/17	2xEV 25C	-41.12	1	71.891	3.1	-33.872	35.548	-1.401	85.772	3.661	-0.135	10.1	12.508	-27.745
7/8/17	2xEV 25C	-41.309	0.7	71.022	2.2	-34.078	34.709	-2.402	84.43	-0.897	-0.122	11.5	12.897	-30.399
7/12/17	2xEV 25C	-41.238	0.8	71.337	1.9	-34.001	35.012	-1.996	86.365	2.32	-0.086	11.2	14.109	-27.92
7/12/18	2xEV 25C	-41.238	0.8	71.337	1.9	-34.001	35.012	-1.996	86.365	2.32	-0.086	11.2	14.109	-27.92
7/18/17	2xEV 25C	-41.355	1	71.247	1.8	-34.114	34.926	-2.235	86.854	-0.365	-0.122	11.9	14.736	-30.243
7/23/17	2xEV 25C	-41.306	0.9	71.568	2	-34.057	35.236	-1.902	87.901	3.414	-0.144	11.1	15.105	-27.211
7/7/17	2xEV HG	-41.203	0.8	57.905	2.3	-34.413	22.048	-15.945	50.348	7.563	-1.341	10.1	5.519	2.098
7/20/17	2xEV HG	-41.202	0.8	57.284	2.7	-34.432	21.449	-16.584	50.537	4.881	-1.394	8.4	6.88	0.604
6/30/17	2xEV HG	-41.579	1.6	50.175	2.5	-35.022	14.586	-23.869	38.997	-0.836	-1.575	11.1	**9.337**	8.825
7/1/17	AAS25C	-41.488	0.9	18.059	2.7	-36.014	-16.412	-54.111	-41.088	12.257	-1.502	10.4	-8.822	87.441
6/30/17	Carrara HG	1.912	1.3	29.957	2.5	5.084	-4.837	-0.557	-12.736	6.25	-1.022	11.9	-3.116	10.408
7/5/17	Carrara HG	1.787	1.1	36.507	2.2	5.187	1.486	6.058	0.51	5.58	-0.757	11.4	-2.456	-2.862
7/16/17	Carrara HG	1.938	1	30.963	2.1	5.143	-3.866	0.509	-9.982	5.071	-0.975	9.9	-2.283	7.229
7/22/17	Carrara HG	1.867	1	34.988	2.2	5.211	0.019	4.529	-1.504	4.598	-0.862	11	-1.543	-0.99
7/25/17	Carrara HG	1.919	1	35.811	2.7	5.288	0.814	5.393	-0.349	7.305	-0.862	9.9	-1.975	0.059
7/10/17	Carrara HG	1.89	0.9	28.821	1.9	5.026	-5.933	-1.647	-17.172	5.836	-0.969	9	-5.404	12.246
7/1/17	EVAP 25C	-41.243	0.9	47.253	2.5	-34.804	11.767	-25.499	25.586	8.611	-0.748	9.6	1.868	23.693
7/3/17	EVAP 25C	-41.198	1	46.99	2.6	-34.771	11.514	-25.702	26.371	3.183	-0.745	10.8	3.138	18.648
7/9/17	EVAP 25C	-41.353	0.8	47.047	1.5	-34.914	11.568	-25.827	27.055	3.86	-0.773	11	3.699	19.39
7/14/17	EVAP 25C	-41.249	0.7	47.188	2.2	-34.812	11.704	-25.574	27.558	4.924	-0.755	9.3	3.92	20.084
7/16/17	EVAP 25C	-41.365	1.3	46.323	2.5	-34.95	10.869	-26.5	28.634	-20.121	-0.748	11	6.633	-3.571
7/24/17	EVAP 25C	-41.117	0.8	47.656	1.5	-34.673	12.157	-25.035	29.272	4.322	-0.79	11.3	4.696	18.423

7/6/17	Evap HG	-41.282	0.7	43.674	2.7	-34.96	8.312	-29.87	18.222	5.657	-1.715	10.1	1.504	27.751
7/11/17	EVAP HG	-41.023	1.1	41.046	2.2	-34.806	5.776	-32.218	12.2	7.846	-1.83	11.1	0.607	34.916
7/4/17	MATH HG	-3.681	1.1	31.216	2.7	-0.118	-3.633	-4.792	-12.009	8.186	-1.103	9.8	-4.791	15.549
7/1/17	MDIW 25C	-41.155	0.8	30.124	2	-35.295	-4.766	-42.046	-13.437	10.388	-1.163	11.6	-3.966	59.788
7/4/17	MDIW 25C	-40.919	0.9	31.312	3	-35.034	-3.618	-40.68	-10.895	8.612	-1.149	11.3	-3.698	55.229
7/7/17	MDIW 25C	4.618	0.7	31.99	1.7	7.691	-2.869	5.129	-8.699	4.055	0.037	10.6	-2.986	1.53
7/15/17	MDIW 25C	-41.176	0.7	32.135	2.4	-35.248	-2.825	-40.209	-9.16	10.067	-1.211	11.3	-3.538	55.351
7/19/17	MDIW 25C	-41.398	0.8	31.65	1.6	-35.472	-3.294	-40.906	-8.799	7.497	-1.236	11.2	-2.238	53.9
7/20/17	MDIW 25C	-41.246	0.8	32.195	2.4	-35.311	-2.767	-40.252	-8.982	10.005	-1.246	10	-3.475	55.239
7/22/17	MDIW 25C	-41.132	0.9	32.336	2.7	-35.199	-2.631	-39.984	-7.824	9.951	-1.22	12.9	-2.583	54.77
7/1/17	MDIW HG	-41.009	1.2	29.141	2.9	-35.192	-5.715	-43.749	-16.299	11.887	-2.114	12.2	-4.96	63.228
7/24/17	MDIW HG2	-41.19	0.8	29.999	1.4	-35.333	-4.887	-43.216	-9.637	7.303	-2.223	11.6	0.113	56.849
6/30/17	MDIW25C	-41.221	0.9	30.553	2.2	-35.343	-4.352	-41.694	-11.785	9.995	-1.151	12	-3.127	58.568
7/9/17	Ooids HG	4.873	1.3	35.2	2.4	8.037	0.23	7.717	-2.351	7.243	-0.797	10.6	-2.811	-1.765
7/18/17	Ooids HG	4.499	1	27.784	2	7.437	-6.928	-0.15	-18.798	2.493	-0.958	11.9	-5.059	8.291
7/21/17	Ooids HG	4.497	0.9	34.784	1.8	7.67	-0.172	7.011	3.25	4.064	-0.727	10.6	3.595	-3.742
7/24/17	Ooids HG	4.41	0.8	24.498	1.9	7.243	-10.1	-3.575	-26.518	4.559	-1.044	9	-6.551	16.952
7/14/17	Ooids HG	4.97	0.8	35.604	2.1	8.141	0.621	8.286	1.177	2	-0.724	10.1	-0.066	-7.832
6/30/17	OoidsHG	4.678	1.4	36.23	2.7	7.889	1.224	8.547	1.877	4.827	-0.799	13	-0.571	-5.945

**Red text denotes samples that were discarded due ^{87}Sr/^{86}Sr and Δ_{47} values that indicate alteration, orange text corresponds to samples interpreted to have been thermal reset, and purple text indicates a replicate that was discarded due to analytical issues.*

C) *Δ_{47}-derived sea surface temperatures calculated from the mean of sample replicates*

Sample Name	Temperature (°C)	1 S.E.†
Merced County, California		
MC-MOR-GLYa	47.3	4.2†
MC-MOR-GLYb	14.7	5.3
MC-MOR-GLYd	26.0	3.2
MC-GAR-GRYa	17.7	4.0
MC-GAR-GRYb	15.1	3.9
Mount Katmai, Alaska		
MK-KAG-BIVa	-22.2	2.0†
MK-KAG-BIVa	40.3	4.9†
MK-KAG-GLYa	49.5	5.6†
MK-KAG-GLYd	44.2	3.6†
AF-KAG-GLYa	32.3	3.7†
IL-KAG-BIVa	32.3	5.0†
North Slope, Alaska		
EL-SCH-BIVa	28.9	3.9†
OP-PRI-CYRa	8.7	1.8
San Juan Islands, Washington		
SI-NAN-VANa	44.6	4.7†
SI-NAN-VANa	50.3	4.7†
WI-NAN-VANa	43.3	4.9†
Neuquén Basin, Argentina		
BJ-VES-M4u	22.8	0.4
BJ-VES-M5u	15.7	5.0

BJ-VES-M8u	14.6	2.8
BJ-VES-M11u	15.6	1.9
Scania, Sweden		
SC-BAL-BELa	21.4	3.1
SC-BAL-BELb	16.1	3.7
SC-BAL-BIVa	9.5	3.1
Fezzan, Libya		
LI-FEZ-UNGa	32.0	2.4
LI-FEZ-UNGb	32.0	1.2

**Red text indicates a sample that has been determined to be likely diagenetically altered by from combined $^{87}Sr/^{86}Sr$ and Δ_{47} values, orange text denotes a sample that has been thermally reset*

†*Denotes samples where sample replicates were n = 1, and we only report analytical uncertainties* (1*σ*)

D) *Carbonate Δ_{47} Transfer Functions and Applicable Windows*

For Santrock parameters:

Window	StartDay	EndDay	SlopeEGL	SlopeETF	IntETF
1	1	2	0.02544532	1.022503	1.049454
2	1	11	0.02589386	1.040552	1.040854
3	1	22	0.02677028	1.046034	1.034779
4	1	26	0.02706007	1.039659	1.033459

For Brand parameters:

Window	StartDay	EndDay	SlopeEGL	SlopeETF	IntETF
1	1	2	0.02557537	1.00358	1.018551
2	1	11	0.02586502	1.019104	1.011247
3	1	22	0.02673221	1.024904	1.005158
4	1	26	0.02701733	1.016248	1.003417

Table 14. Strontium isotopic results

Sample Name	$^{87}Sr/^{86}Sr$ Ratio	2 S.E.	Approximated Mean LOWESS AGE (Ma; after McArthur et al., 2001)*
Mt. Katmai, Alaska			
MK-KAG-BIVa	0.707338	0.000014	90 to 140*
MK-KAG-GLYa	0.707111	0.000022	149
MK-KAG-GLYb	0.707416	0.000016	85 to 140*
MK-KAG-GLYc	0.707115	0.000014	149
MK-KAG-GLYd	0.707536	0.000018	79
MK-KAG-GLYe	0.707366	0.00001	90 to 140*
AF-KAG-GLYa	0.707487	0.000012	82
IL-KAG-BIVa	0.70665	0.000012	N/A**
North Slope, Alaska			
EL-SCH-BIVa	0.707453	0.000012	84.35
OP-PRI-CYRa	0.70779	0.000016	69.43
Merced County, California			
MC-MOR-GLYa	0.707563	0.00001	78
MC-MOR-GLYb	0.707785	0.000008	69.7
MC-GAR-GRYa	0.707748	0.00002	71.5
MC-MOR-GLYd	0.70776	0.000012	71
San Juan Islands, Washington			
WI-NAN-VANa	0.707069	0.00001	150.7
SI-NAN-VANa	0.706961	0.000014	154.1
Scania, Sweden			
SC-BAL-BIVa	0.707795	0.000014	69.2
SC-BAL-BELa	0.707733	0.00001	72.3
Fezzan, Libya			
LI-FEZ-UNGa	0.707763	0.00002	70.9
LI-FEZ-UNGb	0.707751	0.000014	71.4
Kharga Oasis, Egypt			
KO-DAK-EXOa	0.707814	0.000019	68.1
KO-DAK-EXOb	0.707764	0.000015	70.8

*Measured $^{87}Sr/^{86}Sr$ values correspond to non-unique ages with respect to LOWESS model

**Measured $^{87}Sr/^{86}Sr$ value falls below entirety of LOWESS model curve

Table 15. Mercury concentration results

Sample Name	$^{87}Sr/^{86}Sr$ Ratio	2 S.E.	Approximated Mean LOWESS AGE (Ma; after McArthur et al., 2001)*
Mt. Katmai, Alaska			
MK-KAG-BIVa	0.707338	0.000014	90 to 140*
MK-KAG-GLYa	0.707111	0.000022	149
MK-KAG-GLYb	0.707416	0.000016	85 to 140*
MK-KAG-GLYc	0.707115	0.000014	149
MK-KAG-GLYd	0.707536	0.000018	79
MK-KAG-GLYe	0.707366	0.000010	90 to 140*
AF-KAG-GLYa	0.707487	0.000012	82
IL-KAG-BIVa	0.706650	0.000012	N/A**
North Slope, Alaska			
EL-SCH-BIVa	0.707453	0.000012	84.35
OP-PRI-CYRa	0.707790	0.000016	69.43
Merced County, California			
MC-MOR-GLYa	0.707563	0.000010	78
MC-MOR-GLYb	0.707785	0.000008	69.7
MC-GAR-GRYa	0.707748	0.000020	71.5
MC-MOR-GLYd	0.707760	0.000012	71
San Juan Islands, Washington			
WI-NAN-VANa	0.707069	0.000010	150.7
SI-NAN-VANa	0.706961	0.000014	154.1
Scania, Sweden			
SC-BAL-BIVa	0.707795	0.000014	69.2
SC-BAL-BELa	0.707733	0.000010	72.3
Fezzan, Libya			
LI-FEZ-UNGa	0.707763	0.000020	70.9
LI-FEZ-UNGb	0.707751	0.000014	71.4
Kharga Oasis, Egypt			
KO-DAK-EXOa	0.707814	0.000019	68.1
KO-DAK-EXOb	0.707764	0.000015	70.8

*Measured $^{87}Sr/^{86}Sr$ values correspond to non-unique ages with respect to LOWESS model

**Measured $^{87}Sr/^{86}Sr$ value falls below entirety of LOWESS model curve

Appendix B.

Chapter IV Sample Locality Information

Locality Identifier: BJ-VES ("Baja de Jaguël", *vesicularis*) **Formation:** Jaguël

Samples collected here:

- BJ-VES-M4u: *Pycnodonte vesicularis* (Lamarck)
- BJ-VES-M5u: *Pycnodonte vesicularis* (Lamarck)
- BJ-VES-M8u: *Pycnodonte vesicularis* (Lamarck)
- BJ-VES-M11u: *Pycnodonte vesicularis* (Lamarck)

Location: Baja de Jaguel section described in de Winter et al. (2017)

Collection site description: Refer to de Winter et al. (2017)

Collected by: de Winter et al. (2017)

Sample obtained from: Johan Vellekoop

Locality Identifier: IN-KAL ("India, Kallankurchchi") **Formation:** Kallankurchi

Samples collected here:

- IN-KAL-UNGa: *Agerostrea ungulata* (von Schlotheim)
- IN-KAL-UNGb: *Agerostrea ungulata* (von Schlotheim)

Location: Cauvery Basin, India

Collection site description: No stratigraphic details provided. Stratigraphic sections detailed in Nagendra et al. (2011) and Zakharov et al. (2011).

Collected by: R. Nagendra

Sample obtained from: R. Nagendra

Locality Identifier: KO-DAK ("Kharga Oasis, Dakhla") **Formation:** Dakhla
DT-DAK ("Djebel Ter, Dakhla")

Samples collected here:

- KO-DAK-EXOa: *Exogyra overwegi* (von Buch)
- KO-DAK-EXOb: *Exogyra overwegi* (von Buch)
- DT-DAK-EXOa: *Exogyra overwegi* (von Buch)
- DT-DAK-EXOb: *Exogyra overwegi* (von Buch)

Location: Kharga Oasis region, Egypt

Collection site description: "In green slabs of upper beds of Cretaceous near Christian mummy sepulcher near El Deir, Kharga Oasis, Egypt." Precise locations of El Deir and Djebel Ter outcrops best approximated by the authors at clear outcrops visible in aerial/satellite photography. Sample locality descriptions cross-referenced with Ball (1900) and Tantawy et al. (2001).

Collected by: H.H. Hobbs, Jan. 1913

Sample obtained from: University of Michigan Ruthven Museum of Natural History

Locality Identifier: MK-KAG ("Mount Katmai Quadrangle, Kaguyak") **Formation:** Kaguyak
AF-KAG ("Afognak Quadrangle, Kaguyak")
IL-KAG ("Iliamna Quadrangle, Kaguyak")

Samples collected here:

- MK-KAG-GLYa: *Glycermerita aleuta* (Squires)
- MK-KAG-GLYb: *Glycermerita aleuta* (Squires)
- MK-KAG-GLYc: *Glycermerita aleuta* (Squires)
- MK-KAG-GLYd: *Glycermerita aleuta* (Squires)
- MK-KAG-GLYe: *Glycermerita aleuta* (Squires)
- MK-KAG-BIVa: *Unknown bivalve*
- AF-KAG-GLYa: *Glycermerita aleuta* (Squires)
- IL-KAG-BIVa: *Unknown bivalve*

Location: Mount Katmai region, Alaska Peninsula, Alaska

Collection site description: Coordinates provided by the University of California Museum of Paleontology where available (Berkeley, CA). No additional sampling details available.

Collected by: Elder, Squires, and Magoon (dates unknown)

Sample obtained from: University of California Museum of Paleontology (Berkeley, CA).

Locality Identifier: OP-PRI ("Ocean Point, Prince Creek") **Formation:** Prince Creek
EL-SCH ("Elder, Schrader Bluff") **Formation:** Schrader Bluff

Samples collected here:

- OP-PRI-CYRa: *Cyrtodaria* sp.
- EL-SCH-BIVa: *Unknown bivalve*

Location: North Slope Alaska, OP-PRI: Ocean Point, no additional details available. EL-SCH-BIVa: "On Colville River at center of next bluff E of Umiat Mountain. T1N, R1E, sec. 27, Ctr S line." Locations cross-referenced with Jones and Gryc (1960), Detterman et al. (1963), and Brosgé et al. (1966).

Collection site description: Coordinates provided by the University of California Museum of Paleontology where available (Berkeley, CA).

Collected by: L.Marincovich, 1977 (OP-PRI-CYRa); Elder, 1988 (EL-SCH-BIVa)

Sample obtained from: University of California Museum of Paleontology (Berkeley, CA).

Locality Identifier: MC-MOR ("Merced County, Moreno Fm.") **Formation:** Moreno
MC-GAR ("Merced County, Garzas Sand")

Samples collected here:

- MC-MOR-GLYa: *Glycymeris* sp.
- MC-MOR-GLYb: *Glycymeris* sp.
- MC-MOR-GLYd: *Glycymeris* sp.
- MC-GAR-GRYa: *Gryphaea* sp.
- MC-GAR-GRYb: *Gryphaea* sp.

Location: Merced County, California.

Collection site description: Coordinates provided by the University of California Museum of Paleontology where available (Berkeley, CA).

Collected by: A. Bennison 1937, 1939; L. Briggs 1948

Sample obtained from: University of California Museum of Paleontology (Berkeley, CA).

Locality Identifier: WI-NAN ("Waldron Island") **Formation:** Northumberland Fm.
SI-NAN ("Sucia Island")

Samples collected here:

- WI-NAN-VANa: *Arca vancouverensis* (Meek)
- SI-NAN-VANa: *Arca vancouverensis* (Meek)

Location: San Juan Islands, Washington

Collection site description: Coordinates provided by the University of California Museum of Paleontology where available (Berkeley, CA), and were sampled from the Late Campanian/Early Maastrichtian Nanaimo Group, Northumberland Fm. WI-NAN-VANa was retrieved from Wauldron Island and SI-NAN-VANa was retrieved from Sucia Island.

Collected by: Packard, date unknown (WI-NAN); J.W. Durham, 1948 (SI-NAN)

Sample obtained from: University of California Museum of Paleontology (Berkeley, CA).

Locality Identifier: SC-BAL ("Scania, Balsvik Quarry") **Formation:** Unidentified

Samples collected here:

- SC-BAL-BIVa: *Unknown bivalve*
- SC-BAL-BELa: *Belemnitella* sp.
- SC-BAL-BELb: *Belemnitella* sp.

Location: Scania, Sweden

Collection site description: "Quarry at north end of Ivo Island. Limestone with megafossils." Coordinates provided by the University of California Museum of Paleontology (Berkeley, CA)

Collected by: J.T. Gregory 1960

Sample obtained from: University of California Museum of Paleontology (Berkeley, CA).

Locality Identifier: LI-FEZ ("Libya, Fezzan Region") **Formation:** Unknown

Samples collected here:

- LI-FEZ-UNGa: *Agerostrea ungulata* (von Schlotheim)
- SR-CUS-MESa: *Agerostrea ungulata* (von Schlotheim)

Location: Fezzan region, Libya

Collection site description: "According to donor these oysters came from the Fezzan area in Libya. No other data, but kept because of their quality."coordinates approximated from sample description, and location of outcropping Cretaceous limestones near the road in the Fezzan region by the only significant town/outpost (Murzuq). Sample locality descriptions cross-referenced with Goudarzi (1970) and Ali Falefa El-ghali (2005).

Collected by: Unknown ca. 1967(?)

Sample obtained from: University of California Museum of Paleontology (Berkeley, CA).

Locality Identifier: MOD-PRO ("Modern, Providence") **Formation:** N/A

Samples collected here:

- MOD-PRO-VIRa: *Crassostrea virginica* (Gmelin)
- MOD-PRO-FORa: *Crepidula fornicata* (Linneaus)
- MOD-PRO-DEMa: *Geukensia demissa* (Dillwyn)

- MOD-PRO-BIVa: *Unidentified bivalve*

Location: Sabin Point Park, Providence Rhode Island

Collection site description: Along the northern shore of the park among the large death assemblage comprising the shoreline.

Collected by: K. Meyer, July 2017

CHAPTER V

Conclusions

The research presented in this dissertation explores the use of varied geochemical techniques to provide proxy information regarding: (1) high-latitude atmospheric circulation and aerosol transport from the Pleistocene through the Holocene at the summit of the Greenland ice sheet, (2) mid-latitude coastal marine temperatures of the Late Cretaceous of the North American Atlantic and Gulf Coasts, and (3) a global record of sustained semi-continuous volcanic activity as the primary mechanism behind elevated sea surface temperatures during the K-Pg boundary interval.

Strontium and neodymium isotope compositions of sea salt aerosol and mineral dust from the GISP2 ice core (retrieved from the summit camp of the Greenland ice sheet) revealed evidence of changes in the sourcing of dust to the atmosphere through the Pleistocene, which suggested modes of sustained Arctic Oscillation positive anomalies during glacial intervals and prolonged 'polar vortex' conditions (Chapter II). This observation implies that future climate will likely be subject to enhanced North Atlantic Oscillation positive regimes (antiphased with the Arctic Oscillation Index), causing a greater frequency of tropical cyclones to track through the North Atlantic and impacting American and European coastal areas. Many high latitude potential source areas of mineral dust and sea salt aerosol strontium remain largely uncharacterized in terms of strontium and neodymium isotope compositions, therefore, in order to make more conclusive assessments of synoptic scale atmospheric circulation patterns it is essential to inventory the isotopic compositions of dust, bedrock, and surface water masses in these regions. Other ice core records from the Greenland ice sheet and surrounding Canadian ice caps (e.g. Penny, Barnes, Devon) could offer additional insights into high latitude circulation patterns if strontium and neodymium isotopic records could be produced and compared to the record presented in this work.

The marine temperatures of the Atlantic and Gulf Coasts of North America derived from carbonate clumped isotope paleothermometry of Late Cretaceous fossil mollusk remains are very similar to modern temperature ranges in surface waters at proximal coastal monitoring sites (Gulf temperatures: ~7 – 25 °C during the Late Cretaceous versus ~10 – 29 °C in the modern; Atlantic temperatures: ~3 – 14 °C versus ~2 – 24 °C in the modern; Chapter III). The nearly identical temperature ranges suggest that for a dominantly unglaciated time period (with respect to large continental ice sheets/caps) with elevated atmospheric CO_2 concentrations, the mid-latitude climate response to CO_2 forcing is smaller than anticipated with model projections of future climate and increasing anthropogenic emissions. Given that climate response at the poles is disproportionate with respect to the mid- and low latitudes, these results may further suggest that the high latitudes may accommodate more heat transport and serve as a greater thermal buffer than previously thought, or modern climate may be nearer to 'point of no return' scenario with respect to loss of continental ice sheets. The colder coastal temperatures observed from the New Jersey sites of this study may support the existence of the Gulf Stream current adjacent to North America as early as the Late Cretaceous, further suggesting that North Atlantic circulation patterns at this time period were likely similar to today. These assertions, however, require a larger number of samples from more localities to further define the Late Cretaceous latitudinal thermal gradient and prevent the possibility of sample 'aliasing' of the full range of temperatures at any particular sample site.

The first-ever measured mercury concentrations of fossil mollusk biogenic carbonate covary with elevated carbonate clumped isotope temperatures in the same Late Maastrichtian specimens retrieved from Seymour Island (Antarctica) and the Mississippi Embayment in Alabama (Chapter IV). Five total sample regions provide evidence that further corroborates a global signal of elevated mercury concentrations associated with the Deccan Traps Large Igneous Province (Antarctica, Alabama, Alaska, California, and Egypt). Fossil biogenic carbonate mercury concentrations compared to four modern bivalve specimens from Providence, Rhode Island and indicate a possible global background in marine mollusks (<0.7 to 5 ng g^{-1}). The results of this study support the findings of existing published mercury concentration records from bulk rock and sediment samples showing a global pattern of elevated mercury near the Cretaceous-Paleogene extinction boundary. The pattern we observe in biogenic carbonate in tandem with these other records further supports the Deccan Traps as the primary mechanism for contributing excess environmental mercury to the habitats of the fossil organisms in this study.

The unique application of mercury concentrations in fossilized biogenic carbonate may provide insights into mass extinctions and climatic perturbations throughout the geological record. Biogenic carbonate and other biominerals (e.g. hydroxylapatite) offer potential for directly comparable records of temperature (via carbonate clumped isotope analyses), which could possibly address questions of Hg-cycling dynamics of past environments and paleontological trophic position. Marine organisms at higher trophic positions relative to bivalves and other mollusks would be anticipated to bioaccumulate higher concentrations of Hg(II) and MeHg. Biomineral mercury records may also have utility in modern applications. The observation of significant mercury concentrations (~40 ng g^{-1}) in carbonatite lava deposits (USGS COQ-1) and other igneous geological reference materials raises interesting questions regarding the budget of mercury in magmatic settings and residing within the mantle, and how mercury is volatilized, thermally decomposed, and/or retained in crystallized mineral phases.

In all cases, the studies presented in this dissertation open a variety of new questions relating to past climate and environmental conditions that warrant further exploration. The most promising of these is the novel application of mercury concentrations to deep time records, and may provide exciting new insights into the nature of major extinctions, climate anomalies, and even anthropological events in the geological and historical records. Future work expanding upon mercury isotope compositions could allow for fingerprinting sources of mercury in these and other records, providing the strongest evidence to date for such phenomena as the abrupt climatic warming associated with Deccan volcanism detailed here.